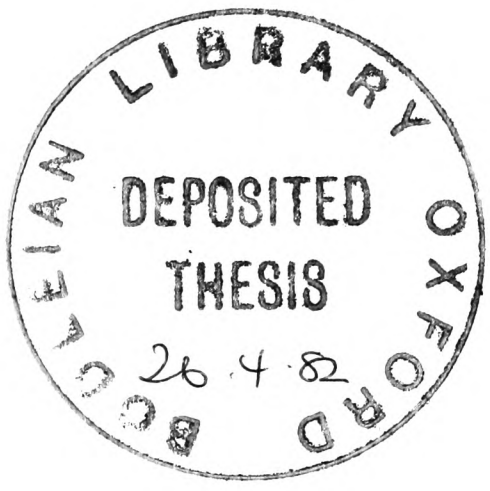
REFLECTION AND SCATTERING FROM CO_2–LASER – PRODUCED PLASMAS

MARTIN HUBBARD

ST JOHN'S COLLEGE



This thesis is submitted in partial fulfilment of the requirements for the degree of Doctor of Philosophy in the University of Oxford

Department of Engineering Science
Parks Road, Oxford

Michaelmas Term
1981

TO MY PARENTS

CONTENTS

Page

CHAPTER 1

THE 'APPLE' LASER SYSTEM 1

1.1 INTRODUCTION 1

1.2 CONSTRUCTION 1

1.3 OUTPUT CHARACTERISTICS 5

1.3.1 *INTRODUCTION* 5
1.3.2 *TEMPORAL PROFILE* 5
1.3.3 *ORGANIC ADDITIVES* 6
1.3.4 *OSCILLATOR CAVITY CONFIGURATIONS* 6

CHAPTER 2

ACHIEVEMENT AND CHARACTERIZATION OF THE 'OPTIMUM' FOCUS 10

2.1 TARGET CHAMBER AND FOCUSING OPTICS 10

2.2 DETERMINATION OF THE TARGET POSITION FOR 'OPTIMUM' FOCUS 12

2.2.1 *INTRODUCTION* 12
2.2.2 *HARD X-RAY EMISSION* 12
2.2.3 *TARGET DAMAGE* 15
2.2.4 *HARTMANN GRID TECHNIQUE* 15

2.3 CHARACTERISTICS OF THE OPTIMUM FOCUS — DETERMINATION OF THE IRRADIANCE 18

2.3.1 *INTRODUCTION* 18
2.3.2 *FIRST APPROXIMATIONS TO THE IRRADIANCE DISTRIBUTION* 19
2.3.3 *DIFFRACTION GRID TECHNIQUE* 21
2.3.4 *CONCLUDING REMARKS* 27

CHAPTER 3

EARLY MEASUREMENTS WITH THE APPLE LASER 28

3.1 INTRODUCTION AND EXPERIMENTAL DETAILS 28

3.2 ANGULAR DISTRIBUTION OF THE BACKSCATTERED RADIATION 29

3.2.1 *RESULTS* 32
3.2.2 *DISCUSSION* 34

3.3 TEMPORAL MODULATION OF THE BACKSCATTERED PULSE 38

3.4 THE SPECULAR CONTRIBUTION TO THE BACKSCATTERED RADIATION 40

3.4.1 *REFLECTIVITY AS A FUNCTION OF ILLUMINATION ANGLE* 41

3.5 SUMMARY AND CONCLUSIONS 44

CHAPTER 4

LASER-PLASMA MEASUREMENTS WITH THE UNSTABLE CAVITY 45

4.1 INTRODUCTION 45

4.2 PARASITIC OSCILLATIONS 46

4.2.1 *VARIATION OF PARASITIC OSCILLATIONS WITH ANGLE OF ILLUMINATION* 47
4.2.2 *PRELIMINARY SPECTRAL ANALYSIS* 52
4.2.3 *CONCLUDING DISCUSSIONS* 53

CONTENTS
(continued)

		Page
CHAPTER 4 (continued)		
4.3	BACKSCATTER REFLECTIVITY	54
	4.3.1 *VARIATION OF BACKSCATTER WITH FOCAL POSITION*	55
4.4	SIDE-SCATTER	57
	4.4.1 2π *COLLECTING MIRROR*	57
	4.4.2 *DIRECT SIDE-SCATTER MEASUREMENTS*	59
	CHAPTER 5	
	CUPID – A RAY TRACING PROGRAM FOR CONTINUOUSLY VARYING REFRACTING MEDIA	69
5.1	INTRODUCTION	69
5.2	THEORY	70
5.3	ACCURACY TESTS	77
	5.3.1 *ANGLE OF INCIDENCE VERSUS DEFLECTION FOR PLANE PARALLEL GEOMETRY*	77
	5.3.2 *ACCURACY OF ROUTINE IN SPHERICAL GEOMETRY*	78
5.4	VALIDITY	80
5.5	RAY TRACING RESULTS FOR VARIOUS NON-PLANAR GEOMETRIES	82
	5.5.1 *INTRODUCTION*	82
	5.5.2 *ELLIPTICAL GEOMETRY*	82
	5.5.3 *RIPPLED GEOMETRY*	84
	5.5.4 *CONCAVE ISO-DENSITY CONTOURS*	88
	5.5.5 *THE EFFECT OF LARGE SCALE FEATURES AT THE CRITICAL SURFACE*	89
	CHAPTER 6	
	SPECTRAL MEASUREMENTS OF THE BACKSCATTERED RADIATION	94
6.1	INTRODUCTION	94
6.2	APPARATUS	94
6.3	INCIDENT AND BACKSCATTERED SPECTRA	97
6.4	STIMULATED BRILLOUIN SCATTERING (SBS) IN AN EXPANDING PLASMA	101
	6.4.1 *POSITION OF THE SBS PROCESS IN AN INHOMOGENEOUS PLASMA*	104
6.5	DETERMINATION OF THE DOPPLER SHIFT	112
6.6	INTERPRETATION OF SPECTRA	114
	6.6.1 *ORIGIN OF RED SHIFTED SIDEBAND*	114
	6.6.2 *RED SHIFT OF MAIN PEAK*	115
	6.6.3 *DETERMINATION OF THE COLD ELECTRON TEMPERATURE*	117

CONTENTS

(continued)

Page

CHAPTER 7

ABSORPTION AND SCATTERING THEORY – COMPARISON WITH EXPERIMENT 119

7.1 INTRODUCTION 119

7.2 ABSORPTION PROCESSES 119

7.2.1 *CLASSICAL ABSORPTION* 119
7.2.2 *RESONANCE ABSORPTION IN NON-PLANAR PLASMAS* 127
7.2.3 *BRIEF REVIEW OF OTHER ABSORPTION RESULTS* 128
7.2.4 *CONCLUDING DISCUSSION* 130

7.3 BACKSCATTER 131

7.3.1 *INTRODUCTION* 131
7.3.2 *BACKSCATTER LEVEL (SATURATION BY ION HEATING)* 132
7.3.3 *BACKSCATTER LEVEL (SECONDARY DECAY INSTABILITIES* 135

CHAPTER 8

CONCLUDING DISCUSSION AND SUGGESTIONS FOR FUTURE WORK 138

8.1 INTRODUCTION 138

8.2 EXPERIMENTAL RESULTS 138

8.2.1 *SPATIAL DISTRIBUTION AND ABSOLUTE REFLECTIVITY OF THE SCATTERED RADIATION* 138
8.2.2 *TEMPORAL STRUCTURE OF THE BACKSCATTER* 140
8.2.3 *SPECTRAL ANALYSIS OF THE BACKSCATTER* 140

8.3 SUGGESTIONS FOR FUTURE WORK 141

APPENDICES

App. A 1 THE CO_2 LASER 143

App. A 2 DIAGNOSTIC ALIGNMENT 147

App. A 3 THE USE OF A 2-D DIFFRACTION ARRAY TO OBTAIN THE FAR FIELD INTENSITY DISTRIBUTION – THEORY 150

App. A 4 RESONANCE ABSORPTION IN NON-PLANAR PLASMAS 153

REFERENCES 155

REFLECTION AND SCATTERING FROM CO_2-LASER - PRODUCED PLASMAS

M. Hubbard, St John's College

A thesis submitted for the degree of Doctor of Philosophy
in the University of Oxford, Michaelmas Term, 1981

ABSTRACT

An experimental study of the interaction between 10.59 μm CO_2-laser radiation and the plasma produced by that radiation on plane, massive targets in a vacuum, is described. The laser used was a TEA double discharge device, giving an (in vacuo) irradiance in the regime of 10^{12} W/cm^2 with 50 ns FWHM gain switched pulses. The laser oscillator cavity was operated in both stable and unstable configurations.

Particular emphasis was placed on the full diagnosis of the scattered light and experiments were, therefore, designed to investigate the spatial, temporal and spectral characteristics of this unabsorbed fraction.

The irradiation conditions under which the experiments were performed were investigated by analysis of the far field energy distribution.

High absorption of the incident radiation was inferred from the low reflectivity level, the fraction of the incident radiation scattered outside the solid angle of the focusing lens being accounted for, using a novel collecting mirror, or by the use of calibrated burn paper. Thus a *total* reflection was measured for the first time. A simple model was developed to enable the classical absorption contribution to the total absorption to be estimated, and results indicated that inverse bremsstrahlung absorption would be an important process for the conditions pertinent to the interaction. The contribution of anomalous absorption and scattering processes was estimated. Predicted cold electron temperatures and density scale lengths from the model, agreed well with those determined experimentally without the need to invoke flux inhibition.

The spectral composition of the backscattered radiation in the region of the fundamental was investigated, and measured spectra were successfully interpreted by considering the stimulated Brillouin scattering process, and the Doppler effect of the expanding plasma corona. In particular, the dependence of the parametric growth rate on electron density was investigated by numerical solution of the ion acoustic wave dispersion relation.

The angular distribution of the backscattered radiation was determined using annular apertures in the backscattered beam and the distribution found to be non-isotropic. Interpretation was based upon the resonance absorption process in a non-planar plasma geometry and invoked the retro—reflecting nature of the stimulated Brillouin scatter mechanism

To investigate the effect of wave refraction in the underdense plasma (exhibiting a continuous density profile), a compact and readily used ray-tracing routine was developed and applied to plasmas with planar, rippled and simple concave or convex iso-density contours.

ACKNOWLEDGEMENTS

It is a pleasure to acknowledge the invaluable advice of my supervisor, Dr Ian Spalding, during the course of this work. I am also glad to record my appreciation to Dr Raoul Franklin for his continued interest and encouragement.

It would be impracticable here to list all of the many other people who have given advice and assistance during the experimental, analytical and narrative phases of this thesis. I would particularly thank, however, Dr T.P. Donaldson for his help in the early stages; Drs A.C. Walker, J.M. Green and T. Stamatakis for many fruitful discussions and for their willingness to give not only much of their time but also much of their equipment; and Drs Antonio Montes and Brian Thomas for the many stimulating hours of discussion and debate.

I gratefully acknowledge the support of a Science Research Council studentship and the facilities afforded me by the UKAEA Culham Laboratory under an EMR contract.

I would finally like to acknowledge the considerable moral support of my wife, Linda, and the meticulous typing and setting out of this thesis by Ina Godwin.

PREFACE

The field of inertial confinement fusion has grown rapidly since the idea of controlled thermonuclear reaction based on laser heating of matter to thermonuclear conditions was first proposed in the open literature (BASOV and KROKHIN, 1964). The concept of fuel compression first appeared in the literature with the oft quoted paper of NUCKOLLS *et al.* (1972), and this led to the development, in many laboratories around the world, of facilities capable of irradiating a spherical fuel pellet in an attempt to achieve the high densities required for thermonuclear burn. Although, to date, the goal of scientific breakeven has not been reached, high fuel compressions have been demonstrated and thermonuclear neutrons (as opposed to those generated by beam-target interactions) have been detected.

A scheme to generate net power from the implosion of a tiny fuel element must necessarily involve many diverse research topics, amongst which, high power laser development, target design and fabrication, diagnostic development and reactor studies, are very important; much work is being performed in these areas. However, an understanding of laser-plasma interaction physics, both experimental and theoretical, is a prerequisite of the scheme, and this thesis will be concerned with this particular aspect.

As diagnostic techniques have become more refined and experiments conducted over a wider range of conditions, it has been found that the interaction physics is characterized by a wealth of classical and anomalous phenomena. The emphasis of research has also broadened. Early work tended to concentrate exclusively on measurements of the fractional absorption of the incident laser light by the target, and it was through this work that the first departures from classical physics came, with the realization that inferred absorptions were higher than expected. Thus, experimental and theoretical studies of the anomalous absorption processes began. However, anomalous scattering mechanisms were also proposed, and observed, and moreover, it was becoming clear that although it was possible to absorb a large fraction of the incident energy in the plasma corona surrounding the target, this energy was not necessarily efficiently coupled to the hydro-drive producing fuel compression. Of particular importance in this respect are the phenomena of electron run-away (or decoupling), fast electron preheat, density profile modification and electron transport inhibition. Mechanisms for

fast electron generation are being extensively studied in an attempt either to negate the detrimental effects on pressure generation; when energy is lost to energetic non-thermal electron distributions which reduce ablation pressure by transferring momentum inefficiently and by smearing out the ablation front, or on compression; when the fuel is prevented from following the correct adiabatic by a small preheat level. Schemes to utilize the fast electron pressure as a drive, via suitable target design are also being examined.

Similarly, experiments and simulation to determine why thermal electron energy should appear to be anomalously constrained to the underdense corona, in certain instances, are being continued. Another potentially damaging phenomenon for ICF is that of compression asymmetry due either to non-uniform irradiation or to instabilities during implosion. It is, perhaps, true to say that of all the topics so far mentioned, least experimental work has been carried out on this aspect.

Current diagnostics of laser-plasma interaction or ICF experiments involve either the measurement of those entities emitted *from* the interaction region or the analysis of perturbations to an external probe, caused *by* the interaction region. The former type can be divided into those diagnostics concerned with the detection either of emitted radiation or of emitted particles. Radiation detection can be further subdivided into analysis of that emitted by the plasma (or target) as a result of its excited state and that emitted as a result of classical reflection, nonlinear harmonic generation or stimulated scattering. Although this thesis will occasionally refer to other diagnostic techniques employed during the course of the experimental work, its main theme is the study of the unabsorbed fraction of the incident radiation and will describe the spatial, temporal and spectral measurements made on this particular entity.

The laser used for the experiments was a TEA (Transversely Excited Atmospheric) CO_2, double discharge device and its 10.59 μm wavelength output beam was focused onto plane massive targets in a vacuum, using refractive optics. The laser, its principles of operation and its output characteristics are described in Chapter 1. The measurements of the focal irradiance is discussed in Chapter 2, and the effects of spatial and temporal structure on the far field are described. The value of the (in vacuo) irradiance which characterized the conditions under which experiments were performed is presented. The limitations of ascribing a single parameter to describe

focal conditions is discussed in the chapter.

In Chapter 3, experiments performed with the laser giving multimode output are described. Measurements to determine the angular distribution of the backscattered radiation were performed. Significant structure was found and interpretation is presented. Emphasis was also placed upon determination of the *total* reflectivity, i.e., including that portion of the unabsorbed radiation scattered outside the solid angle of the focusing lens. To this end, a collecting mirror was employed to direct the side-scattered component onto an external detector. The results indicated very high total absorption, and the accuracy of the measurement is discussed. It was observed that the backscattered pulse was temporally modulated with a correlation with the temporal structure of the incident pulse. Possible explanations are examined. Finally, measurement of the contribution of specular reflection to the backscattered fraction is described.

In order to more fully quantify the experimental conditions, the oscillator cavity was changed to an unstable configuration thus giving a single transverse mode output with better focal properties. Chapter 4 describes the experiments performed with this beam. Once again, total reflectivity was measured and in this case the 2π-collecting mirror technique was complimented by the use of calibrated burn paper (exposed polaroid film) positioned in an arc around the target. High absorption was again measured. The observation of parasitic oscillations is described and implications with regard to plasma processes are analysed. Side-scatter distributions were recorded on burn paper for non-normal illumination of the target. An unexpected effect, whereby the scattered radiation appeared to be refracted to angles greater than specular is described.

The need for a ray tracing program to investigate the effect of refraction on the scattered light during its passage out through the corona was indicated by the experiments described in Chapter 4. In Chapter 5, a simple compact and readily usable ray tracing program is presented, results of accuracy tests discussed and refraction effects in non-planar geometries described. Although no evidence was found to link the effects described in Chapter 4 with coronal refraction, the ray trace routine was a useful tool in its own right and was, in fact, extended to allow resonance absorption to be estimated in non-planar plasmas (Appendix A4).

Spectral analysis of the backscattered radiation was performed and the experiments are described in Chapter 6. Spectra were built up on a

shot-to-shot basis tuning the spectrometer grating between shots, and were also obtained for a single shot, using a linear pyroelectric detector array. A sideband on the long wavelength side of the fundamental position was observed and the Doppler contribution to the spectrum was found by measuring spectral content as a function of target illumination angle. Results were successfully interpreted by considering the stimulated Brillouin scattering process in an expanding plasma. From the theory of this process it was possible to deduce the electron temperature in the sub-critical region and this value was found to be in good agreement with that obtained from X-ray bremsstrahlung spectra. In order to interpret the results it was necessary to know the electron density of the region of origin of the scattered radiation. This was accomplished by numerical solution of the ion-acoustic wave dispersion relation in order to find the variation of growth rate with density.

In Chapter 7, a simple model is described which enabled an estimate of the inverse bremsstrahlung contribution to the overall absorption to be made. This work was extended to consider the importance of other absorption processes; in particular, resonance absorption in a non-planar plasma. The expected level of stimulated Brillouin scattering was derived and various saturation processes considered. It is shown that the experimental results of high absorption and the presence of parametric processes are not inconsistent with the results of the simple models.

CHAPTER 1

THE 'APPLE' LASER SYSTEM

1.1 INTRODUCTION

In this chapter, the CO_2-laser used during the course of this work will be described. To obtain maximum insight into the operation of this laser in particular, it is useful to have a brief review of the theory of CO_2-lasers in general. This is done in Appendix A1.

1.2 CONSTRUCTION

The basic APPLE laser (Atmosphere Pressure Pulsed Laser Experiment) was built at the U K A E A Culham Laboratory approximately 8 years ago. During the work of this thesis, modifications and changes to the original system have been made, mainly in the oscillator cavity configuration. Fig. 1.1 shows a general view of the laser room.

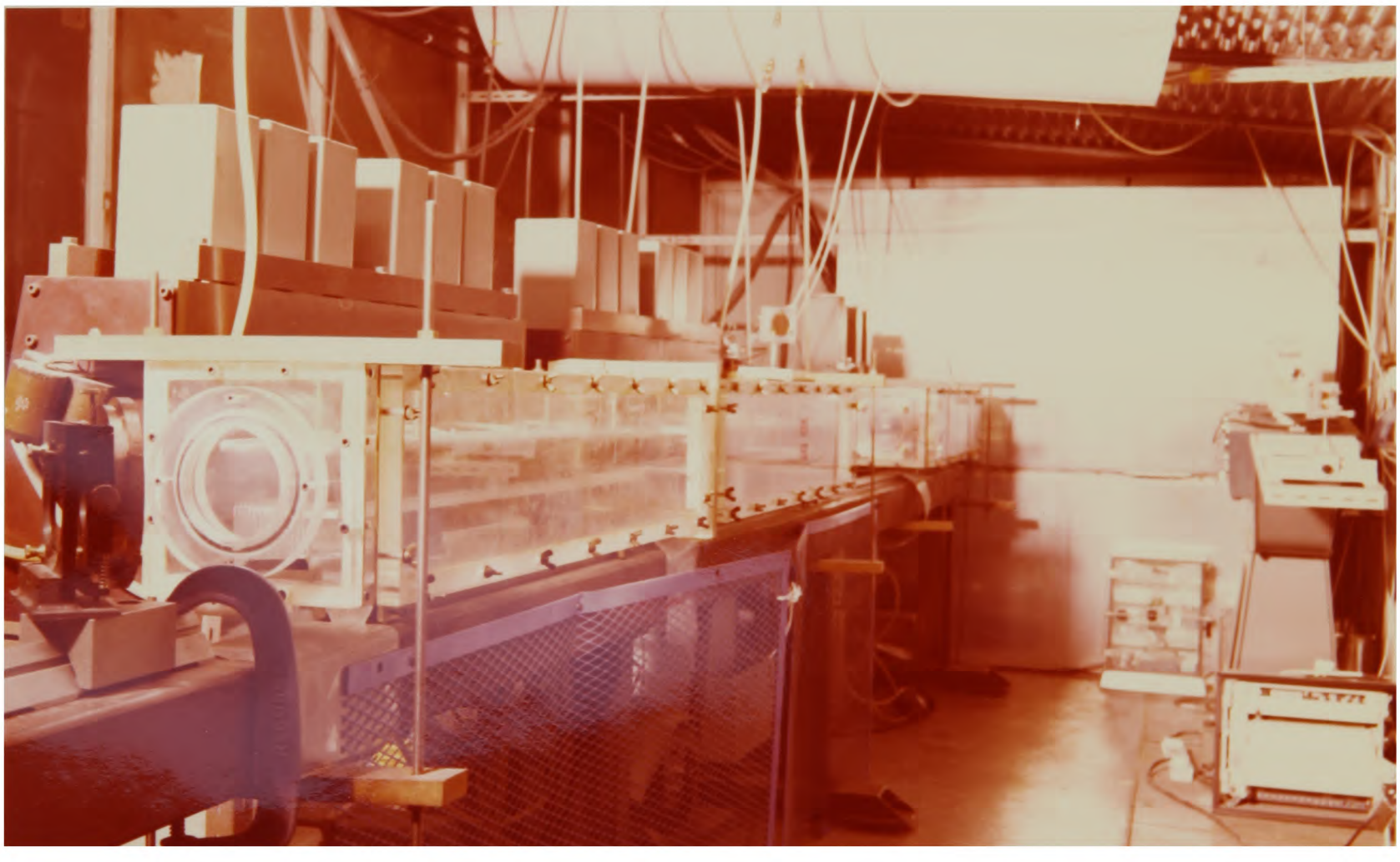


Fig. 1.1
General view of the laser room showing the oscillator (background) and amplifier (foreground) modules, the main turning mirror and the alignment He-Ne laser (right-background)

The laser consisted of an oscillator module ~1.3 meters long, and two amplifier modules each of the same length. All the modules had the same electrode configuration; namely an 11 cm wide aluminium anode and cathode, separated by a 5 cm gap. Machined aluminium vanes on the cathode were essential to the double discharge mode of operation (see later) and also provided for the glass encapsulated trigger wires. The wires were at the same height as the top of the vanes.

The gas composition was adjusted by independent flow meters on each of the three gas lines, prior to mixing in the single line leading to the modules. The exact proportion of each gas constituent will be discussed below.

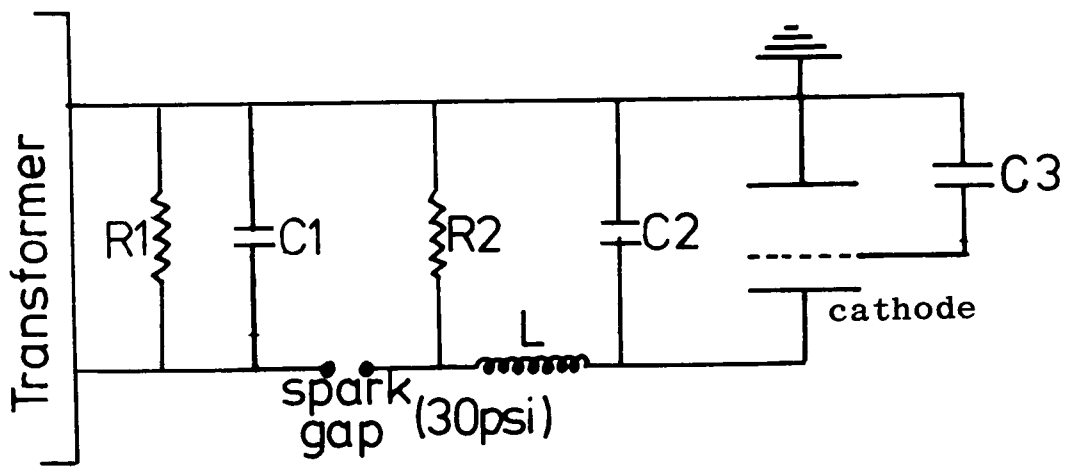


Fig. 1.2
Schematic of the laser electrical circuit
R1 = 200 Ω, R2 = 100 Ω
C1 = 0.3 μF, C2 = 0.15 μF
C3 = 1200 pF, L = 6.0 μH

The electrical circuit is shown schematically in Fig. 1.2.

The low inductance storage capacitor C_1 is charged by the Culham built transformer. Upon breakdown of the dry air filled spark gap, the stored electrical energy is fed to the pulse shaping netweork formed by L and C_2, and voltage applied to the cathode. As the voltage rises, the electric field gradient between the trigger wires and the cathode, grows more rapidly than across the electrodes. A corona discharge forms between the cathode vanes and the trigger wires. The coupling capacitor C_3 then charges up, reducing the field between the trigger wires and the cathode, and trapping an electron cloud in the cathode vicinity. These electrons, together with the U.V. also formed by the corona discharge, lower the discharge impedance in the main volume and initiates the main glow discharge between cathode and

anode. (This discharge can be seen as a blue glow in Fig. 1.3, which is a general view of an amplifier module. The train of air sparks seen in the upper half of the photograph was produced by focusing the output with a 3.2 meter focal length mirror (out of view to the left).) Laser action

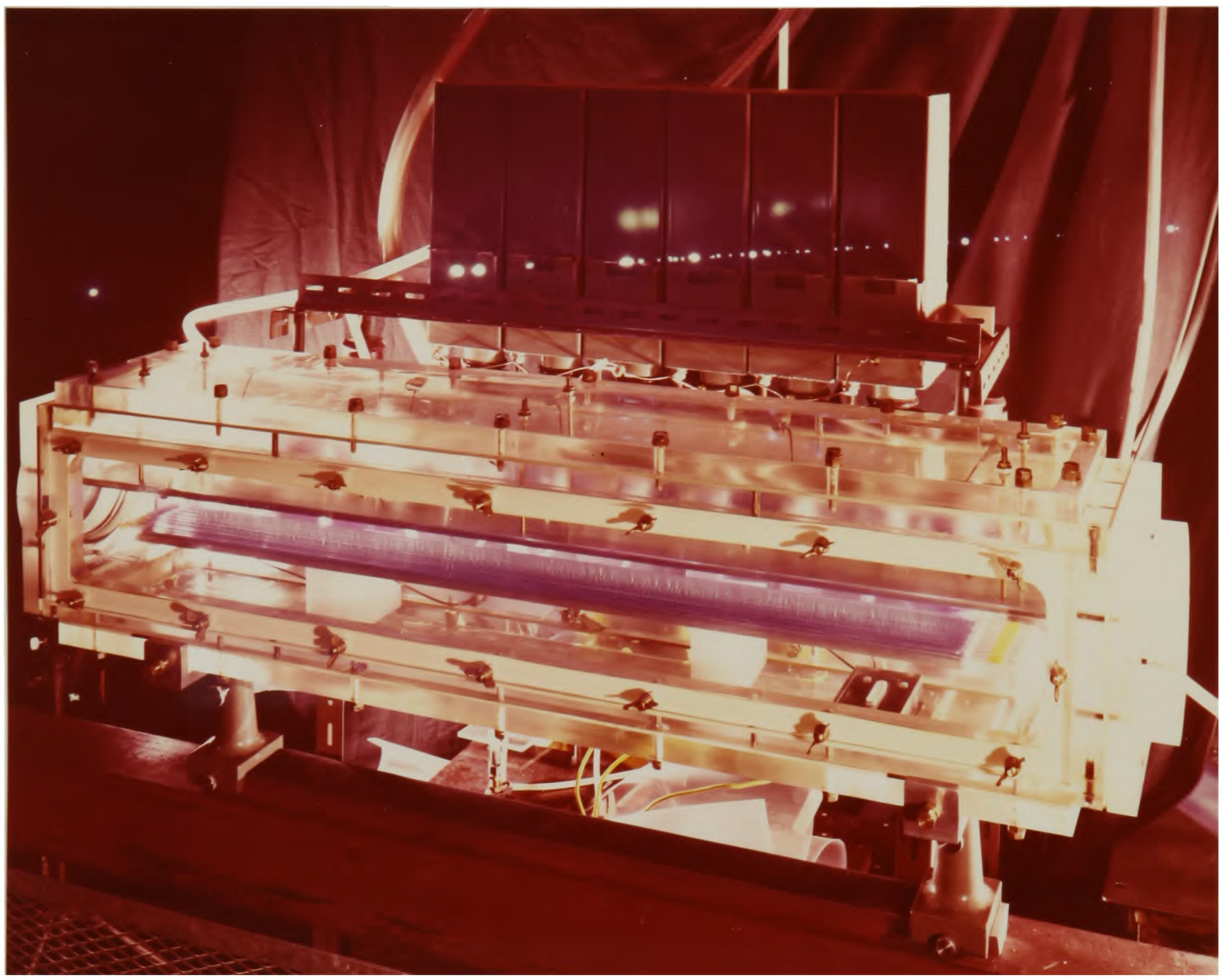


Fig. 1.3
Amplifier module during discharge

occurs and the ~ 10 cm X 5 cm output beam emerges from the oscillator cavity and enters the amplifier modules. These have already been pre-ionized in the same manner as the oscillator. The optimum time delay between ionization of the amplifier and oscillator was found empirically to be ~ 1 μs.

The oscillator cavity contained an NaCl flat set at the Brewster angle to form a multi-pass polarizer producing vertically polarized output, Input and output windows of the amplifier chain also consisted of NaCl plates, polished to a surface finish of λ/10 at 10.6 μm. Salt optics were

used extensively throughout this work, the advantages being relative cheapness, and ease of alignment with visible He-Ne beams. The disadvantage was that the unprotected surfaces of the hygroscopic substrates absorbed moisture and degraded rapidly. Heat lamps were thus used in the laser and target areas to raise the ambient temperature and keep the optics moisture free. Another problem with the use of salt optics was the difficulty of providing anti-reflection coatings that would withstand the high energy densities of the experiments. Although tests were carried out on A.R. coatings provided by the Department of Cybernetics of Reading University (SEELEY, 1978), no suitable coating was found and so uncoated salt optics were used throughout the course of this work.

Early experiments were performed with the oscillator cavity in a plane/plane configuration consisting of an ~ 100% reflecting, diamond turned oxygen-free copper substrate, gold coated, rear cavity mirror and a 50% transmitting germanium front mirror which also constituted the exit window of the oscillator module. The mirrors were mounted kinematically and were adjustable via three micrometers on each mount. Later experiments employed the unstable cavity configuration described later (section 1.3.4). The output parameters for both arrangements will also be described later in section 1.3.

Gross cavity adjustments were made using a He-Ne alignment laser whilst fine tuning to maximize the output energy and beam quality was performed empirically employing a pyroelectric joulemeter and exposed polaroid burn paper. In the case of the plane/plane configuration the gross cavity alignment was performed by first adjusting the rear mirror, with the germanium mirror removed, so that a back-reflected He-Ne beam passed centrally through the amplifier chain. The front mirror was then replaced and adjusted until back-reflection from it passed along the same line. In the case of the unstable cavity, an alignment hole in the rear mirror was employed as will be described in section 1.3.4.

1.3 OUTPUT CHARACTERISTICS

1.3.1 *INTRODUCTION*

The output pulse shape (temporal), energy and mode structure, varied throughout the course of this work and the relevant sections of this thesis will detail the absolute values of these parameters. The purpose of the next section is to show how variation of gas composition and cavity configuration affected the output characteristics in general.

1.3.2 *TEMPORAL PROFILE*

The temporal shape of the pulse, as measured with a photon drag detector, was composed of an initial gain switched spike of FWHM ~ 50 ns and a low intensity tail of much greater length. The length of this tail, and the total energy in the whole pulse (spike and tail) could be varied by adjustment of the proportion of nitrogen in the laser gas mixture (see for example STAMATAKIS, 1977). Increasing the nitrogen content increased the total energy in the pulse at the same time increasing the length of the tail. It was decided to operate with a 50:50 energy division between the spike and the tail and it was found empirically that a CO_2:N_2:He gas mixture of ~ 1:0.4 : 5.0 provided this ratio. A typical output pulse from the plane/plane cavity configuration is shown in Fig. 1.4. An output pulse from the unstable cavity can be seen in section 1.3.4 (Fig. 1.5).

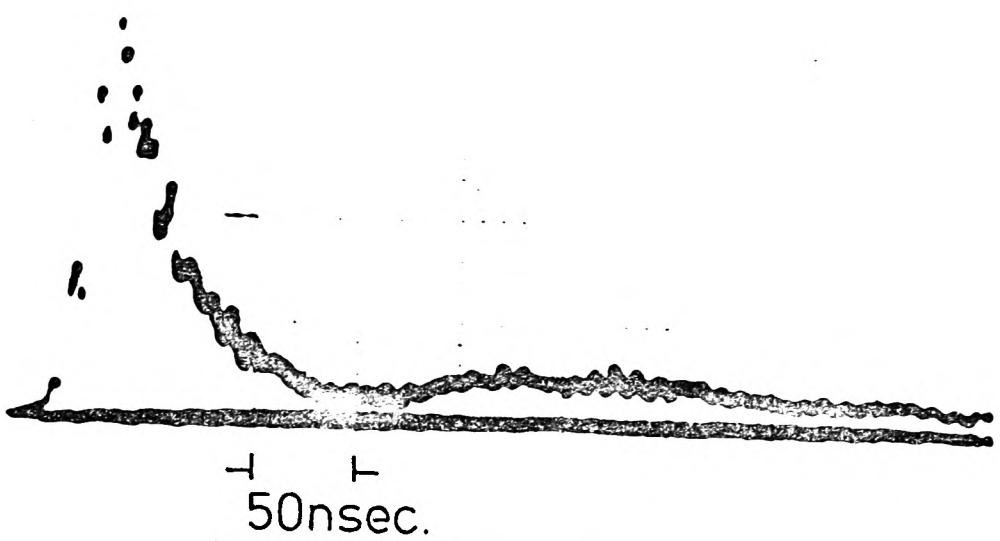


Fig. 1.4
Output pulse from laser with the oscillator cavity in the stable configuration

Typical energies in the initial spike were of the order of 75 J giving an output power (peak) of 1.5 GW (see section 2.3). The helium concentration was adjusted to be the optimum for maximum energy output (as a function of charging voltage) without arc formation.

1.3.3 *ORGANIC ADDITIVES*

At this stage, the effects of organic additives on the laser performance should be briefly mentioned. There are three main reasons why an additive such as triethylamine, $(C_2H_5)_3N$, should be inserted into the gain medium (STAMATAKIS, 1977). First, by seeding the laser gas mixture with an organic vapour of low ionization potential (7.5 eV), the quantity of helium needed to prevent arc formation can be reduced. In this aspect, more efficient use is made of the ultra-violet radiation from the corona-discharge. Secondly, spatial non-uniformities in the laser output tend to be reduced by the seedant through an increase of gain uniformity in the gas volume. This effect is believed to be due to photo-ionization of the seedant gas which is then evenly distributed in the laser gas. A third effect relates to the reduction of parasitic oscillations (see Chapter 4).

However, although the benefits listed above appear attractive, tests carried out with triethylamine vapour showed that overall benefits in terms of energy increase, beam quality and parasitic reduction, were not sufficiently great to warrant the difficulties of pumping the noxious substance through the laser modules. These modules, being at atmospheric pressure, invariably leaked into the laser and target rooms, producing a very unpleasant working environment.

1.3.4 *OSCILLATOR CAVITY CONFIGURATIONS*

In this section, the effect of oscillator cavity configuration on the output characteristics will be dealt with.

When operated in the stable plane/plane configuration, the oscillator

output had a multimode structure in both the transverse and longitudinal forms. The effect of this on the near-field pattern was to give an approximation to a 'top-hat' profile by the superposition of many spatial modes. Burns on exposed polaroid confirmed that this was generally the case. However, hot spots did occur from reflection off the electrodes if the oscillator and amplifier modules were not in accurate relative alignment. There was also inherent structure of large spatial frequency on the beam due to the ionization inhomogeneity caused by the trigger wires. (These last two points of course apply to the unstable cavity also.)

It was experimentally verified that total output energy was greater from the system operating with the stable rather than the unstable configuration. This was due to the more efficient use of the active volume in the former arrangement. Typical energies in the whole pulse for the stable oscillator and both amplifiers could be as high as 150 Joules.

As can be seen in Fig. 1.4, the output pulse shape is not smooth but has a superimposed modulation on it. This was caused by beating between the longitudinal modes. However, for the stable cavity, each particular transverse mode has its own set of longitudinal modes. These sets are not mode locked and so the Fourier transform tends to be a smooth function in time, producing a low contrast ripple on the gain switched envelope. The frequency of this ripple is the reciprocal of the oscillator cavity round trip transit time, and is ~ 8.5 ns.

In contrast, the depth of modulation on the single transverse mode output from the unstable cavity is much greater as can be seen from Fig. 1.5, which shows the gain switched spike from the unstable oscillator as recorded on a Tektroniks 7633, 100 MHz bandwidth storage oscilloscope. Of course a single transverse and longitudinal mode output would result in a perfectly smooth pulse and the production of such pulses from a CO_2-laser is described by STAMATAKIS and SELDEN, (1976).

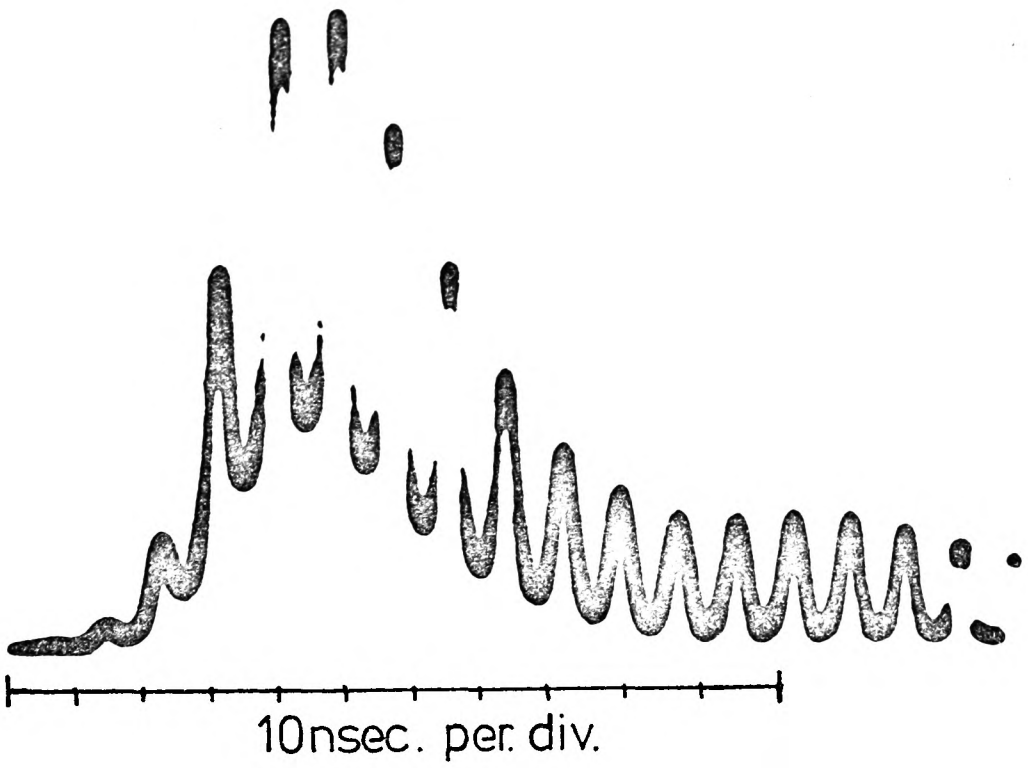


Fig. 1.5
Gain switched spike from the oscillator cavity operating in the unstable configuration

The inherent difficulty with the plane/plane configuration was the problem of focusing the multimode output. The point will be discussed in Chapter 2. It was due to the fact that small focal spots could not be achieved with the stable oscillator (each transverse mode having its own divergence), that later experiments (described in Chapters 4 and 6) employed the unstable, confocal system. This geometry results in a single transverse mode output still lasing on many axial modes. The beam spatial profile is a Gaussian TEM_{00} with a central shadow due to the front mirror. Figure 1.6 shows this mirror arrangement.

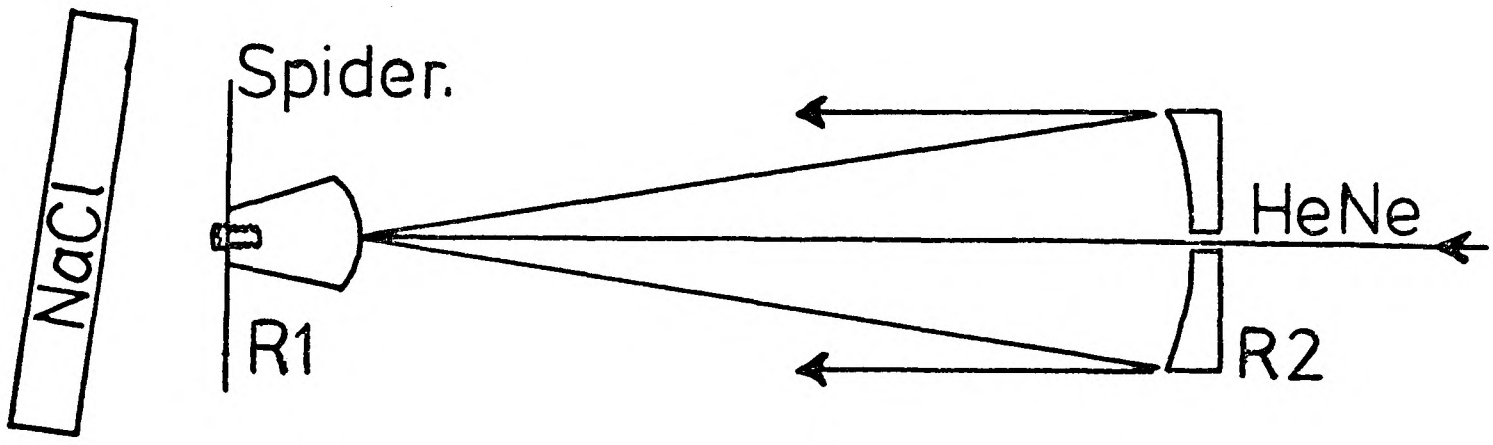


Fig. 1.6
The oscillator cavity mirror arrangement for operation in the unstable configuration. The NaCl output window is shown but not the polarizing flat. Values for R_1 and R_2 are given in the text

The mirrors were designed using a magnification M equal to 4. From the usual equation for an unstable cavity of this type (SIEGMAN, 1971)

$$R_1 = \frac{L}{1-g_1} \quad \text{and} \quad R_2 = \frac{L}{1-g_2}$$

where

$$g_1 = \frac{M+1}{2} \quad \text{and} \quad g_2 = \frac{M+1}{2M} \ .$$

For a cavity with $L = 1.31$ metres (set by the module length and mirror mounts available), $R_1 = -0.87$ metres, and $R_2 = 3.49$ metres. These mirrors were diamond turned at Culham from oxygen free copper, and gold coated.

The convex mirror was mounted by a single screw onto a three strut spider machined so that it was accurately positioned on the axis of the cavity. It was tapered to avoid edge diffraction effects and its cross-section was of basic dimensions 25 mm X 11.7 mm to match the cross section of the cavity's active region. The concave mirror was of 12 cms diameter with a 2 mm diameter hole drilled on axis. This hole allowed a He-Ne beam to be shone into the cavity where it was expanded by the mirror system and output through the salt window in front of the spider. In this way the cavity could be tuned, as the He-Ne beam thus defined the same path as the CO_2 output. The mirror was mounted into the same mount as the plane mirror in the original stable cavity. The alignment hole was covered with a microscope slide to prevent impurities entering the module.

The FWHM of the temporal shape of the output pulse was still ~ 50 ns as can be seen from Fig. 1.5, and the energy distribution between spike and tail remained the same as for the stable cavity operating with the same gas mixture.

Typical output energies were found to be lower for the unstable configuration but the improvement in focusability due to improved mode structure and divergence adequately compensated for this as far as peak target irradiance was concerned. The next chapter will deal with the focussing arrangements used during this work and will discuss the characterisation of the focal parameters obtained when an optimum focus was achieved.

CHAPTER 2

ACHIEVEMENT AND CHARACTERIZATION OF THE 'OPTIMUM' FOCUS

2.1 TARGET CHAMBER AND FOCUSING OPTICS

Figure 2.1 shows a general view of the target chamber. Its reasonably mobile construction enabled ease of alignment relative to a coaxial alignment beam. (The diagnostic alignment system and calibration procedures are described in Appendix A2.) Its position was adjusted until the beam passed centrally through its entrance and exit windows. This figure is an

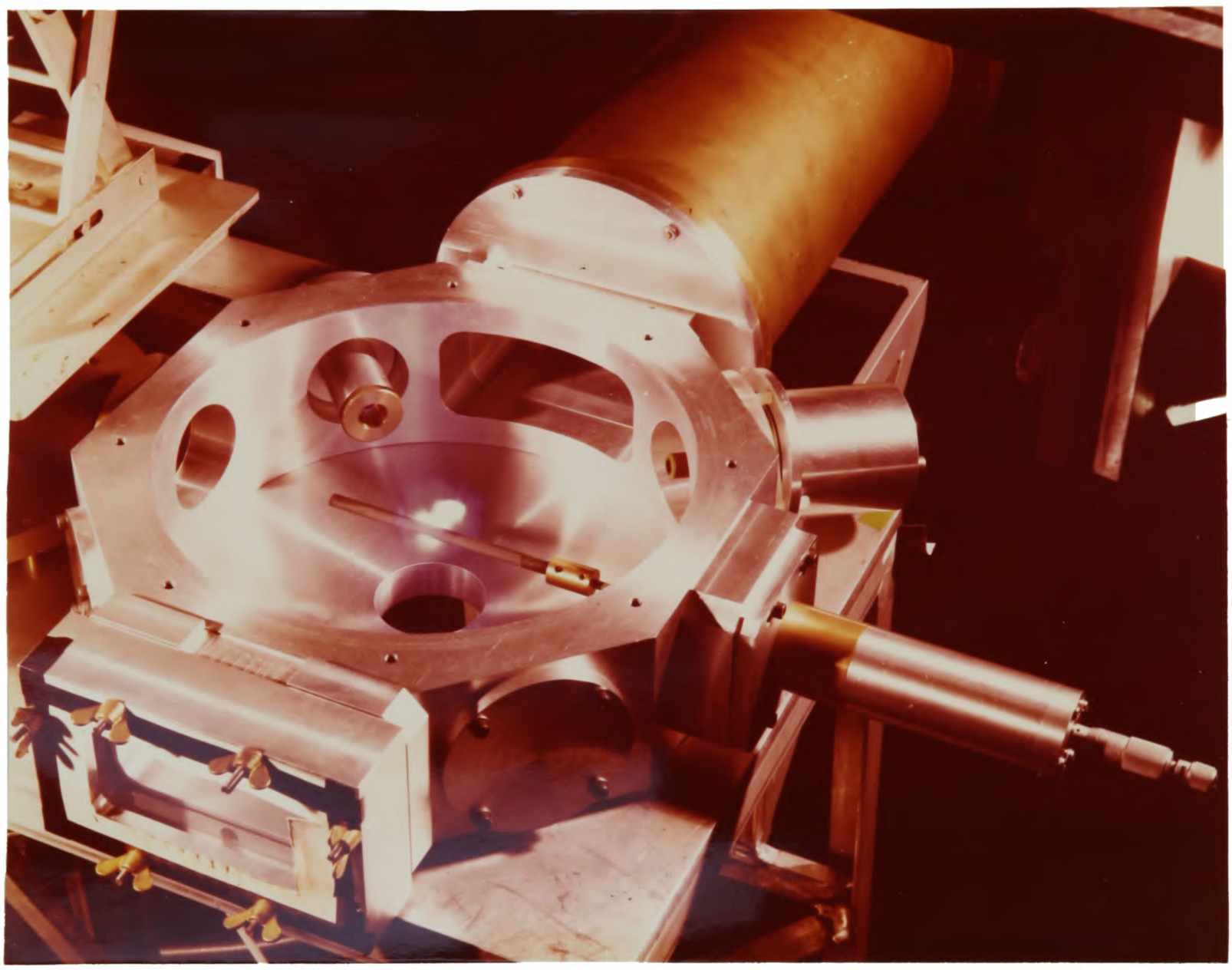


Fig. 2.1

Early photograph of the target chamber. Plasma formed in air by the CO_2 beam focused onto a carbon target can be seen. The beam is incident through the salt window (left-foreground) and passes the target before being focused by a spherical mirror (situated inside the brass cylinder attached to the chamber)

early photograph of the chamber with the top removed and the laser focused onto a carbon target in air, using a 30 cm focal length, gold coated, spherical mirror. This illustrates the focusing geometry employed for very early work (see for example DONALDSON and SPALDING, 1976). The incident laser beam, being focused onto the target by an on-axis mirror, was shadowed by the target. The advantage of reflective focusing was that visible radiation, i.e. the He-Ne alignment laser, could be used to focus the system. However, it was decided that the aberrations introduced by the spherical mirror, and the energy attenuation due to shadowing, warranted a change to refractive focusing, and all the work discussed in this thesis was performed with a lens as the focusing element.

The lens used in this work was made from KCl, was uncoated (see section 1.2) and was of meniscus design (shape factor $q = 1.32 = (r_2 + r_1)/(r_2 - r_1)$) with focal length of $\sim$ 22 cm at 10.6 μm. The lens was held in a variable tilt frame and inserted into the target chamber via three Wilson seal sliding rails. The lens orientation relative to the alignment He-Ne was adjusted until the lens axis was co-linear with the beam axis. This was achieved by observation of the retro-reflected He-Ne radiation from the lens surfaces.

Targets were positioned in the target chamber either on fixed mounts or held in a rotating target manipulator connected via a Wilson seal, to a micrometer position adjuster (shown in Fig. 2.1).

The chamber vacuum was achieved by a single diffusion pump, backed by an Edwards rotary pump. The pressure inside the chamber was monitored with an ion gauge and experiments were carried out with typical chamber pressures of a few $\times 10^{-5}$ torr. Such pressures could be realized after about 30 minutes pumping.

Care was taken throughout all experiments, to ensure that the target surface was held at accurately reproducible positions relative to the lens.

These positions were varied by holding the target fixed, and moving the lens with the slide rails. To obtain a good He-Ne focus for initial alignment of the target, the diffraction pattern of a wire mesh was observed on the target surface through an optical microscope. This position of best focus was then taken to be the reference position from which all other lens positions were measured.

The next sections will deal with the focusing, and focal characteristics, of the CO_2 beam.

2.2 DETERMINATION OF THE TARGET POSITION FOR 'OPTIMUM FOCUS'

2.2.1 *INTRODUCTION*

In theory, the target surface could have been positioned at the geometric focus of the lens by knowledge of the lens refractive index at 10.59 μm and the figuring of its surfaces. For reasons which will be discussed later, however, the actual position of the target surface that maximized the power density (irradiance) of the interaction, could not be assumed to coincide with the geometric focus and was found empirically, using one or more of the methods described below. Each method involved the observation of some parameter as it varied with target position until a turning point was obtained; this position being termed the 'optimum focus'. The characteristics of this optimum focus were then determined (section 2.3) and used in the interpretation of the experimental results.

2.2.2 *HARD X-RAY EMISSION*

The determination of electron temperature from the X-ray transmission through various edge filters is a widely employed method in laser plasma interaction experiments. Although it will not be described in this thesis, the technique was used on the apparatus (KLER, 1980) and thus the necessary photomultiplier-foil combinations were readily positioned on the target chamber ports and were easily brought into service in order to find the optimum focus as will now be described.

Aluminium foils, 100 μm thick, and having a transmission greater than $1/e^2$ from unity for X-ray photon energies $\gtrsim$ 7 keV, were used in front of NaI scintillators. The visible radiation produced by these scintillators was 'piped' via plastic light guides to the photomultipliers. Fig. 2.2 shows a plot of the relative photomultiplier output versus lens position (relative to the lens position giving the best He-Ne focus on a fixed carbon target) for the laser operating in an unstable configuration with constant (monitored) output.

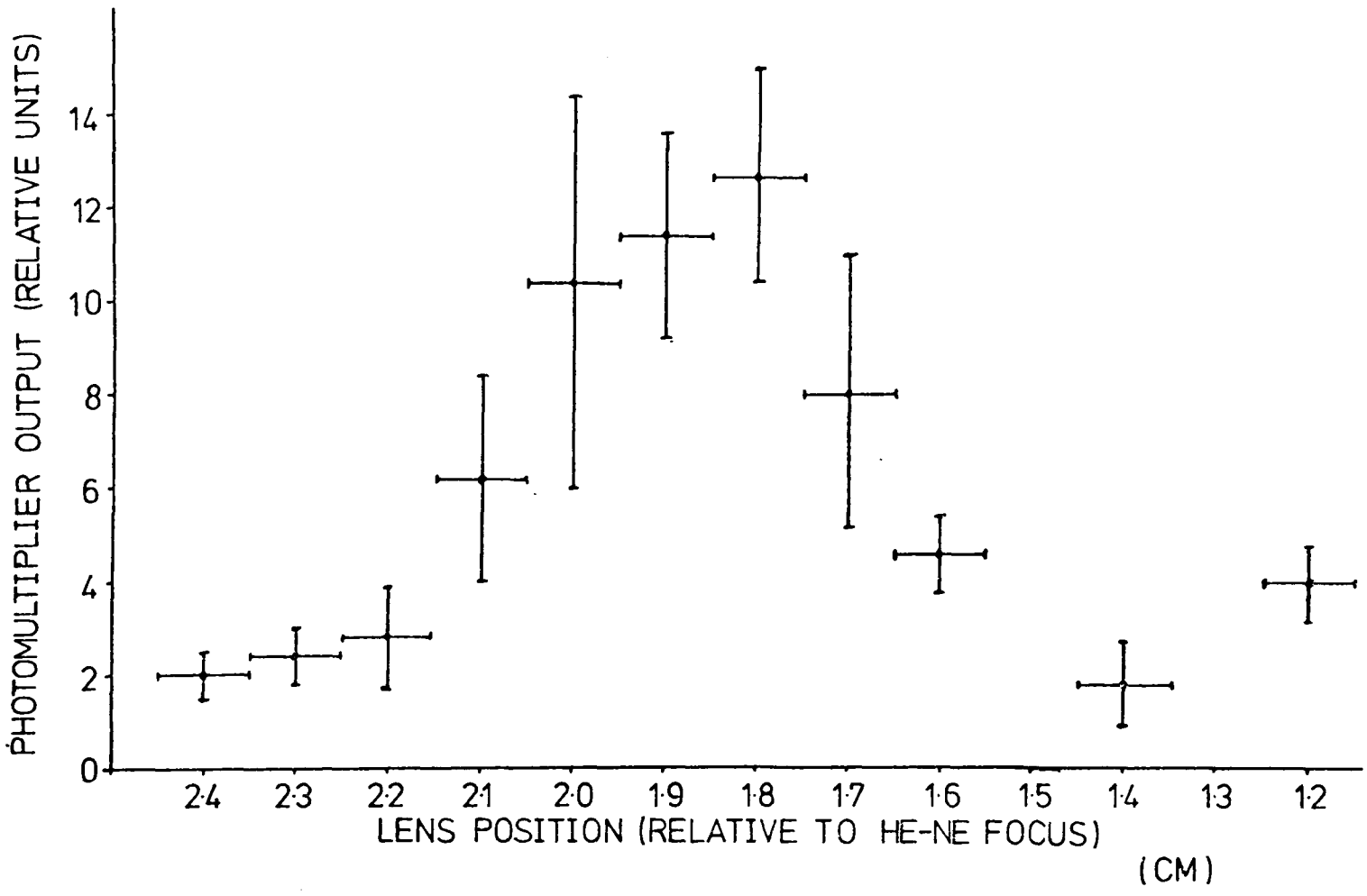


Fig. 2.2

Relative photomultiplier output, (proportional to hard X-ray flux) from a fixed irradiated target, versus relative lens position (measured with respect to the He-Ne focus)

The intensity error bars resulted from an average over at least five shots per lens position. The lens positioning error was estimated as ± 500 μm and arose mainly from the accuracy with which the best focus of the He-Ne alignment beam could be determined.

As can be seen, a clearly defined maximum is apparent in the distribution and by defining the optimum focus as the lens position for which

this maximum occurs, we thus specify this focus to an accuracy of ± 500 μm. This may seem an unreasonably large degree of focusing uncertainty in view of the comments made by GODWIN *et al.* (1977) in one of several papers from Garching, reporting a strong variation in plasma properties over focal position variations of tens of microns. However, the work of the Garching group was carried out at incident wavelengths of 1 μm with the associated small Rayleigh length of the focal region. For the 10.59 μm radiation considered here, the Rayleigh length is of the order of 2 mm and a focusing uncertainty of 0.5 mm would thus not be expected to affect experimental results.

It is emphasized here, that we are in no way assuming that the optimum focus as determined above, coincides with the geometric focus of the lens for the incident radiation. Experiments at AWRE (FOSTER *et al*, 1979) for example, showed that for 1 ns and 90 ps pulses at 1 μm, incident on targets of CH_2, Al and Au, the maximum hard X-ray yield occurred ~ 200 μm from the position of best focus, as determined by low power CW transmission through pinholes. The authors discuss possible reasons for this discrepancy including plasma expansion effects, self focusing, coronal refraction and spherical aberration differences between the CW and pulsed beam. It is interesting that the hard X-ray focus found by the AWRE group, coincides with the focus as determined by the Hartmann test. The same result was found in this work and the method is reported in section 2.2.4.

To conclude this section we note that the backscatter through the focusing lens was also found to peak at a lens position that coincided with the optimum focus (as determined by hard X-ray emission). The interpretation of experiments conducted with varying foci is very difficult, especially as it does not seem obvious that a direct correlation between focal position and target irradiance can be made. For this reason, such experiments were performed predominantly as focusing tests, and were regarded with caution when performed otherwise (see, e.g., Chapter 6).

2.2.3 *TARGET DAMAGE*

Although the surface condition of a polished carbon flat was noticeably affected by the incident laser beam, the variation of the observed damage was not sufficiently strong with focal position variation, to find the optimum focus in this way. Several shots on the target were required to produce a crater and the effect of a single shot was to cause a region of low contrast, consistent with the expected size of the focal spot, to be produced surrounded by a large area of discolouration which was assumed to be due either to lateral plasma expansion, or to low energy scattered radiation from the focusing optics.

The situation was different, however, for a metal target in that a well defined crater and damage pattern was produced by a single shot, the size of the crater being a function of lens focus. Thus, by observing crater formation as a function of lens position, a second method for optimum focus determination could be used. It was found that the optimum position coincided with the position determined in section 2.2.2. The method was used only as a position indicator, however, and no attempt was made to relate crater size to the far field distribution of the laser beam. This was because the effect of material ejection from the focal region due to shock waves in the target, and molten material flow, were assumed to enlarge the crater.

2.2.4 *HARTMANN GRID TECHNIQUE*

This simple technique was used in early experiments with the plane/plane oscillator configuration and consisted of observing how a pattern of apertures placed in the near field of the incident beam, focused down as the far field was approached.

The Hartmann grid used was an array of circular apertures of 5 mm diameter on 1, 2, 3 and 4 cm radius spacings (see insert in Fig.2.3). The

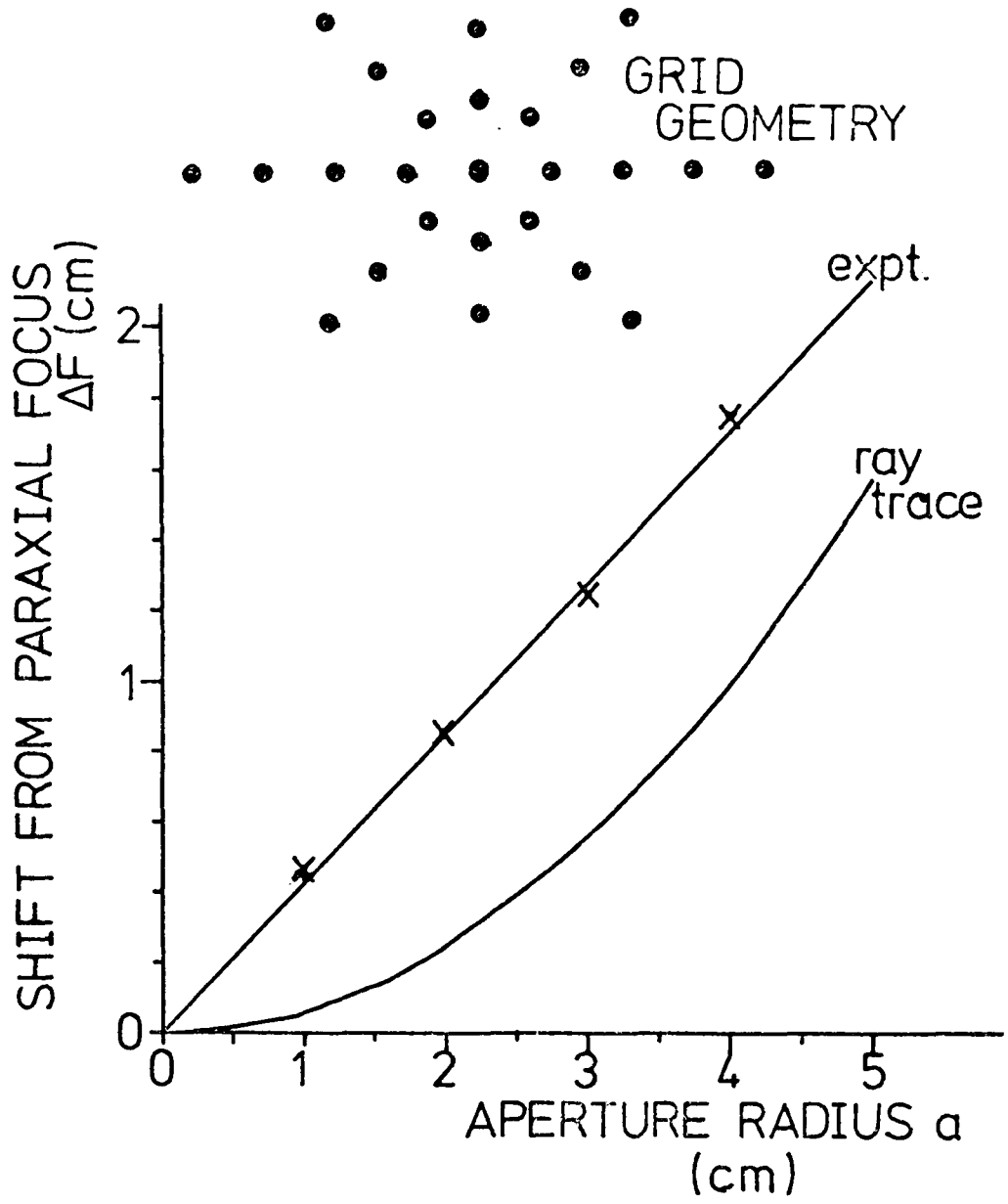


Fig. 2.3

Focal shift (relative to the paraxial focus) of rays from regions of various aperture radius. The experimental points were obtained using the Hartmann grid technique. A theoretical curve from a ray trace computation is also shown. The grid holes were placed on co-axial circles with 1 cm spacings, in the geometry shown in the insert.

burn patterns for several axial positions of an exposed polaroid film recording plane were then examined. As the recording plane approached the far field, the burn spots merged into a single large burn. The radial distance of the centre of each spot from the centre of the burn pattern was plotted as a function of recording plane position, until the point was reached where burns from individual apertures could no longer be clearly defined. No azimuthal asymmetry was found in the pattern and consequently, burns at the same radial distance from the axis, but at different orientations, were all used to obtain the necessary focusing relations.

A least squares fit to the data enabled the focal position of rays from different aperture radii to be found by extrapolation to the optic axis.

A focal position versus lens aperture plot was then made. (The focal position of each ray was initially defined relative to the focus of a ray at a radius of 1 cm from the beam axis). By an extrapolation of this graph to zero aperture radius, the paraxial focal position was found and the data were then replotted as a difference from this focal position ΔF, versus the aperture radius, a. This graph is shown in Fig. 2.3.

The least squares fit to the data gives the relation:

$$\Delta F = 0.4286\, a\,. \qquad (2.1)$$

Also shown on the figure is the variation of ΔF with aperture radius obtained from a ray trace computation using the particular lens parameters. ΔF varies as a^2 in this case, which is consistent with the presence of primary spherical aberration in the meniscus lens. It can be seen that, although the measured variation of ΔF is only linear, the absolute value of the focal shift is much larger in practice than predicted. For example, at an aperture radius of 1 cm, the predicted longitudinal aberration from the ray trace is 600 μm, whereas the empirical relation gives an aberration of ~ 4 mm (i.e. nearly an order of magnitude greater). This result is believed to show the dominance of aberration on the incident beam due to its multimode nature and its passage through imperfect optics. The problems associated with obtaining a good, well characterized focus were thus highlighted by this test.

In order to make some attempt at finding an optimum target position relative to the lens, the ray data obtained from the Hartmann grid test was used to calculate the position of the disc of least confusion. The method used was that of CONRADY (1957) and the empirical relation (Eq. (2.1)) relating the longitudinal focal change with aperture was employed. It is easily shown that with this relation, the disc of least confusion is situated at a distance $d_{LC} = 2(\sqrt{2}-1)\,\Delta F_M$ from the paraxial focus where ΔF_M is the longitudinal focal shift of the marginal ray. For the case considered here, the

incident beam was of dimensions 5 X 10 cm. An equivalent aperture radius a_e is thus given by $\pi a_e^2 = 50$, and we can then find the corresponding value of ΔF from Eq. (2.1). Using this value to find d_{LC} we obtain d_{LC} = 1.4 cm. This distance is consistent with the optimum position of the target found by the other methods described in the chapter, given the approximations made. It is perhaps most important to note the neglect of diffraction effects in the above analysis. The most important result of the Hartmann test, however, is believed to be the indication of the dominance of beam aberration over lens aberration, and its effect on the focal properties.

2.3 CHARACTERISTICS OF THE OPTIMUM FOCUS — DETERMINATION OF THE IRRADIANCE

2.3.1 *INTRODUCTION*

Sensible interpretation of the results of any laser-plasma interaction experiment relies upon the knowledge of the conditions of the experiment; in particular the irradiance I_0, at which the interaction occurred. Furthermore, such knowledge facilitates comparison of the results between different experiments and different laboratories. Unfortunately, it is by no means obvious that the single parameter I_0 can adequately represent the far field intensity distribution of high power pulsed laser radiation focused by a nonideal lens. This comes about because in any real experiment, the focusing properties of the incident beam are perturbed both spatially and temporally by the plasma which it produces and by the structure (spatial and temporal) of the incident beam itself. To ascribe a single parameter to the conditions of the experiment, therefore, we must make approximations.

The first approximation was made for all experiments reported in this work. It involved the estimation of power in the incident probe. The incident pulse was approximated to a top-hat profile, having a width equal to the measured FWHM, and energy content equal to that determined by pyroelectric joulemeter monitors (and a knowledge of the energy distribution

between spike and tail). The power value used, therefore, was the peak power P_0. It did not account for variations introduced by temporal perturbation on the incident pulse. The peak power of a Gaussian pulse is equal to 0.94 X the power obtained by considering the total energy to be delivered in a pulse of time = FWHM. Our method, therefore, overestimates the peak power if we consider the pulse shape to be Gaussian. However, the actual pulse shape approximates more nearly to a triangular pulse for which the method is exact.

The second approximation involved the distribution of power P_0 over the region of optimum focus (i.e. the irradiance distribution) in order to define some irradiance I_0 characteristic of the experiment. The approximation was made differently at different stages in the work and the resulting irradiance will now be defined.

2.3.2 *FIRST APPROXIMATIONS TO THE IRRADIANCE DISTRIBUTION*

The simplest means of estimating the focal irradiance I_0 is to determine the size of the region over which uniform illumination may be assumed. This dimension D, was found by measuring the divergence of the incident beam ϕ and subsequent application of the usual formula:

$$D = f \cdot \phi \qquad (2.2)$$

where f is the focal length of the focusing lens.

No account of aberrations introduced by the optics in the beam path or on the beam itself, can be taken, and the percentage energy falling within the area $\pi D^2/4$, must be estimated.

The method was performed using burns on exposed polaroid film to record the beam diameter at several distances between the final amplifier and the target chamber. The divergence measurement was also carried out by recording the energy passing through a 5 cm square aperture for various aperture positions along the incident beam. The energy was recorded with a

Gen-Tec®Joulemeter placed behind the aperture. The arrangement and method is illustrated schematically in Fig. 2.4.

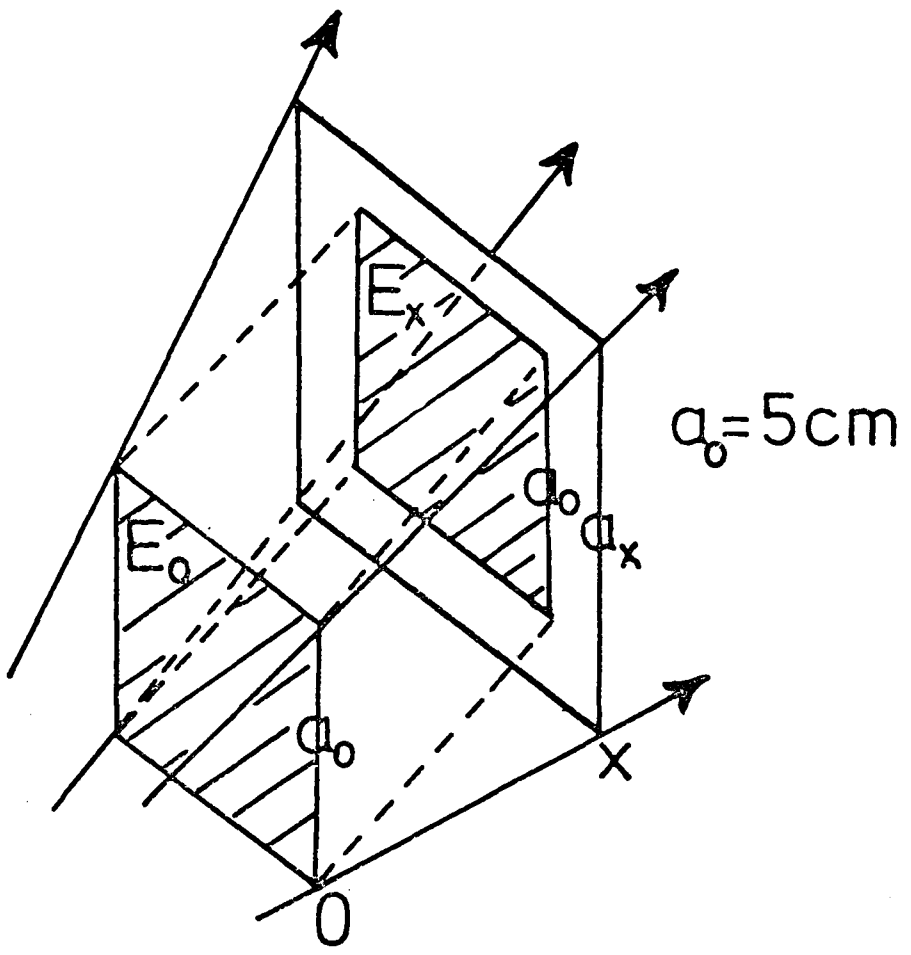


Fig. 2.4
Schematic, illustrating one of the divergence measurement techniques employed

The dimension of the beam a_x is given by:

$$a_x = \left\{ \frac{E_0}{E_x} \cdot a_0^2 \right\}^{\frac{1}{2}} \qquad (2.3)$$

where E_0 is the energy measured at the initial position of the aperture and E_x is the energy through the same aperture at a position x along the beam. The gradient of the $\frac{1}{2} a_x$ versus x plot is thus the divergence of the beam averaged over the area a_0^2, in this case 25 cm^2.

Figure 2.5 shows the $\frac{1}{2} a_x$ vs x plot and from the linear regressional fit to the data points, the gradient and hence divergence, was found to be 1.28 mrad. This divergence gives an estimated spot size of 281 μm diameter for the multimode output beam upon which the measurement was made.

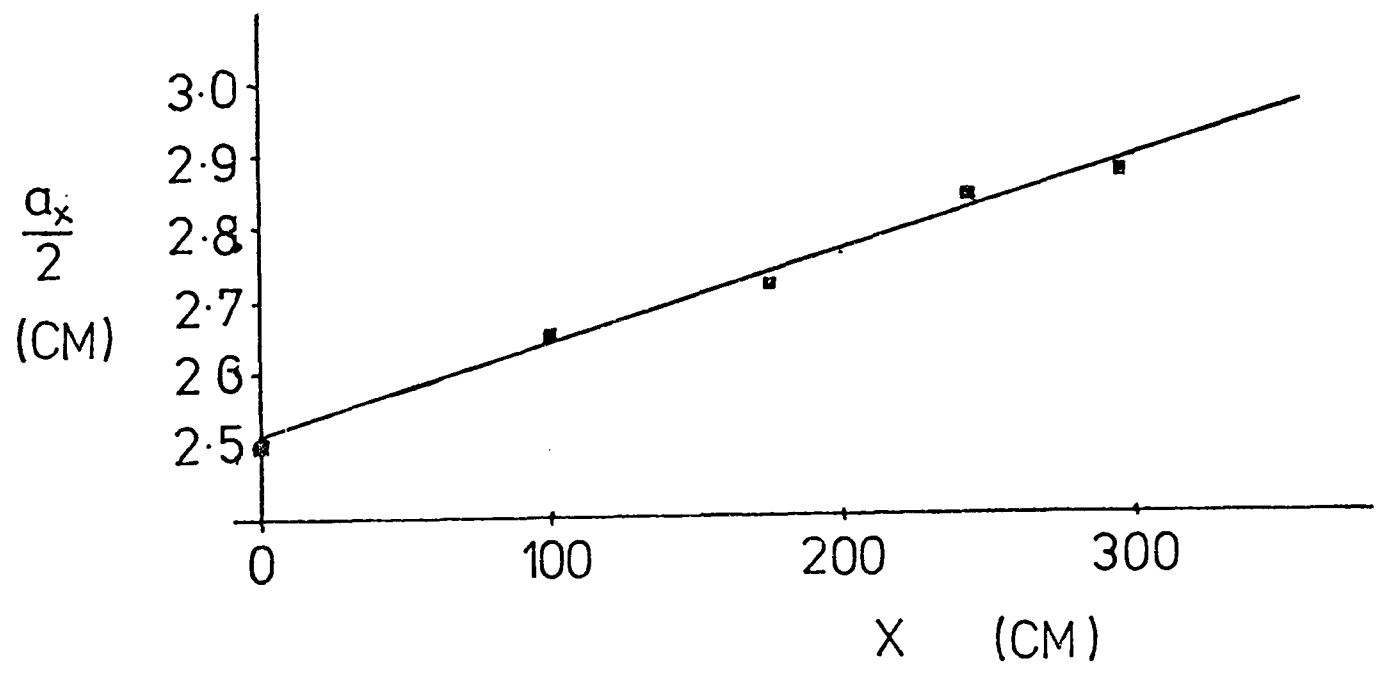


Fig. 2.5
Results of a beam divergence measurement. The notation is explained in the text.

For an incident beam operating on a single transverse mode, the theoretical distribution of energy into the focal region is known and hence the energy into this focal region can be estimated. For a multimode beam, the exact combination and relative amplitudes of each mode would need to be specified in order to obtain a theoretical distribution. In the absence of this information, however, it was assumed that all the incident energy was present within a spot of diameter $D = 281\,\mu m$. Thus for a 1.5 GW incident pulse, a peak irradiance of 2.4×10^{12} W/cm^2 was estimated.

2.3.3 *DIFFRACTION GRID TECHNIQUE*

The method now to be described enables the irradiance distribution at a particular focal plane to be found on a single shot and leads to an improved definition of the parameter I_0. It was used as the standard technique on later experiments with the APPLE laser system.

The principle of the method lies in the fact that each principal maximum of the Fraunhofer diffraction pattern of a transmission diffraction grating in the incident beam and formed by the focusing lens, has the same functional distribution as the focal spot in the absence of the grating. The diffraction pattern is formed on a material with a clearly defined damage threshold, and measurement of the dimensions of each order enables a normalized distribution to be built up, when the parameters of the grating are known. A brief theory of the technique is given in Appendix A3.

Diffraction patterns were made on pieces of exposed polaroid film, the grating used being a wire mesh with aperture to pitch ratio $a/d = 0.64$. This particular mesh was found to give adequate transmission $\{(a/d)^2 \times 100\%\}$ and a large number of spots in the diffraction pattern having an intensity above the recording material threshold. The spot separation was also large enough to facilitate ease of dimension measurement but the absolute dimension was not so large that outer orders were significantly distorted due to

focusing onto a plane. The mesh was placed immediately in front of the focusing lens in order that all radiation diffracted by it should be collected and focused onto the polaroid film. The experimental arrangement is shown in Fig. 2.6.

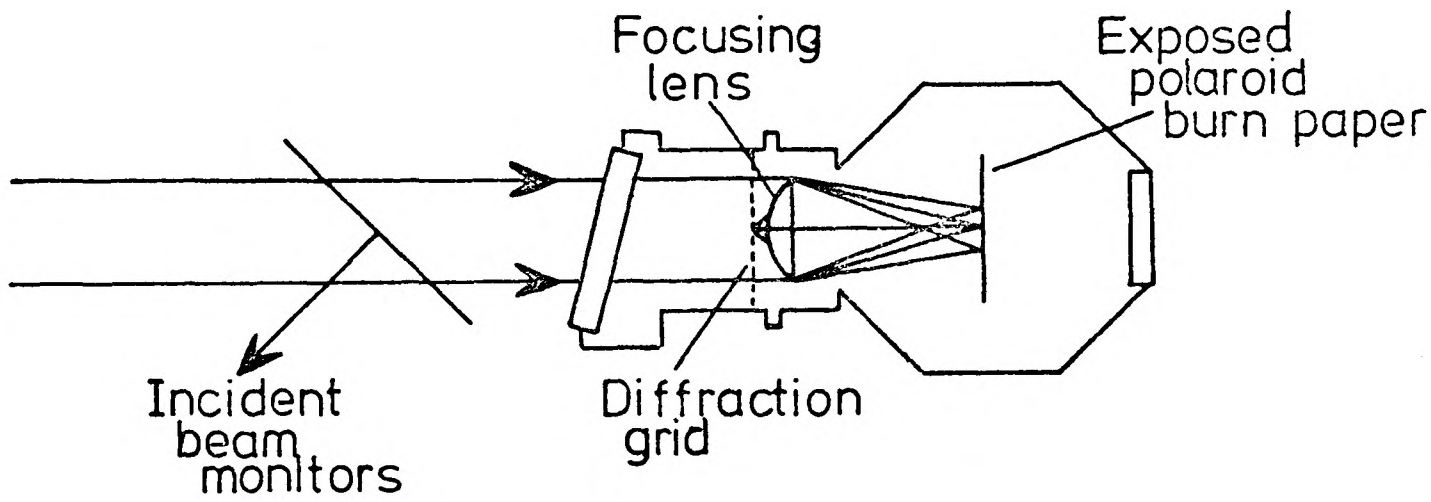


Fig. 2.6
Diffraction grid technique to measure the far-field irradiance distribution — Experimental arrangement

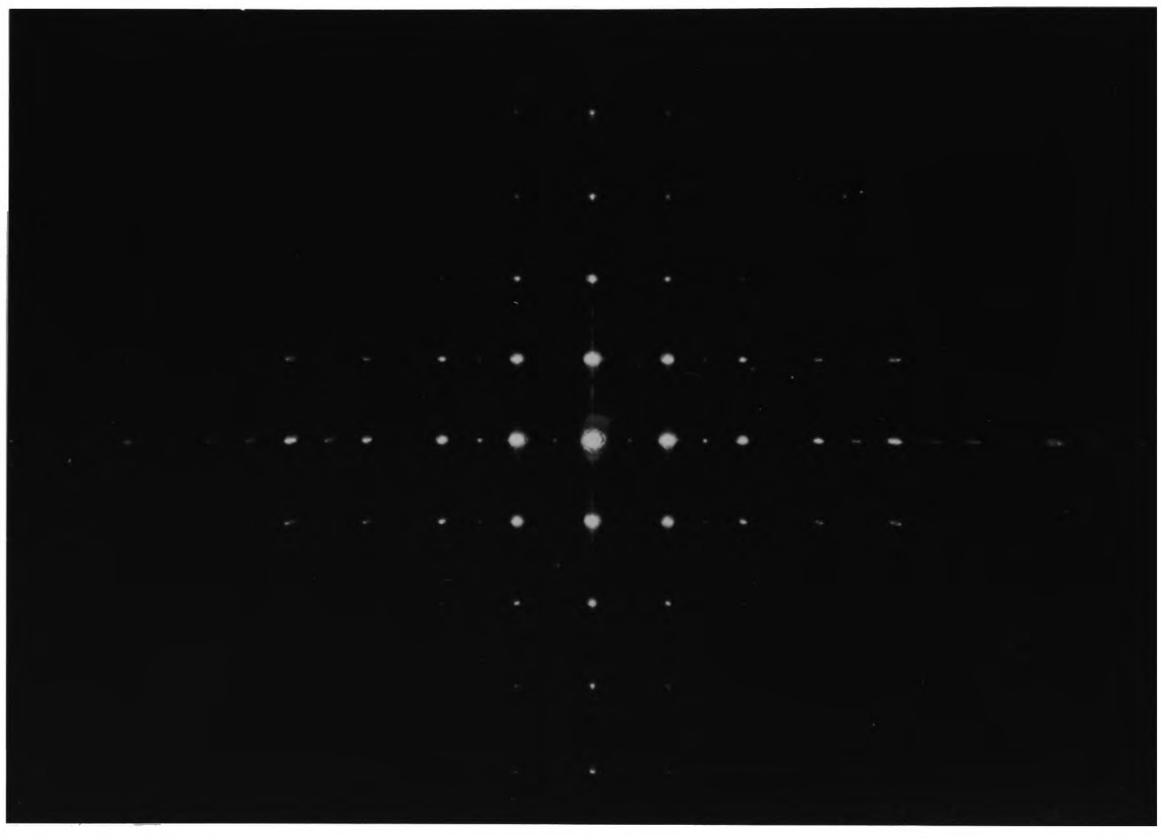


Fig. 2.7
A diffraction pattern obtained at optimum focus. Secondary maxima can be observed as well as the distorting effect of a plane recording medium at the left and right hand edges of the pattern

A diffraction pattern taken at the optimum focus position with the laser operating in the unstable mode with an output beam diameter of 5 cm, is shown in Fig. 2.7.

The dimensions of each order in the diffraction pattern was measured under a high power microscope taking the size of the white region of the burn in each case.

The square of the radius of each diffraction order burn was plotted against $\log_{10}(I_{00}/I_{ij})\{=\log_{10} I\}$ evaluated for the ratio (I_{00}/I_{ij}) pertaining to the order of the burn (see Appendix A3). A typical case for the annular, single transverse mode beam is now described.

It was found that the data points could best be represented by two straight lines as shown in Fig. 2.8, implying that the intensity distribution consisted of two Gaussians of the form:

$$I = I_p \, e^{-r^2/2\sigma^2},$$

The measured values of σ for both Gaussians are shown in the figure. Normalization of intensities was accomplished as follows.

The peak power P_0 incident on the target was equated to the volume under the distribution (assuming rotational symmetry).

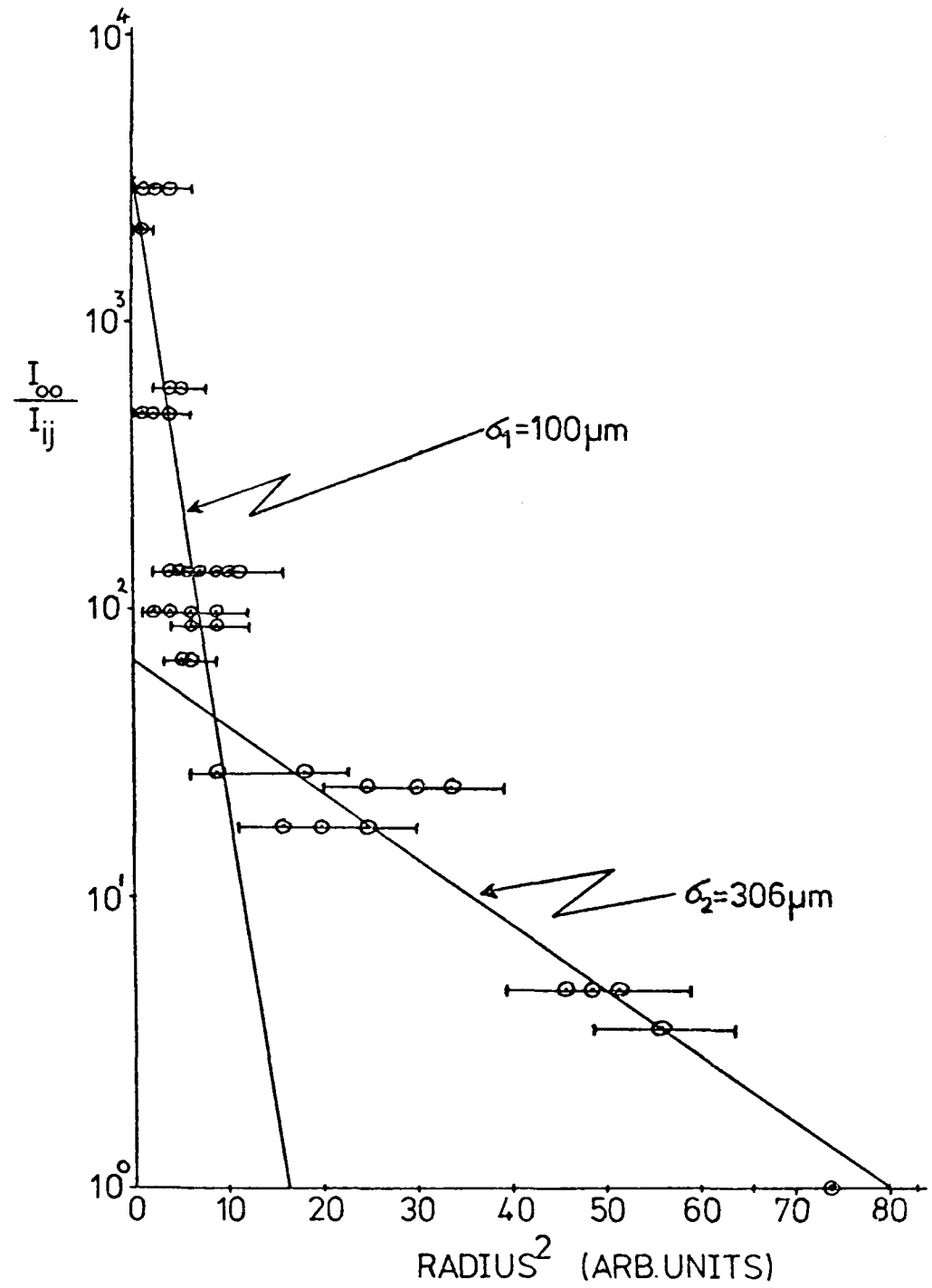


Fig. 2.8
Experimental results from the diffraction grid technique. The solid lines represent the best fit to the data. Values of the Gaussian parameter σ for each line are shown on the figure

Now
$$\text{Vol} = \int_0^{r_c} I_{p_1} e^{-r^2/2\sigma_1^2} \cdot 2\pi r\,dr + \int_{r_c}^{\infty} I_{p_2} e^{-r^2/2\sigma_2^2} \cdot 2\pi r\,dr$$

Thus
$$P_0 = \pi I_{p_1} \int_0^{r_c} e^{-r^2/2\sigma_1^2}\, d(r^2) + \pi I_{p_2} \int_{r_c}^{\infty} e^{-r^2/2\sigma_2^2}\, d(r^2)$$

where r_c is the radius at which the Gaussians intersect. Thus

$$P_0 = 2\pi\sigma_1^2 I_{p_1} \left[-e^{-x_1}\right]_0^{r_c} + 2\pi\sigma_2^2 I_{p_2} \left[-e^{-x_2}\right]_{r_c}^{\infty}$$

where

$$x_1 = r^2/2\sigma_1^2 \quad \text{and} \quad x_2 = r^2/2\sigma_2^2 .$$

Using the measured ratio of I_{p_1}/I_{p_2} $(=45.7)$ and the values of σ_1 and σ_2 from Fig. 2.8, we obtain

$$I_{p_1} \approx 1.4 \times 10^{12}\ W/cm^2 \quad \text{and} \quad I_{p_2} \approx 3 \times 10^{10}\ \text{W/cm}^2$$

for a 1 GW peak power P_0.

The normalized distributions are shown in Fig. 2.9(a). (For clarity, the low intensity Gaussian wing is also shown separately on an enlarged scale in Fig. 2.9(b).

We now equate the peak irradiance of the most intense Gaussian I_{p_1} to the irradiance I_0 at which the experiments were performed. Thus for the example shown, an irradiance $I_0 \geqslant 10^{12}\ \text{W/cm}^2$ would characterise the experiments.

Also shown on Fig. 2.9 is the Airy pattern representing the theoretical intensity distribution for the particular unstable cavity configuration used (Magnification $M = \times 4$), lens aperture $2a = 5$ cm and focal length $f = 22$ cm. This Airy function has been normalized to the peak of the Gaussian and is of the form:

$$I = \frac{4 I_A}{(1-\varepsilon)^2} \left[\frac{J_1(ka^{x}/f)}{(ka^{x}/f)} - \frac{\varepsilon J_1(\varepsilon ka^{x}/f)}{(ka^{x}/f)} \right]^2$$

where $\varepsilon = 1/M$ and J_1 is a first order Bessel function. The absolute

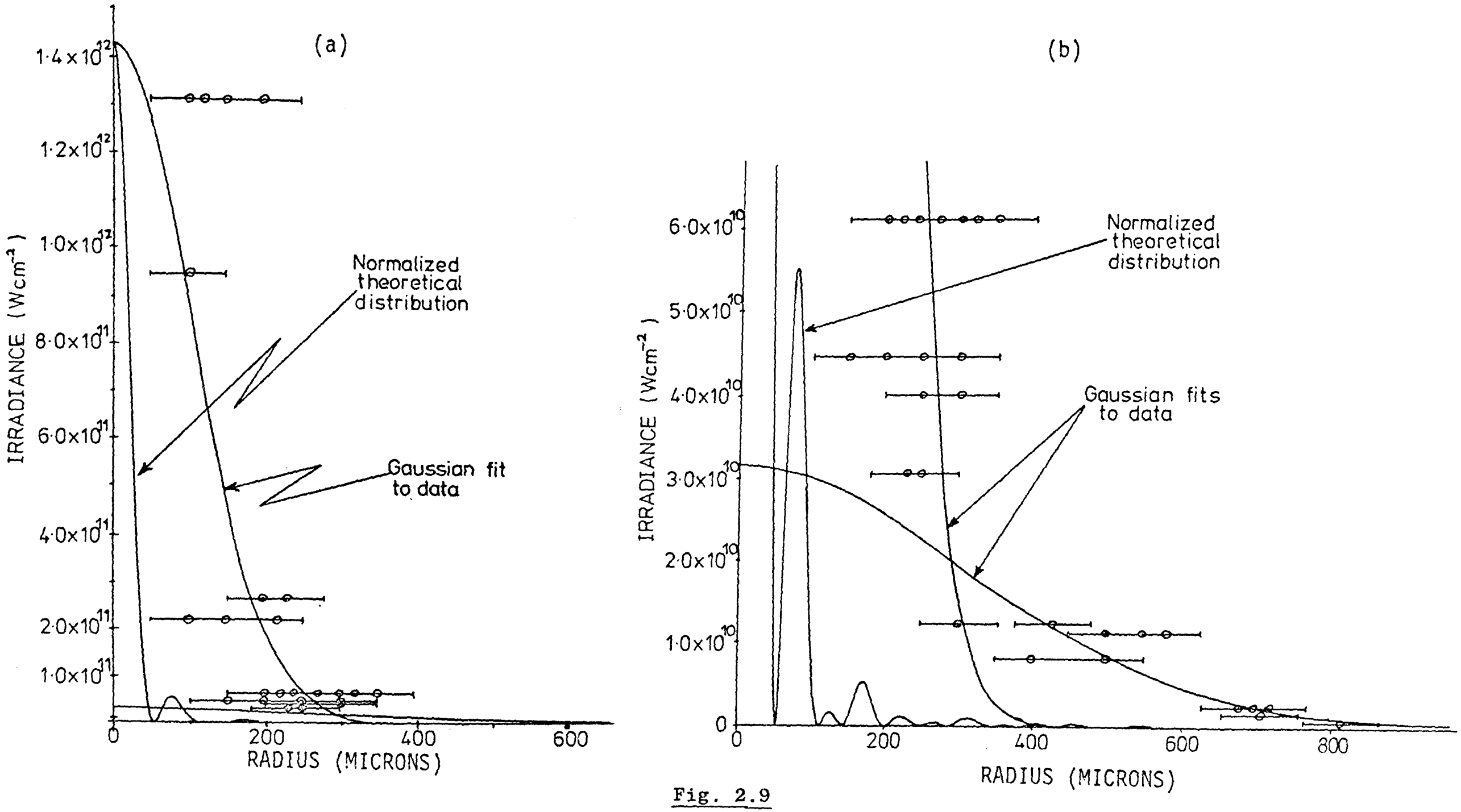


Fig. 2.9

High irradiance (2.9(a)) and low irradiance (2.9(b)) portions of the distribution plotted on absolute scales. The theoretical far field distribution is also shown on the figure

magnitude of the peak irradiance I_A for an annular beam is given by:

$$I_A = \left(1 - \frac{1}{M^2}\right) \frac{\pi a^2}{\lambda^2 f^2} \cdot P_0$$

$$= 3 \times 10^{13}\ \mathrm{W/cm^2} \quad \text{for} \quad P_0 = 1\ \mathrm{GW}.$$

This is more than an order of magnitude greater than the experimentally determined value. We have not, however, estimated the effect of the lens aberrations on the peak value. It was mentioned earlier, that a ray trace had been performed for the lens used in the experiments. This computation resulted in a wavefront aberration w, which was determined by primary spherical aberration and given by the relation:

$$w = A_{040} \left(\frac{a}{a_0}\right)^4 \tag{2.4}$$

where

$$A_{040} = 0.62\,\lambda \quad \text{for} \quad a_0 = 2.5\ \mathrm{cm}.$$

We can use this relation to estimate the Strehl intensity ratio I_s, which is defined as the ratio of the irradiance at an axial point to that at the centre of the aberration free spherical wave. I_s is given by (FRANKE, 1966):

$$I_s = 4\left[\frac{1}{a_0}\right]^4 \left\{\left(\int_0^{a_0} \cos kw(a) \cdot a\,da\right)^2 + \left(\int_0^{a_0} \sin kw(a) \cdot a\,da\right)^2\right\} \tag{2.5}$$

where $k = \frac{2\pi}{\lambda}$ and w is given by equation (2.4).

The integrals in equation (2.5) are easily numerically integrated and give a value for $I_s = 0.24$. This is the normalized irradiance at the axial point corresponding to the paraxial focus and does not, therefore, represent the maximum obtainable irradiance. This is obtained by placing the receiving plane at the diffraction focus. We can find the Strehl intensity in this position by letting $A_{040} \rightarrow A_{040} \times \frac{\sqrt{2}}{6}$, (BORN and WOLF, 1970) and evaluating equation (2.5) once again. When this is done we obtain $I_s = 0.93$. Thus even in the presence of primary spherical aberration whose magnitude is a sizeable fraction of the wavelength, the peak irradiance is

greater than 90% of the aberration free value (for the correct axial position). We note, therefore, that the experimentally determined peak irradiance is more than an order of magnitude down on the theoretical value, even taking into account the spherical aberration introduced by the focusing lens. The axial position at which the irradiance was measured was optimized using the methods described in section 2.2 and we, therefore, do not believe that this reduction in irradiance from the theoretical value was caused by a poor choice of target position. We thus repeat the assertion made in section 2.2.4, namely, that the far field irradiance distribution was largely determined by beam, rather than by focusing lens, aberrations.

2.3.4 *CONCLUDING REMARKS*

To conclude this section it should be emphasized that because of the approximations made in the definition of I_0, such a parameter must be regarded as a regime indicator only. Also, it will be noticed that throughout this work, all experiments have been performed in the same irradiance regime (apart from those measurements involving the variation of the relative target position). There are two reasons for this. First, it was required to perform all experiments under the same irradiance conditions to facilitate comparison and analysis. A value of $I_0 \sim 10^{12}$ W/cm^2 was the maximum that could be obtained with the system and was thus, the irradiance used. Secondly, to have performed experiments at lower irradiance (for fixed illumination geometry) the beam energy would have had to have been substantially reduced. No attenuators were available that would have ensured large energy reduction, unchanged beam parameters and, therefore, unchanged irradiance distribution at optimum focus.

CHAPTER 3

EARLY MEASUREMENTS WITH THE APPLE LASER

3.1 INTRODUCTION AND EXPERIMENTAL DETAILS

In this chapter, experiments performed with the APPLE laser operating with a plane/plane oscillator cavity, will be described. The primary motivation was to investigate the spatial structure of the backscattered radiation, i.e., the angular distribution. Information was also obtained on the absolute reflectivity and the temporal shape of the backscattered pulse. (In this, and subsequent chapters, the term, 'backscattered', refers to radiation backreflected through the focusing lens.)

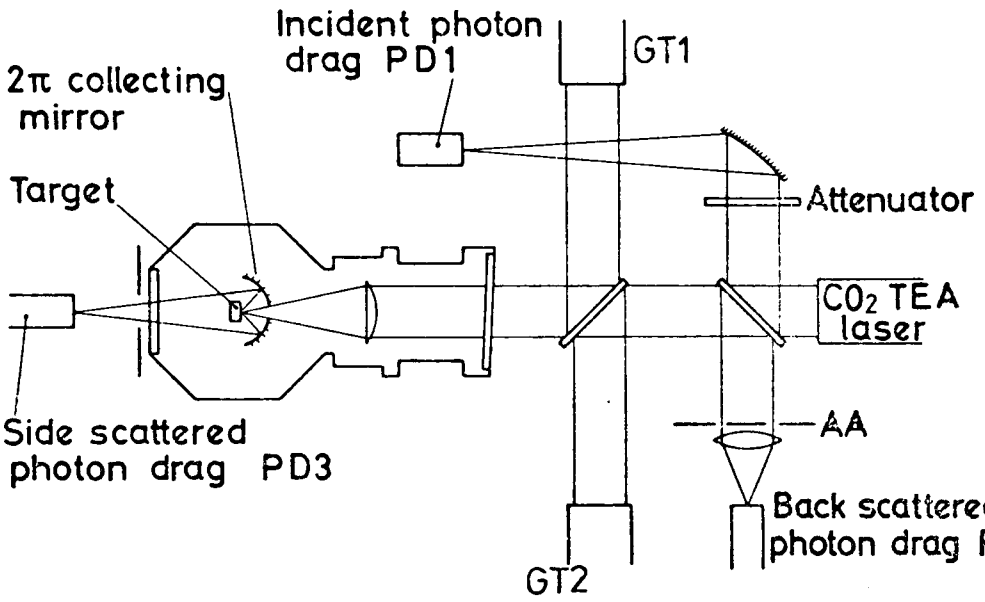


Fig. 3.1
Experimental arrangement used for early measurements GT1 and GT2 are the incident and backscattered energy monitors respectively. AA is an annular aperture used for defining the backscatter angle

The experimental arrangement is shown in Fig. 3.1.

The incident beam was focused onto the flat polished face of a massive carbon slab. Incident and reflected temporal profiles were measured with photon drag detectors PD1 and PD2 respectively. These photon drag detectors were linked via 50 Ω impedance coaxial cable to a dual beam Tektronix 7844 scope with a 7A19 amplifier module giving an overall bandwidth of 400 MHz. The incident and backscattered energies were monitored with Gen-Tec® pyroelectric Joulemeters GT1 and GT2 respectively. The total energy in the incident pulse was typically measured to be ~ 150 J of which 50% was in the 50 ns FWHM gain switched spike (see section 1.3.2). The full irradiance on target has previously been stated as $\leqslant 10^{13}$ W/cm^2 (DONALDSON *et al*, 1976). The actual focal spot distribution was not known, however, (the

technique described in section 2.3.3 not being employed until later) and it is likely that the energy in the wings of the focal region, due to the large and varied divergence of the multimode beam, was a non-negligible quantity. It is now believed that the vacuum irradiance was approximately a factor of five down from the previously stated value. This is not considered to in any way invalidate the conclusions reached in the above reference (and discussed in this chapter).

Radiation scattered outside the collection angle of the focusing lens was collected by a polished copper spherical section and refocused past the target onto a detector positioned outside the target chamber. As can be seen from Fig. 3.1, the incident beam was thus required to pass through a hole in this collecting mirror. The diameter of this aperture, therefore, was made to match the cone of incident radiation, in order that no reflected light should be lost through the hole and then outside the lens aperture, or the incident beam clipped. A certain fraction of the sidescattered radiation was masked by the target, and was unrecorded. This fraction was allowed for in subsequent total absorption measurements. Fine positioning of the detector behind the target chamber was accomplished using a highly polished surrogate target and the alignment He-Ne beam.

3.2 ANGULAR DISTRIBUTION OF THE BACKSCATTERED RADIATION

Annular apertures placed before the collecting lens for photon drag detector PD2, sampled the backscattered radiation distribution across the beam. Hence an angular distribution was obtained with spatial integration around the axis of the backscattered beam and basic resolution determined by the width of the aperture. The apertures were positioned in the centre of the backscattered beam using a retro-reflecting mirror in front of the target chamber and the coaxial alignment He-Ne. This procedure was carried out whenever the aperture was changed, to ensure accurate relative repositioning with respect to the reflected beam. Figure 3.2 illustrates the

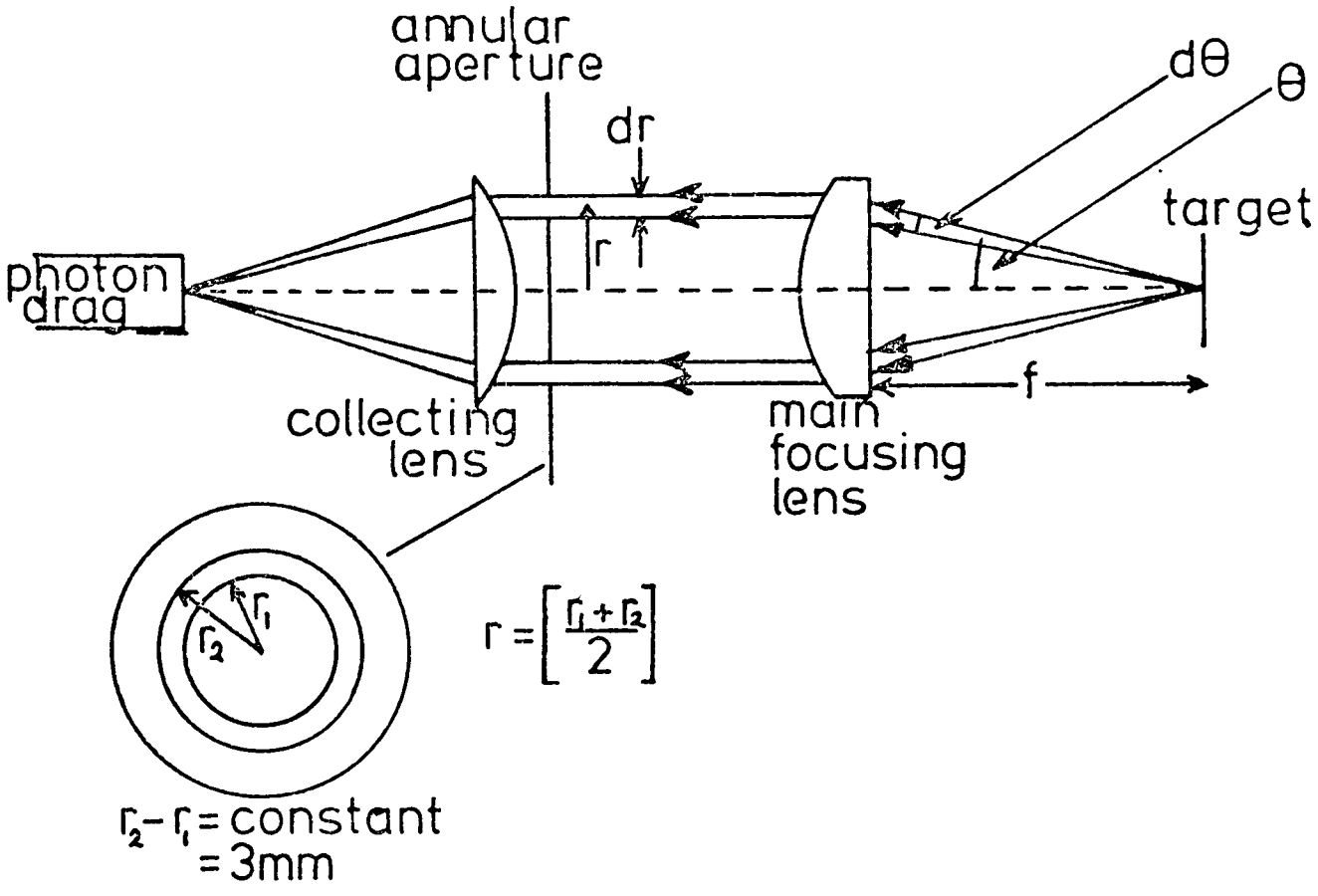


Fig. 3.2

Schematic of the experimental technique for backscatter angular distribution. The nomenclature used in the text is defined in the figure.

nomenclature used in this section.

In the figure, the following relations apply:

$$\theta = \tan^{-1}\left\{\left(\frac{r_1 + r_2}{2}\right)\Big/ f\right\} \quad \text{and} \quad d\theta = \left\{\frac{r_2 - r_1}{f}\right\}$$

where r_1 and r_2 are the radii of the annular apertures, and f is the focal length of the focusing lens. In the experiments $r_2 - r_1$ was kept constant at 3 mm, giving a basic angular resolution $d\theta$ of 13.6 mrad or 0.8° for $f = 22$ cm.

In the experiment, the assumption was made that the backscattered radiation was re-collimated by the focusing lens such that a linear mapping between the annular aperture dimension $r = \left(\frac{r_1 + r_2}{2}\right)$ and the angular distribution, could be defined. This assumption was thought valid provided the backscattered radiation originated from a volume with dimension much less than the focal length of the focusing lens and that the plasma was situated at, or very near to, the focus of this lens.

It should now be mentioned that due to the finite thickness of the

beamsplitters and the fact that these components are uncoated, the spatial distribution incident upon the apertures was, in fact, comprised of two overlapping patterns; one from each face of the beamsplitter. Pellicle membranes comprising of tightly stretched mylar were used as beam splitters in an attempt to overcome this problem, but were found to be unsuitable due to their extremely low damage threshold. The use of a highly wedged beam splitter to separate the images would have presented serious alignment problems when using the coaxial He-Ne system. It was finally decided to continue the use of the readily available 1 cm thick beam splitters and bear in mind that there would be a reduction in the spatial resolution of the measurement due to the ghost images. (The angular error bars in Fig. 3.4(a) arise from the overlap of the two images and represent the limiting factor in the resolution determination.)

It was also ensured that the wedge fringes (see LITTLE *et al*, 1974) resulting from the two overlapping images had a spacing that was smaller than the spatial resolution of the experiment (i.e. an accurately parallel beam splitter, forming an etalon, was not suitable). To test that this fringe effect was not problematic, the beam splitter was taken and wedge fringes directly measured for a 30° angle of incidence beam, by recording the reflected beam from the Culham kJ CO_2 laser, Trojan, on exposed polaroid film. (The Trojan laser was used to enable sufficient energy for polaroid burning with an unfocused beam, to be available.) The measured fringe spacing was found to be 0.87 mm for the 30° angle of incidence of the measurement. Application of the standard formula

$$\phi = \left(\frac{\lambda}{2\eta d}\right) \cos\theta \qquad (3.1)$$

gave a wedge angle ϕ of 12 min. of arc for $\theta = 30^\circ$, $d = 0.87$ mm, refractive index $\eta = 1.49$ and $\lambda = 10.59\,\mu$m. A second application of equation 3.1 gave a fringe spacing of 0.71 mm for $\theta = 45^\circ$ (i.e. the angle at which the beam splitters were used in the experiment) which was consistent with our requirement that it should be less than the spatial resolution.

The relative reflectivity for a particular scattering angle θ was then taken to be simply the ratio of the peak height of the incident and reflected pulses as measured on photon drags PD1 and PD2. This value was then corrected to a percentage of the total reflectivity back through the focusing lens (measured without an aperture in front of PD2), and normalized to a value per unit solid angle to account for the variation in aperture area as θ increased. It should also be mentioned at this point that for the five largest apertures, part of the transmitting region fell outside the minor dimension of the laser beam and the resultant reduction in area was also taken into account. The normalization and correction procedure and the experimental results are now described and discussed.

3.2.1 *RESULTS*

Let D_θ = the ratio of the peak signals from photon drags PD1 and PD2 at a scattering angle θ.

Let T = the total absolute reflectivity back through the focusing lens.

Let $\Delta\Omega_\theta$ = the solid angle subtended by an aperture at the appropriate scattering angle θ. This solid angle was calculated from tables and the known inner and outer radii, r_1 and r_2 of the annular aperture.

The absolute reflectivity per unit solid angle into a backscatter direction θ can be written as ρ_θ where,

$$\rho_\theta = \frac{D_\theta}{\sum_\theta D_\theta} \cdot T \cdot \frac{1}{\Delta\Omega_\theta} \qquad (3.2)$$

ρ_θ was then plotted versus θ and the results for several experimental runs under the same irradiance conditions, are shown in Fig. 3.3. An average over all the runs is shown in Fig. 3.4(a) and the same results in polar coordinates in Fig. 3.4(b).

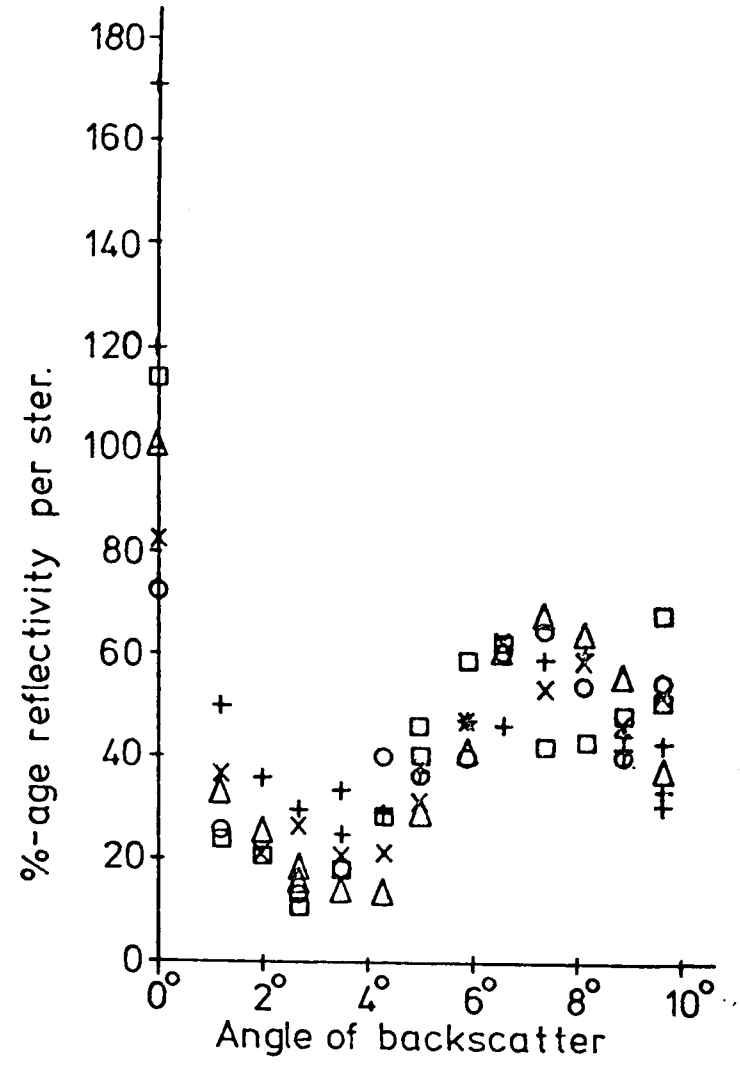
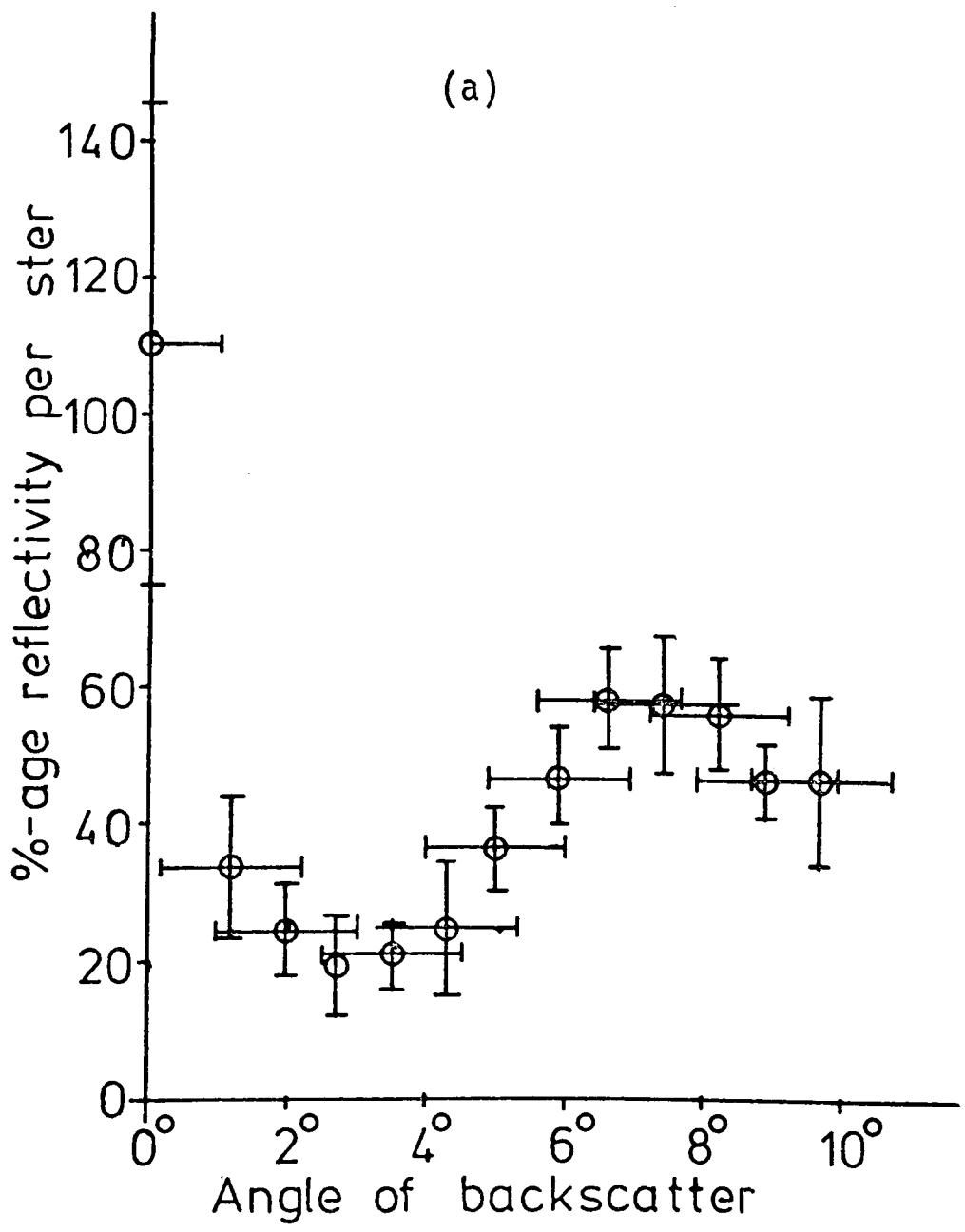


Fig. 3.3
Backscatter angular distribution data for several experimental runs



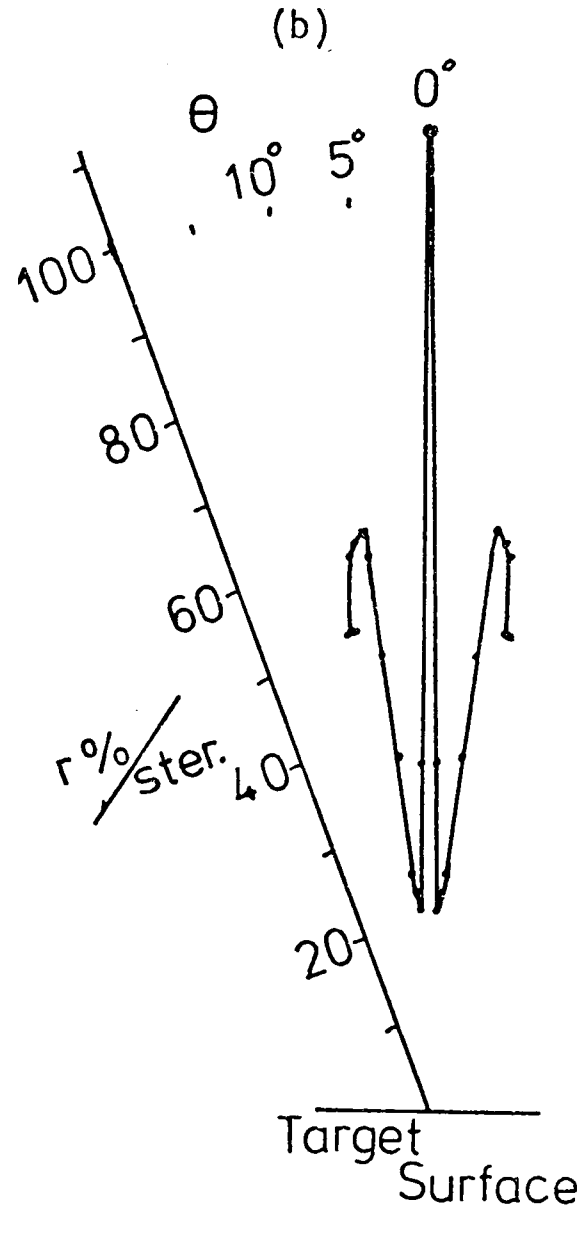


Fig. 3.4
(a) Average of all data shown in Fig. 3.3.
(b) As in Fig. 3.4(a) but on a polar plot.

The total peak reflectivity measured back through the focusing lens (T) was found to be ~3%. The percentage scattered outside the lens angle was found to be approximately 5% from the spherical mirror reflector. A total reflectivity of ~8% was thus measured.

In the nature of this measurement, this value will always be an underestimate due to losses around the entrance hole of the collecting mirror, which had been made slightly larger than the entrance cone to prevent vignetting. However, estimates of the 'unaccounted solid angles' indicate that such errors are small, so that there is still a large fractional conversion of incident laser energy into the plasma. This large percentage ~90%, cannot be accounted for on the basis of classical inverse bremmstrahlung and it is believed that anomalous processes are important (Chapter 7). The indication of one such anomalous process, namely resonance absorption, in the experiment will now be discussed.

3.2.2 *DISCUSSION*

The most apparent feature of the angular distribution results, is the fact that the backscattered radiation appears to be distributed into preferred angles. To explain this characteristic shape we must consider a mechanism that would cause preferential perturbations in the backscatter process. The resonance absorption mechanism (see, for example, DENISOV, 1957; WHITE and CHEN, 1974, for introductory discussions) seems to be a suitable candidate due to its dependence on the angle of the incident wavefront relative to the critical surface normal. If we consider the incident wavefront to be planar at focus, then the shape of the critical surface would determine the spatial absorption across the wavefront. In particular, a situation could be envisaged where a certain portion of the beam incident on a curved critical surface was preferentially absorbed and the rest of the beam reflected. In order for the resultant spatial distribution of the

reflected radiation from the critical region to correlate with the measured near field pattern of the backscatter, a one to one relationship must apply. For example, if the measured backscatter near-field pattern was assumed to be predominantly specular in content, we would not be justified in relating it to any particular critical surface shape; or to put it another way, a particular scattering angle could result from any part of the critical surface. If we consider, however, the ray-retracing aspect of the stimulated Brillouin scattering process (SBS) (LEHMBERG, 1978), we could relate the radiation from a particular part of the critical surface to a spatially defined region in the underdense plasma, and in this region the SBS process would occur. In effect, we have assumed that the SBS is 'pumped' by the specular reflection from the critical surface. (We note that no spectral identification was made at this stage — an important measurement to determine the presence of the SBS instability. Backscatter spectral measurements are discussed in Chapter 6.) This process was originally proposed by BEGG and CAIRNS (1976) and developed later by RANDELL *et al.* (1979). The basic concept is as follows.

For a plasma expanding with velocity close to the ion sound speed c_s, the instability grows, not from the usual thermal fluctuation source, but from specularly reflected light from the critical surface. The effect can be considered as mode beating between the incident and reflected waves (relative to the rest frame of the plasma). The incident wave is Doppler up-shifted to a frequency $\omega_L = \omega_0 + k_0 M c_s$ where M is the Mach number of the expanding plasma, and the reflected wave is Doppler down-shifted to a frequency $\omega_r = \omega_0 - k_0 M c_s$ (for reflection from a stationary critical surface). Thus the beat frequency is given as,

$$\omega_L - \omega_r = 2 k_0 M c_s .$$

We will see later (section 6.4) that the frequency of an ion acoustic wave is $\sim 2 k_0 \eta c_s$, where η is the plasma refractive index. For densities where

$\eta \simeq M$, therefore, there is a resonance, and ion acoustic waves may be driven. It is from these waves that the incident photons are scattered in the SBS process.

We thus relate the near field pattern of the backscattered beam to the absorption process occurring at the critical surface through the specularly pumped stimulated Brillouin scattering instability. We thus see how the spatial variation of the resonance absorption across the focal spot could be manifest in the angular distribution of the backscattered light.

A similar explanation is implied by PANT *et al.* (1980), who consider that the dip in the angular intensity distribution of diffusely reflected light observed by GODWIN *et al.* (1977) indicates the enhancement of resonance absorption at an optimum position on a density crater at the critical surface. The authors do not propose, however, a mechanism for mapping this spatial information in the far field to spatial information in the near field.

An alternative explanation for the observed angular distribution is suggested by the simulation performed by ESTABROOK and KRUER (1977). In this work the angular distribution of scattered light from an inhomogeneous 500 eV plasma irradiated with 1 μm radiation at 2.7×10^{14} W/cm^2, was found using a two-dimensional, one fluid plasma simulation which included the Brillouin side-scatter process. The results indicated that the side-scatter gave rise to lobes at angles of $\sim 20^\circ - 40^\circ$. The authors state that the angular position of these lobes is correlated with the density at which the side-scatter occurs and indicate that the smallest angles occur for scattering at lowest density.

It is noted here that a similar pattern in the reflected radiation was observed at Osaka (AZECHI *et al.* 1978). In this case the angular distribution was measured for CO_2-laser radiation incident at an angle of 35° to

the surface of a plane polyethylene target. For p-polarized radiation a dip in the reflected radiation was observed in the specular direction and was attributed to resonance absorption reducing reflectivity into the specular cone. An interesting feature, also observed, was a side lobe outside the angle subtended by the lens, for s-polarized radiation. This was attributed to diffraction effects from a rippled critical surface.

At this stage it is pertinent to consider mechanisms that would produce critical surface curvature, as this seems to be a major factor in interpretation of the experimental results. The most obvious mechanisms stems simply from consideration of the hydrodynamics. As will again be discussed in Chapter 7, we can consider the density scale length L to be proportional to the ion sound speed c_s, it is thus proportional to $T_e^{\frac{1}{2}}$. A lateral temperature gradient ∇T_e would thus give rise to a lateral variation in the scale height, i.e. a non-planar plasma. Lateral temperature gradients are invoked in the thermoelectric source explanation of self generated magnetic fields measured by STAMPER and RIPIN, 1978, and RAVEN *et al.* 1978. A lateral variation in irradiance across the focal region would be the simplest explanation for the presence of a temperature gradient, and that variation could be caused by self focusing, beam aberrations, or diffraction effects in the far field. Lateral thermal conduction would be expected to smooth out the temperature gradient, but competing processes such as caviton formation (evidence for which has been found under similar experimental conditions (DONALDSON and SPALDING, 1976)) and associated ponderomotive effects, including preferential profile steepening (RANDALL and DeGROOT, 1979) occur. The determination of whether the density contours are concave or convex with respect to the incident beam is not answered by the present experiments. The effect of such surfaces on the refraction of the incident beam is discussed in Chapter 6 where differences between positive and negative contours are examined.

3.3 TEMPORAL MODULATION OF THE BACKSCATTERED PULSE

As well as the angular distribution of the backscattered radiation, another important feature was the observed modulation of the scattered intensity. Fig. 3.5 shows incident and scattered pulses as recorded on photon drag detectors PD1 and PD2 respectively for three shots. The full backscattered beam was collected by the detector PD2, for incident illumination as described at the beginning of this chapter. As discussed in Chapter 2, the periodicity of the modulations on the pulse envelope of the incident pulse is equal to the characteristic oscillator round trip transit time. The modulations on the backscattered pulse have the same periodicity. This structure was also observed at all collecting angles when the annular apertures were in place. However, the modulation depth was greater on the reflected pulse. Thus it appeared that although the original frequency spectrum was maintained in the interaction, the individual modes were acted upon non-linearly to give this increased contrast. In particular, the

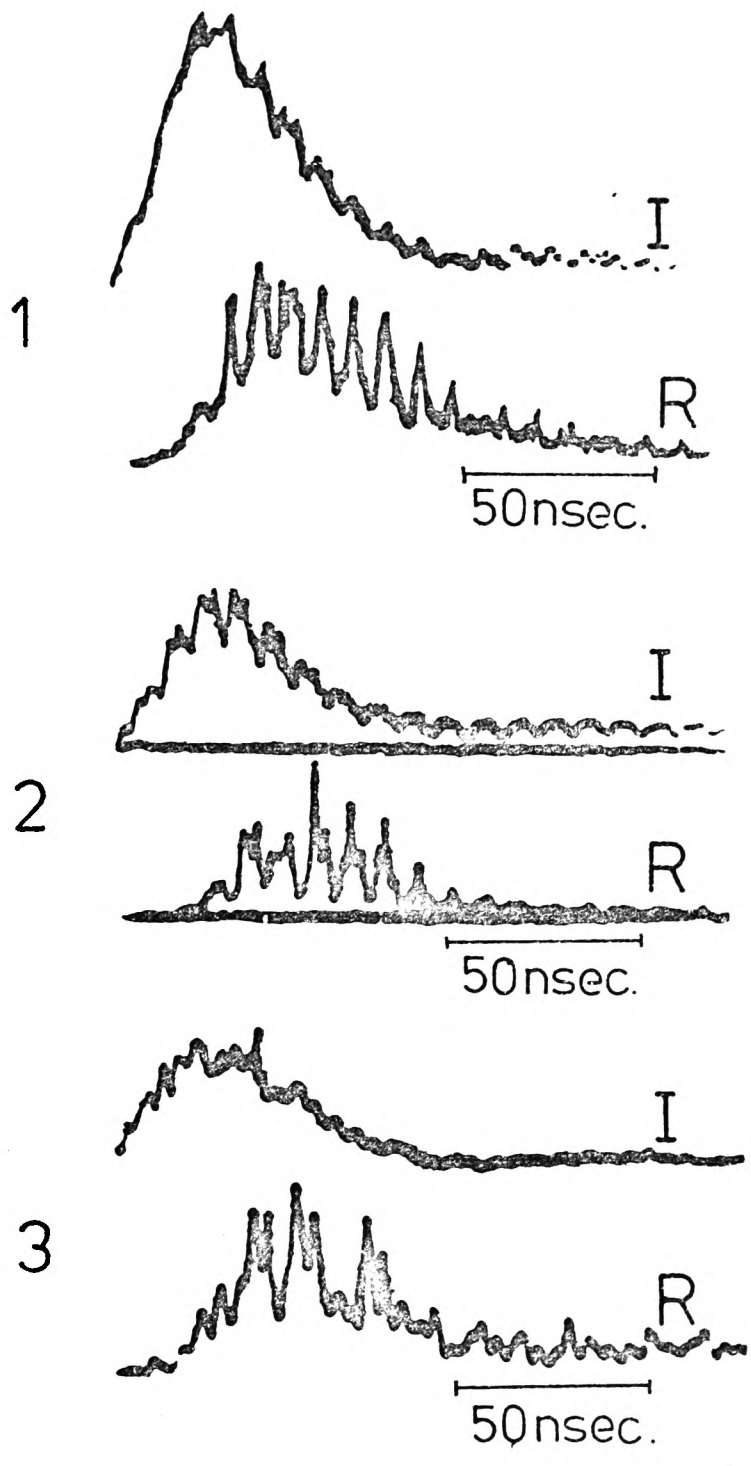


Fig. 3.5
Incident (top trace) and backscattered (lower trace) pulses for three separate shots showing the enhanced modulation of the backscattered temporal profile

modes in the reflected beam appear to have suffered a nonlinear 'amplification' in the reflection process, weaker modes being less strongly reflected by the correspondingly more weakly pumped SBS gain region. This region thus acts as a mode locking element and results in the observed enhancement of the modulation depth. To further investigate the process, a single transverse mode laser, which had a similar risetime and lased on a single axial mode (STAMATAKIS and SELDEN, 1976) was employed to repeat the interaction with identical experimental conditions (except for the irradiance which was less than for the original experiment due to the reduced output). No modulation was expected or observed in the incident beam as recorded on PD1. The reflected beam as recorded on PD2 also had a smooth envelope. A second test was made by readjusting the cavity of the auxilliary laser to permit lasing on four axial modes. Once again, a modulation was observed on incident and reflected pulses, the depth of modulation being greater on the reflected signal. Figure 3.6 shows the incident and reflected pulses for both the above cases. This test was not conclusive, however, due to the

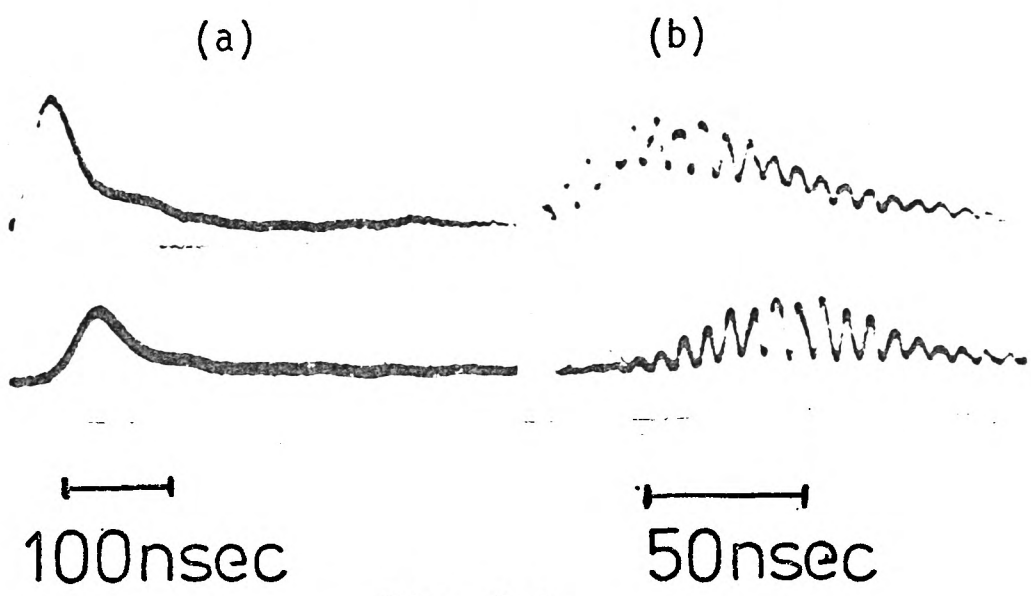


Fig. 3.6

Incident (top trace) and backscattered (lower trace) pulses for incident pulse consisting of (a) one, and (b) four, axial modes

discrepancy in the irradiances provided by both laser systems. However, the absence of modulation in the reflected beam for a single mode incident pulse strongly suggests a nonlinear reflectivity correlated to incident mode structure.

Several groups have reported temporal modulation of the reflected radiation. BASOV *et al* (1975) attributed their observations to the effect of time dependent turbulent parametric noise, established as a result of the development of one of the parametric instabilities. A dependence on target material was predicted, however, and experiments recording the reflected pulse from targets of Carbon, Aluminium, Perspex, Iron and Tantalum revealed no such effect in our own work.

Another mechanism for the temporal modulation of the back-reflected pulse was put forward by NG *et al.* (1979a) at Alberta. This group explained large scale modulations seen in the back-reflected radiation from an underdense preformed hydrogen gas target, as being due to saturation of the SBS by wave breaking. They comment that the small periodicity oscillations also seen on the pulse are apparently not correlated to the mode beating modulations on the incident signal envelope. From the examples given, however, the periodicity appears to be the same. (It is noted that MONTES and PEYRAUD (1980), attempt to explain the large scale modulations by considering the stimulated ion Compton scattering process, i.e., the limit of the SBS process as the ions reach a temperature >2 Te.)

Temporal modulations on the backscattered pulse from the interaction of 1 ns and 3 ns, 1.06 μm radiation at $> 5 \times 10^{13}$ W/cm^2 with gold and polyethylene targets was also observed at AWRE (HULL *et al.* 1979). No structure was initially present on the incident pulse, however, suggesting a different mechanism from the nonlinear amplification proposed here.

3.4 THE SPECULAR CONTRIBUTION TO THE BACKSCATTERED RADIATION

It was stated in section 3.2 that although no spectral identification had been made, the stimulated Brillouin scattering process was believed to be a dominant constituent of the reflected radiation. In order to obtain more evidence for this statement, an experiment was performed whose sole object was to estimate the importance of non-specular effects.

3.4.1 *REFLECTIVITY AS A FUNCTION OF ILLUMINATION ANGLE*

The energy backscattered through the focusing lens was monitored with a Gen Tec® joulemeter for various angles of target normal tilt, θ with respect to the incident laser axis (and such that the incident beam was s-polarized). By this simple experiment it was hoped to obtain an indication of the relative contributions to the backscattered signal from specular and other scattering processes. The focusing arrangement remained as in Fig. 3.1, and so, (apart from an obliquity factor – see below), we characterized the experimental conditions by an irradiance $\geqslant 10^{12}$ W/cm^2. The experimental results are shown in Fig. 3.7.

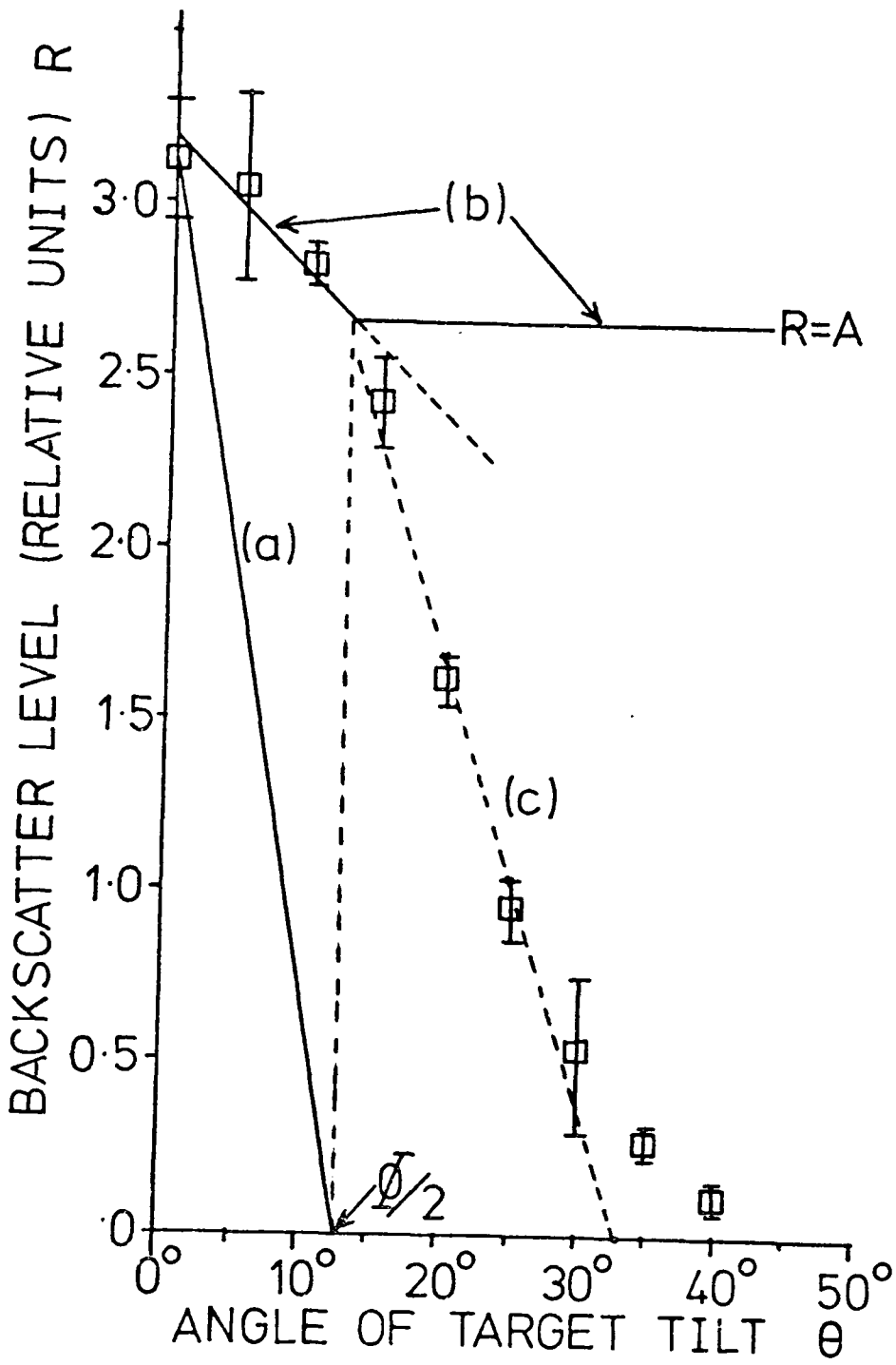


Fig. 3.7

Relative backscatter level as a function of target tilt. The error bars represent the scatter over several shots. Line (a) shows the expected variation for specular reflection only. Line (b) shows the expected variation assuming a combination of angularly dependent specular reflection and a constant stimulated backscatter fraction. Line (c) is a best fit for target angles between 15° and 30°

As can be seen, the relative reflectivity drops off slowly for target angles $\leqslant 15°$ and decreases thereafter fairly rapidly down to background level. An assumption that the backscattered signal was entirely specular from a plane critical surface (and the incident beam rectangular) would have resulted in a variation of R with θ as shown by line (a) in Fig. 3.7 where all the backscattered signal would be stopped by the entrance aperture for tilt angles greater than half the

incident cone angle Φ in a plane containing the target normal. For the experimental conditions, $\Phi/2 \sim 13^{\circ}$. As discussed in section 3.2, a planar critical surface may be an inappropriate assumption, and so a backscattered signal for target tilt angles $> 13^{\circ}$ may well be expected.

The stimulated Brillouin backscatter mechanism would be expected to produce a fairly constant back-reflected signal as the angle of target normal was varied relative to the beam axis. In practice we may expect some variation due to the reduction in intensity caused by obliquity effects in the focal area. However, the effect scales as $\cos\theta$ and, therefore, even at target angles of 40°, the irradiance is still 80% of its value at normal incidence. The other important consideration must be the variation of scale length in the backscatter direction as θ is varied. If we consider that the contour shape remains constant as the target is tilted, then for a planar plasma, the axial scale length varies at $(\cos\theta)^{-1}$. Again, therefore, this should have minimal effect on the absolute Brillouin backscatter level until large θ values are reached (although, see the discussion in section 4.2.1). Thus SBS alone does not explain the R versus θ variation shown in Fig. 3.7. If we assume, therefore, that the backscattered signal results from a combination of specular and stimulated contributions, a variation of the form:

$$\left.\begin{aligned} R &= A + B\{1 - 2\theta/\Phi\} \quad \text{for} \quad \theta \leqslant \Phi/2 \\ R &= A \qquad\qquad\qquad\quad \text{for} \quad \theta > \Phi/2 \end{aligned}\right\} \tag{3.3}$$

might be expected, where R represents the backscatter level. A is an angular independent stimulated contribution and B the magnitude of the specular reflection at normal incidence. The line marked (b) in Fig. 3.7 represents a fit, to the experimental data, of the variational form given by equation (3.3).

It can be seen that the simple variation predicted by equation (3.3) can be used for small angles of incidence but does not explain the observed variation in the relative reflectivity for angles $> \sim 15^{\circ}$.

It was initially postulated that the persistence of backscatter for target angles where the specular contribution should not have returned

through the incident lens, was an indication that the critical surface normal presented a smaller angle to the beam axis than the target surface normal. In particular, the observed variation by backscatter level from $15^\circ < \theta < 30^\circ$ would be fitted quite well by a line of slope only slightly less than that of line (a) on Fig. 3.7. This fitted line is shown as line (c) on the figure. From the equations of lines (a) and (c) we can derive an apparent relation between the angle of target tilt θ and the angle of critical surface tilt θ_c in the region $15^\circ < \theta < 30^\circ$ which can be written:

$$\theta_c \approx 0.5 \cdot \theta - 4.7^\circ .$$

Thus for example, when the target normal was at an angle of 20° to the beam axis, the critical surface normal presented at angle of only $\sim 5^\circ$ with the corresponding enhancement to the specular backscatter level. However, this mechanism would have resulted in reduced specular sidescatter and subsequent experiments (Chapter 4) showed that this was not the case. In fact, it was concluded (Chapter 5) that for certain cases, the critical surface normal presented a larger angle to the incident beam axis than the target normal.

An alternative explanation of the observation that backscatter levels were greater than expected on a specular basis, but less than expected from consideration of a stimulated contribution, was provided by recalling the earlier assertion that the SBS process grew from specularly reflected light from the critical surface rather than from thermal noise. It was, therefore, proposed that for angles $\geq 15^\circ$, the stimulated backscatter level in the lens direction was reduced due to the absence of the necessary growth signal in this direction but that the finite backscatter levels for these angles resulted from the shape of the critical surface allowing some specular reflection back into the incident cone, thus providing a pump for the stimulated Brillouin backscatter.

As a final, simple, test in this series of experiments, for the dominant presence of the stimulated Brillouin scattering process, a 'Dee' shaped aperture was placed in front of the entrance window of the target chamber, the target normal reset parallel to the laser axis, and the incident and

backscattered energies monitored. This very crude experiment employed the ray retracing characteristics of the SBS process. It was found that with the 'Dee' in position, the relative reflectivity was only slightly less than half of that measured with the full aperture. If the backscattered signal had been predominantly specular in nature, it would have been blocked by the 'Dee', upon exit from the chamber. This was taken as qualitative evidence for the dominance of the stimulated scattering process in the backscatter; at least for near normal illumination.

3.5 SUMMARY AND CONCLUSIONS

The experiments reported in this chapter are not conclusive. The following processes are strongly indicated however:

(1) Anomalous absorption as an important contribution to the total absorption. The resonance absorption process is indicated.

(2) Non-planar density contours.

(3) Stimulated Brillouin backscattering as the dominant contribution to the back-reflected signal for near normal illumination of the target.

(4) SBS growth from specular reflection from the critical surface.

The multimode nature of the incident beam adds considerably to the difficulties of interpretation of the experiments as well as severely perturbing the beam focusing properties. For these reasons, therefore, subsequent experiments were performed with the unstable cavity configuration described in Chapter 1. In order to provide better evidence for the presence of SBS in the experiments, the spectral content of the backscattered radiation was measured and the results described in Chapter 6.

The next chapter describes the first experiments performed with the unstable cavity and extends the themes originating from the above work, namely, the composition of the scattered radiation with emphasis on absorption, reflection and refraction processes in the focal volume.

CHAPTER 4

LASER-PLASMA MEASUREMENTS WITH THE UNSTABLE CAVITY

4.1 INTRODUCTION

The measurement of the focal properties of the single transverse mode annular beam from the confocal cavity was described in Chapter 2, section 2.3.3. For a typical 1 GW gain switched output pulse, a peak irradiance of $> 10^{12}$ W/cm^2 was shown to characterize experiments performed with this beam. In this chapter, and Chapter 6, these experiments will be described. The diagnostic arrangement used was similar to that shown in Fig. 3.1 with the following improvements:

(1) The beam splitters were positioned at an angle of 30° relative to the beam axis to provide greater throughput of the incident flux.

(2) The reflected beam was focused onto the monitors with a lens.

(3) In addition to the 2π collecting mirror to monitor the side-scattered radiation, provision was made to surround the target with calibrated burn paper.

(4) A basic debris shield was positioned inside the target chamber, consisting of an aperture slightly larger than the incident focal cone. This was found to significantly improve the problem of lens protection from target blow-off.

The basic experimental arrangement is shown in Fig. 4.1. Experiments were performed on highly polished massive graphite flats as before.

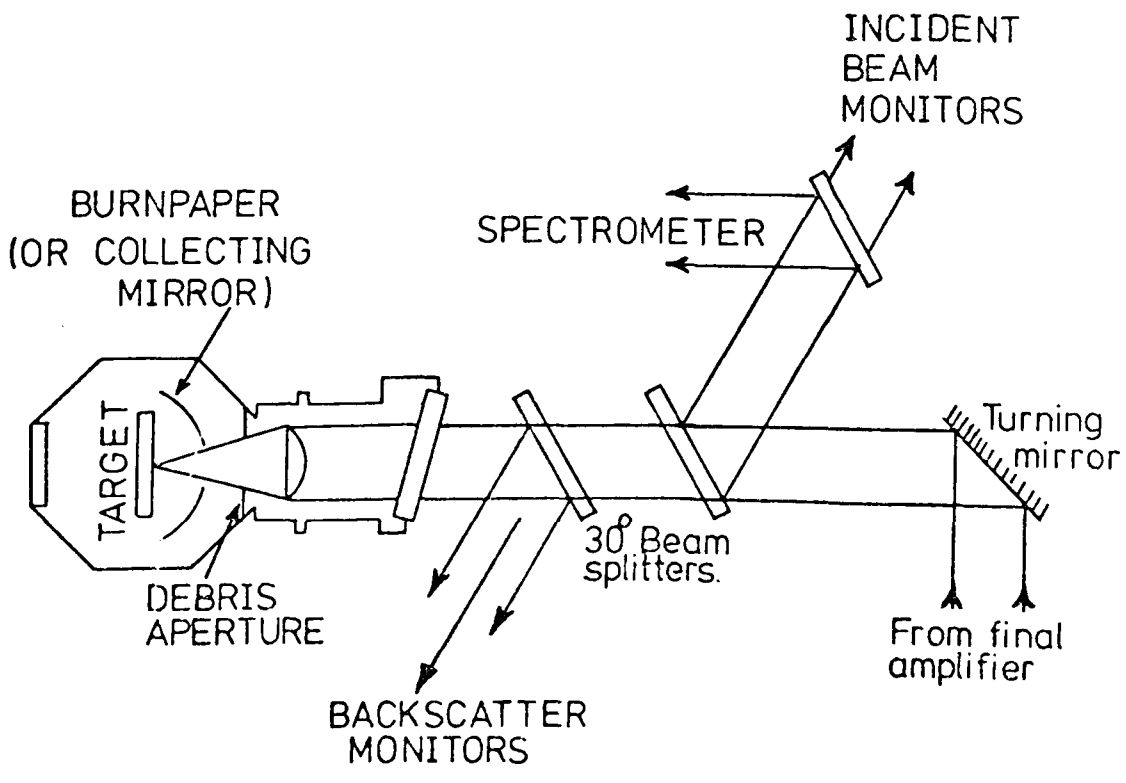


Fig. 4.1
Basic experimental arrangement for work performed with oscillator in the unstable configuration.

4.2 PARASITIC OSCILLATIONS

It was observed that when the target was exposed to the laser radiation, regular spikes separated by ~ 80 ns were present on both incident and reflected photon drag signals. This periodicity corresponds to a cavity length of ~ 12 meters, and it was found that for an assumption that the pulse made three passes inside the oscillator, this length corresponded to a cavity formed between the target and the oscillator. It was initially assumed that the parasitic oscillation originated from early specular reflection from the polished target surface, however, subsequent investigation showed that this was unlikely for two reasons:

(1) The effect did not decrease for subsequent shots onto the target surface after the first. Microscopic examination, see section 2.2.3, showed that the first shot produced a considerably roughened surface on the carbon target.

(2) The effect did not decrease for non-normal angles of incidence.

These two observations indicated that one 'mirror' of the parasitic cavity was formed by the laser-produced-plasma on the target surface and not the target itself.

Figure 4.2 shows incident pulses with target exposed and covered, and a reflected pulse from the target.

Sufficient energy to produce damage to the target surface was extracted by the parasitic cavity when just the amplifier modules alone were fired. In this case the resulting pulse had a FWHM of 100 ns and a highly structured profile similar to that observed from the earlier stable cavity output. The peak power of this pulse was a factor of three down on the peak power of the gain switched spike shown, for example, in Figs. 4.2(a) and (b). The pulse disappeared when either mirror of the oscillator cavity was covered, indicating that the cavity as a whole was acting as a mirror for the parasitics and not any individual component such as exit

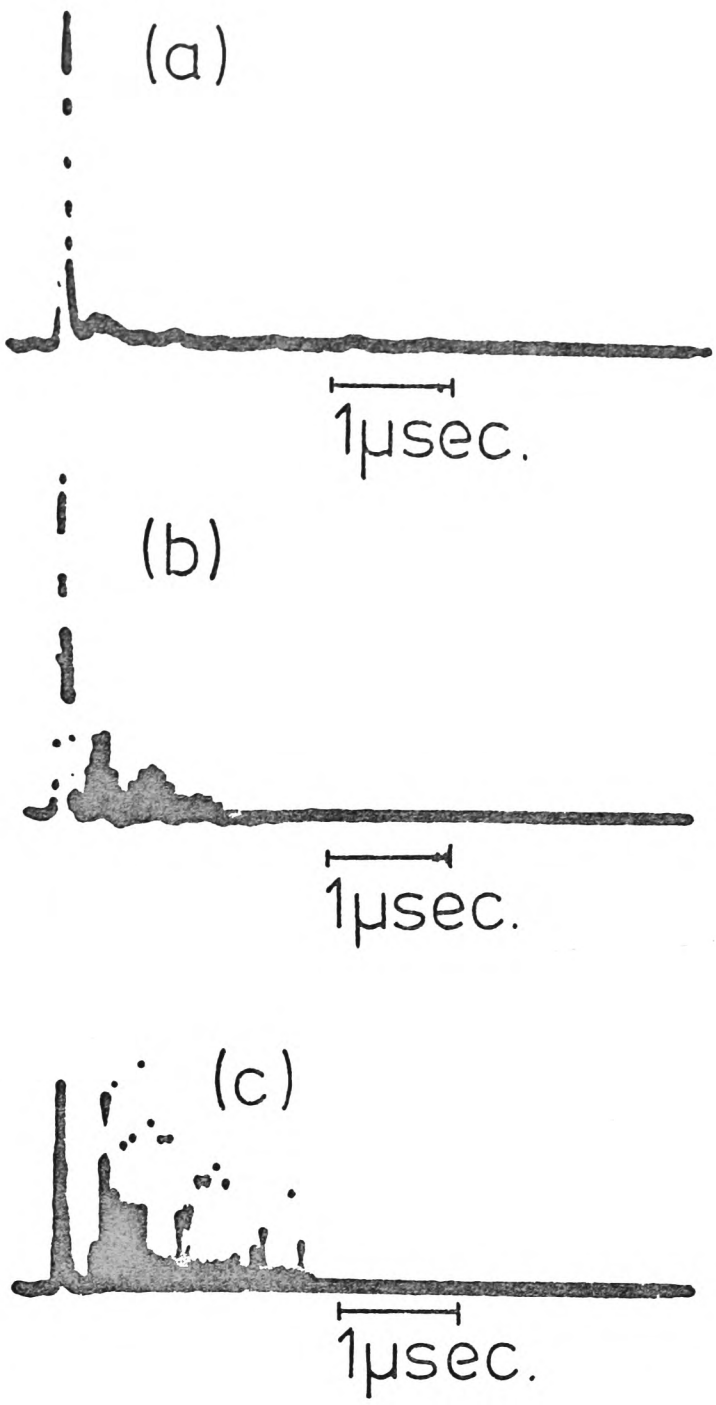


Fig. 4.2
(a) Incident pulse with target covered. (b) Incident pulse with target exposed. (c) Backscattered pulse from target; illustrating the effect of the target in the production of parasitic oscillations

window, spider, polarizer or mirror mounts. Similarly, it was checked that the components of the target chamber did not contribute to the parasitic oscillations by removing the target, whereupon the oscillations stopped.

4.2.1 *VARIATION OF PARASITIC OSCILLATIONS WITH ANGLE OF ILLUMINATION*

It was decided that the effect warranted further investigation as it was clear that it originated in the plasma, and as such, was liable to provide useful information concerning the backscatter processes. Due to the fact that it was a feedback phenomenon, experiments were performed that monitored the oscillations as the target was tilted from normal incidence. A particular series of shots is shown in Fig. 4.3.

Several interesting features are apparent in this figure:

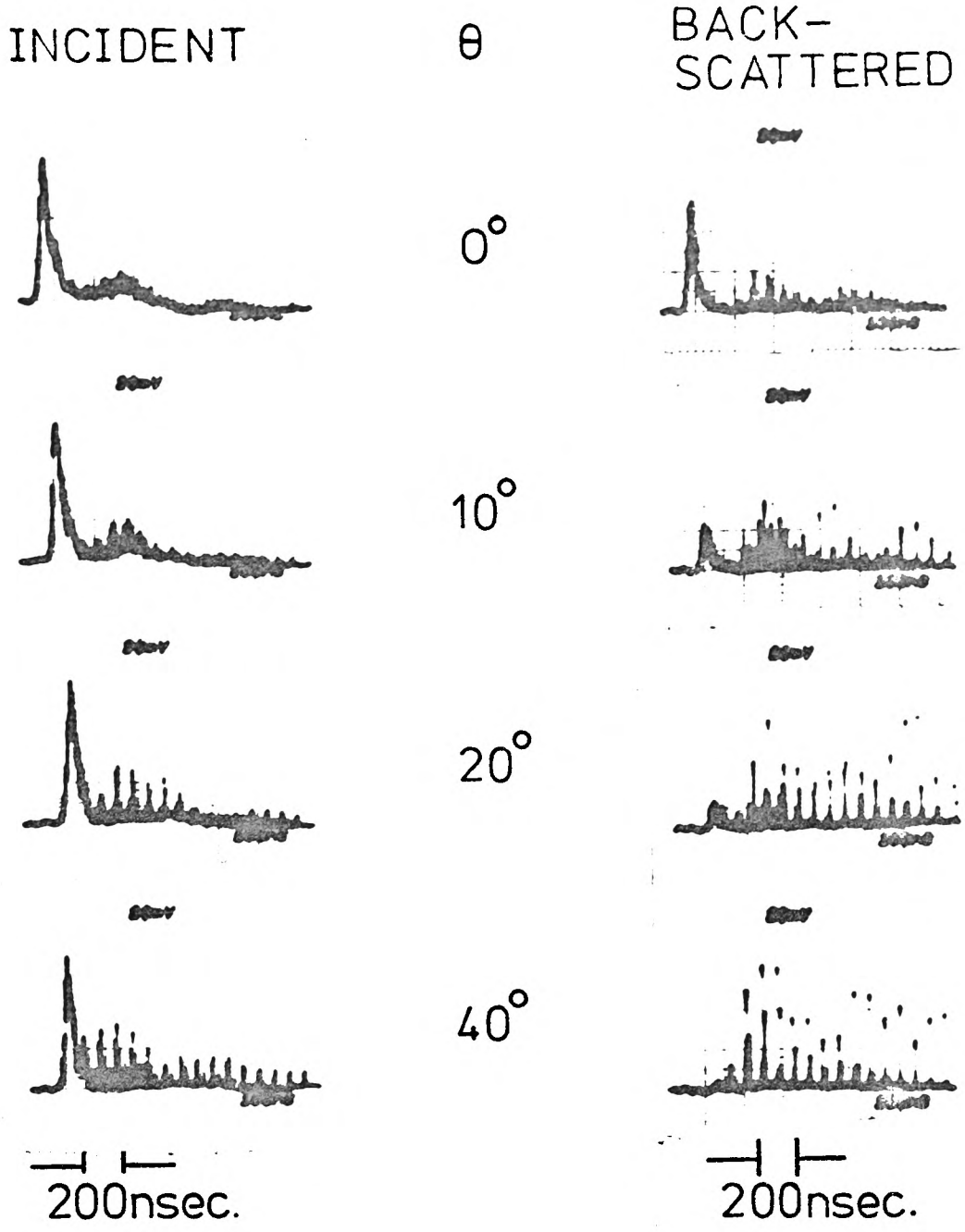


Fig. 4.3

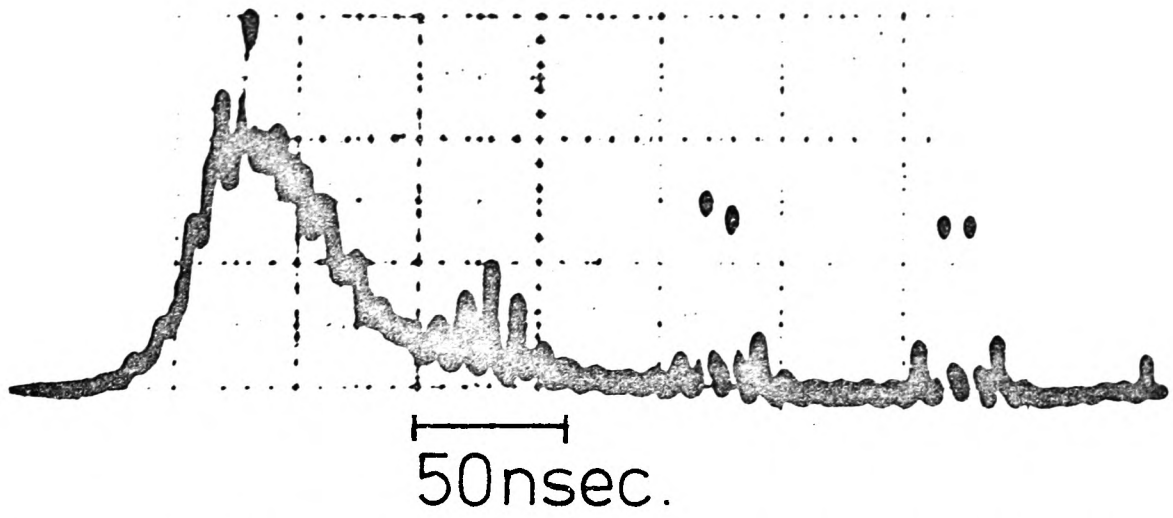
Photon drag signals of incident and backscattered pulses showing the effect of varying the angle of target illumination θ

(1) The magnitude of the parasitic oscillations increased as the angle of incidence was increased.

(2) The magnitude of the reflected spike decreased as the angle of incidence was increased.

(3) The depth of the modulations of the 80 ns periodicity oscillations was nearly 100% in the reflected pulse.

(4) Examination of the fine structure within the 80 ns period showed it to have the same periodicity, i.e. ~ 8.5 ns, as that due to longitudinal mode beating in the oscillator cavity. Fig. 4.4 shows the incident pulse with the target angled at 45° to the beam axis. The parasitic periodicity of ~ 80 ns and the mode beating periodicity of ~ 8.5 ns can be clearly seen.



Photon drag signal of incident pulse showing the fine structure of the parasitic oscillations

(5) The parasitics started much nearer to the back-reflected spike as the angle of incidence was increased

It was also observed that the magnitude of the parasitics was sometimes modulated with an envelope of period ~ 500 ns. This effect was apparent on a contracted time base and is shown in Fig. 4.5, for a shot at normal illumination of the target. (Note that the variation in the absolute magnitudes of the pulse height between Figs. 4.3, 4.4 and 4.5 is due to different attenuations in front of the detectors and not to differences in the incident energy.)

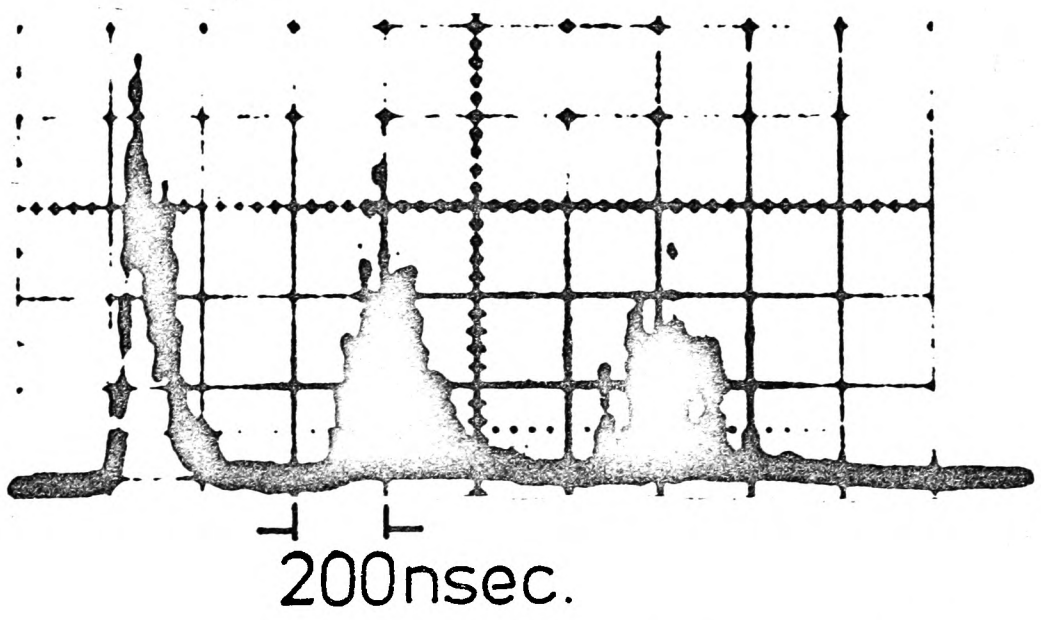


Fig. 4.5
Photon drag signal of the backscattered pulse showing the long period (~ 500 ns) modulation

The assumption that the parasitic oscillations do not originate from specular reflection from either the target surface, or the critical surface in the plasma, necessitates accounting for the feedback mechanism. In Chapter 3, evidence was presented that indicated the presence of the

stimulated Brillouin scattering process in the underdense corona. If we assume that parametrically generated radiation acts as the feedback source we must confirm that it would be amplified by the laser gain medium. In other words we must check that, given a wavelength shift in the backscattered light, it still lies on the gain curve of the amplifier. The FWHM of this curve is ~ 4 GHz for a 2:1:10 CO_2:N_2:He gas mixture at atmospheric pressure and room temperature. This value was derived from the expression given by ABRAMS (1974), namely,

$$\Delta\nu(\mathrm{MHz}) = 7.58\,(\psi_{CO_2} + 0.73\,\psi_{N_2} + 0.64\,\psi_{He})\,P_{\mathrm{Torr}}\left(\frac{300}{T}\right)^{\frac{1}{2}},$$

where ψ_x is the partial fraction of gas x, P is the pressure in torr, and T is the absolute temperature.

We can then give the normalized small signal gain, $\alpha(\nu)$ as a function of frequency by fitting $\Delta\nu$ to the Lorentzian given by SCHAPPERT *et al.* (1975) as follows,

$$\frac{\alpha(\nu)}{\alpha_0} = \frac{(\frac{1}{2}\Delta\nu)^2}{(\frac{1}{2}\Delta\nu)^2 + (\nu - \nu_0)^2}\,.$$

This gain curve is plotted in Fig. 4.6.

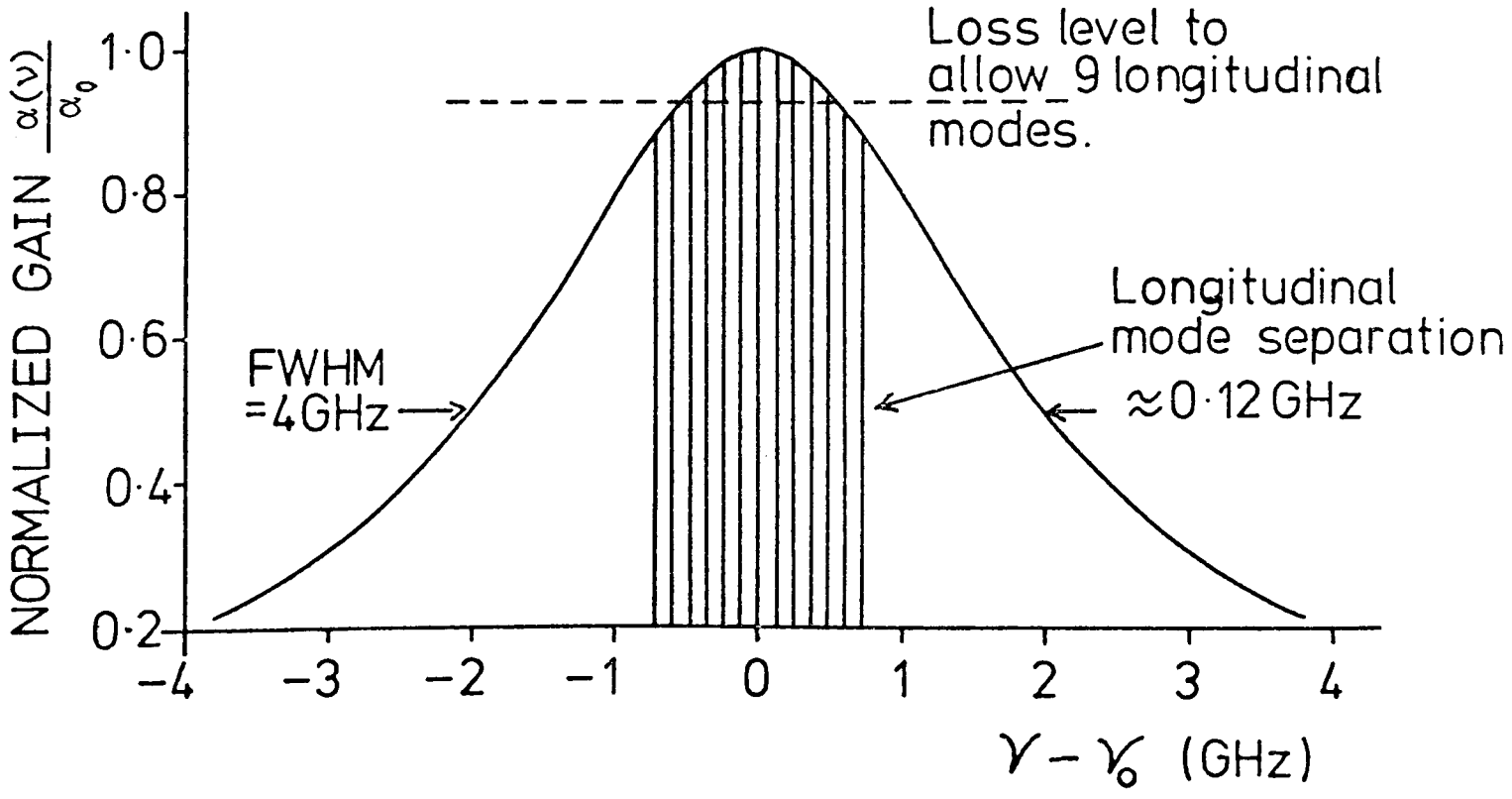


Fig. 4.6

CO_2-amplifier gain curve for 2:1:10 CO_2:N_2:He gas mix. Longitudinal mode spacings are illustrated. $\nu_0 = 2.83 \times 10^4$ GHz.

Also shown in the figure are the longitudinal cavity frequencies separated by ~ 0.12 GHz (corresponding to the round trip cavity periodicity). Diffraction loss levels limit the number of modes that can oscillate in the cavity, and, thus, in practice, the output bandwidth is reduced, typically to ~ 1 GHz. However, for parasitic feedback the original gain curve with a width of 4 GHz still applies, and thus oscillation would be possible over a large range of frequency shifts. In particular, a frequency shift to the $1/e^2$ down points of the gain curve would correspond to a wavelength shift of ~ 20 Å. It will be seen in Chapter 6 that the backscattered spectrum is significantly broadened from the incident spectrum and would thus act as a broadband pump for the parasitic cavity. We may thus proceed to account for the behaviour of the parasitic signal by postulating that the properties of the parametrically generated backscatter vary with angle of incidence. This leads us to three possibilities: (i) an increase in the backscatter level, or, (ii) a change in the backscatter spectrum, or (iii) a change in the spatial distribution of the backscattered emission, as the target is tilted.

The theory of the SBS process leads us to expect the backscattered level to increase with the density scale length (see for example equation (7.13)). Experiments performed at Rochester (TURNER and GOLDMAN, 1980) have measured this effect. At NRL also (RIPIN and McLEAN, 1979) the increased SBS reflectivity with scale length increase due to long pulse illumination, has been demonstrated. We might suppose that the density scale length in the backscatter direction increased as the target was tilted away from normal illumination. This would depend, of course, on the shape of the density contours and on refraction effects of the incident and reflected rays in the corona. As was discussed in section 3.4.1, however, we would not expect variation in L to be an important effect until large angles of incidence were reached. In any case, Fig. 4.3 shows that the energy in the initial reflected spike decreased with increasing θ. If we assume, though, that

the backscattered energy was temporally distributed over the whole signal rather than being contained in the first spike, this observation does not exclude an increase of *total* backscatter as the target was tilted. We could assume, for example, that the first spike represents the specular contribution to the backscattered signal which, naturally decreases with increasing θ (although the spike decreases too slowly for pure specular reflection, it would appear, from the variation discussed in section 3.4.1 and illustrated by line (a) on Fig. 3.7).

After a delay, τ, the parametric growth results in an oscillation, characteristic of the round trip transit time of the parasitic cavity. This delay τ represents the time required to set up the stimulated scattering process and we may expect this parameter to be reduced as conditions for SBS become more favourable, e.g., scale length increases. It has been noted above that this effect has indeed been observed and for large θ, the parasitic oscillations even seem to perturb the initial spike – see for example, the incident pulse at 40° angle of incidence in Fig. 4.3.

Of course it is also possible to ascribe the delay between the initial reflected spike and the onset of the parasitics, as due to the time required to re-establish gain in the amplifiers after their depletion by the initial gain switched spike. This would not, however, explain the variation of this delay with angle of incidence, although a dependence on temporal behaviour of the amplifier gain may well have a connection with the long time envelope modulations shown in Fig. 4.5.

4.2.2 *PRELIMINARY SPECTRAL ANALYSIS*

In order to check that the plasma was not behaving as a diffraction grating (e.g. via rippled density contours) and tuning the laser to another line, an investigation was carried out using an Optical Engineering Inc.® Laser Spectrum analyser. This instrument was designed to visually display CO_2

laser lines on an ultra-violet excited thermal sensitive screen. The back-scattered radiation was found to be the result of lasing only on the $P(20)$ line for all angles of incidence (it was, of course, confirmed that the incident beam also resulted from lasing on this line). The poor spectral resolution of the analyser permitted only such gross features as line change, to be observed and not spectral features within the lasing band. A change in these features with angle of incidence was considered at this stage as a possible explanation for the parasitic behaviour. In particular, it was envisaged that the backscattered spectrum might be dominated by the Doppler effect of the expanding plasma, resulting in a nett blue shift even in the presence of stimulated Brillouin scatter. This being true, then a reduction in the Doppler contribution (such as would be introduced by tilting the target) would shift the backscattered spectrum towards the λ_0 position again and hence back towards the peak of the gain curve (increasing the backscatter level). The results of a spectral analysis, presented in Chapter 6, do not bear out this hypothesis, however, for the backscattered spectrum was found to be broadened to the red, even at normal incidence. A reduction in the Doppler contribution in this case would shift the back-scattered radiation even further from the gain curve maximum.

4.2.3 *CONCLUDING DISCUSSIONS*

It is finally mentioned that filamentation of the backscattered radiation is possible in the corona and that the resulting localized channels of high irradiance could act as a pump source for parasitic instabilities. Experiments with preformed plasma targets at Alberta (NG *et al.* 1979) have indicated the existence of backscatter filamentation from observations of the spatial distribution of the X-ray emission formed in the self-focusing channels.

Coupling between the laser and the plasma has previously been

observed at Hull (DYER *et al.* 1976) for the interaction of a 60 ns pulse of 10 μm radiation with various solid targets at ~ 10^{11} W/cm^2. The phenomenon was manifest in the appearance of short duration (< 10 ns) spikes in the tail of the incident laser pulse and was particularly strong for high Z targets of silver and lead. Parasitic oscillations have been utilized by workers at the Lebedev Institute to construct a laser incorporating a plasma mirror (BASOV *et al.* 1979). In this particular experiment, an electro-ionized CO_2 laser, with the plasma formed at the focus of a spherical mirror at one end of the laser cavity, produced a prepulse of 100 ns duration followed by a train of nanosecond pulses.

The above discussion of parasitic behaviour with angle of incidence variation is very tentative. The basic result of this work seems to be that the origin of the parasitics is due to a parametric process within the corona, probably the stimulated Brillouin backscattering mechanism. We will now continue to describe further experiments performed with the unstable cavity. First, section 4.3 describes reflectivity measurements on the backscattered radiation.

4.3 BACKSCATTER REFLECTIVITY

Despite the fact that the parasitic oscillations described in the previous section tend to make interpretation of reflectivity experiments difficult if total backscattered energy is monitored, experiments to measure the reflectivity of the initial gain switched spike are still very useful and will be described in this section. The experimental arrangement remained as in Fig. 4.1, and the first experiments were performed for normal illumination of the plane carbon target at optimum focus. The irradiance remained at ~ 10^{12} W/cm^2. Over a large number of shots the backscatter peak reflectivity was found to be 3 ± 1% using calibrated photon drag detectors. This is in good agreement with the reflectivity found in similar experiments

performed with the multimode beam. Thus the mode structure of the incident pulse did not appear to have a large effect on the backscattered reflectivity of the initial gain switched spike.

4.3.1 *VARIATION OF BACKSCATTER WITH FOCAL POSITION*

The variation of backscatter reflectivity with target position (relative to the beam focus) was described in Chapter 2 as a possible indication of the optimum focal position. It is again stressed here that such experiments were predominantly performed as an aid to target positioning and not as a means of gaining insight into backscatter properties. This being said, however, it is still interesting to observe the variation of backscatter with target position and to compare the result with those obtained by other groups. Results of one such run are presented in Fig. 4.7.

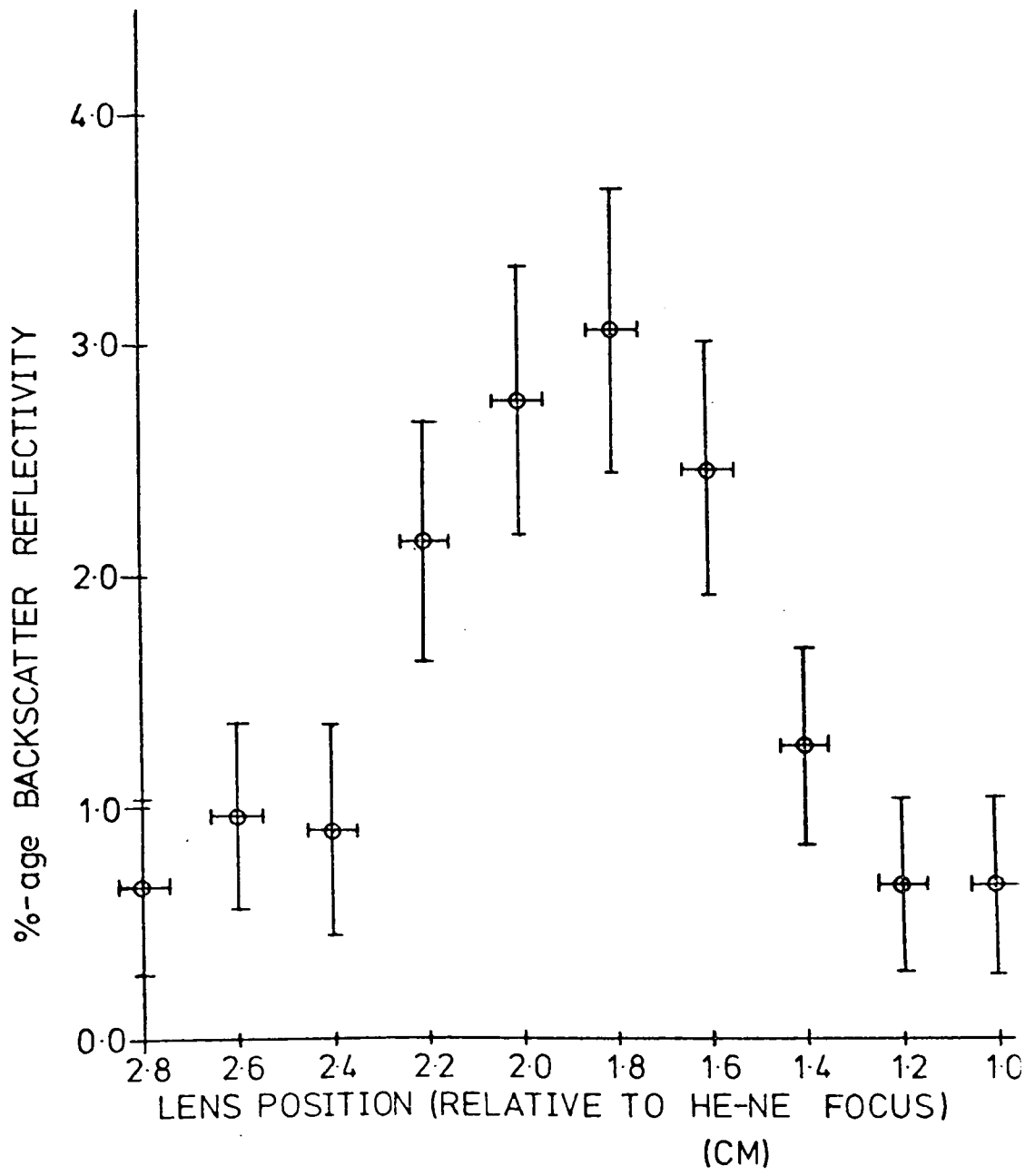


Fig. 4.7

Percentage backscatter reflectivity versus relative position of target in the far field of the focusing lens

We note that the reflectivity reached a maximum, and from subsidiary experiments (as described in Chapter 2) it was confirmed that the position of this maximum coincided with the optimum focus position. As with the X-ray emission variation of Fig. 2.2, it is seen that the backscatter reflectivity change with focus was not a sharply peaked function.

The behaviour of the backscatter with focal position has been studied at several laboratories. The results indicate that the illumination geometry and the laser wavelength and pulselength, have at least as much effect on the behaviour as the change in irradiance caused by the focus change. For example, at Limeil, MARTINEAU *et al.* (1974) observed that backscatter maximization coincided with focusing onto the target surface for a 60 ns CO_2 pulse at $\sim 10^{11}$ W/cm^2 irradiance on a solid deuterium target. FABRÉ *et al.* (1974) reported that reflection into the focusing mirror reached a peak for a focus ~ 1 mm from the surface of a plane polyethylene target irradiated by a CO_2 laser at $\sim 10^{12}$ W/cm^2. It was noted, however, that the absolute focal position was known only to an accuracy of ± 1 mm. Moreoever, the experimentally determined position of maximum backscatter did not coincide with the position of maximum X-ray emission (as recorded through a 30 μm aluminium filter). JANNITTI and TONDELLO (1974), for ruby laser irradiation between 10^{12} and 10^{13} W/cm^2 onto a wide range of target materials, noted that the target position of maximum back-reflection coincided with the soft X-ray emission. Their experimental results show a FWHM of the reflectivity versus target position curve of ~3 mm. At 1.06 μm, results from Garching (GODWIN *et al.* 1977) show a very strong dependence of backscatter with focus. For example, the absolute backscatter reflectivity from a copper target dropped from ~ 70% to ~ 30% for ~ 100 μm change in focal position. These experiments were performed with a 30 ps pulse. Experiments with a 1 ns 10 μm pulse at AWRE (MORGAN *et al.* 1978) show a weak variation of backscatter with focal position; the backscattered energy peaking ~100 μm

from the optical focus for both gold and polyethylene targets at $\sim 10^{12}$ W/cm^2. A weak variation of backscatter with target position was also reported by RIPIN (1977) for 1.06 μm irradiation of polyethylene and aluminium targets at $10^{15} - 10^{16}$ W/cm^2. In this case, however, the backscatter percentage was observed to decrease as the target passed through the focus.

The large variation between laboratories for this type of measurement shows the care that must be taken in attempting any interpretation of the results. Many separate parameters are involved in the final variation. This was the basic reason why the experiments of this thesis were performed for fixed and well-defined conditions with regard to focal geometry. Recent work by COLOMBANT and MANHEIMER (1980) has indicated that violent spatial and temporal changes in the irradiance, during an interaction, can considerably vary the absorption. As we have no measurement of the spatial irradiance distribution variation with focus, or high resolution spatial irradiance measurements at optimum focus (and cannot, therefore, account for possible hot spots in the far field), experiments performed for fixed geometry seemed to be a sensible procedure.

The next section describes measurements with the unstable cavity that extended the investigation of the scattered radiation outside the collection range of the focusing lens. These simple experiments were performed by monitoring the side-scattered radiation using calibrated burn paper as the recording medium. The variation with angle of incidence was also observed. In this way, the total reflectivity was estimated and information concerning scattering processes obtained.

4.4 SIDE-SCATTER

4.4.1 *2π COLLECTING MIRROR*

In order to measure the fraction of the incident energy sidescattered outside the collecting angle of the focusing lens, the technique described in Chapter 3 was used, namely a spherical collector, reflecting the

sidescattered radiation onto a detector. The particular method described in Chapter 3 was only possible for small targets in order that the collected radiation was not significantly obstructed as it propagated to the detector. The inevitable fraction that was obstructed was accounted for in subsequent energy balance calculations. In order that a more efficient collection be made, a modified device to that described in Chapter 3, was used. This device consisted of a diamond turned oxygen free copper substrate, which was then hand polished and gold coated. The mirror radius of curvature was 41 mm and the diameter 68 mm. A 9 mm diameter tapered hole on the mirror axis allowed the incident beam to focus onto the target. This diameter was set by measuring the maximum dimension of the burn at the appropriate distance from the focus. Due to the fact that the incident beam was of 10 cm X 5 cm aperture, this entrance hole was unmatched in one direction and thus a small amount of side-scattered energy was not collected.

By replacing the detector with calibrated burn paper and arranging the mirror to target distance, so that the side-scattered light was reflected as a collimated beam, spatial information was obtained. However, this information was limited by the obstruction caused by the target. The following results were obtained from the above experiments (all performed, as before, at $\sim 10^{12}$ W/cm^2 with plane carbon targets).

(1) The measured fraction of the incident energy in the side-scattered radiation was found to be $10 \pm 2\%$. This figure was, of course, arrived at by accounting for the energy obstructed by the target and thus inherently assumes that no localized regions of high reflectivity were 'hidden' in this way. The results presented in the next section confirm that this assumption was valid. Thus it appears that for experiments with the single transverse mode pulse, the percentage side-scatter was higher than that reported for the multimode experiments of Chapter 3. As pointed out in

section 4.3, however, we have to take care with any interpretation due to the presence of parasitics.

(2) From the burn on the exposed polaroid film, it was found that the sidescattered radiation was emitted into a cone of half angle equal to $\sim 18^{\circ}$. This figure is to be compared to the effective incident cone half angle of $\sim 10^{\circ}$. The extent of the recorded side-scattered radiation was, of course, limited by the threshold intensity of the exposed polaroid burnpaper. By subsidiary calibration experiments performed on the Trojan system, it was found that the threshold flux density for the film was ~ 0.1 Joules/cm^2. Thus we must qualify the above result by stating that side-scattered light with emissivity greater than ~ 0.4 Joules per steradian, is emitted into a scattered light cone of 18° half-angle. (Here we have used the fact that the polaroid is at an effective distance of 20.5 mm from the target). It is noted that the above experiments were performed for normal illumination of the target.

In order to obtain information about the angular distribution of the side-scattered radiation that was unaffected by the shadowing effect of the target, or possible aberrations and perturbations caused by the 2π mirror, an arrangement was devised that effectively replaced the mirror by the polaroid burn paper and thus enabled direct side-scatter records to be made. The measurements were extended to study the behaviour of the side-scattered radiation as the target was tilted away from normal illumination.

4.4.2 *DIRECT SIDE-SCATTER MEASUREMENTS*

Initial experiments were performed with a plane piece of exposed polaroid film, with a hole to allow the incident beam to pass through, positioned facing the target at a distance of 2 cm from the target surface. The resultant burn showed a symmetric distribution of side-scatter radiation with no localized regions of high flux. The burn also confirmed the angular spread reported in section 4.4.1, and calibration of the burn confirmed a

side-scattered percentage of ~ 10%. There was no change in the appearance of the burn as the target position was changed by up to 3 mm on either side of the optimum focus. For larger shifts than this, the side-scattered burn became less intense as the angular spread increased.

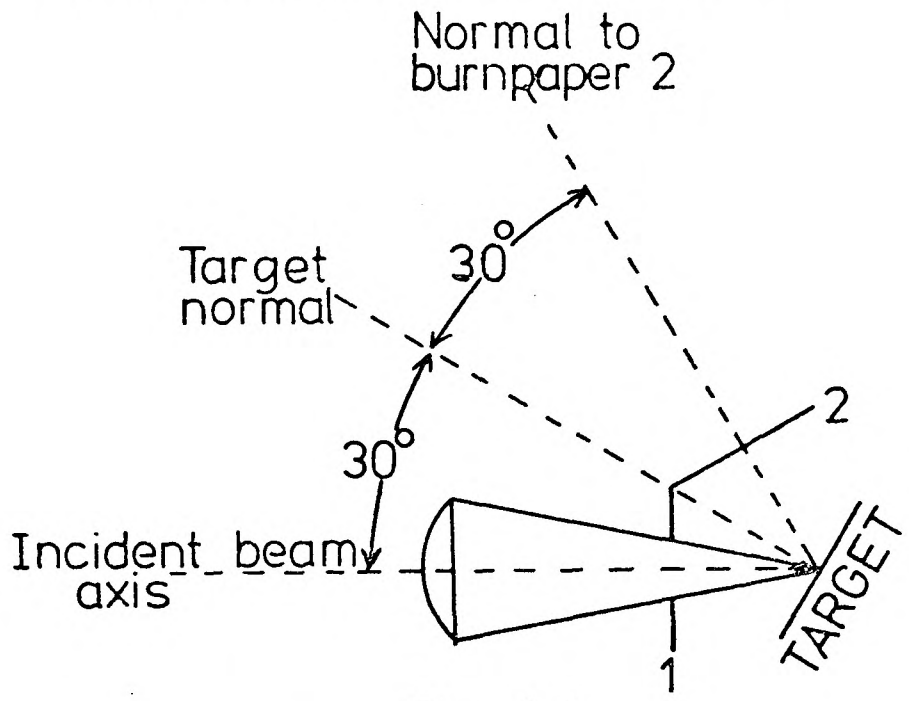


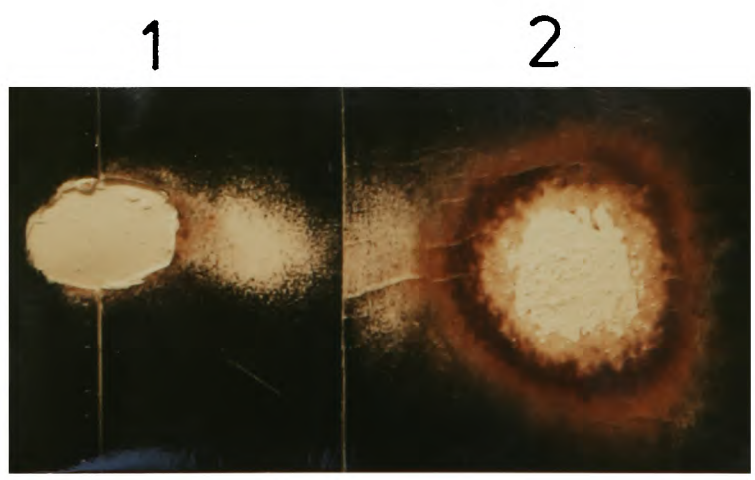
Fig. 4.8

Geometry of the initial burn paper technique for side-scatter study. 1 and 2 are sheets of exposed polaroid film. Sheet 1 is normal to the beam axis and has a hole to allow the incident beam through. Sheet 2 is positioned normal to the expected specular direction for a target illuminated at 30°.

To obtain information concerning the relative proportions of specular and anomalous reflections, the target was tilted in the horizontal plane (giving *s*-polarized illumination) and a second piece of polaroid film positioned as in Fig. 4.8 above, to record the specular burn. The result for $\theta = 30^\circ$ is shown in Fig. 4.9

Fig. 4.9

Resulting burn on exposed polaroid sheets placed as in Fig. 4.8.



The broad angular distribution of radiation into specular directions is apparent, but the spread of radiation into all angles back to the laser axis is an interesting feature, as is the indication of strong backscatter given by the region of more intense burn around the incident beam aperture. It would appear from this result that the scattered distribution peaks into the solid angle of the incident beam and that the specular reflection is considerably broadened — probably by reflection from a non-planar critical surface. Also, the fact that the specular reflection now *appears* to be emitted into the expected direction for specular light, gives further evidence for postulating that the parasitic oscillations described in the first part of the chapter arise from anomalous reflection from the corona rather than specular from the critical surface or target surface.

The experiment just described had two disadvantages, however. First, the scattered radiation, being recorded on a plane surface, suffered from a spatial distortion. Secondly, the angular scale of the resultant burn was not accurately known. To remedy these two failings, a cylindrical former for the exposed polaroid burn paper was constructed which rotated accurately about a fixed pedestal. The vertical axis of both former and pedestal passed through the optimum focus on the plane target surface. Thus the target, once mounted on the pedestal, was capable of being accurately positioned, whilst the angular directions relative to the focal point, were accurately known ($\pm 2^{\circ}$). The arrangement is sketched in Fig. 4.10. The side-scattered distribution was studied as a function of angle of illumination and the result of a particular run is shown in Fig. 4.11.

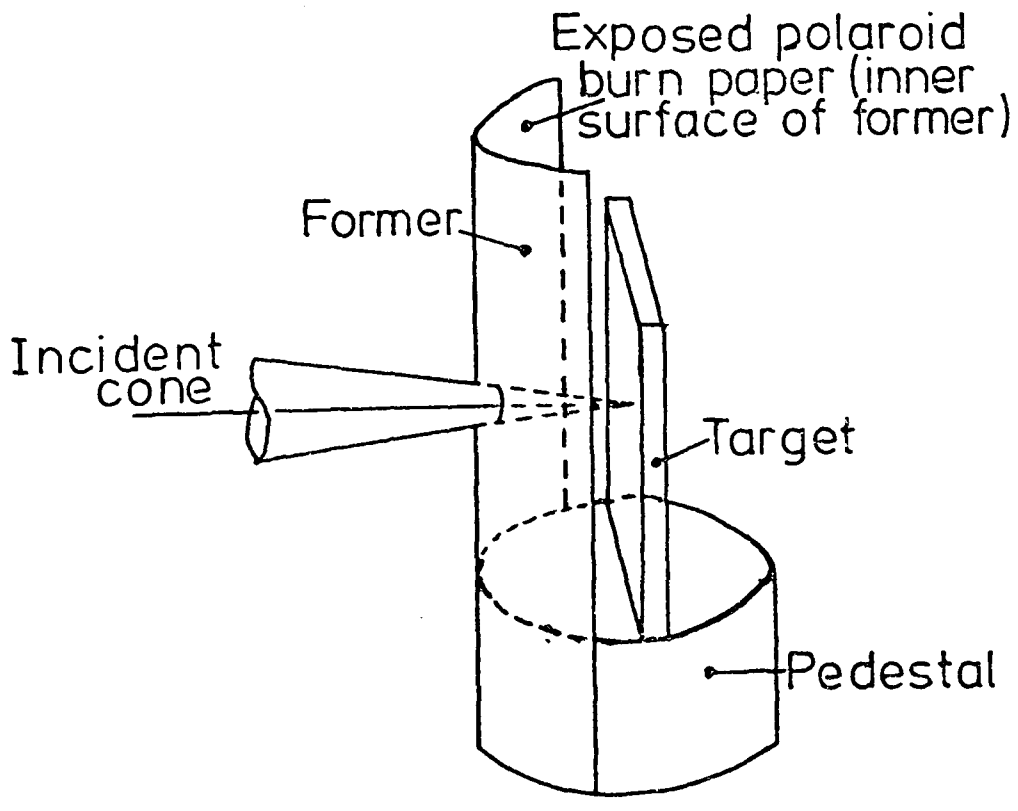


Fig. 4.10
Improved arrangement for side-scatter study

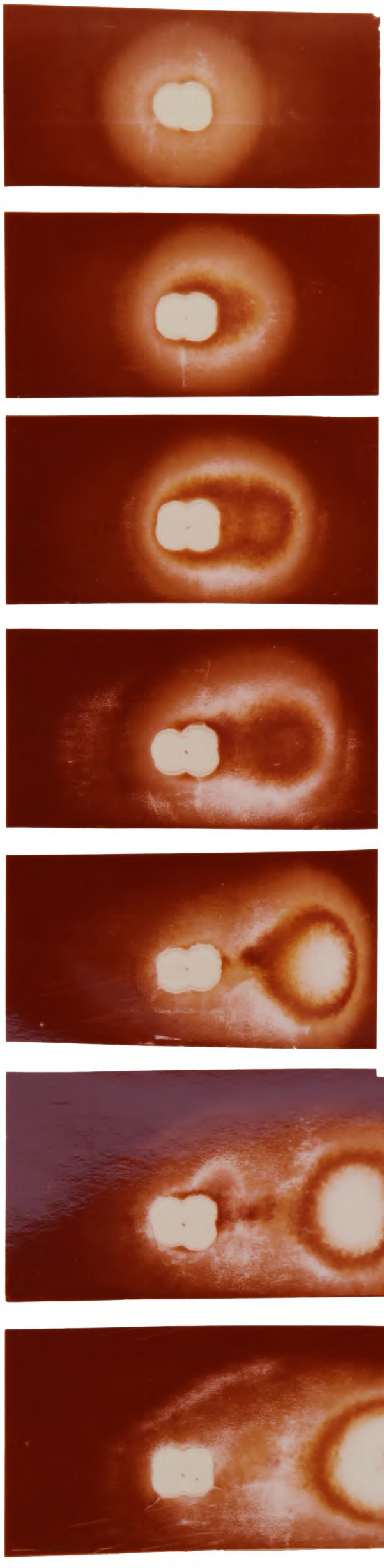


Fig. 4.11

Results of an experimental run, using method illustrated in Fig. 4.10 to study side-scatter distribution vs angle of illumination

As in the previous experiment, side-scattering occurred over a wide distribution of angles. There was an obvious maximum of emissivity into angles that at first sight appeared to define the specular direction for a particular target tilt angle. However, upon careful calibration of the burns, it was found that for all non-normal angles of illumination, this 'specular' radiation was not, in fact, in the specular direction, and in all cases occurred at greater angles. Fig. 4.12 plots the position of the side-scatter peak versus angle of incidence. The deviation from the locus defining specular reflection is apparent from this figure.

This phenomenon was also observed by WALKER *et al.* (1978) for interaction experiments performed with the Trojan laser at Culham Laboratory upon plane polythene targets. The angular distribution of the side-scattered radiation for 1.3 kJ pulses with 1.5 μs duration, is shown in Fig. 4.13.

It can be seen that for target illumination at 18°, the specular peak occurred at ~ 50°, i.e. 14° greater than the expected specular angle. It was postulated by the authors that the plasma acted as an off-axis negative lens which both deflected and diverged the reflected light. This particular result is also plotted in Fig. 4.13.

It is noted that because of the interesting nature of this effect, the scattering experiments on APPLE were performed many times and with great care taken over angular calibration to eliminate any possible error from this source. In all cases the effect persisted and the specular reflection was observed at angles greater than specular.

It seemed likely that refraction effects in the corona were responsible for the shift away from the specular direction. However, shifts of the magnitude of those measured cannot be accounted for by refraction from a plasma with plane parallel density contours. It is true that a spatial shift relative to the axis of the incident beam would be expected for radiation reflected by plane parallel plasmas, due to refraction effects. In

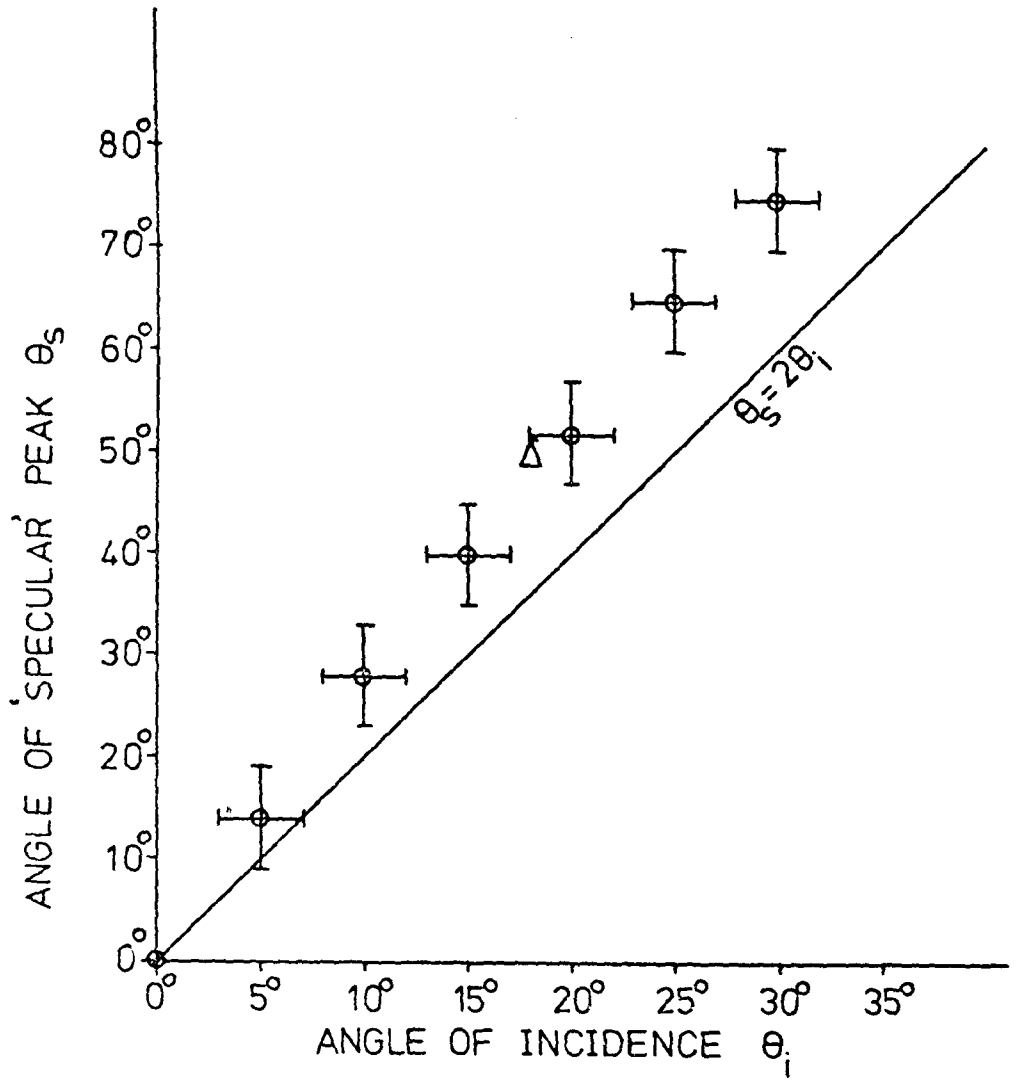


Fig. 4.12

Position of the 'specular' peak versus angle of illumination from results shown in Fig. 4.11. The solid line shows the expected variation assuming specular reflection. The triangle is the result obtained by WALKER *et al.* (1978)

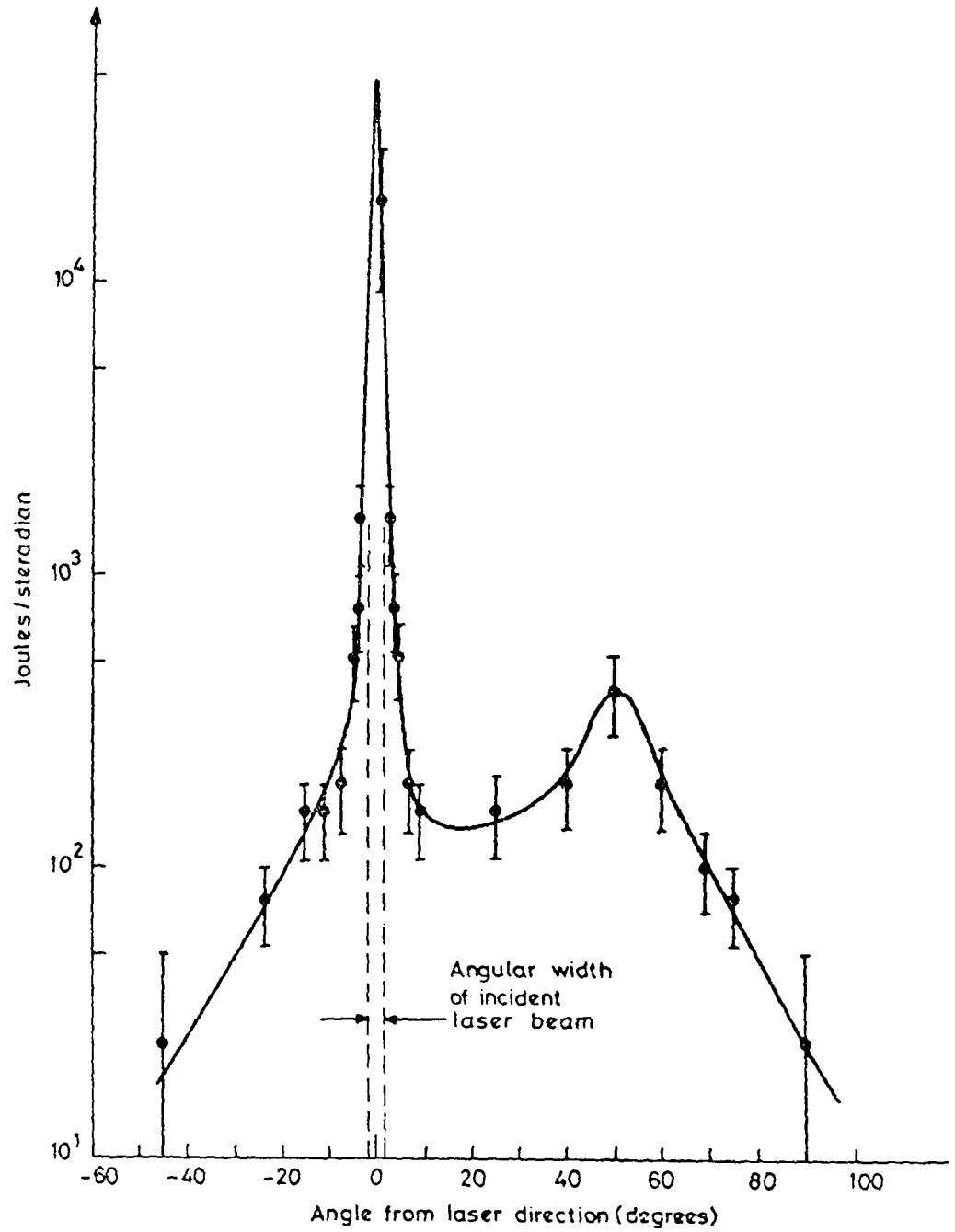


Fig. 4.13

Angular distribution of side-scatter from WALKER *et al.* (1978) — reproduced with permission.

other words there is a displacement of the ray trajectory vertex by an amount Δy from the point on the critical surface at which the ray is originally aimed.

Consider the invariant equation for a refracting ray in plane parallel geometry, i.e.

$$\eta(x) \sin \psi(x) = 1.0 \sin \theta \qquad (4.1)$$

where $\psi(x)$ is the local angle between the ray tangent and the critical surface normal, $\eta(x)$ is the refractive index of the point on the ray at which ψ is measured, and θ is the angle of incidence (assumed equal to ψ when $\eta = 1.0$). Using this equation, an analytic expression for Δy as a function of θ can be derived (see HOWARD, 1977). For an exponential density profile:

$$\Delta y = 2L \tan \theta \ \ell n(2 \cos \theta) \ . \qquad (4.2)$$

This equation is accurate providing that the ray starts sufficiently far out in the plasma that the local refractive index can be considered as unity. Thus the ray path is initially linear.

We can generalize this treatment to give an expression for the apparent angular shift of a refracted ray when angles are measured from the focus point on the target surface, the ray is recorded on burn paper a known distance R from this point, and the critical surface is not constrained to be co-incident with the target surface, The situation is illustrated in Fig. 4.14, where the geometrical constructions leading to an expression for the apparent angular shift $\Delta\theta$ as a function of θ, L and X_c are indicated. L is the density scale length and X_c is the separation of the critical surface from the target surface.

The expression is as follows

$$\Delta\theta = \sin^{-1}\left[\frac{\sin\theta}{R} \left\{ 4L \cdot \ell n(2 \cos\theta) - 2X_c \right\} \right] . \qquad (4.3)$$

It is noted that X_c can be made either positive or negative. Negative

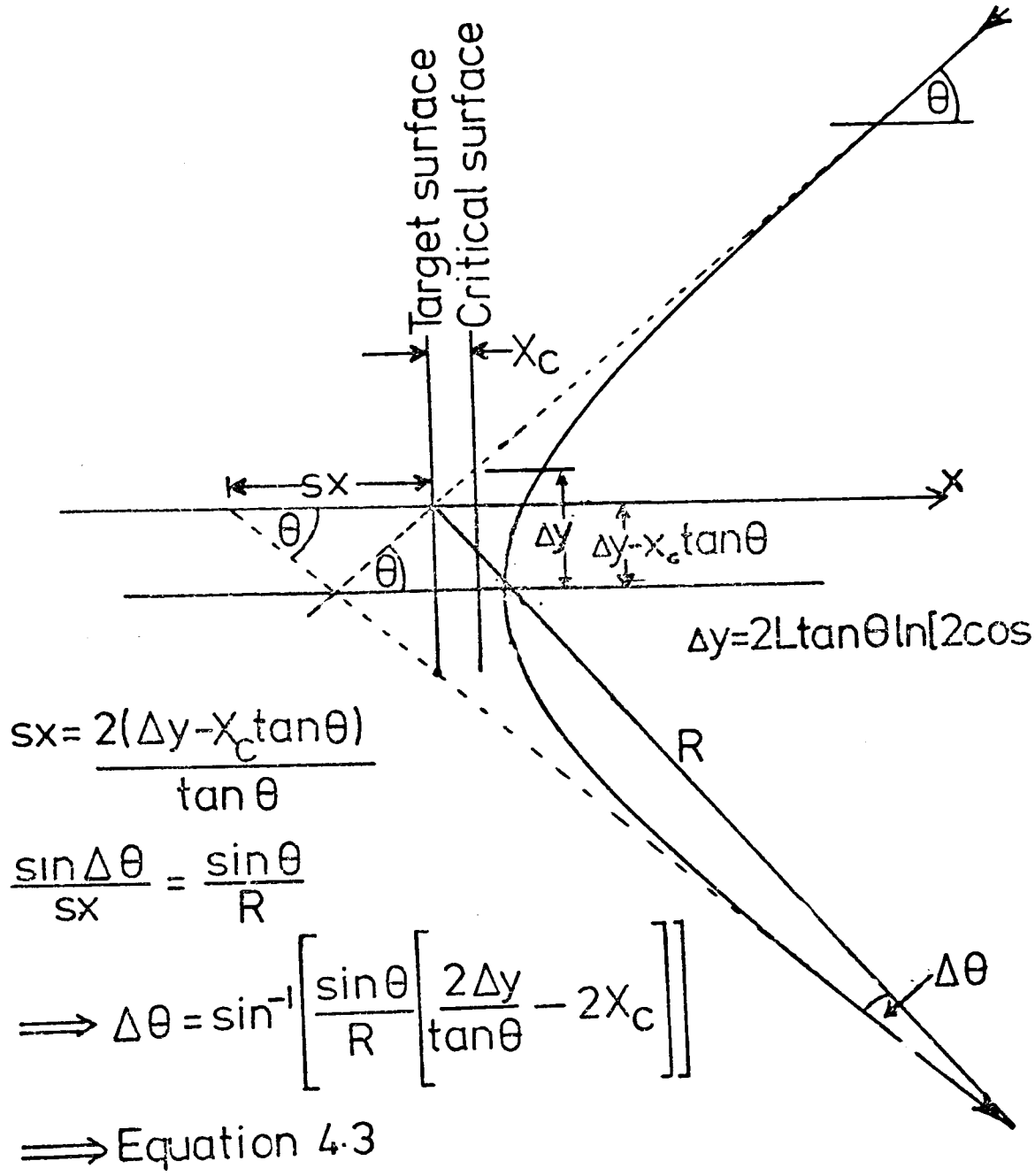


Fig. 4.14

Illustration of the refraction mechanism causing an apparent focal shift. The derivation of equation (4.3) is outlined

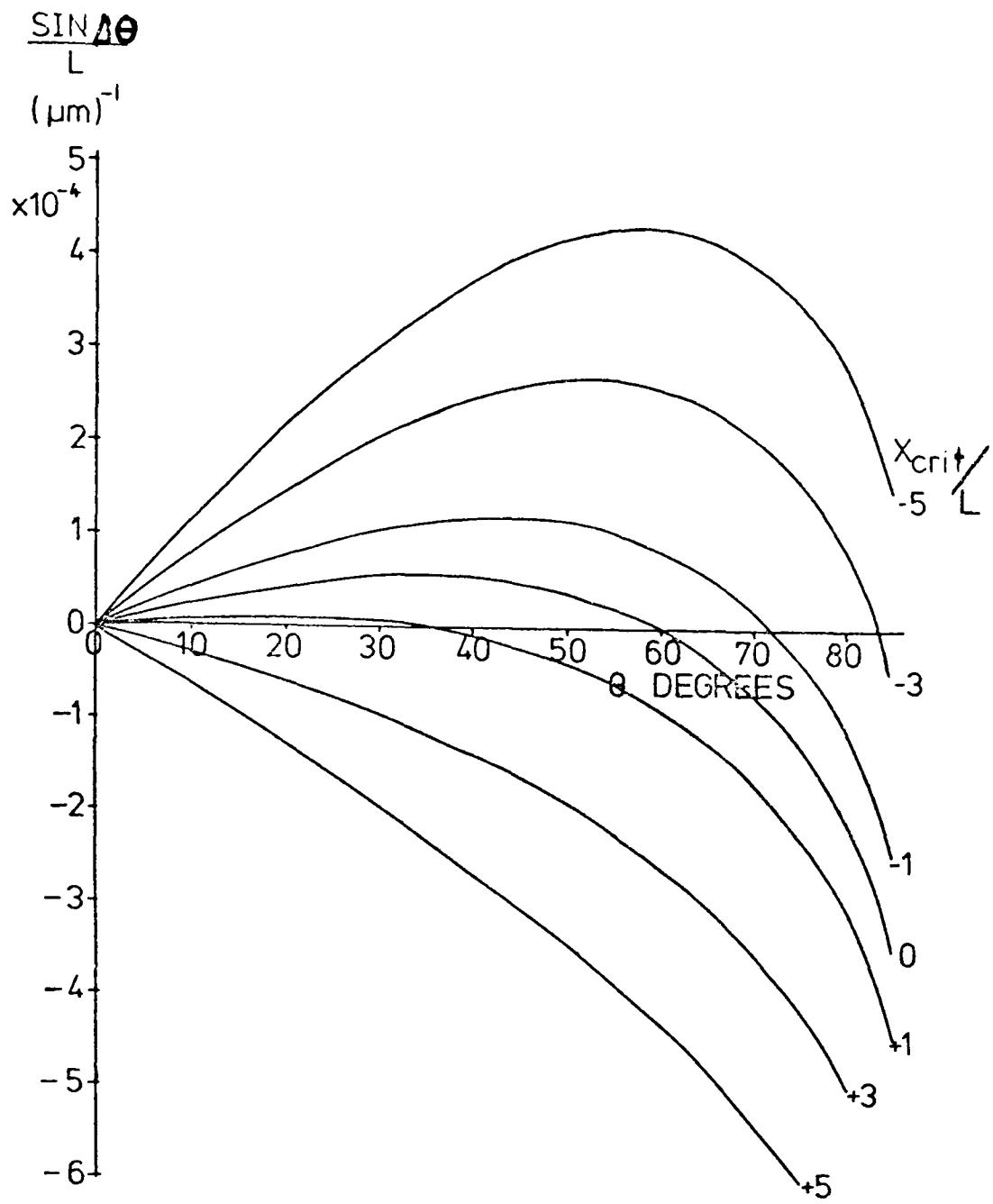


Fig. 4.15
The magnitude of the angular shift, $\Delta\theta$, as illustrated in Fig. 4.14 and defined in the text, as a function of illumination angle θ

values of X_c might be expected, for example, at late times during the pulse if target surface cratering occurs. The sign of the resultant value of $\Delta\theta$ is indicative of whether the apparent angle of refraction is greater than, or less than, the angle of incidence. We experimentally observe, therefore, positive values of $\Delta\theta$. By rearranging equation (4.3) we obtain:

$$\frac{\sin\Delta\theta}{L} = \frac{\sin\theta}{R}\left\{4\,\ell n\,(2\cos\theta) - \frac{2.0\,X_c}{L}\right\} . \qquad (4.4)$$

$\frac{\sin\Delta\theta}{L}$ is plotted as a function of θ in Fig. 4.15 for several values of X_c/L (and for $R = 2$ cm).

From this figure it can be seen that for a critical surface coincident with the target surface ($X_c/L = 0$), positive values of $\Delta\theta$ result for angles of incidence up to $\theta = 60°$. The peak of this curve gives an angular

shift, however, of only $\sim 0.6^{\circ}$ for a density scale length of 200 μm (and $\sim 1.6^{\circ}$ for $L = 500\,\mu m$). These angular shifts, although of the same sign as experimentally measured, would not be resolved by the burn paper technique and are certainly not large enough to explain the experimentally measured shifts of 10° or more. For finite *positive* values of X_c, the situation is worse in that the model predicts negative angular shifts for $\frac{X_c}{L} \gtrsim 1.4$. Even for large negative values of X_c, the predicted values of $\Delta\theta$ are not nearly large enough; for example, a critical surface 1 mm behind the target surface, and $L = 200\,\mu m$ (i.e. $X_c/L = -5$) gives a maximum angular shift of $\sim +5^{\circ}$. We might, alternatively, consider the magnitude of X_c to be representative of the accuracy with which the position of the target surface is known. It can thus be seen that even errors of 1 mm or greater (much larger than we in fact estimate) do not explain the experimental results. Alternative explanations for the effect must therefore be sought.

The above has assumed, of course, that the plasma expands normally to the target surface — a valid assumption from both theoretical and experimental observations. An alternative explanation would be that refraction effects in plasmas with non-planar density profiles, could account for the effect. This could not be verified easily without the aid of a ray tracing routine and the next chapter describes such a routine that was developed initially to study this angular shift effect, but was extended to enable resonance absorption effects in non-planar and rippled plasmas to be studied (Appendix A4) as well as being used to study refraction effects in probe beam experiments.

CHAPTER 5

CUPID – A RAY TRACING PROGRAM FOR CONTINUOUSLY VARYING REFRACTING MEDIA

5.1 INTRODUCTION

The experimental results of Chapter 4 concerning the side-scatter distribution from a plane target illuminated at various angles of incidence, indicated that the effects of refraction in the plasma corona needed to be studied; in particular for plasmas with non-planar density contours. For such geometries the ray trajectories cannot be determined analytically, and a numerical ray tracing routine must be employed.

This chapter describes such a routine, CUPID (HUBBARD and MONTES, 1978), and its use. The method employed is applicable to all plasma geometries provided an analytic expression for the iso-density contours (or, equivalently, surfaces of constant refractive index) can be found.

In particular, refraction effects in plasmas with elliptical geometry were initially studied, followed by an extension of the program to enable cosinusoidal modulations on planar density contours (i.e. a rippled corona) to be investigated. Refraction effects in a plasma with concave iso-density contours were next treated. Finally, a procedure for incorporating resonance absorption was developed in order that the effects of refraction on this important process could be assessed; this particular aspect will be briefly discussed in Chapter 7 (and Appendix A6).

The program was also found sufficiently versatile to be used in an examination of the refraction of ruby-laser radiation through the plasma formed by CO_2-laser irradiation of isolated deuterium targets (GATENBY and WALKER, 1979). This study was necessary to ensure that lack of fringe contrast observed in holographic interferometric measurements of the electron density, was due to effects other than refraction of the ruby probe beam outside the collecting angle of the optics.

5.2 THEORY

Given an initial point on a ray, the routine utilizes two successive Taylor expansions to enable the position vector of the next point on the ray, and the associated unit vector tangential to the ray at that point, to be found. This is illustrated in Fig. 5.1.

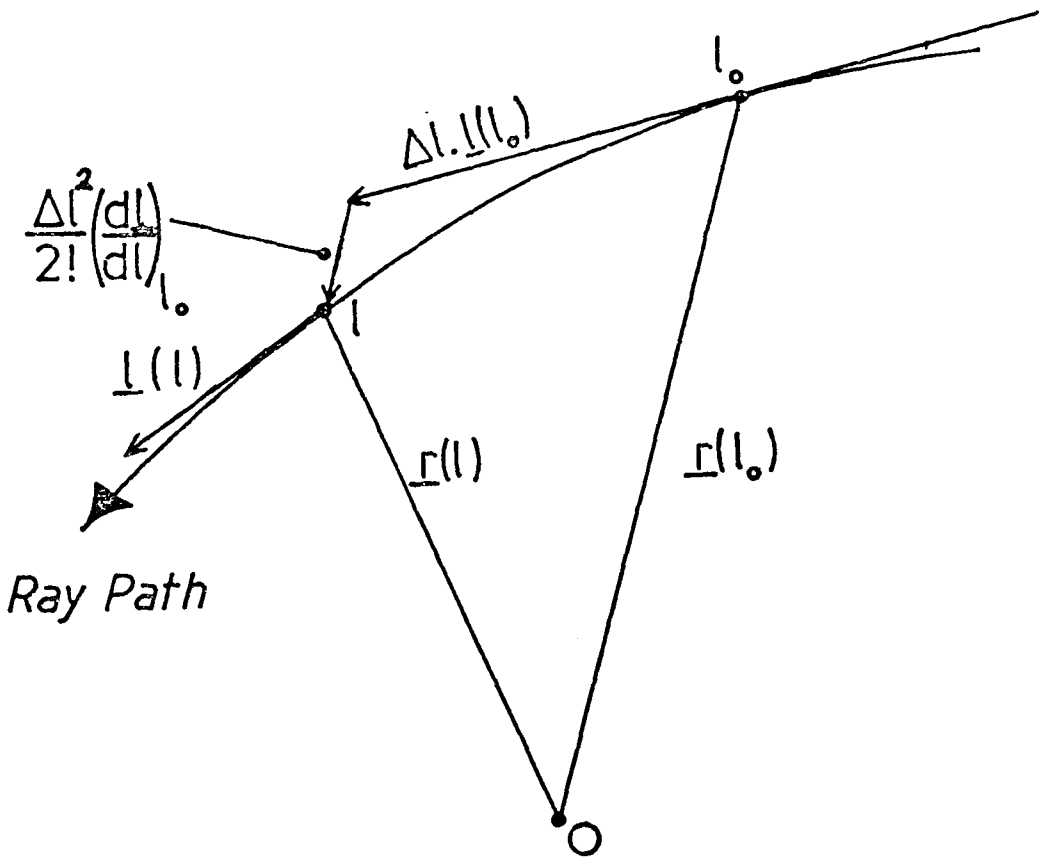


Fig. 5.1
Schematic, illustrating the basic theory of the ray tracing routine. The vector notation is defined in the text by equations 5.1 – 5.4

Let $r(l)$ be the position vector of a general point on a ray, (a function of the arc length l of the ray). Then, if we give the position vector of a previous point in the neighbourhood $r(l_0)$, we can use a Taylor expansion as follows, to find $r(l)$:

$$r(l) \approx r(l_0) + (l-l_0)\left[\frac{dr}{dl}\right]_{l=l_0} + \frac{(l-l_0)^2}{2!}\left[\frac{d^2r}{dl^2}\right]_{l=l_0} . \qquad (5.1)$$

From simple differential geometry :

$$\left[\frac{dr}{dl}\right]_{l=l_0} = l(l_0)$$

and hence

$$\left[\frac{d^2r}{dl^2}\right]_{l=l_0} = \left[\frac{dl}{dl}\right]_{l=l_0} .$$

Thus we can write equation (5.1) as follows:

$$\boldsymbol{r}(l) = \boldsymbol{r}(l_0) + \Delta l \; \boldsymbol{l}(l_0) + \frac{(\Delta l)^2}{2!} \left[\frac{d\boldsymbol{l}}{dl}\right]_{l=l_0} \tag{5.2}$$

where $\boldsymbol{l}$ is a unit vector tangential to the ray, and $\Delta l = l - l_0$.

Now it can be shown (LANDAU and LIFSHITZ, 1960) that within the validity of geometrical optics (see section 5.3), the general equation for a ray path can be written,

$$\frac{d\boldsymbol{l}}{dl} = \frac{1}{\eta}\left\{\nabla\eta - \boldsymbol{l}(\boldsymbol{l}\cdot\nabla\eta)\right\} \tag{5.3}$$

where η is the refractive index. Therefore, given $\boldsymbol{r}(l_0)$ and $\boldsymbol{l}(l_0)$, and calculating $(d\boldsymbol{l}/dl)$ at $l = l_0$ from equation (5.3), we can obtain the position vector of the next point on the ray (for sufficiently small Δl), using equation (5.2). It remains to calculate the unit tangent vector at this point to proceed further, and this is accomplished by using another Taylor expansion as follows :

$$\boldsymbol{l}(l) = \boldsymbol{l}(l_0) + \Delta l \left[\frac{d\boldsymbol{l}}{dl}\right]_{l=l_0} . \tag{5.4}$$

Thus, by repeating the procedure, the next, and subsequent points on the ray can be found, provided that the refractive index and its gradient are known, or can be calculated, at each coordinate position. To do this, an analytic expression for the density contours is given in terms of the rectangular coordinate system X, Y, Z where the X direction defines the target normal, and is also the direction along which the density scale length is specified. (It was found that a rectangular coordinate system greatly simplified the numerical procedures and, therefore, although the basic equations are given in this text in polar form, in the program listing, conversions to separate equations for each direction were made.)

The first results were obtained for plasmas with elliptical density contours defined by :

$$n(X,Y,Z) = n_{crit} \exp\left[-\frac{1}{L}\left\{\sqrt{X^2 + \frac{Y^2 + Z^2}{E^2}} - A_{crit}\right]\right. \tag{5.5}$$

where A_{crit} is the distance, measured along the X-axis, from the critical surface (at density n_{crit}) to the origin. E defines the shape of the ellipsoidal coaxial surfaces of constant density n. The density profile was exponentially decreasing with scale length L. The situation is as shown in Fig. 5.2.

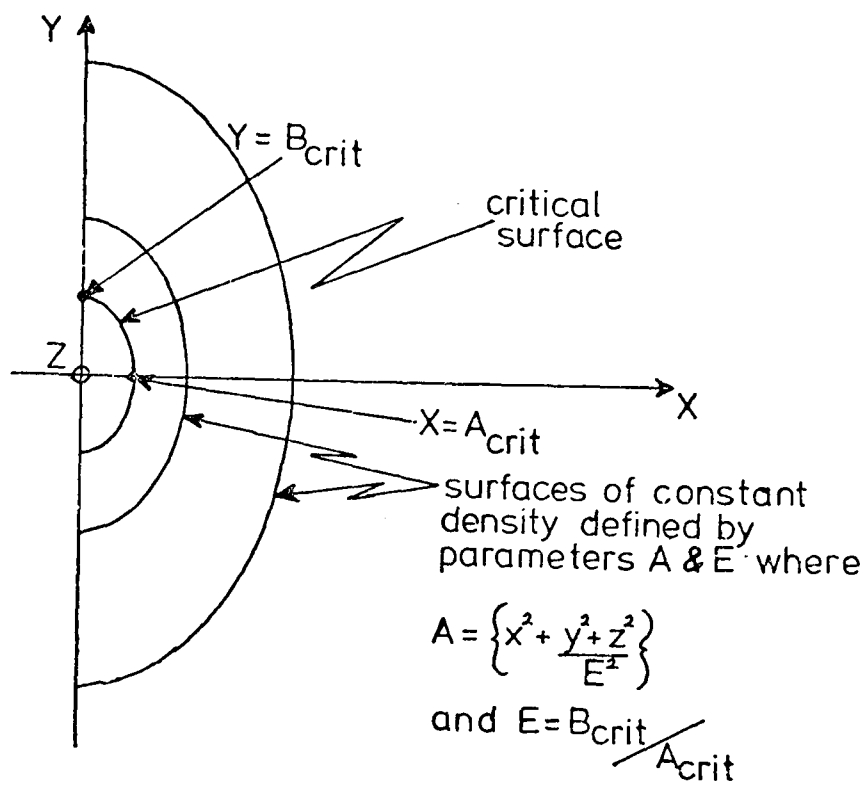


Fig. 5.2
Geometry for elliptical iso-density contours, illustrating the definition of A_{crit}, B_{crit} and E. The incident beam axis is directed towards the origin of the coordinate system.

The incident beam was considered to be composed of a large number of individual rays, each ray being traced separately through the plasma. The dimension of the critical surface in the Y direction, for elliptical geometry, was usually set to be slightly larger than the width of the set of rays defining the incident beam. This was an attempt to simulate the expected situation, whereby, the plasma size exceeds the focal spot size due to lateral flow. The beam width was usually set to be 200 μm as this approximated to the measured spot size from experiments. Rays in the incident beam all had the same angle of incidence θ, to simulate the collimated situation in the far field of the focused CO_2 beam, i.e. we assumed planar wavefronts in the focal volume. Also, the number density of rays in the beam was made uniform across the beam, and thus a constant intensity profile was simulated. We believe that this procedure was justified as the basic aim of the study was to investigate geometrical effects on the refraction, rather than to simulate scattered light intensity distributions. Of

course, for later work, where the ray tracing routine was used to investigate the absorption of an incident beam, the consequences of the uniform model have to be more carefully considered (HOWARD, 1979). This point will be further mentioned in Appendix A4.

In order that computer time was not needlessly excessive, the step length Δl was made relatively large ($\sim$ 10 μm) in the outer regions of the plasma where deviations of the ray from a straight trajectory were very small. As soon as higher densities were reached, however, the increment was automatically reduced to a small fraction of the density scale length. In most cases, $\Delta l = L/400$, was found to be adequate. As will be seen later, the accuracy of the routine was investigated using several methods. The density where the step length Δl was changed was taken to be the region 3 e-folding lengths from the critical surface which is a density $\sim$ 5% of the critical density. It is noted that this criterion was used for determining when the step length should be changed rather than changing it near the ray's turning point, because for some rays (e.g. those incident at oblique angles) the turning point occurred far out in the plasma and dl/dl was small.

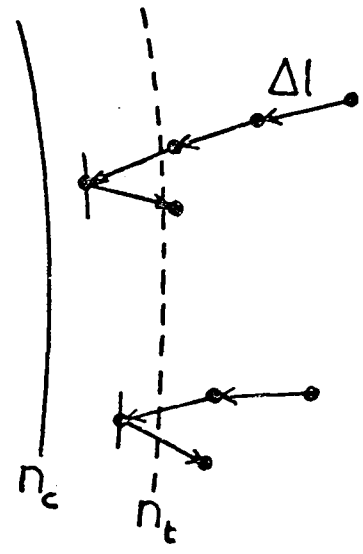


Fig. 5.3
Schematic of the reflection routine which comes into operation when the ray closely approaches the critical surface. The broken line represents the isodensity contour of the reflection sheath; the density of this contour was set to be 0.995 n_c .

When a ray approached to within a very small distance of the critical surface, a subroutine caused it to be reflected as if by a mirror. This procedure is illustrated in Fig. 5.3 above. The density n_t which defined the boundary of the 'reflection sheath' was set to be 99.5% of the critical density. The reflection procedure was tested using normally incident light on planar density contours where accurate ray-retracing was found to occur.

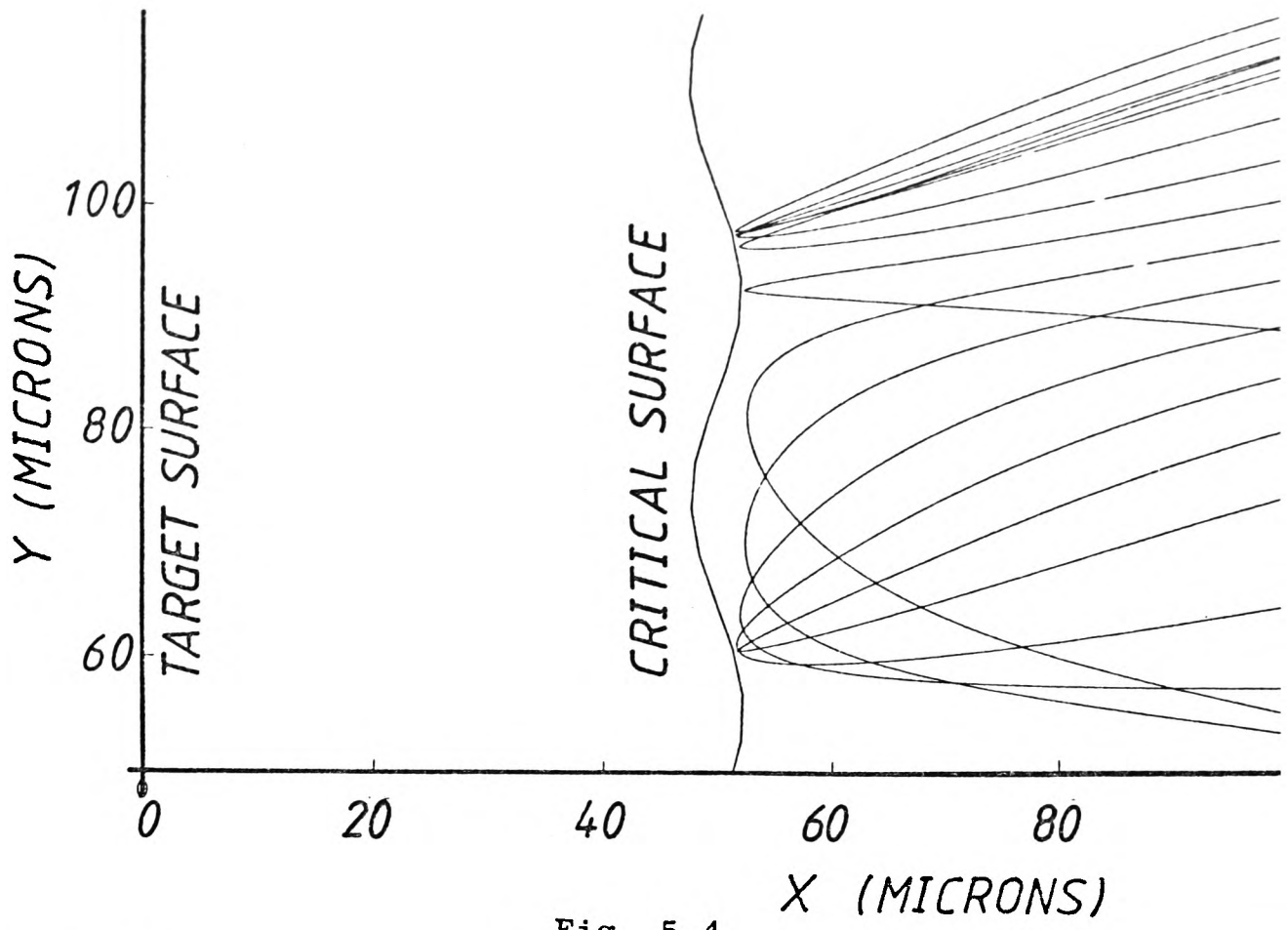


Fig. 5.4

Actual ray paths for a rippled plasma. In the case illustrated, some of the rays have approached so close to the critical surface that the reflection routine has come into operation.

In practice the sub-routine was brought into operation very infrequently in elliptical and concave geometry (this included the special cases of planar and spherical geometry), but was found important when the program was extended to allow a rippled plasma to be considered. Ray paths near to the critical surface of a rippled plasma are shown in Fig. 5.4 in order to demonstrate the reflection subroutine. A reflection routine was only necessary due to the finite value of Δl not allowing proper refraction for rays very close to normal incidence (relative to the critical surface contour).

A rippled plasma geometry was modelled by assuming contours of constant density to be defined as follows:

$$n(X, Y) = n_{crit} \exp\left[-\frac{1}{L}\left\{X - X_{crit} + a\cos bY\right\}\right] . \qquad (5.6)$$

It will be noticed in this case that only two dimensional effects were modelled; this was because refraction out of the plane of incidence did not occur, there being no density gradients in the Z-direction. All investigations were, therefore, carried out in the $X-Y$ coordinate space which was used for all later work.

In equation (5.6), the amplitude, a and spatial frequency, b of the rippling were chosen such that plasma inhomogeneity effects were much larger than the wavelength of the incident radiation in order that the geometrical optics approximation (WKB) was satisfied (see equation (5.12)). Also, in equation (5.6), X_{crit} represented the mean distance of the critical surface from the Y-axis (which represents the target surface) measured along the X-axis. From equation (5.6) it is seen that the critical surface is defined by

$$X = X_{crit} - a\cos(bY) \tag{5.7}$$

and the geometry of the model is shown in Fig. 5.5.

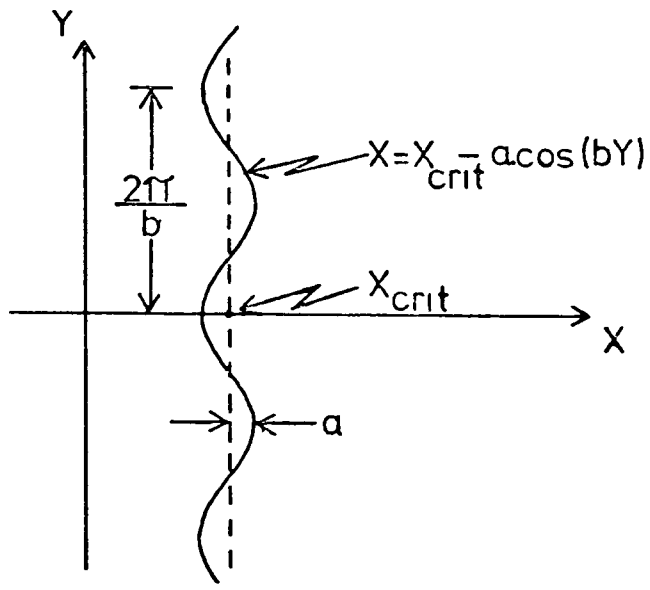


Fig. 5.5
Geometry for rippled isodensity contours illustrating the definition of a, b and X_{crit}. As for the elliptical case, the incident beam axis is initially directed towards the origin.

Apart from the differences in expression for the density contours and the associated contours of constant refractive index (and derivatives), the CUPID ray tracing routine was unchanged for each geometry.

The theory of the ray tracing routine is summarized in the flow diagram of Fig. 5.6. In the following section, some examples of the models that were used to test the accuracy of the ray tracing routine are given. Section 5.4, discusses the validity of the routine and the results of some runs to investigate refraction effects in simple curved, and rippled geometry, are given in section 5.5.

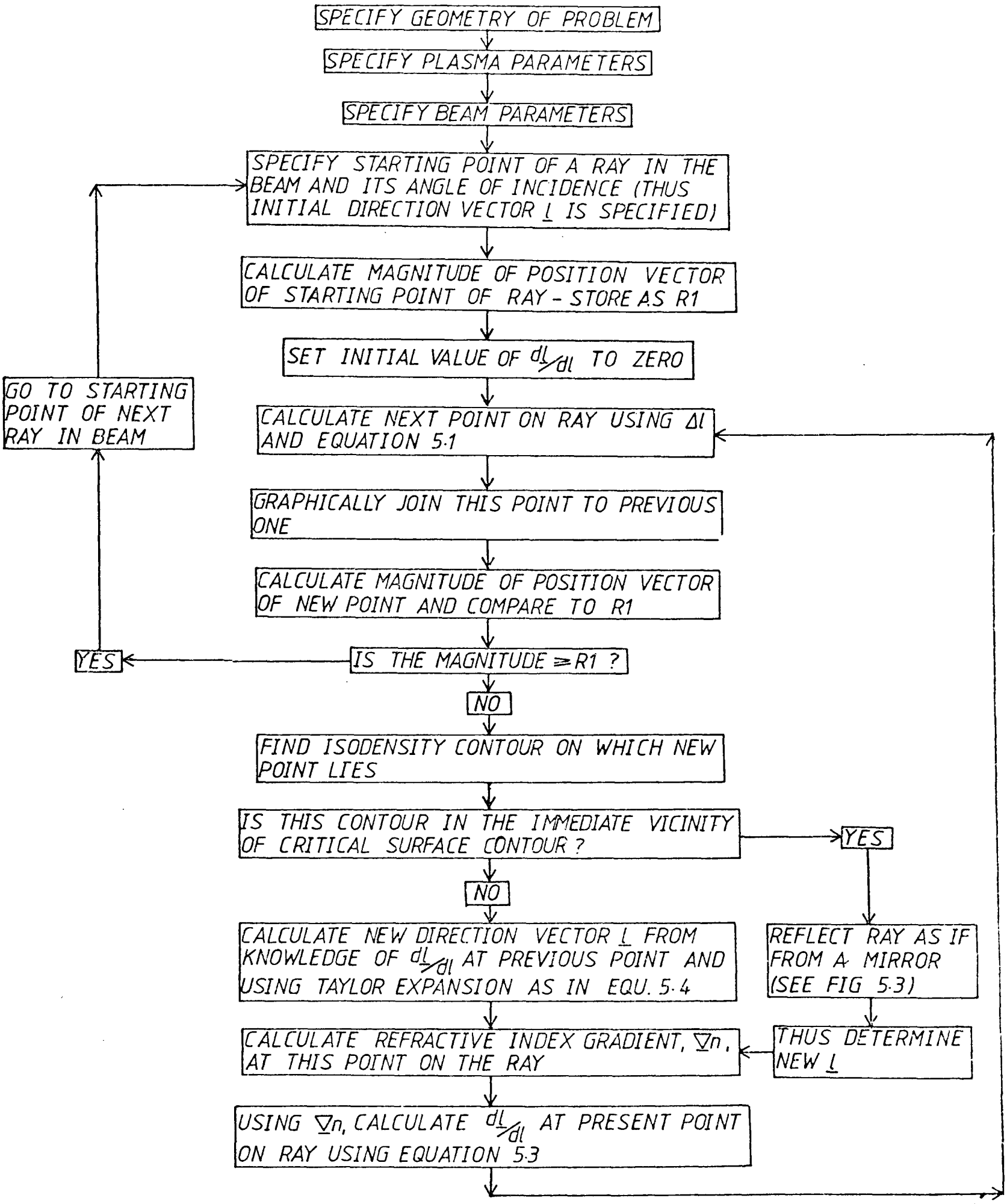


Fig. 5.6
Flow diagram summarizing the mode of operation of the ray tracing program

5.3 ACCURACY TESTS

5.3.1 *ANGLE OF INCIDENCE VERSUS DEFLECTION FOR PLANE PARALLEL GEOMETRY*

The initial and simplest method used to test the accuracy of the ray tracing routine was to model plane parallel density contours (either by setting E to a very large value in equation (5.5) or setting a to zero in equation (5.6)). For the plane parallel case the ray trajectories are analytically soluble and hence a comparison between the numerical and theoretical trajectories could easily be effected. In addition to the simplest tests of ensuring that angle of incidence equalled angle of refraction, or that the ray turned at a density given by

$$n_t = n_c \cos^2\theta ,$$

an investigation of lateral shift Δy versus angle of incidence was carried out, where Δy was defined as the displacement of the turning point of the ray (in a direction parallel to the critical surface) from the position to which the ray was initially pointing (see Fig. 4.15). As described in section 4.3.2, this effect had previously been used to check whether the apparent asymmetric refraction seen in experiments could be attributed to this refraction shift of the turning point. Figure 5.7 shows the results of the ray tracing plotted along with the analytic solution as given by equation (4.2). The excellent agreement is apparent.

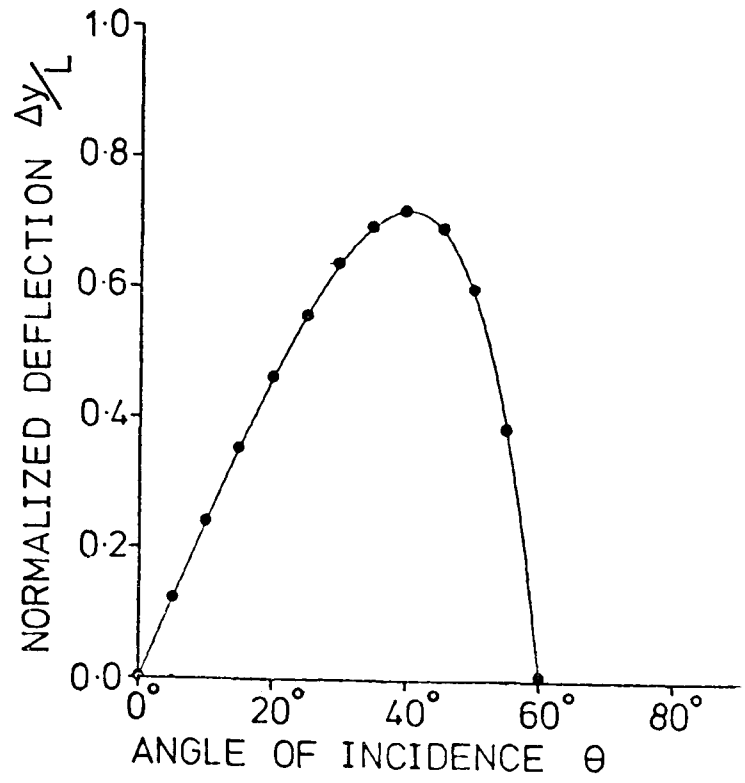


Fig. 5.7
Normalized transverse shift of the turning point $\Delta y/L$, as a function of angle of incidence θ. The solid line is the analytic curve given by equation (4.2). The full circles are the results of the ray tracing routine.

5.3.2 *ACCURACY OF ROUTINE IN SPHERICAL GEOMETRY*

As a further check on the routine accuracy, this time for non-planar profiles, it was decided to compare the results of the CUPID routine with those of the routine developed by Mueller at LANSL (MUELLER, 1977). In particular, refraction by a spherical plasma with a steepened density profile was studied for a collimated probe beam with impact parameter ranging from 20 μm to 100 μm. In the work of Mueller, the wavelength of the incident beam was 0.53 μm and the density profile had a steep step at quarter-critical density for this wavelength. In our routine, the density profile was normalized to the critical density and hence no wavelength had to be specified. The density profile used in the simulation is shown in Fig. 5.8, and the density scale lengths of the three distinct regions are given in the figure.

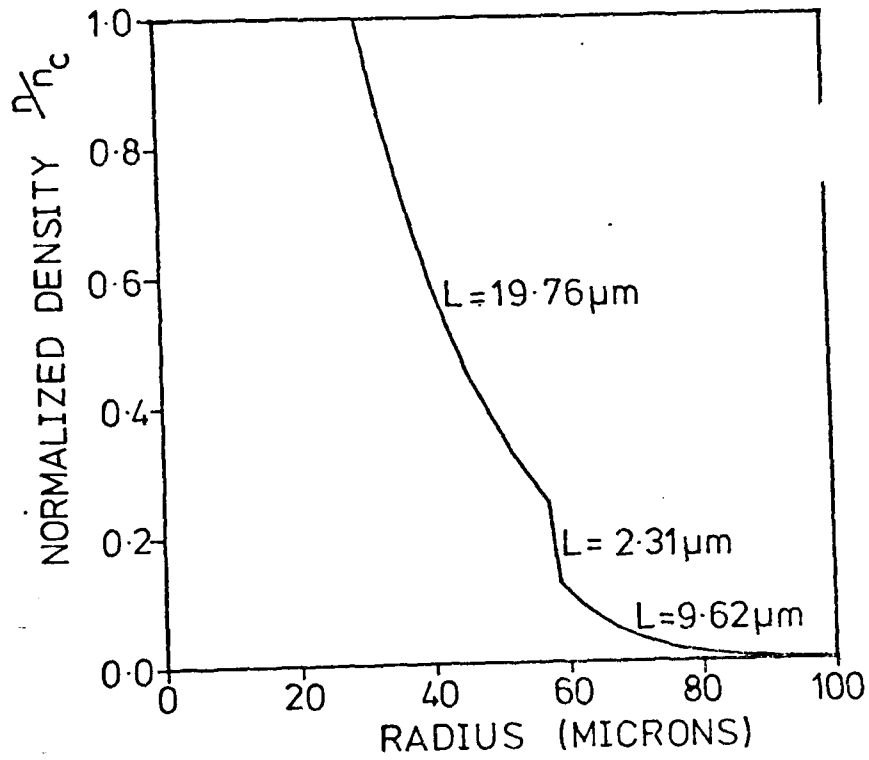


Fig. 5.8
Density profile used in accuracy test of the ray tracing routine. A region of steepened profile at the quarter critical density of the incident beam, is simulated. The scale lengths of the individual exponential profiles are given in the figure.

The results of the test are shown in Figs 5.9(a) and (b); (a) where the ray trace is presented, and (b) the deflection of each ray in the probe beam from its original direction plotted as a function of impact parameter. The original work of Mueller is shown for comparison in Figs 5.9(c) and (d).

(It is noted that Muellers work was performed to show that profile steepening could be observed by measuring the variation of the probe beam refraction angle as a function of impact parameter. In practice, the impact parameter of a particular ray cannot be determined, and it is suggested that

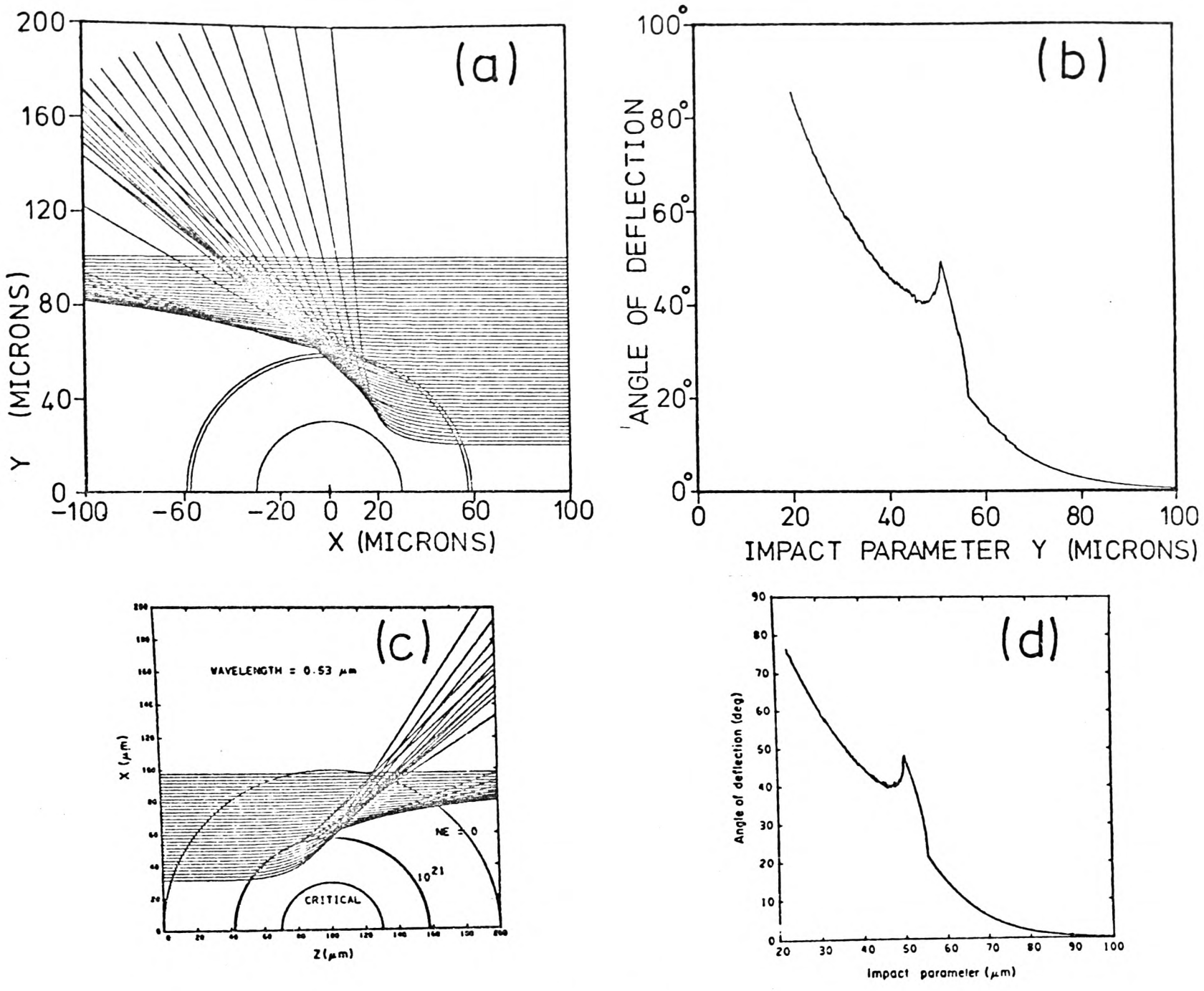


Fig. 5.9

(a) Ray trace for the profile shown in Fig. 5.8 using the CUPID routine. The incident beam can be considered to represent a probe beam traversing the spherical plasma. The inner semicircle represents the critical surface contour and the two closely spaced outer contours represent the boundaries of the steepened region.
(b) Ray tracing results, showing the angle of deflection of each ray in the probe beam as a function of its impact parameter.
(c) and (d) The equivalent figures to (a) and (b) respectively but taken from the work of MUELLER (1977).

measurement of the scattered light intensity as a function of deflection angle would give the same information providing that the intensity distribution across the probe beam was known. Mueller also comments that the variation shown in Figs 5.9(b) or (d) would be smeared out in practice due to the neglect of diffraction effects in the ray tracing.)

5.4 VALIDITY

The most important equation in the ray-tracing program is equation (5.3), i.e., the general expression for the ray trajectory. It was pointed out earlier that this equation is applicable only within the validity of geometrical optics. This implies, therefore, that any plasma inhomogeneity scale lengths must be much larger than the wavelength of the incident radiation, i.e.,

$$\left|\frac{\nabla n}{n}\right| \ll k_0 \,. \tag{5.11}$$

In a rippled plasma, for example, this inequality can be examined by differentiating equation (5.6) to give:

$$\frac{\partial n}{\partial X} = -\, n\left(\frac{1}{L}\right) \quad \text{and} \quad \frac{\partial n}{\partial Y} = n\left(\frac{1}{L}\, ab\, \sin bY\right) .$$

Considering the maximum value of each partial derivative, we then obtain:

$$|\nabla n| = \frac{n}{L}\left(1 + a^2 b^2\right)^{\frac{1}{2}}$$

and hence, the inequality can be rewritten:

$$\frac{1}{L}\left\{1 + a^2 b^2\right\} \ll k_0 \,. \tag{5.12}$$

Now, it has also been stated, and it is obvious from the theory of section 5.2, that the wavelength is not specified in the program, the density profile being normalized to the critical density. We can, therefore, regard the geometrical optics limitation, as expressed in equations (5.11) or (5.12), as specifying a maximum valid wavelength value once a density scale length has been fixed and/or rippling parameters set. It may be the case, however, that the somewhat stringent requirements implied by equation (5.11) can be relaxed somewhat, in the light of some work by MUELLER, (1977), who compared resonance absorption calculated from ray tracing with that calculated using a wave optics code (see for example MUELLER, 1973). He found that absorption calculated from ray optics was reasonably accurate up to wavelengths of three times the plasma scale length. This result is of

great interest in connection with the extension of CUPID to allow resonance absorption to be estimated (see Chapter 7 and Appendix A4), but also implies that in many situations, actual ray trajectories can be confidently studied without underlying worries concerning the absence of diffraction in the routine. However, this does not imply that diffraction effects can be ignored, for, although the accuracy of a particular ray's trajectory may not be affected by using geometrical optics alone, when we consider a large number of rays constituting a beam, diffraction must certainly be considered.

Two cases in particular may be mentioned. First, the apparent focusing of a beam at its turning point as seen in planar and simple curved geometry (see for example Fig. 5.10(b)) may be compensated to a certain extent by diffraction effects. Secondly, the strong focusing observed in density depressions (e.g., Fig. 5.15) will be opposed in a similar manner by diffraction, although self focusing may enhance the effect even more by further perturbation of the density contours in a bootstrap process. The competing effects of geometrical focusing, diffraction spreading and self focussing are discussed by TEWARI *et al.* (1979), who conclude that as a beam approaches its reflection point, the irradiance decreases, due to the dominance of the diffraction effect over geometrical focusing. The effects of self-focusing near to the critical layer are not well discussed, however.

Finally, we must exercise care in predicting macroscopic scattered intensity distributions from the refraction of a beam in the vicinity of its turning point. This can be seen by considering that a spherically converging wavefront can be considered planar in the far field, but, conversely, a parallel bundle of rays emitted from the region of the critical surface would not be expected to remain as a parallel beam as it propagated out of the plasma. Beam spreading due to diffraction would occur.

We summarize by making a clear distinction between the accuracy of ray tracing in a plasma where refraction effects of a ray can be modelled

using geometrical optics alone, and the validity of whole beam effects where diffraction has not been considered. The latter situation is a wave-front phenomenon and is not dependent on plasma effects at all.

5.5 RAY TRACING RESULTS FOR VARIOUS NON-PLANAR GEOMETRIES

5.5.1 *INTRODUCTION*

Having discussed the accuracy and validity of the CUPID ray tracing routine in the previous sections, the results of ray tracing carried out for plasmas having elliptical, rippled and concave iso-density profiles are presented and examined here. The basic aim of this work was to determine whether any particular geometry could give rise to the asymmetric refraction effect described in Chapter 4. The general influence of iso-density shape on beam refractive behaviour is also discussed.

5.5.2 *ELLIPTICAL GEOMETRY*

The effects of an elliptical geometry on the refraction of an incident beam are illustrated in the examples shown in Fig. 5.10, which demonstrates the situation for a collimated beam initially inclined at angles of 45° or 11° to the target normal, and iso-density contours defined by $E = 2, 4$ and 8. The density scale length was set to 200 μm, and, as mentioned earlier, the magnitude of the critical surface contour in the transverse direction was set to be only slightly larger than the incident beam width. As expected, for small values of E (i.e. a large deviation from planar geometry), there was considerable spreading of the refracted beam (Fig. 5.10(c)) and back-scattering for small angles of incidence (Fig. 5.10(e)). The refracted beam still appeared to be uniform, however, as the ray spacing remained constant across the beam.

Geometrical focusing at the turning point is very marked in certain situations (Figs. 5.10(a), (b) and (c)). As has been mentioned in section 5.4, however, geometrical focusing was found to be dominated by diffraction

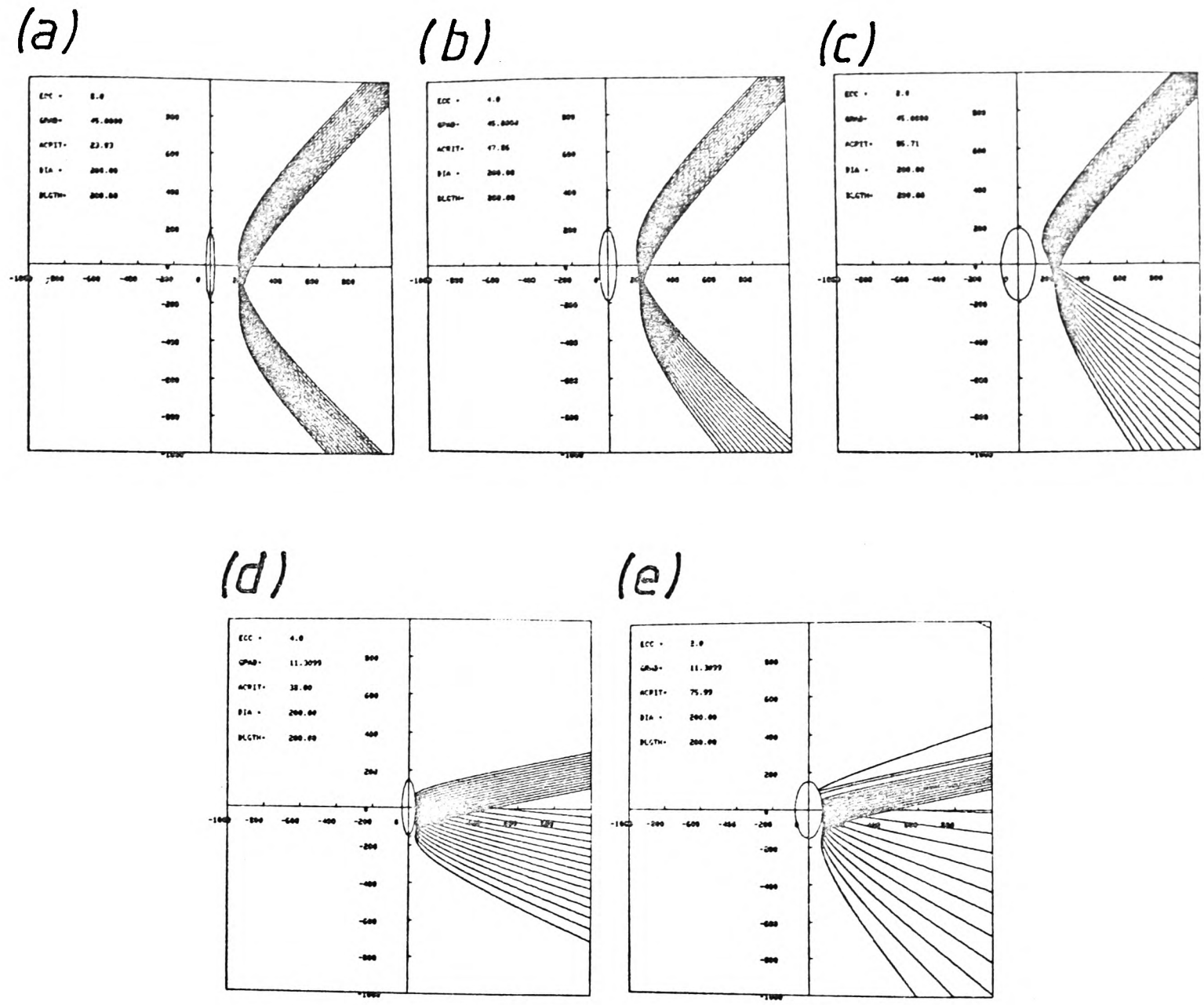


Fig. 5.10

Ray traces for elliptical iso-density contours. The 200 μm diameter beam is incident from the upper right hand quadrant and the density scale length is given by $k_0 L \approx 120$. (a) – (c) the angle of incidence is equal to 45°, E is set to 8.0, 4.0 and 2.0 respectively. (d) and (e) the angle of incidence is equal to 11.3°, E is set to 4.0 and 2.0 respectively.

spreading by TEWARI *et al.* (1979) and we cannot, therefore, propose that a localized region of high irradiance in these situations, would automatically be expected to occur.

No evidence was found of an increase in the beam scattering angle from its expected value. Even in cases where there was beam spreading upon exit from the plasma (until the spreading became so large that the refracted rays could no longer be considered to form a beam) the axis of symmetry of the refracted beam was still at approximately the same angle to the target normal as the incident beam. This was found to be true for a range

of density scale lengths and eccentricities. As in the case of planar geometry, the turning point shift in the Y-direction was also apparent for the elliptical geometry,

5.5.3 *RIPPLED GEOMETRY*

A rippled plasma was not expected to cause asymmetric refraction of an obliquely incident beam due to the fact that the rippling was a small perturbation to an otherwise plane contour. However, it was thought necessary to devote some time to the study of the refractive effects of rippled geometry in view of the possible important consequences for the resonance absorption process.

The expected gross refraction was observed for large density scale length, and small perturbation to planar geometry. However, even in the weakly modified situation, the incident and reflected beams were spatially disturbed and this is illustrated in Fig. 5.11, where radiation with $k_0 L \approx 120$ is incident at 10° to a plasma with rippled iso-density contours of amplitude 2 μm and spatial frequency 27 per mm. The effect of the rippling can be seen on the incident beam ~ 100 μm before the turning point is reached when refractive filamentation starts to occur. After the turning point this structure is seen to develop into a strong spatial modulation across the width of the refracted beam.

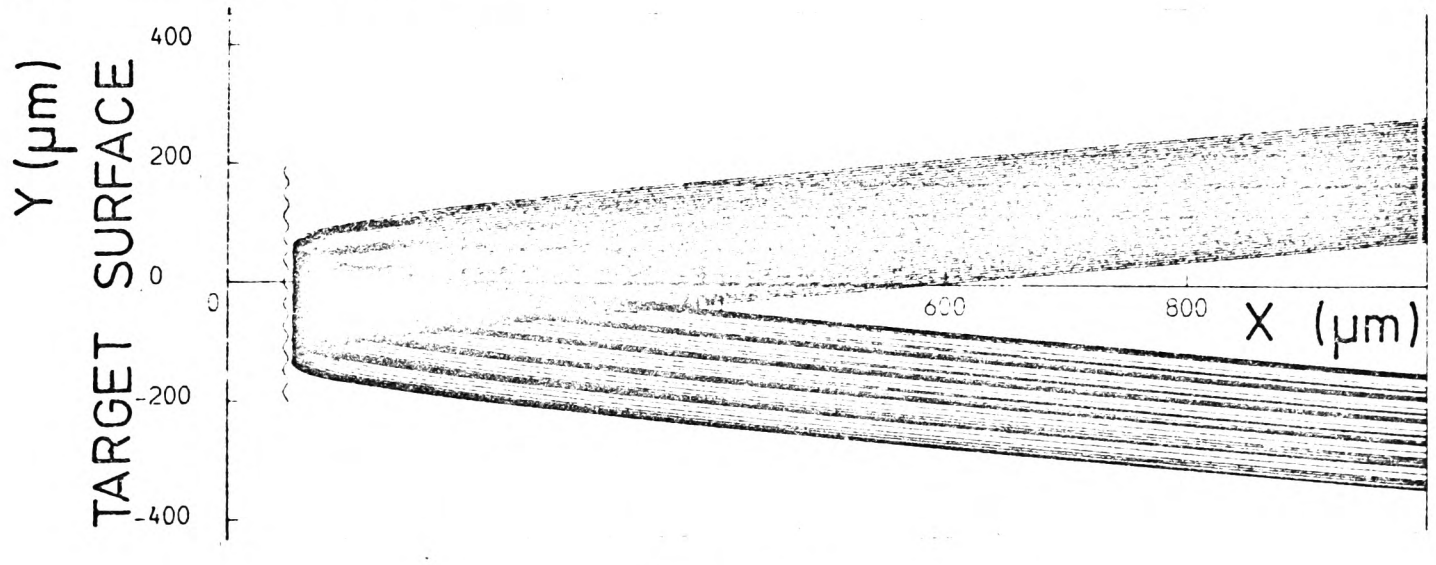


Fig. 5.11

Ray trace in a rippled plasma. $a = 2$ μm, $2\pi/b = 37$ μm. The 200 μm diameter beam is incident from the upper right-hand quadrant at an angle of 10° to the target normal. ($X_{crit} = 50$ μm, $k_0 L \approx 120$)

The modulation of the incident beam was only apparent in situations of long density scale length. In contrast, Fig. 5.12 shows a beam propagating through plasma with similar ripple parameters (amplitude = 1.5 μm, spatial frequency = 26 per mm) but for $k_0 L \approx 15$.

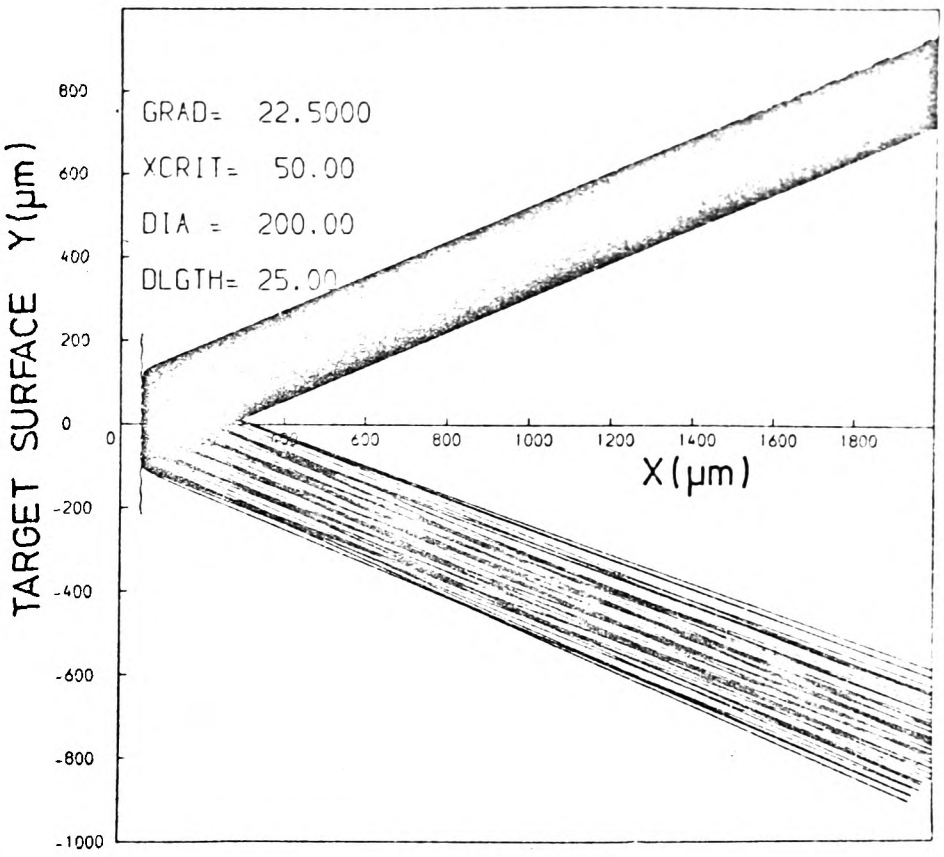


Fig. 5.12
Ray trace in a rippled plasma. $a = 1.5$ μm, $2\pi/b = 39$ μm. The 200 μm diameter beam is incident from the upper right-hand quadrant at an angle of 22.5° to the target normal. ($X_{crit} = 50$ μm $k_0 L \approx 15$)

No structure is apparent on the incoming beam, although the refracted beam is now more disturbed due to the rapid refractive index variation in the turning point region. It is thus apparent that a small perturbation to the geometry for a plasma with short density scale length, does not affect the incoming beam. This is true provided that the combination of ripple geometry, density scale length and angle of incidence are such that the turning point is close to, but not at, the critical surface. In this latter case, the incident ray is approximately parallel to the local critical surface normal, and specular effects dominated by the local, rather than the gross, geometry are seen to occur. This is illustrated in Fig. 5.13 where specular backscatter of part of the incident beam is apparent.

Although, in this example the ripple characteristics and the angle of incidence were the same as in Fig. 5.11, a reduction in the density scale length by a factor of 2, to $k_0 L = 60$, is seen to have been sufficient to destroy the domination of the gross planar geometry. A further reduction in the density scale length (other conditions unchanged) gives rise to a major

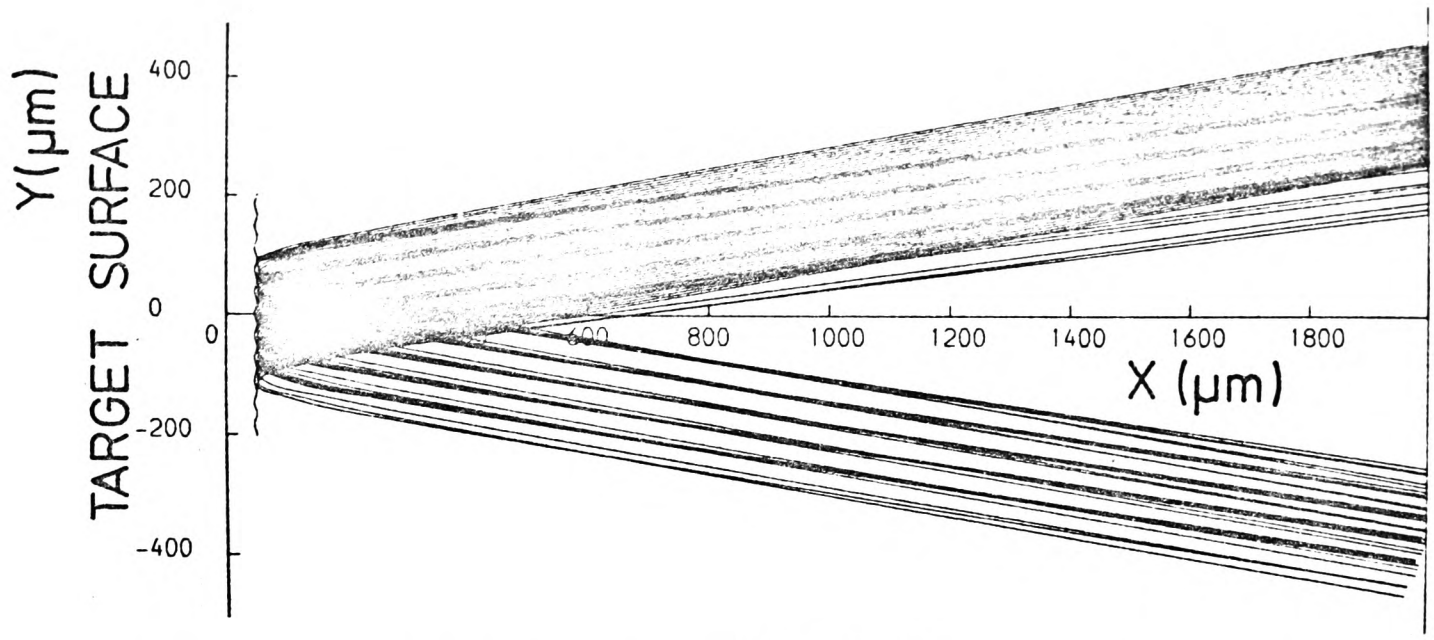


Fig. 5.13

Ray trace in a rippled plasma. a = 2 μm, $2\pi/b$ = 37 μm. The 200 μm diameter beam is incident from the upper right hand quadrant at an angle of 10° to the target normal. (X_{crit} = 50 μm, $k_0 L \approx 60$)

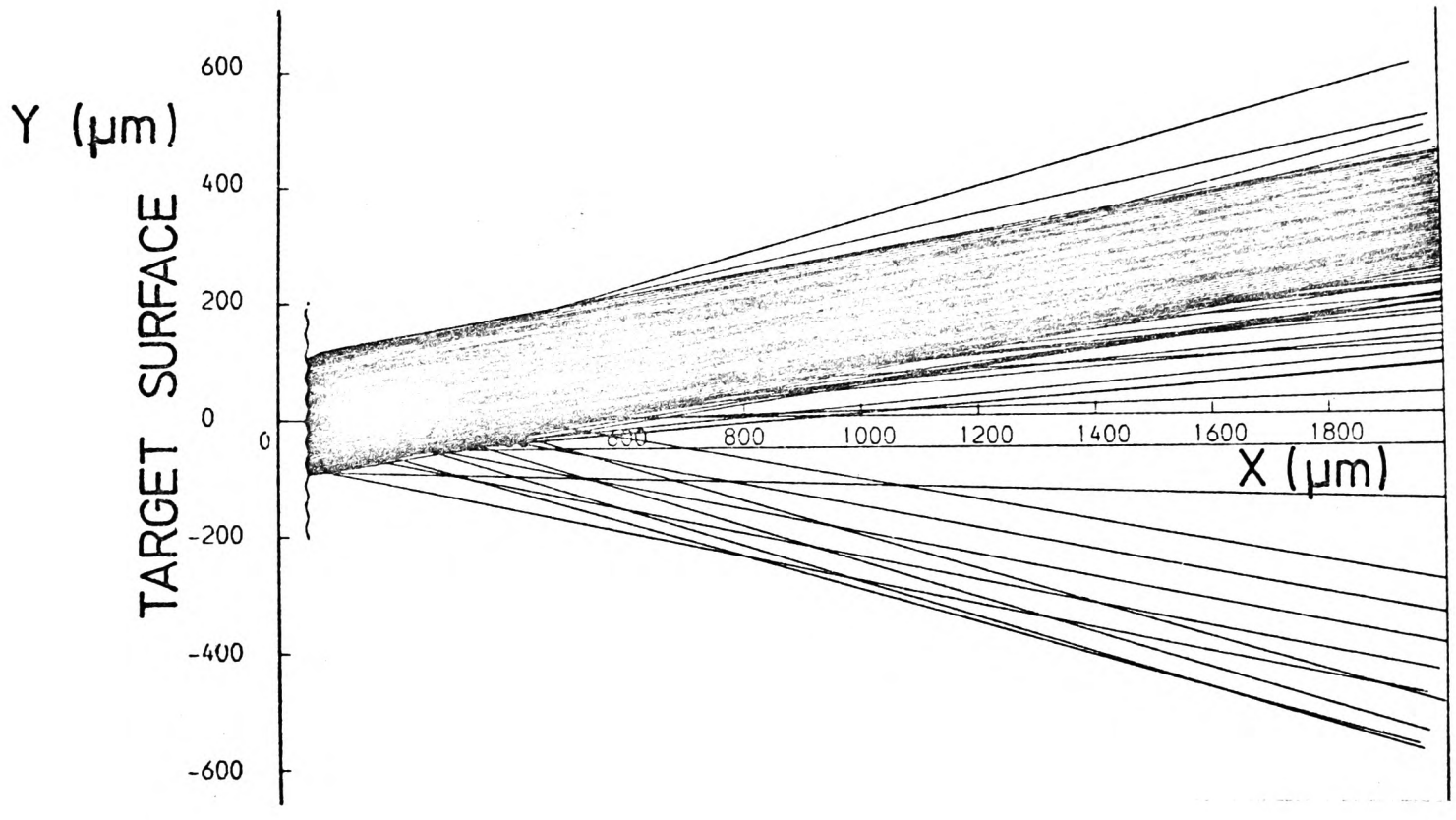


Fig. 5.14

Ray trace in a rippled plasma. a = 2 μm, $2\pi/b$ = 37 μm The 200 μm diameter beam is incident from the upper right-hand quadrant at an angle of 10° to the target normal. (X_{crit} = 50 μm, $k_0 L \approx 15$).

part of the incident beam reaching the perturbed critical surface, with scatter consequently dominated by local geometry. This is illustrated in Fig. 5.14, where almost completely diffuse scatter is seen to occur for $k_0 L = 15$.

Care must be taken, however, when conditions are such that this type of local geometry dominated scatter occurs. We should not attach physical importance to ray paths in such cases, due to the neglect of diffraction effects; although general trends may still be usefully indicated. To illustrate the point we conclude this section by showing a ray trace for a beam normally incident upon a highly modulated planar critical surface; Fig. 5.15.

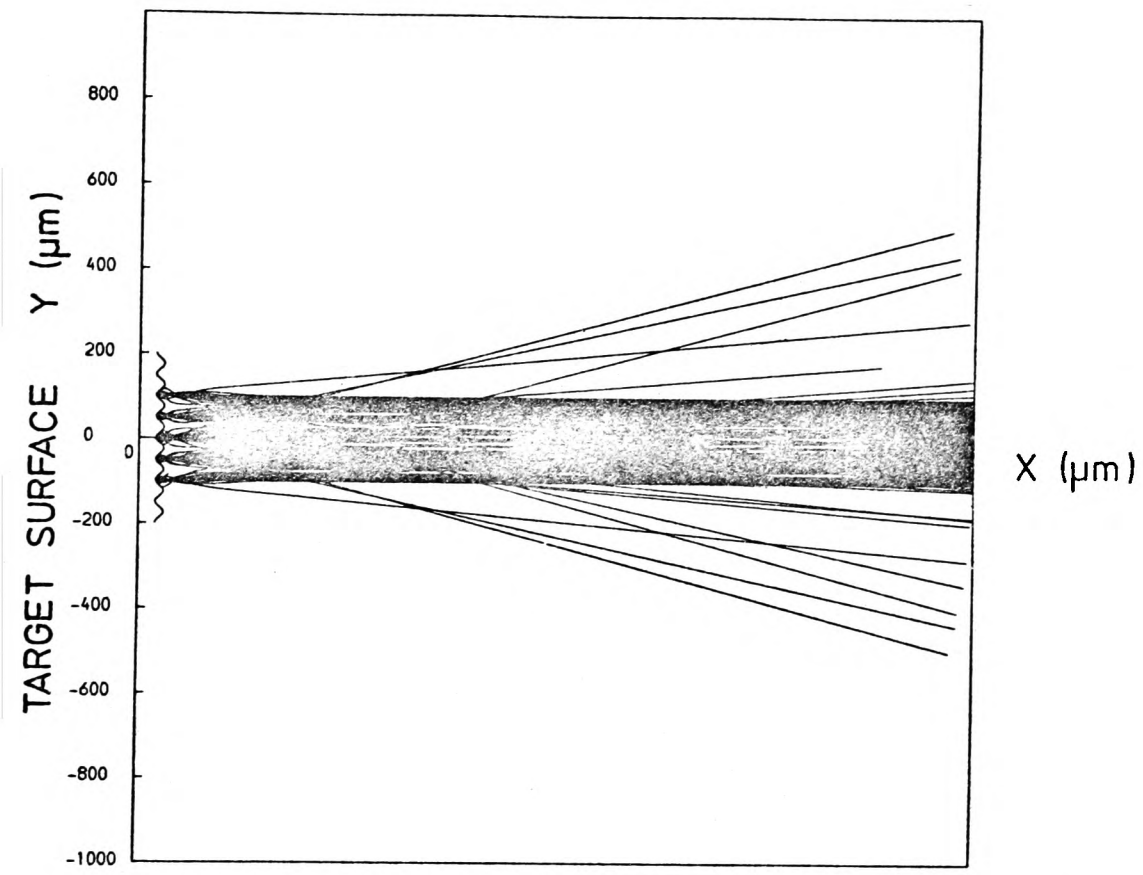


Fig. 5.15

Ray trace in a highly rippled plasma with ripple amplitude $a = 9\,\mu m$ and spatial wavelength $2\pi/b = 50\,\mu m$. The 200 μm diameter beam is incident normally to the target surface and the plasma has a density scale length given by $k_0 L \approx 30$ ($X_{crit} = 50\,\mu m$)

Strong focusing into the ripple wells is observed and we suppose that this example illustrates a general trend whereby large amplitude ripples can trap portions of the beam into regions of high intensity and in so doing, initiate a self focusing effect which in turn enhances the ripple amplitude. Actual ray paths have no significance in this case, however.

5.5.4 *CONCAVE ISO-DENSITY CONTOURS*

The situation where iso-density contours are concave with respect to the incident beam, was modelled in order that the effect of caviton features at the critical surface could be studied. The contours were produced by using a version of the rippled geometry package, and setting the spatial frequency such that there was only one cycle across the beam. In particular, it was initially arranged that the dimension of the beam in the lateral direction was of the same order as the density cavity dimension. The reason for this was simply that for the situation where a beam of much smaller width than the cavity dimension was used, the angle of refraction was determined just by the shape of a small portion of the contour and not by the whole cavity. We will return to this point later.

The most obvious feature of ray tracing in the concave geometry was the '*curved mirror*' behaviour producing a focused refracted beam. This is illustrated in Fig. 5.16, where a beam initially incident at 30° to a plasma with concave iso-density contours, is focused to a region approximately 750 μm from the critical surface. In this case the angle made by the axis of symmetry of the exciting beam with the target normal was ~27° and was thus smaller than the angle of incidence, in contradiction to the experimental results. It was found that for all of the many conditions tested, no situation could be found that

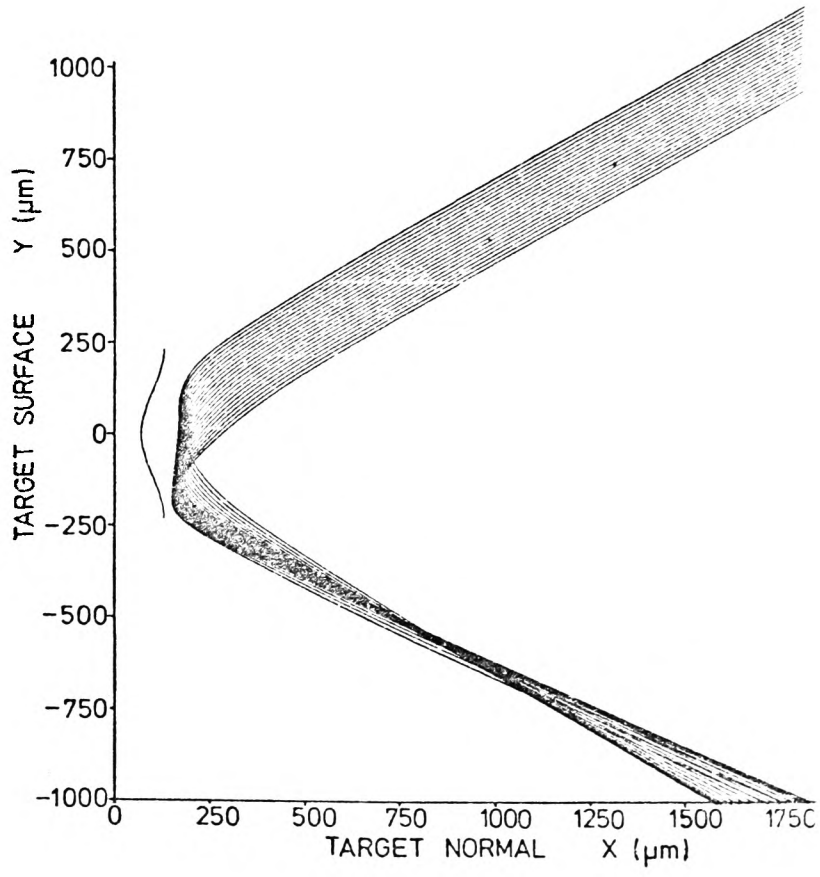


Fig. 5.16

Ray trace for a 200 μm diameter beam incident from the upper right-hand quadrant at an angle of 30°. The concave critical density contour is of lateral dimension 462 μm and has a depth of 60 μ. (X_{crit} = 100 μm) $k_0 L \approx 120$.

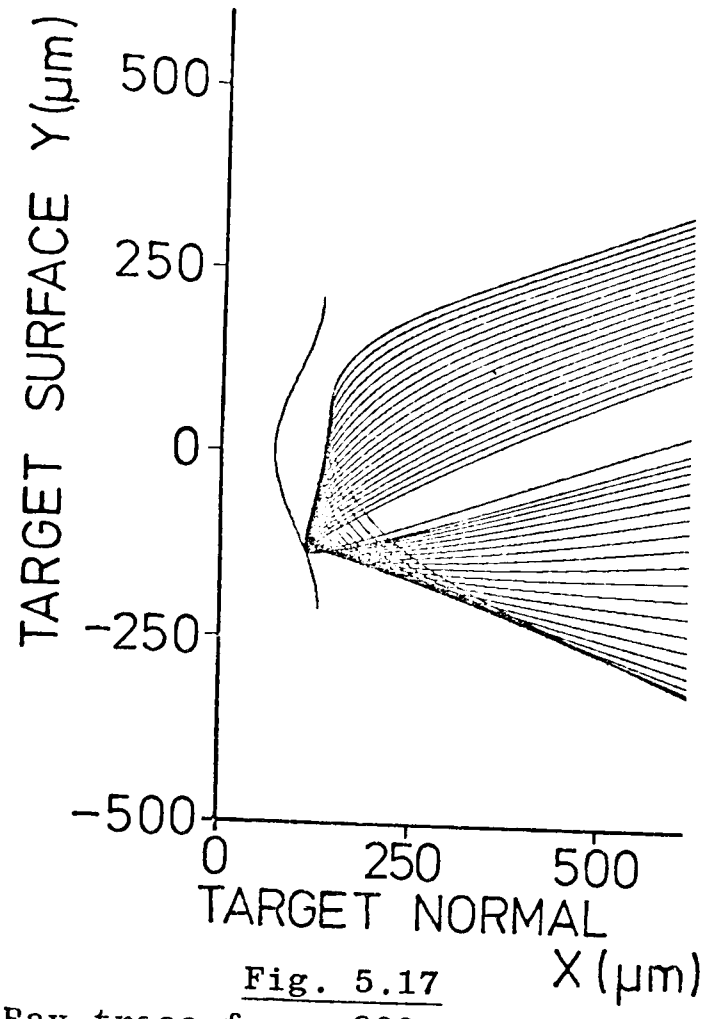


Fig. 5.17
Ray trace for a 200 μm diameter beam incident from the upper right-hand quadrant at an angle of 20°. The plasma conditions are the same as in Fig. 5.16

gave *gross* refraction of the beam to larger angles than the angle of incidence. Parts of the incident beam were initially refracted at larger angles by the upper part of the cavity but the lower portion always seemed to have the effect of returning the nett refraction angle equal to, or less than, the angle of incidence. In Fig. 5.17, for example, a beam incident at 20° to a plasma with approximately the same conditions as in Fig. 5.16, is refracted in such a manner that the exiting beam appears as if reflected from a tilted plane mirror (tilt determined by the local tangent of part of the lower portion of the critical surface). The axis of symmetry of the refracted beam is approximately parallel to the target normal in this case. By following a ray in the upper part of the beam, the upper part of the cavity can be seen to dominate early on in the refraction, and large angles are made with the target normal. Eventually, however, the lower part of the contour starts to bring the ray back towards smaller angles.

It was found that the refracted beam, although not quite so uniform as for elliptical geometry, was still capable of being represented by an axis of symmetry in all cases studied.

5.5.5 *THE EFFECT OF LARGE SCALE FEATURES AT THE CRITICAL SURFACE*

It has not, so far, been possible in any of the geometries investigated in this section, to reproduce the experimental observation of *whole beam* refraction to larger angles than the angle of incidence. In all three

situations studied, spreading of the refracted beam was apparent and for simple convex (elliptical) and concave iso-density contours, whole beam geometrical focusing, both at the turning point (e.g. Figs. 5.10(a) – (c)), and out in the underdense plasma (e.g. Fig. 5.16) could be seen. However, a distinct angular change of the exciting beam's axis of symmetry from the angle of incidence, has not yet been demonstrated. (We believe that we are justified in taking the axis of symmetry of the refracted beam to be representative of whole beam behaviour because, as has been mentioned in relevant sections, the refracted beam still appeared to be uniform, even though in many cases spreading occurred.)

We now note that, to date, the beam size has been comparable to the lateral contour dimension. Now, it is obviously possible to take individual rays in the beam and find a distinct increase in angle upon refraction in some circumstances. Let us, therefore, consider the case where the beam width is much smaller than the non-planar feature at the critical surface. Obviously, we should now be able to reproduce asymmetric refraction because the refraction is determined by the local critical surface shape and we can always define a suitable portion of a suitable contour, where the local tangent gives the required behaviour. In particular, because of the relative magnitude of the critical surface contour, the local tangent remains approximately constant across the beam. Fig. 5.18 shows an illustration of the point. A 200 μm diameter beam, incident at an angle of 20° to a target with a large scale density cavity at the critical surface, is refracted at an angle of ~ 31° (with an angular spread of ~ 4°) with respect to the target normal.

We can produce a similar effect in convex geometry, and Fig. 5.19 shows a 200 μm beam incident towards the lower half of an elliptical critical surface (E = 4.0). The angle of refraction is similar in this case to that shown in Fig. 5.18, but with an angular spread of ~ 2°,

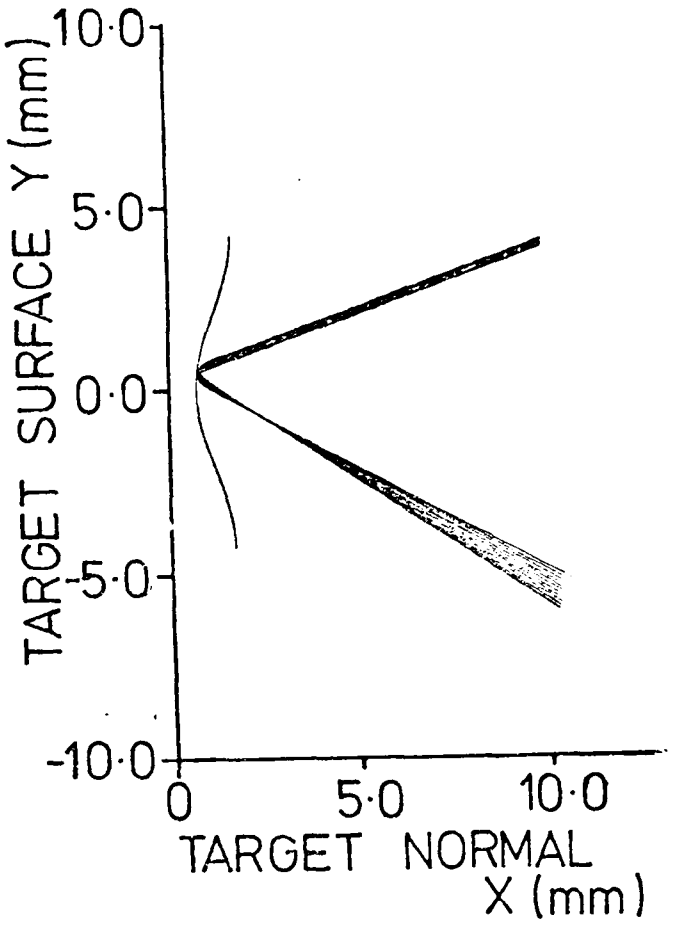
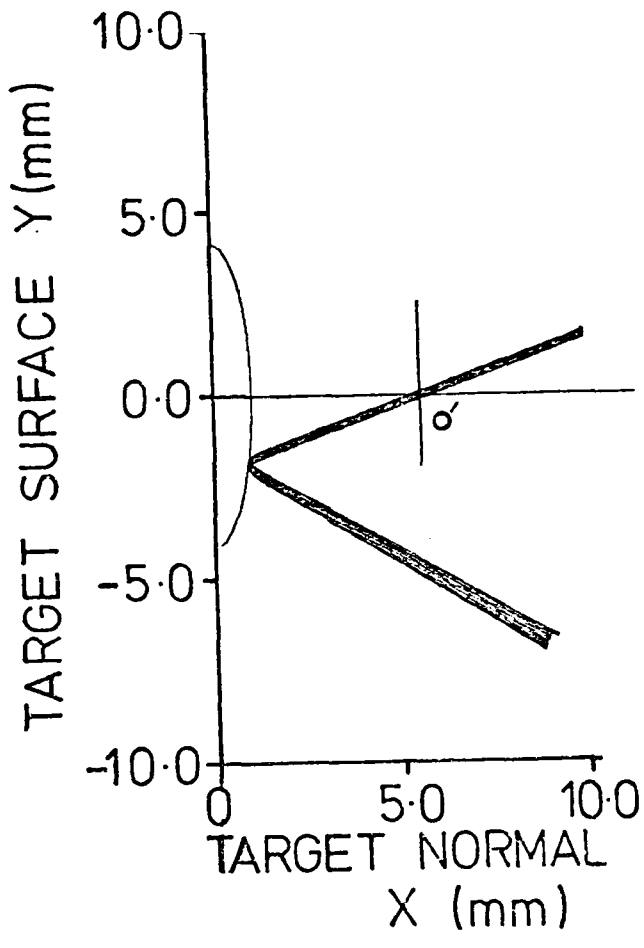


Fig. 5.18

Ray trace for a 200 μm diameter beam incident from the upper right-hand quadrant at an angle of 20°. The concave critical surface has an overall lateral dimension of 8.5 mm and a depth of ~ 1 mm. $k_0 L \approx 120$ (X_{crit} = 1.2 mm)

Fig. 5.19

Ray trace for a 200 μm diameter beam incident from the upper right hand quadrant at an angle of 20°. The elliptical critical density contour has a major radius of ~ 4 mm and a minor radius of ~1 mm. $k_0 L \approx 120$



We might conclude, therefore, that the experimental observation of apparent specular reflection at a non-specular angle does, after all, result from non-planar iso-density contours, but the dimension of the incident beam is required to be small compared to the overall contour dimension, for in this case, the variation of contour gradient across the beam is small. In such a case, we effectively have a local critical surface which is not parallel to the plane of the target surface (and it is with respect to this plane that experimental measurements were made). It is also necessary that the incident beam is not directed at the critical surface vertex, for in this particular situation, the local critical surface would still be parallel to the target surface even for a non-planar geometry. The lateral shift of the turning point away from the origin (i.e. the point at which the beam is initially aimed) has previously been discussed (Chapter 4). Since our plasma model for ray tracing constrains the iso-density contours to be symmetric about an axis which passes through this point (the X-axis), it can be seen that the incident beam is unlikely to be refracted about this axis. In addition, the fact that the critical surface vertex is not constrained to be at the origin of the coordinate system on the target surface, introduces another mechanism for a relative transverse shift of the incident beam away from this vertex. In particular, we see in Fig. 5.18, that the critical surface vertex is approximately 720 μm in front of the plane representing the target surface, whereas, in Fig. 5.19, it is approximately 1 mm. X_{crit} and A_{crit} (see definitions in section 5.2) obviously have an important influence on the refraction angle. For example, for a fixed beam relative to the coordinate system, increasing the value of X_{crit} tends to increase the refraction angle for a given concave shape, because the incident beam will be directed towards a portion making a shallower angle with the target normal. In elliptical geometry, however, the reverse is true and an increase in A_{crit} (for constant E) reduces the refraction angle.

It was found much more difficult to produce significant refraction asymmetry for realistic plasma models in elliptical geometry. Indeed, in order to produce the required behaviour, the incident beam had either to be directed a significant way from the origin of the coordinate system (as, for example, in Fig. 5.19), or it had to be assumed that the critical surface was formed behind the target surface. In this case the effective origin would be shown as O' in Fig. 5.19. For the above reasons we believe that the observed effect of asymmetric refraction is more likely to be the result of concave, rather than convex, geometry.

It would, of course, also be possible to produce the same asymmetric refraction with respect to the target normal, by considering planar plasma expansion with the expansion velocity non-normal to the target surface. From Fig. 4.13, we see that the deviation of refraction angle from specular angle appears to increase with the angle of incidence. For an angle of incidence of 20° for example, a planar critical surface at an angle of 12° to the target normal would be necessary, whilst at 30° this deviation has increased to 15°.

In order to proceed further it would be necessary to simulate the situation with a 2-D code in order to see whether non-normal planar, or large scale curved, iso-density contours would be produced for the conditions of the experiment. The absence of such work here, leaves us with the conclusion that non-planar plasma contours (or non-normal planar plasma expansion), account for the observed asymmetric refraction reported in Chapter 4. The situation is, however, complicated by the requirement of an expansion asymmetry and/or an iso-density contour perturbation of larger scale than the beam dimension.

CHAPTER 6

SPECTRAL MEASUREMENTS OF THE BACKSCATTERED RADIATION

6.1 INTRODUCTION

Spectral measurements of the radiation which is scattered by the corona of a laser-produced plasma, can give us much information about that plasma and the processes occurring in it. From amongst the numerous references by many research groups, we can cite experiments using incident wavelengths λ_0, of 0.52 μm (COLE *et al.* 1981), 0.694 μm (JANNITTI *et al.* 1975), 1.06 μm (BÜCHL *et al.* 1972; GOLDMAN *et al.* 1973; RIPIN, 1977; ROSEN *et al.* 1978; GRAY *et al.* 1980) and 10.6 μm (MITCHELL *et al.* 1975; GREK *et al.* 1977; GARBAN *et al.* 1978) as examples of spectral measurements of the backscatter, made in the region of λ_0. In this chapter, the spectral measurements made on the backscattered radiation from the interaction of the APPLE laser and the plasma formed on solid graphite targets are described. We note that the parameters of the laser were such that the oscillator cavity was still being operated in the unstable configuration described previously, giving a single transverse mode output.

6.2 APPARATUS

The incident pulse was focused by the salt lens to a focal spot distribution giving a peak irradiance of approximately 10^{12} W/cm^2, as described in Chapter 2.

Spectra were taken using the grating monochromator and detector system shown in the experimental schematic of Fig. 6.1.

The monochromator was a MONOSPEK 1000 device, having a symmetrical Czerny-Turner format and a 1 meter focal length f. A 102 mm square ruled area grating was used having 150 grooves/mm and an 8 μm blaze wavelength. With this grating and configuration, the theoretical grating resolution of 7 Å (at 10 μm wavelength) was approached with an entrance slit width of

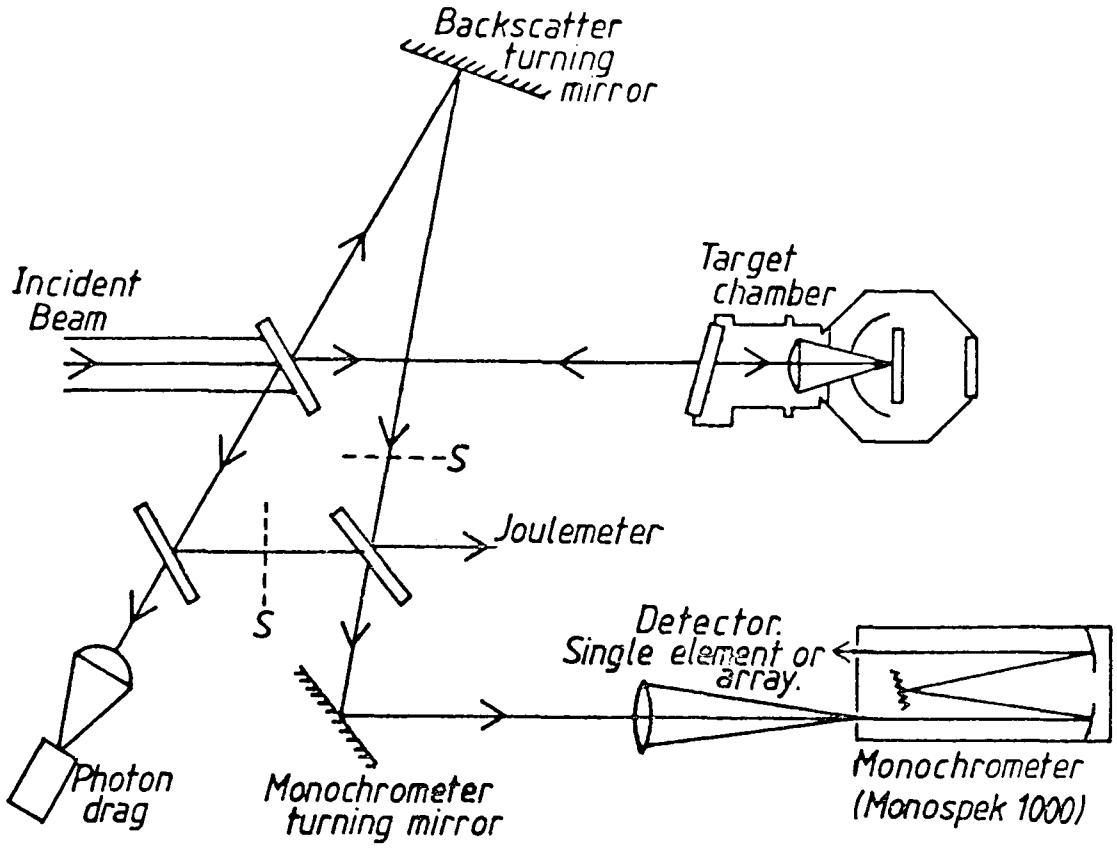


Fig. 6.1

Schematic of the experimental arrangement for backscatter spectral analysis. Polyethylene attenuators or beam blocks were placed at positions S in the figure thus allowing controllable amounts of either incident or backscattered radiation — or both — into the Monospek spectrometer.

150 μm. The reciprocal linear dispersion at 10.59 μm was calculated to be 4.51 *nm/mm* (in 1st order) using the expression:

$$\frac{d\lambda}{dx}\ (nm/mm) = \frac{10^6 \cos\left\{\sin^{-1}\left(\frac{m\lambda}{2d\cos\delta/2}\right) - \frac{\delta}{2}\right\}}{m(f/d)}$$

where δ, the angle between incident and diffracted rays was measured to be 11°. A plot of the calculated variation of $\frac{d\lambda}{dx}$ vs λ (for $d = \frac{1}{150}$ mm) in the region around $\lambda = 10.59\,\mu m$ is shown in Fig. 6.2.

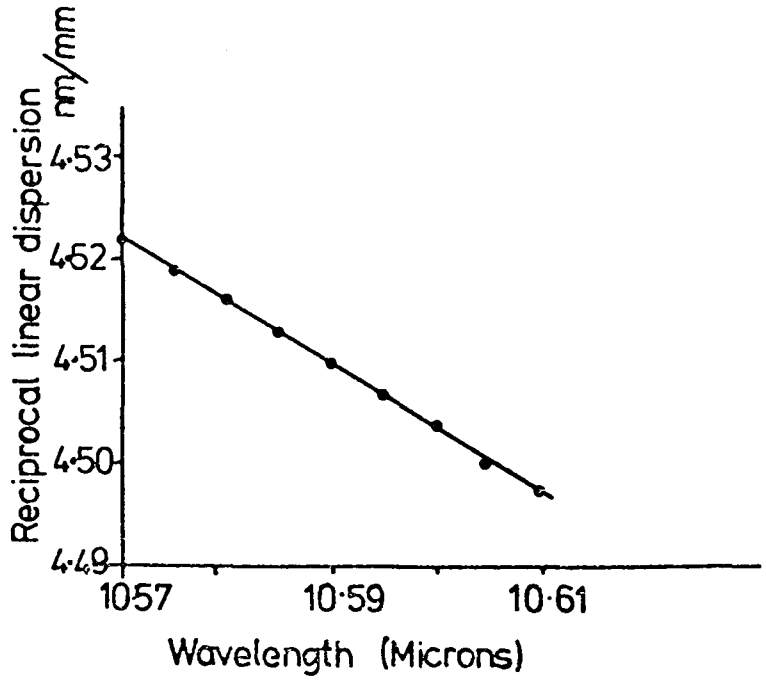


Fig. 6.2

Reciprocal linear dispersion of the Monospek 1000 spectrometer (with 150 line/mm grating) as a function of wavelength, for the region around 10.59 μm.

For preliminary measurements a high sensitivity, slow response, pyroelectric detector (MOLECTRON P3-01) was used, and the spectrum obtained by a many shot experiment, tilting the grating between shots to scan the spectrum. In this arrangement, the exit slit of the monochromator was imaged by an NaCl lens onto the detector element. The obvious disadvantages of the method were that the spectra were averaged over many shots, and required a long experimental run to obtain.

Subsequent results were obtained by replacing the single element detector by a pyroelectric array (manufactured by Plessey Ltd) consisting of 32 individual elements of 1 mm X 200 μm dimension on a 250 μm pitch. Each element had a responsivity of 10^5 V/J. The energy profile at the detector plane was stored by a set of sample and hold amplifiers and then read out at a rate of 1 kHz by a multiplexer, giving a scan which was then displayed on a TEKTRONIX 7904 oscilloscope. This scope was triggered from a reference output line from the array circuitry. A sample hold pulse was provided whose falling edge occurred at the time when the data was to be stored (at the end of the laser pulse). The pulse was initiated by the APPLE laser control circuitry, and its height, duration and timing was adjusted to give maximum detector signal. A schematic of the array is shown in Fig. 6.3. The array was placed at the exit plane of the monochromator after removal of the slit, the resolution in this case being set by

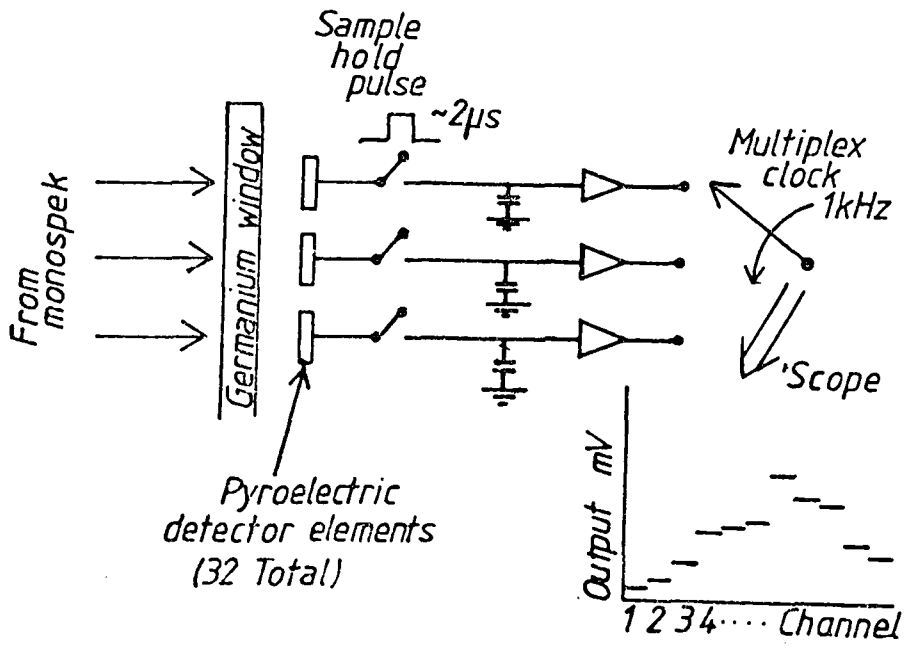


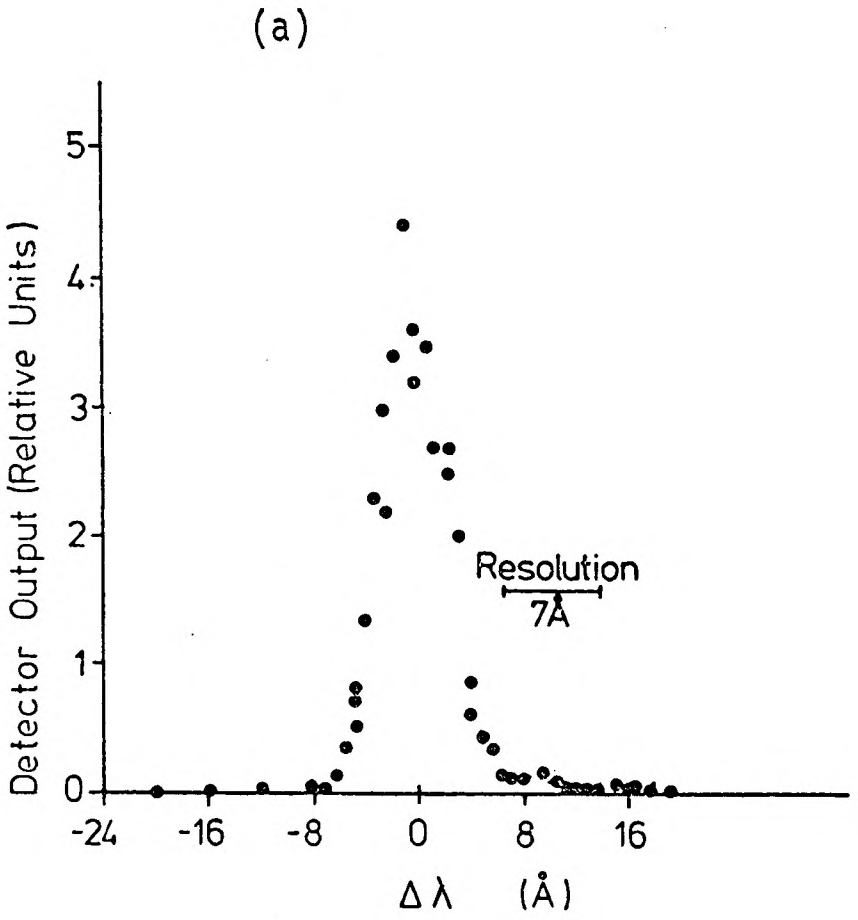
Fig. 6.3
Schematic illustrating the principle of operation of the Plessey pyroelectric detector array

the pitch of the detector elements. Thus, for a 250 μm pitch and a reciprocal linear dispersion of 4.5 *nm/mm*, a resolution of ~11 Å was now obtained.

The incident pulse shape and the total energy into the monochromator were monitored with a photon drag detector and a pyroelectric joulemeter, respectively, as shown in Fig. 6.1. To calibrate the monochromator and test the resolving power of the system, the beam splitter arrangement shown in the figure was used to deflect a portion of the incident beam into the monochromator along the same path as the backscattered beam. (The system was aligned using a 5 mW He-Ne beam coaxial to the CO_2 laser output (see Chapter 1).

6.3 INCIDENT AND BACKSCATTERED SPECTRA

The spectrum of the incident radiation is shown in Figs 6.4(a) and 6.4(b). Figure 6.4(a) shows the spectrum as measured with the single element detector over many shots, and in this case the FWHM is slightly less than the resolution of the system and agrees very well with the theoretical bandwidth of the laser, namely 3.7 Å (1.0 GHz). Figure 6.4(b) shows the incident spectrum as recorded by the array. (The signals observed on the left-hand side of the oscillograph arise from pick-up in the detector electronics, are reproducible from shot-to-shot, and can be ignored.) As can be seen, the width in this case is one channel corresponding to a bandwidth of ~ 11 Å. It should be noted at this point that a change in the position of the detector array in the exit plane of the monochrometer, would cause a change in the distribution of the resulting spectrum. For example, the incident spectrum of Fig. 6.4(b) could be made to have a width of two channels of half the original magnitude, by physically moving the array across the exit plane by an amount equal to half a detector dimension, i.e., 125 microns (or by tilting the grating to shift the spectrum across the array). Thus before recording the spectra of backscattered radiation, the position of



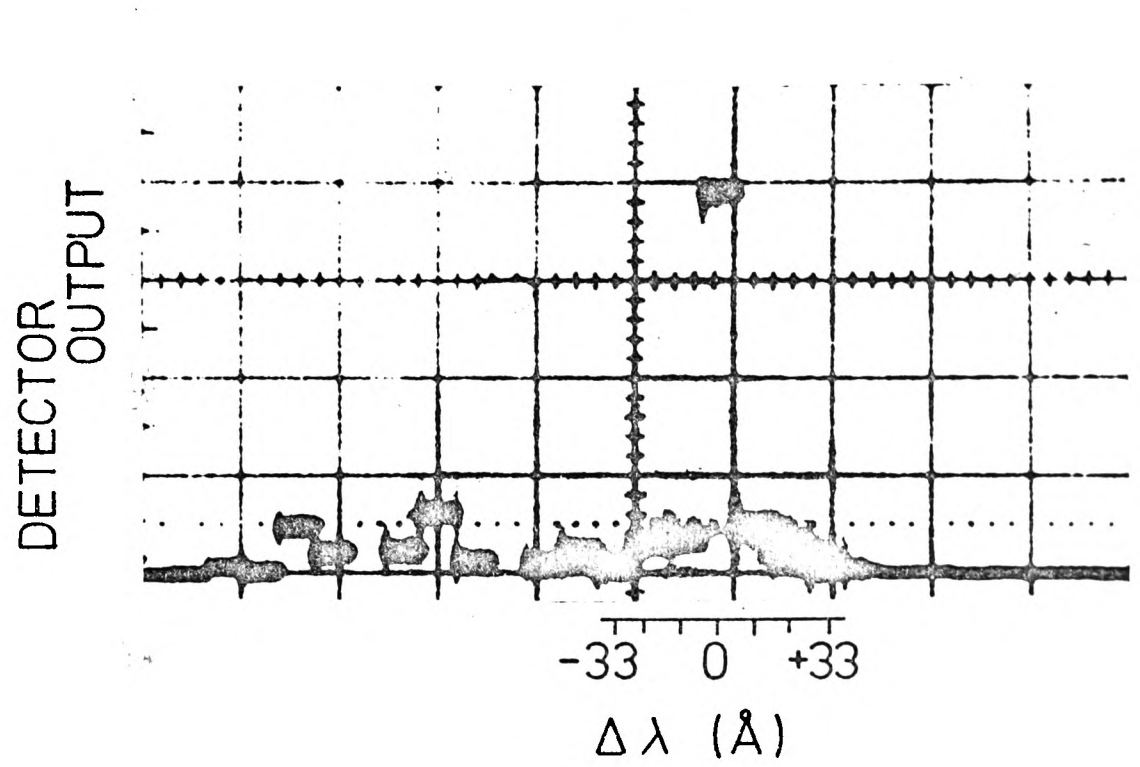


Fig. 6.4

Spectrum of the APPLE laser output (unstable cavity) as recorded using the Monospek 1000 optically coupled to (a), the single element Molectron detector; the spectrum having been built up over many shots, and (b), the Plessey pyroelectric array; the spectrum having been recorded on a single shot

the detector was set, by comparison with the spectrum shown in Fig. 6.4(b), so that the recorded incident line was positioned at the centre of a single element. The detector position was then kept fixed throughout subsequent experiments (as was the grating tilt).

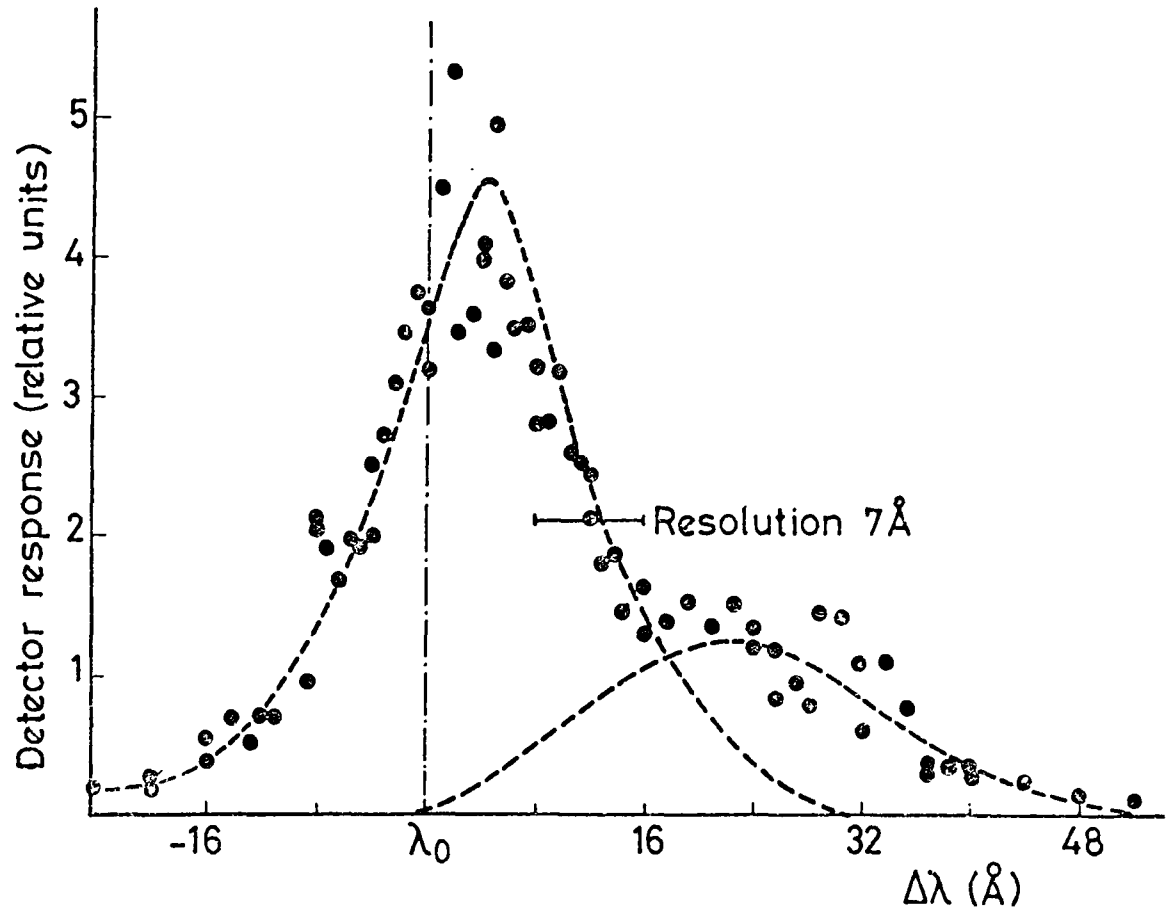


Fig. 6.5

Backscattered spectrum from a carbon target situated at the optimum focus and irradiated normally at $\sim 10^{12}$ W/cm^2. The spectrum was built up over many shots using the single element detector

Figure 6.5 shows the spectrum of the backscattered radiation as measured with the single element detector. The target was in the position of best focus, as defined in Chapter 2. There appears to be a sideband to the distribution on the red side of a peak that is itself slightly shifted from the position of 10.59 μm radiation. The position of the sideband is ~ 24 Å from this reference position. The main peak exhibits a red shift of < 5 Å and although this is less than the resolution of the system, it is believed to be physically significant, as will be discussed in section 6.6.2.

The backscattered spectrum at best focus, as measured using the array, is shown in Fig. 6.6. The spectrum was taken for normal illumination

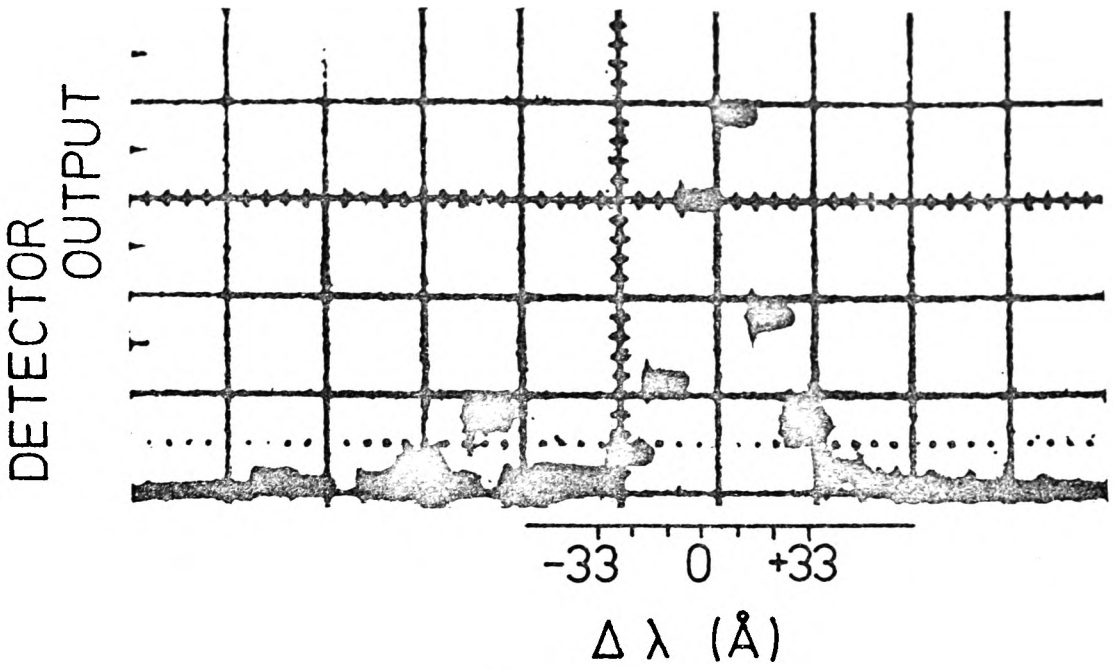


Fig. 6.6

As Fig. 6.5 but the spectrum was obtained on a single shot using the linear detector array

of the graphite target. The peak of the distribution occurred in the next channel to the red from the 10.59 micron channel (hereafter called the reference channel). The centroid of the distribution is at a position of ~ 7.5 Å to the red, relative to the reference channel.

It is believed that the backscattered spectrum is modified by a red shifted component due to a parametric scattering process in the underdense plasma, and a blue shifted component arising from the Doppler effect of plasma expansion into the vacuum. Obviously the fact that both shifts are in the opposite sense, considerably complicates any attempt to compare measured spectra with theoretical predictions. Experiments with stationary gas targets, (NG *et al.* 1978, 1979, 1981; OFFENBERGER *et al.* 1978; MAYER *et al.* 1980), have produced results that do not contain any Doppler component and hence clarify the situation with regard to the parametric processes. With laser interaction with solid targets, however, a method must be found of estimating the Doppler component in the spectra of backscattered radiation, in order to fully investigate the parametric process.

In order to ensure that the recorded backscattered spectra were not modified by higher order contributions from harmonics of the incident

radiation, a LiF flat was used as a short wave-pass blocking filter ($1/e^2$ transmission measured at 7.6 μm) to remove the fundamental and allow only harmonics into the monochromator. No signal was recorded either for the single element detector (with monochromator tuned to 10.59 μm) or for the detector array. The attenuation in the backscatter line was kept as for the original experiments and thus the above test cannot be regarded as demonstrating the absence of plasma generated harmonics. Further tests were subsequently performed (TUTTLEBEE, 1979) using narrow band pass filters at ω_0, $\frac{3}{2}\omega_0$, $2\omega_0$ and $3\omega_0$, and a Thompson−CSF Pyricon® to image the plasma from a direction of 45° to the incident beam axis. No evidence of harmonic generation was found but the work was not regarded as conclusive.

6.4 STIMULATED BRILLOUIN SCATTERING, (SBS), IN AN EXPANDING PLASMA

For the irradiances considered in the present experiments it is likely that the parametric process contributing to the back-scattered signal is the Stimulated Brillouin Scattering effect. The threshold irradiance can be found from the general expression given by LIU (1976) namely :

$$\frac{(v_0/v_e)^2\ (\omega_{pe}/\omega_0)^2\ k_0\ L_u}{\left|\frac{u}{c_s}\left\{1+\frac{c_s}{u}\cdot\frac{\omega_{pe}^2}{\omega_0^2}\cdot\frac{L_u}{L_n}\left[\frac{u}{c_s}-1\right]\right\}\right|} > 1 \qquad (6.1)$$

(where we have assumed that the scale length for temperature variation, $L_T, \to \infty$ in Liu's original expression). In equation (6.1) v_0/v_e is the ratio of electron quiver velocity to thermal velocity, c_s is the ion sound speed given by

$$c_s = \left\{\frac{Z k_B T_e}{A m_p}\right\}^{\frac{1}{2}} ,$$

(where Z is the effective ion charge state), and the other parameters are defined below.

For a stationary plasma, equation (6.1) reduces to :

$$\left(\frac{v_0}{v_e}\right)^2 k_0 L_n > 1$$

which gives us a threshold irradiance of $6 \times 10^{10}\,\mathrm{W/cm^2}$ for an electron temperature $T_e = 300\,\mathrm{eV}$, a density scale length $L_n = 200\,\mu\mathrm{m}$ and $\lambda_0 = 10.59\,\mu\mathrm{m}$. The situation is complicated when plasma expansion is considered, for we then need to know the velocity scale length L_u, the normalized electron density n/n_c $(= \omega_{pe}^2/\omega_0^2)$ at which the scattering occurs, and the plasma expansion velocity u. (We note that u is the velocity of the plasma moving *through* the density profile and not the velocity of the profile itself.) The threshold irradiance given by equation (6.1) is plotted as a function of Mach number u/c_s, in Fig. 6.7, for $L_n/L_u = 1$ and 0 (the expected limits). As in the previous example, $T_e = 300\,\mathrm{eV}$, $L_n = 200\,\mu\mathrm{m}$ and we have anticipated the result of the next section and put $n/n_c = 0.4$. It can be

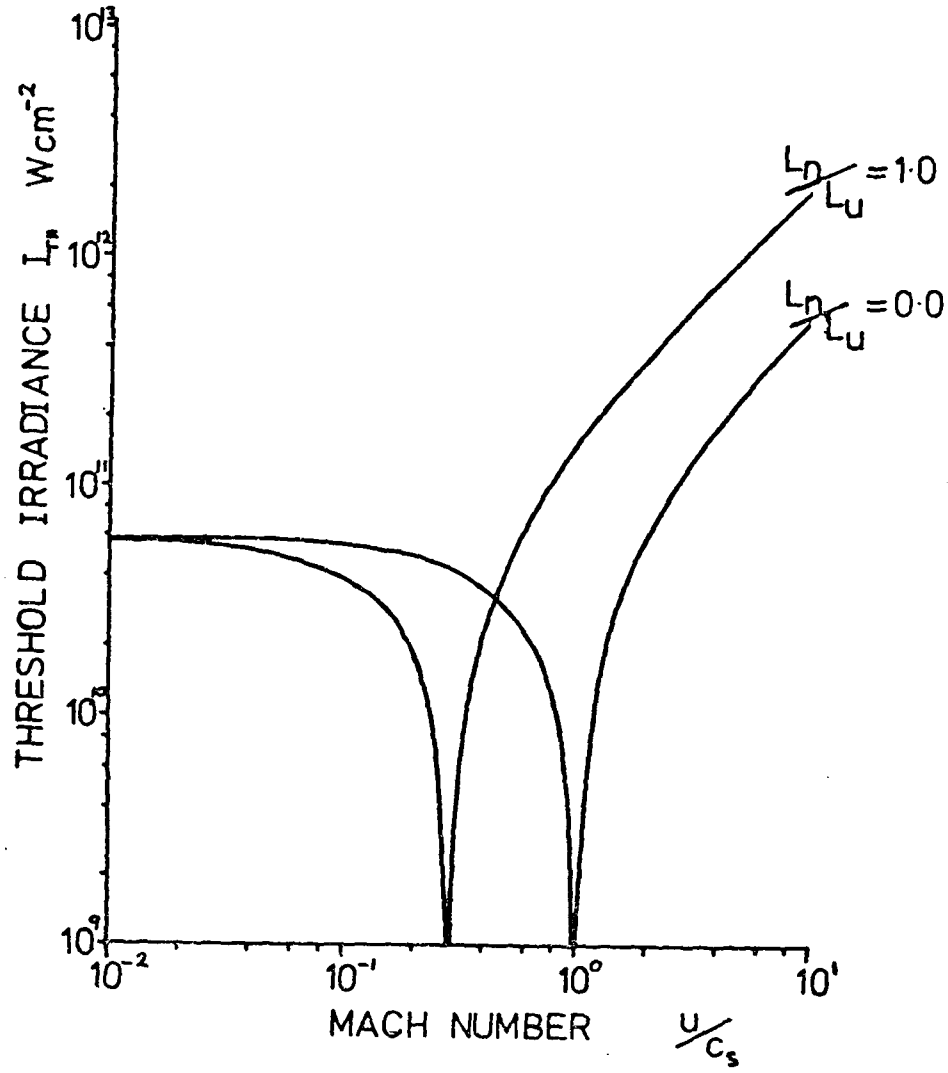


Fig. 6.7

Threshold irradiance for the stimulated Brillouin backscattering process as a function of expanding plasma Mach number, for L_n/L_u = 1.0 and 0.0

seen that for certain plasma conditions (e.g. $L_n/L_u = 0.0$, $u/c_s = 1.0$) the required irradiance becomes vanishingly small. The figure also shows that the threshold irradiance would be exceeded in the experiments unless the Mach number greatly exceeded unity. In fact, as will be seen in section

6.5, u/c_s was found to be $\sim \frac{2}{3}$ and for this case a threshold irradiance of 8×10^{10} W/cm^2 is predicted by equation (6.1).

We now consider the wave matching relations for the SBS process. If we transform from the frame of reference of the moving plasma to that of an observer in the laboratory frame, a Doppler component is introduced and we obtain the relation:

$$\Delta\lambda = \frac{2\lambda_0}{c} (c_s - u \cos\theta) \sqrt{1 - \frac{n(x)}{n_c}} \qquad (6.2)$$

where $\Delta\lambda$ is the wavelength shift of the backscattered radiation from the fundamental λ_0. θ is the angle of the target normal to the backscatter direction. We can write equation (6.2) in the following form:

$$\Delta\lambda_{\text{OBSERVED}} = \Delta\lambda_{\text{SBS}} - \Delta\lambda_{\text{DOPPLER}} \cos\theta \qquad (6.3)$$

where

$$\Delta\lambda_{\text{SBS}} = \frac{2\lambda_0}{c} \cdot c_s \eta(x) \ , \qquad (6.4)$$

and

$$\Delta\lambda_{\text{DOPPLER}} = \frac{2\lambda_0}{c} \cdot u \eta(x) \ , \qquad (6.5)$$

$\eta(x) = (1 - n(x)/n_c)^{\frac{1}{2}}$ is the refractive index at the density $n(x)$ in the plasma where the SBS process occurs. Hence, by measuring the wavelength shift of the backscattered spectrum as a function of θ, we can obtain, for the region at density n, a value for the Doppler shift using equation (6.3), and a value for the expansion velocity, u, from equation (6.5). The results of the Doppler shift determination are presented in section 6.5.

In order to use equations (6.3) – (6.5) to obtain plasma parameter values from observed shifts, an explicit electron density must be obtained and this is accomplished in the following section. An alternative approach was adopted by GORBUNOV *et al.* (1978) who assumed functional dependences for $n(x)$ and $u(x)$ and then obtained $\Delta\lambda(x)$ by a convolution of these two spatially varying parameters. The authors then state that the backscatter spectrum can be calculated by convoluting $\Delta\lambda(x)$ with the gain $G(x)$ in order to obtain the intensity of the radiation scattered by different parts

of the corona. It was claimed that calculated spectra could be fitted to observed spectra by variation of free parameters such as I_0 and T_e. Spectra were subsequently calculated by GORBUNOV and POLYANICHEV (1979) using an expression for the gain given by GORBUNOV and POLYANICHEV (1978). It was stated, however, that the procedure was only applicable to plasmas with Mach number greater than unity over the entire underdense corona due to the presence of a turning point (or 'red boundary') in the functional variation of $\Delta\lambda(x)$ in this situation.

6.4.1 *POSITION OF THE SBS PROCESS IN AN INHOMOGENEOUS PLASMA*

To obtain an estimate of the region in an inhomogeneous plasma where the SBS process most strongly occurs, a numerical solution of a dispersion equation for the ion acoustic wave was found, in order to find the electron density corresponding to maximum growth. A dispersion relation pertaining to a homogeneous plasma was taken and the complex solution traced as the density was varied. The plasma was, therefore, considered to have a quasi-inhomogeneous density profile and it was assumed that the local magnitude of any interaction was effectively that of a uniform plasma with the relevant local density (FRANKLIN, 1977). A consequence of this modelling was that the damping effect of convection out of the region of matching was not taken into account and the two damping processes considered were collisional damping of the electromagnetic wave and Landau damping of the ion acoustic wave. The effect of pump depletion on the processes was not introduced.

The dispersion relation used was that of DRAKE *et al.* (1974) :

$$(\omega - \Delta\omega + i\Gamma_-)\ \frac{(\omega^2 - \omega_a^2 + 2i\Gamma_a\omega_a)}{(\omega^2 - \omega_{pi}^2)} = 2\left(\frac{ck_0}{\omega_0}\right)\ \frac{ck_0}{(1+k^2\lambda_D^2)} \cdot \frac{v_0^2}{c^2} \cdot \psi \qquad (6.6)$$

(For backscattering and when the backscattered polarization vector = incident, $\psi = 1$). Γ_-, the collisional damping rate of the electromagnetic wave is given by,

$$\Gamma_- = \frac{\nu_{ei}}{2} \cdot \frac{n(x)}{n_c} \quad , \qquad (6.7)$$

where ν_{ei}, the electron-ion collision frequency, is given by,

$$\nu_{ei} = \frac{Kc}{(n/n_c)}$$

with K, the inverse bremsstrahlung absorption coefficient from JOHNSTON and DAWSON (1973). (See Chapter 7).

Γ_a, the Landau damping rate of the ion acoustic wave can be written,

$$\Gamma_a = \sqrt{\frac{\pi}{8}}\ \omega_a \left\{ \left(\frac{Z T_e}{T_i} \right)^{\frac{3}{2}} \exp\left(-\frac{1}{2} \left(\frac{Z T_e}{T_i} \right) \right) + \sqrt{\frac{Z m_e}{A m_p}} \right\} , \qquad (6.8)$$

ω_a, the ion acoustic frequency, is written as follows,

$$\omega_a = \frac{k c_s}{\sqrt{1 + k^2 \lambda_D^2}}$$

where $k \sim 2 k_0 \eta$. $\Delta\omega$ is the frequency mismatch of the decay process where,

$$\omega_0 - \omega_s - \omega = \Delta\omega \qquad (6.9)$$

ω_0 and ω_s are the frequencies of the incident and scattered electromagnetic waves respectively. We introduce $\Delta\omega$ as a variable parameter in the numerical routine. All other parameters have their usual definition.

We required the solution of equation (6.6) for complex ion acoustic wave frequency ω where $\omega = \Omega + i\gamma$. We then studied, in particular, the growth rate γ as a function of electron density for varying parameters including $\Delta\omega$, T_e and I_0. The equation, being a complex cubic, the roots were conveniently found using the Culham routine ZERINT (MARTIN, 1971). Before using this routine, equation (6.6) was put into the following form:

$$F(\omega') = (\omega' - \Delta\omega' + i\Gamma_-')(\omega'^2 - \omega_a'^2 + 2i\Gamma_a'\omega_a') - 2(\omega'^2 - \omega_{pi}'^2) \frac{\omega_0'}{(1 + k^2 \lambda_D^2)} (1 - D) \frac{v_0^2}{c^2} , \qquad (6.10)$$

where the primed quantities indicate a normalizing division by ω_{pi} (evaluated at $n = n_c$), and $D = n/n_c$. We require solutions of $|F(\omega')| = 0$, and Fig. 6.8 shows a 3-D contour plot of $|F(\omega')|$ evaluated over part of the complex plane. The plasma parameters are indicated in the figure caption.

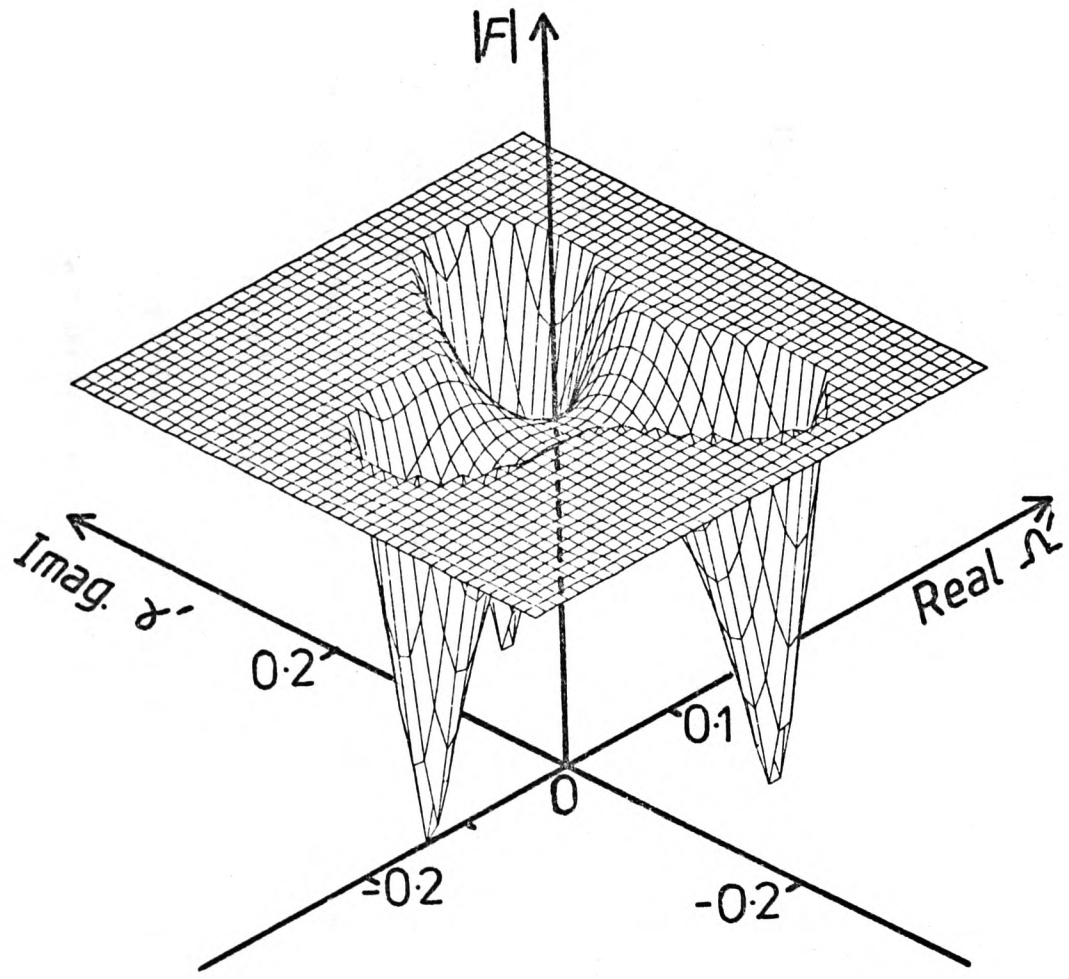


Fig. 6.8

Pseudo-three dimensional contour plot of the function $|F(\omega')|$ evaluated over a portion of the complex plane and showing the three roots of equation (6.10). For the situation shown, the model parameters were: $\lambda_0 = 10.59\ \mu m$, $I_0 = 10^{12}\ W/cm^2$, $T_e = 300\ eV$, $n/n_c = 0.5$, $Z/A = 0.5$, $T_e/T_i = 10$ and $\Delta\omega' = 0.0$

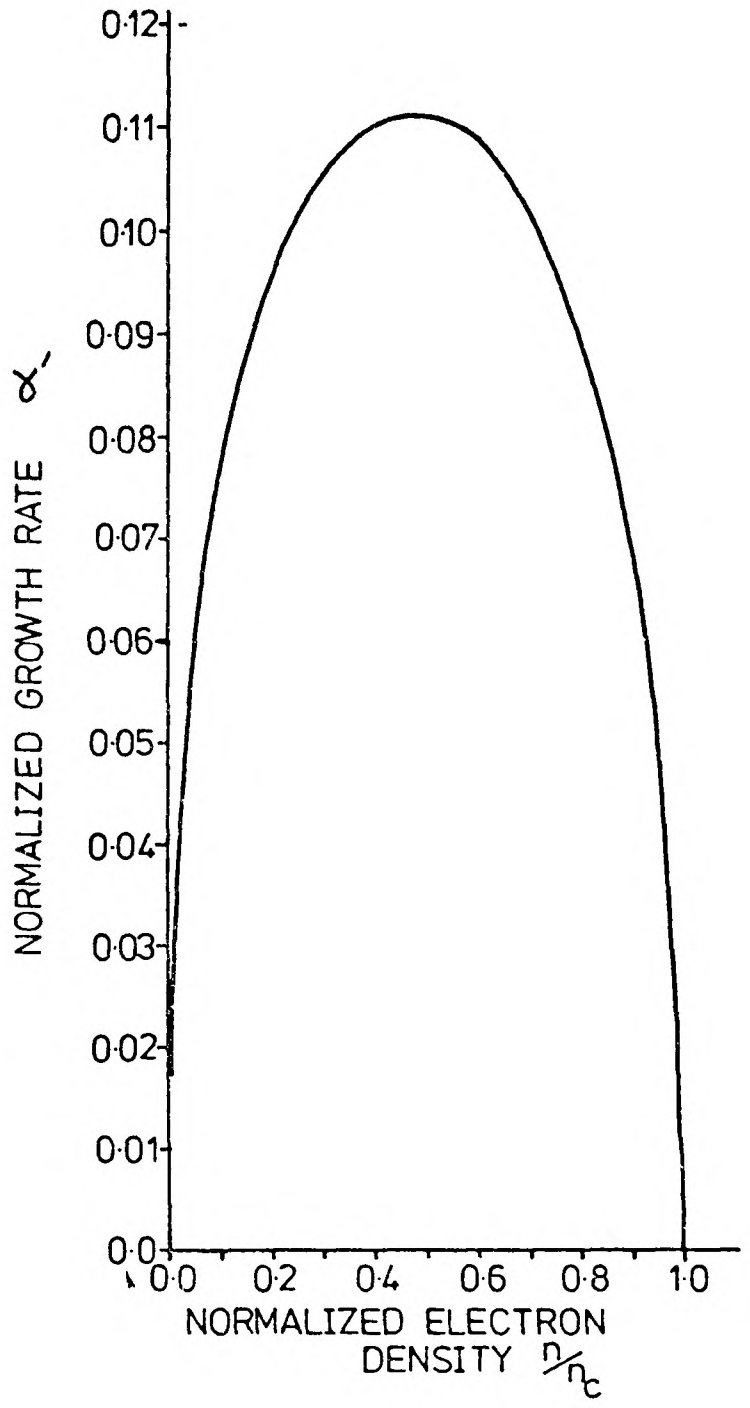


Fig. 6.9

Normalized growth rate γ/ω_{pi} of the ion acoustic wave as a function of normalized electron density n/n_c. The model parameters are as stated for Fig.6.8

The three roots given by $|F(\omega')| = 0$ are clearly shown. Only one of these roots represents a growing mode for the figure parameters ($\Omega' = +0.07$, $\gamma' = +0.11$) and it was the variation of this root with changing parameters that was studied. Figure 6.9 shows the growth rate of the ion acoustic mode as a function of density ratio for the same model parameters as Fig. 6.8. As can be seen, the growth rate peaks at a density ratio of $0.475\, n_c$.

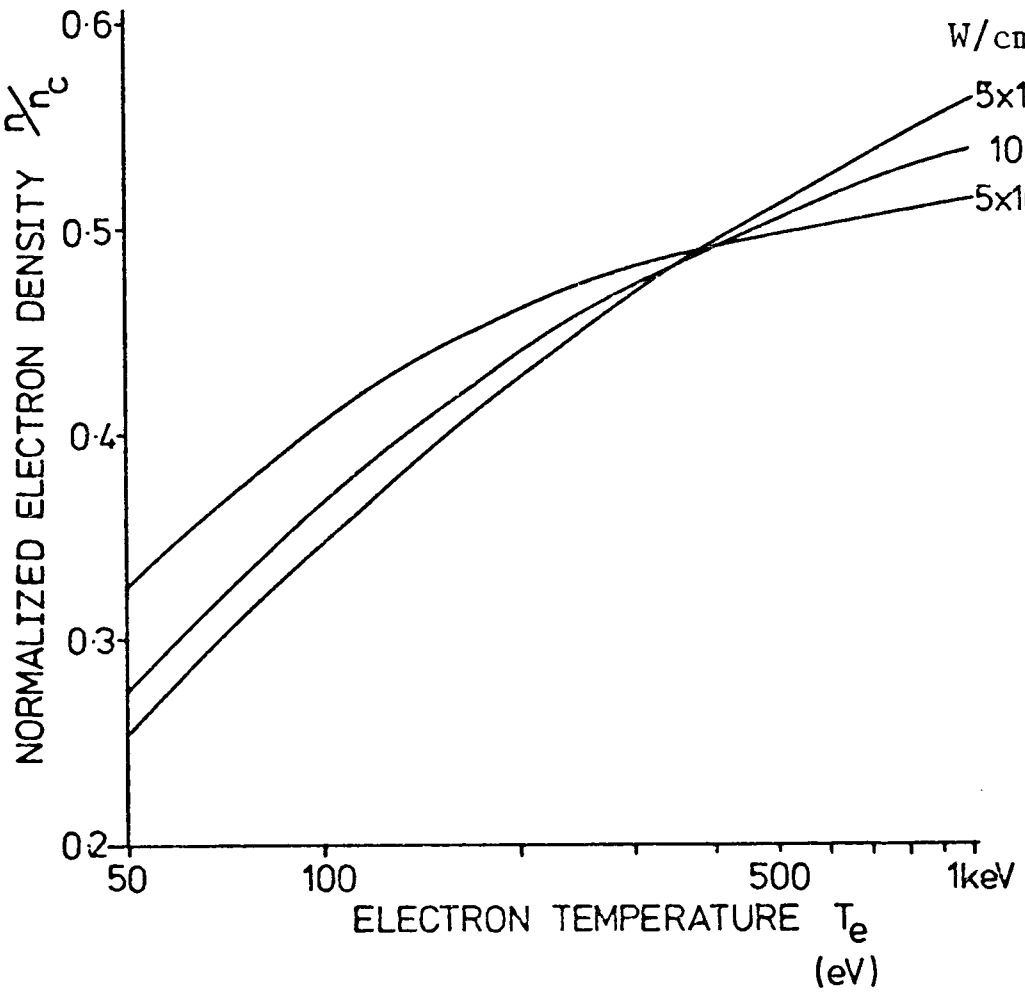


Fig. 6.10
Variation with electron temperature of the electron density corresponding to the peak ion acoustic wave growth rate. Curves are drawn for three values of incident irradiance. Other model parameters are as stated for Fig. 6.8

We now wish to illustrate the sensitivity of this value to T_e and I_0. In Fig. 6.10, the density ratio corresponding to peak growth is plotted as a function of T_e for three values of I_0. From these curves, therefore, it appears that in the temperature range from 50 eV − 500 eV, for irradiance from $5.0 \times 10^{11} - 5.0 \times 10^{12}$ W/cm^2, the density of peak growth for the ion acoustic wave can be given as $n/n_c = 0.4 \pm 0.1$. In view of the large range of the parameters (an order of magnitude variation in both T_e and I_0) the variation of 25% in the position of peak growth is sufficiently small to enable the value to be used with confidence in subsequent analysis of SBS backscatter spectra (section 6.6)

Further investigation established that the position of the peak was very insensitive to the charge state Z, temperature ratio T_e/T_i and mismatch $\Delta\omega'$. However, the variation of the absolute magnitude of the growth rate γ' with I_0 at a particular density ratio, provided a check on the validity of the routine. This variation is shown in Fig. 6.11 for an electron temperature of 300 eV and a density ratio of 0.5. A threshold irradiance of $\sim 10^9$ W/cm^2 is indicated from the figure, in very good agreement with the value obtained from the analytic expression given by DRAKE *et al.* (1974), i.e.

$$\left(\frac{v_0}{c}\right)^2 = \frac{2\,\Gamma_a\,\Gamma_-}{\omega_{pi}^2}\,\frac{\omega_0}{k_0 c}\cdot\frac{c_s}{c}\ .$$

Of course, this threshold is for a homogeneous plasma and is much lower than would be expected when convective effects, introduced by a finite density gradient, are considered. (See earlier comments in this section.)



Fig. 6.11
Normalized ion acoustic wave growth rate as a function of incident irradiance, illustrating a threshold irradiance of $\sim 10^9$ W/cm^2

Although we are primarily concerned with the imaginary part of the solution, i.e., the growth rate of the ion acoustic wave, it is interesting to briefly remark on the real part of the root, namely the wave frequency Ω'. Figure 6.12 shows the variation of this parameter with density ratio under the same conditions as Fig. 6.8. Also shown on this figure is the

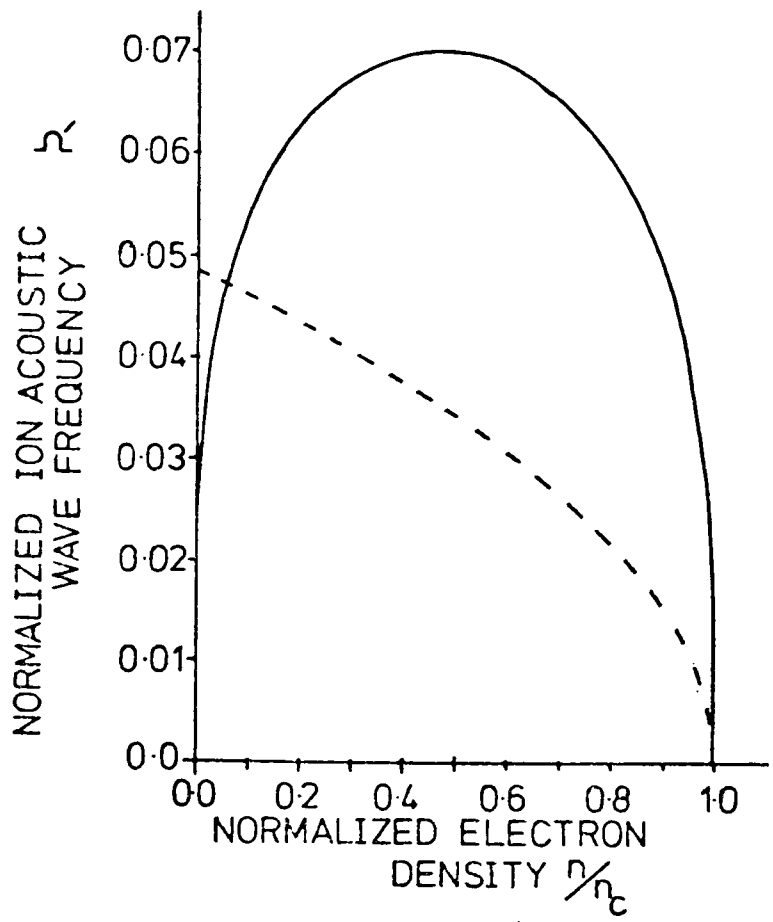


Fig. 6.12
Variation, with electron density ratio n/n_c, of the normalized ion acoustic wave frequency Ω/ω_{pi} (solid line). The broken line shows the variation, with n/n_c, of the usual expression for the ion acoustic wave frequency in stimulated Brillouin scattering, namely the normal mode dispersion $\omega_a = 2k_0 \eta c_s$. Model parameters are as stated in Fig. 6.8

usual expression for the ion acoustic wave frequency in the absence of the pump, namely, $2k_0 \eta c_s$. It can be seen that, except at low density, there is a significant deviation from the frequency predicted by the code and that given by this expression for a normal mode of the plasma. It was found that by reducing the irradiance in the model to values approaching the threshold value of 10^9 W/cm^2 (Fig. 6.11), $\Omega'(n/n_c)$ and $2k_0 \eta c_s$ (n/n_c) could be brought back into agreement. If, however, we take the normalized peak frequency from Fig. 6.12, and let this value be the frequency difference between incident and scattered waves ($\Delta\omega = 0$), a Brillouin shift of $\sim$ 120 Å is predicted. This is not in good agreement with the experimentally determined value after accounting for the Doppler contribution (see section 6.5). However, from equation (6.9) we see that the frequency difference between incident and scattered waves is, in fact, $\Omega + \Delta\omega$ and thus a suitable choice of the parameter $\Delta\omega$ could be used to bring the wavelength shift predicted by the model back into agreement with the value given by equation (6.4). In the particular case illustrated by Fig. 6.12, a negative mismatch given by $\Delta\omega' = -0.03$

would be required at the density of peak gain as found from Fig. 6.9. Variation of the growth rate with $\Delta\omega'$ is shown in Fig. 6.13, where it can be seen that although peak growth is reached for zero mismatch, the introduction of a small negative value of $\Delta\omega'$ does not affect the growth rate appreciably. Also, as has already been mentioned, variation of $\Delta\omega'$ does not affect position of peak growth significantly. It remains to point out that a quantity such as the mismatch must necessarily be used as a free fitting parameter within the limitations of this model, for we have no analytic expression to give its value when we consider its expected dependence on density scale length, density, temperature, and irradiance, in a real plasma.

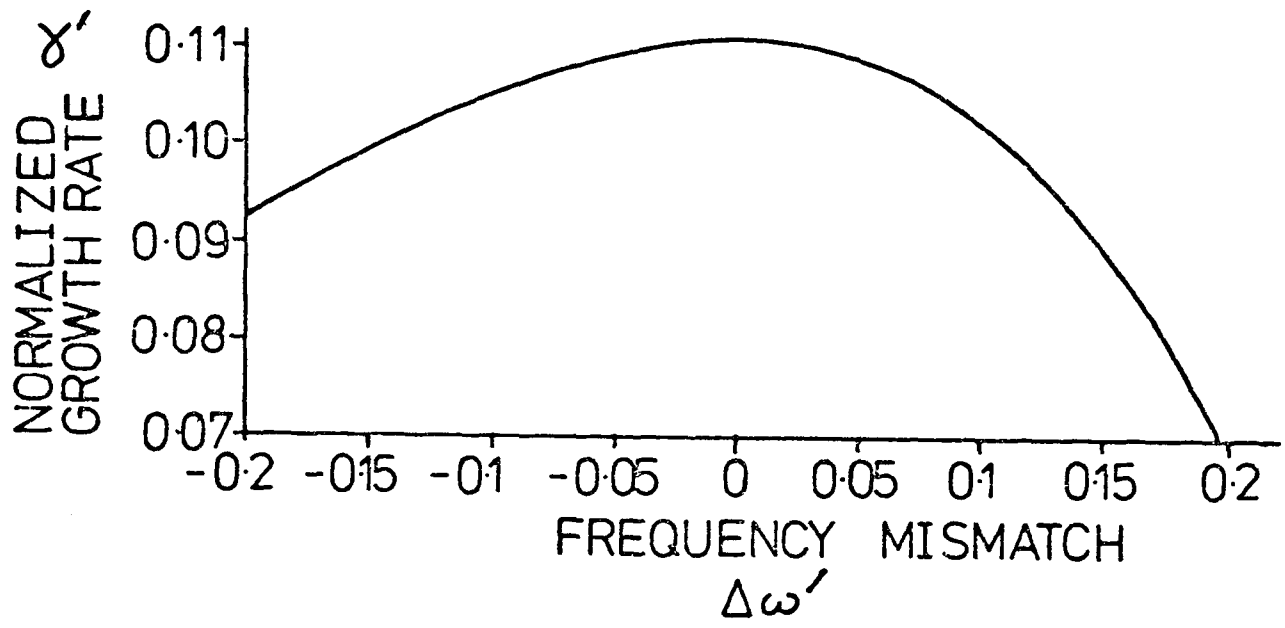


Fig. 6.13
Variation of the ion acoustic wave growth rate γ' with frequency mismatch $\Delta\omega'$. The model parameters are as stated in Fig. 6.8

To conclude this section it is necessary to emphasize that the motivation for this numerical work was to obtain a feel for the position of the SBS process in an inhomogeneous plasma under conditions applying to those of the experiments. This has been achieved, and a density range of 0.3—0.5 n_c has been obtained. It is interesting to compare this value with that obtained by other groups. A density of $n_c/3.0$ is given by ROSEN *et al.*(1978). The justification for this particular value being that it is the density where steepening of the profile begins (KRUER, 1979). This point is also

discussed by TURNER and GOLDMAN (1980), who reason that, as the convective amplification of the ion acoustic wave is proportional to ω_{pi}, the region of reflection would be expected to occur at the highest density consistent with an unsteepened density gradient.

A value of $n/n_c < 0.14$ was given by RIPIN (1977), who monitored the backscattered signal whilst varying the angle of incidence θ, thus probing the underdense plasma as the electromagnetic penetration depth was reduced. The backscattered signal was found to remain high to within 8° of grazing incidence giving a minimum density for the SBS process from the usual expression $n_t = n_c \cos^2\theta$. Certain features of this experiment should, however, be noted. First, a prepulse was applied ahead of the main laser pulse with the corresponding changes to the backscatter parameters described by the author. Secondly, the probing technique has the serious disadvantage that the scale length (along the ray path) increases with increasing angle of incidence (for planar geometry), thus enhancing the backscatter. Also the irradiance is very much reduced at large angles of incidence due to the obliquity factor. The backscatter is, therefore, not studied for constant irradiation geometry. This point will be further discussed in the next section. A density position of $0.85\, n_c$ was estimated by GARBAN *et al.* (1978), in a CO_2-laser interaction experiment, where a polyethylene target was illuminated with 10.59 micron radiation. The observed position of the red sideband for $I_0 = 10^{12}$ W/cm^2 was 36 Å to the red of the incident wavelength λ_0. The density position was then obtained by taking an electron temperature of 300 eV (from previous X-ray transmission experiments) and substituting into an equivalent form of equation (6.4). Thus, no account of the Doppler contribution was taken, explaining the large value of the electron density needed to explain the experimental shift. The Doppler effect was also not considered in the experiments of GOLDMAN *et al.* (1973), where red shifts from 2—6 Å of the peak of the backscattered spectrum were seen, in a Nd-glass laser

interaction with LiD and D_2 targets at $< 10^{16}$ W/cm^2. These shifts were accounted for by assuming an electron temperature of 1 keV and electron densities of $0.98-0.90\ n_c$.

6.5 DETERMINATION OF THE DOPPLER SHIFT

Figures 6.14(a) and (b) show raw backscatter spectra taken for two values of θ, using the detector array. It can be seen from these oscillograms that the centroid of the distribution moves to longer wavelengths as the angle of incidence is increased (and hence the Doppler contribution is decreased). This effect is also reported by RIPIN (1977) and ROSEN *et al.* (1978). An experiment was thus performed, recording the backscattered spectrum on a single shot for various angles of incidence. The centroid shift from the reference channel, $\Delta\lambda$, was then plotted against $\cos\theta$, as shown in Fig. 6.15. The best fit line is drawn on this figure.

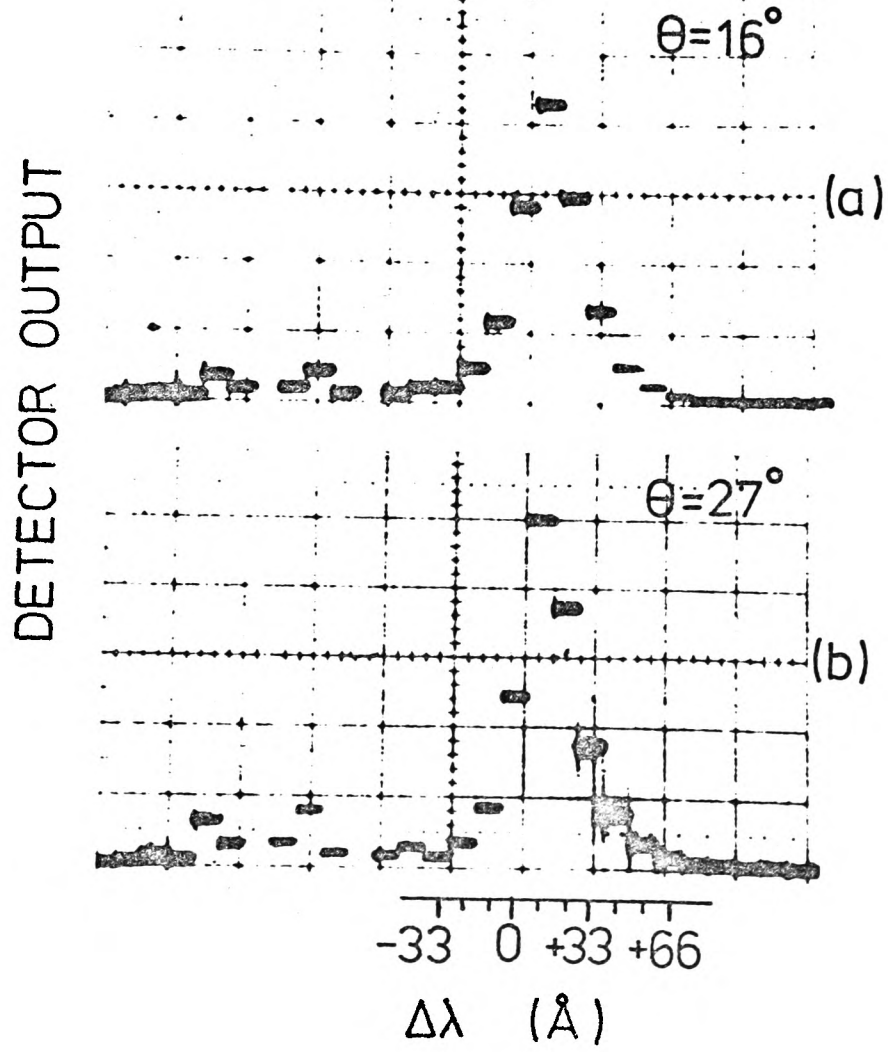


Fig. 6.14
Backscatter spectra as recorded with the detector array for angle of illumination, (a) $\theta = 16^\circ$, (b) $\theta = 27^\circ$

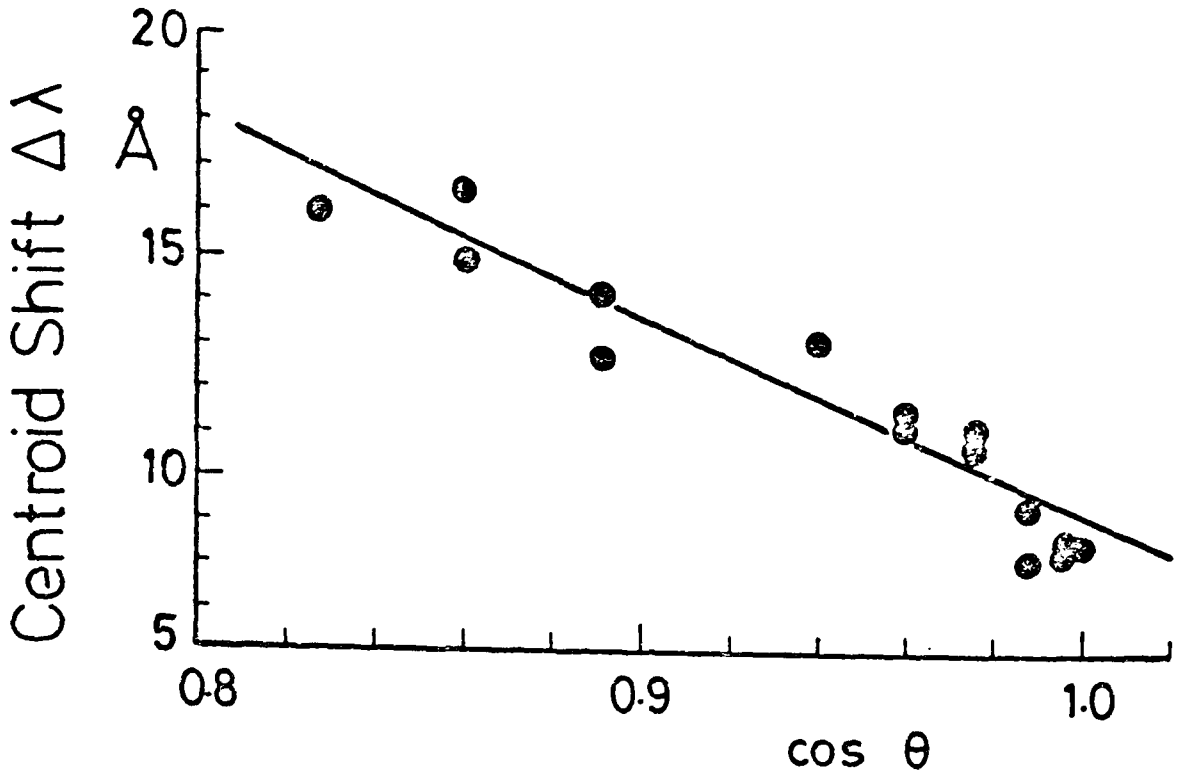


Fig. 6.15

Plot of the shift of the centroid of the backscattered spectrum (as measured with the linear array), with the angle of illumination. The shift $\Delta\lambda$ is measured relative to the channel of the incident spectrum and is plotted as a function of $\cos\theta$. The linear relation is expected from equation (6.3) and the regressional fit to the data is shown as the solid line. The gradient of this line gives a Doppler shift of 45 Å and the intercept at $\cos\theta = 0.0$, a pure Brillouin shift $\Delta\lambda_{SBS}$ of 54 Å. This value is not expected to be accurate, however, for the reasons given in the text

The measured gradient of this line gives a Doppler shift of 45 Å from equation (6.3). Using equation (6.5) gives us an expansion velocity $u = 8 \times 10^6$ cm/s, for a refractive index calculated at $n/n_c = 0.4$. It can be seen that, according to equation (6.3), the intercept of the best fit line in Fig. 6.15, would give the Brillouin shift $\Delta\lambda_{SBS}$. However, it must be remembered that the relative red shift with angle of incidence, represented by the gradient of the line in Fig. 6.15, would be unaffected by the finite resolution of the system, but not the absolute magnitude of this shift. For this reason, therefore, only the gradient was thought to be an accurate result and an absolute magnitude for the red shift was obtained with the higher resolution, single element detector experiment.

The comments made in section 6.4.1, concerning constancy of irradiation conditions and the angle of incidence is changed also, apply, of course,

to the use of such a technique to determine the Doppler component of the backscattered spectrum. However, the maximum angle of incidence for which data was recorded was 34° with a corresponding irradiance at focus of $I_0(0) \cos\theta = 0.8\, I_0(0)$, where $I_0(0)$ is the irradiance at normal incidence. The routine of the previous section indicates that the position of maximum growth would be relatively insensitive to such an irradiance change and as the turning density for $\theta = 34^\circ$ is $\sim 0.7\, n_c$, it seems unlikely that the position of the SBS process will be greatly affected by angles of incidence variations $\leqslant 34^\circ$. Although we might expect such a technique to alter the *level* of backscatter, therefore, it seems reasonable to assume that the spectral content will not be greatly affected. We can further expand this point by stating that we do not expect the electron temperature, ionization state or expansion velocity to be greatly affected either, as the target is angled from normal illumination. Similar comments are made by ROSEN *et al.* (1978) where backscatter spectral measurements for a gold target irradiated with 1.06 micron radiation at intensities between 7.0×10^{13} and 3.0×10^{15} W/cm^2 are described. In order to determine the Doppler shift, spectra were recorded at two angles of incidence, 0° and 45°.

Finally, the best way of justifying the procedure, perhaps, is to note in Fig. 6.15 that the results for experiments at 9 angles of incidence fit a linear plot well, as would be expected for no variation of parameters other than the contribution of expansion velocity along the backscatter direction.

6.6 INTERPRETATION OF SPECTRA

6.6.1 *ORIGIN OF RED SHIFTED SIDEBAND*

Assuming an electron temperature (cold) of 300 eV (as measured from the slope of the bremsstrahlung continuum) we calculate an ion sound speed c_s of 1.2×10^7 cm/s. In this calculation we have assumed that the carbon

ions are fully ionized ($Z = 6$). On the basis of a coronal equilibrium model, (SHEARER and BARNES, 1971), an electron temperature of 300 eV will produce a nearly fully ionized plasma. It should also be noted, that even when a time dependent model is used, fully stripped states are reached after ~10 ns. for $n/n_c = 0.4$ (TONON and RABEAU, 1973). Substituting c_s into equation (6.4) and combining the resulting value of $\Delta\lambda_{SBS}$ with the measured Doppler shift of 45 Å, in equation (6.3), gives us a predicted shift of ~20 Å. We note that this is in good agreement with the 24 Å shift measured for the sideband of the spectrum shown in Fig. 6.5. This seems to confirm that the sideband results from the Brillouin shifted radiation.

6.6.2 *RED SHIFT OF MAIN PEAK*

Figure 6.15 shows the backscattered spectra for five positions of the target relative to the optimum focus. The curves represent a best fit to the data points, and all show a peak shifted by 7.5 Å ± 3.3 Å to the red. All are broadened compared to the incident spectrum of Fig. 6.4(a). Only the curve at best focus exhibits the red shifted sideband. The magnitude of the peak drops sharply as the target is moved out of focus. It is therefore, very likely that this peak represents the specular component of the backscattered radiation. The variation in position of the peak of 3 Å is less than the resolution of the system and is unlikely to be significant. However, the fact that all curves are consistently shifted to the red by an amount approximately equal to the resolution, leads to the conclusion that this shift is not due to inaccurate calibration. (The incident spectrum was remeasured at the end of the run and found to be unchanged.) If we assume that the peak is due to specular processes from the critical surface, then the only mechanism capable of producing a wavelength shift is the Doppler effect, A red shift of 7.5 Å would be produced by critical surface motion, in the direction of the incident laser beam, of approximately 2.0×10^6 cm/s. Such inward motion might indeed be expected at some stage during a long

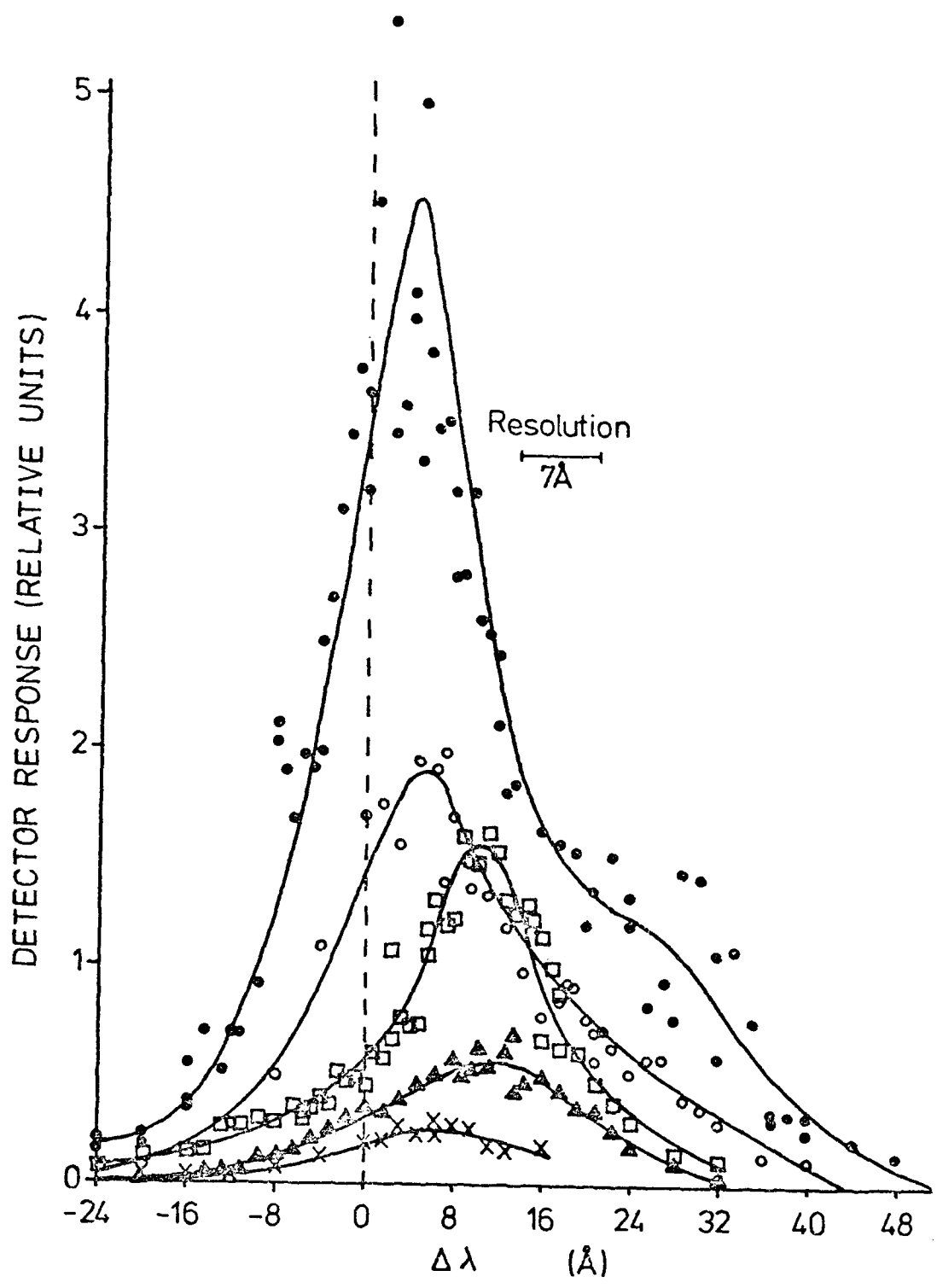


Fig. 6.16

Backscattered spectra as recorded over many shots using the single element detector, as a function of target position relative to the lens focus. The full circles are data points obtained for the target at optimum focus (i.e. as presented in Fig. 6.5). The open circles, open squares, closed triangles and crosses are data for relative target positions of 1 mm, 2 mm, 4 mm and 6 mm towards the lens, respectively, from the optimum position

pulse interaction, and would be manifest in time integrated spectra. Inward motion of the critical surface has been seen in 2-D computer simulations and is also discussed by KRUER (1975) in relation to the limitation of Brillouin scattering in plasmas by momentum and energy deposition, as a result of the reflection.

It is interesting to observe that for the mode beating process described in section 3.2, to *pump* stimulated Brillouin backscatter at a density of $0.4\,n_c$, the velocity of the critical surface must be given by.

$$M - M_c = \sqrt{1 - 0.4} \qquad (6.11)$$

where M is the Mach number of the plasma; experimentally determined to be 0.67. (From $u = 8 \times 10^6$ cm/s, and $c_s = 1.2 \times 10^7$ cm/s — see sections 6.5 and 6.6.1 above.) M_c is the Mach number of the critical surface. From equation (6.11) we obtain a value for M_c of -0.108, i.e. a critical surface velocity, V_c, of 1.3×10^6 cm/s in the direction of the incident laser radiation. Such a velocity would give rise to a red shift in the backscattered radiation of $\Delta\lambda_c$ given by:

$$\Delta\lambda_c = \frac{2\lambda_0}{c} \cdot V_c \,.$$

For $\lambda_0 = 10.59\,\mu$m, $\Delta\lambda_c$ is ~ 9 Å which compares well with the 7.5 Å measured in the experiments.

Inward motion of the critical surface has also previously been proposed by BÜCHL *et al.* (1972), and JANNITTI *et al.* (1975). The previously mentioned experiment performed by GARBAN *et al.* (1978), as well as measuring a red shifted sideband, also showed the peak of the spectrum to be slightly shifted to the red. The authors do not comment on this effect, however.

6.6.3 *DETERMINATION OF THE COLD ELECTRON TEMPERATURE*

We can alternatively interpret the results by using the measured value of the Doppler shift and the position of the sideband shown in Fig. 6.5, to give a value for the true Brillouin shift $\Delta\lambda_{SBS}$. This value

used in equation (6.4) to find the electron temperature through the ion sound speed c_s. From equation (6.4) and the expression for c_s we obtain

$$k_B T_e = \frac{\Delta\lambda_{SBS}^2}{4(Z/A\, m_p)\,\lambda_0^2} \cdot \frac{c^2}{(1-n/n_c)}$$

which can be rewritten as :

$$T_e\,(\mathrm{eV}) = 0.02 \cdot \left(\frac{A}{Z}\right) \cdot \frac{\Delta\lambda_{SBS}(\text{Å})}{(1-n/n_c)} \qquad (6.12)$$

for $\lambda_0 = 10.59\,\mu$m. T_e is plotted versus n/n_c for $\Delta\lambda_{SBS} = 69$ Å (24 Å observed plus Doppler reduction of 45 Å) and $A/Z = 2$, in Fig. 6.17.

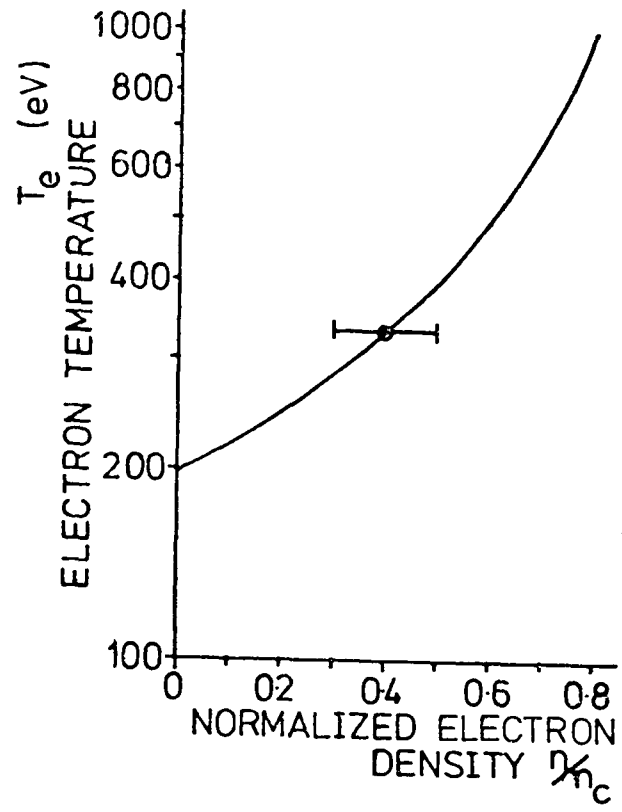


Fig. 6.17
Variation of electron temperature with normalized electron density as predicted by equation (6.12). The point on the curve represents the electron density at which the model predicts occurrence of the SBS process (section 6.4.1). The error bars on the point represent the variation of this prediction as the model parameters vary

Setting $n/n_c = 0.4 \pm 0.1$ from section 6.4.1, an electron temperature between 280 and 400 eV is obtained by this procedure. The significance of this result is that it is a temperature in the underdense plasma (the X-ray technique being spatially integrated over the whole plasma volume). When obtaining the electron temperature from the SBS shift in this way it should be remembered that the optimum value for n/n_c, as derived in section 6.4.1, is used under the assumption that there is a direct correlation between the position of maximum growth and the peak of the backscattered spectrum. This would, in general, be true only if the saturation mechanisms of the SBS process also peaked in the same region as the growth. This criticism could, of course, also be applied to the method of calculating the backscattered spectrum employed by Soviet authors (GORBUNOV and POLYANICHEV, 1979) which was briefly dscribed in section 6.4.

CHAPTER 7

ABSORPTION AND SCATTERING THEORY – COMPARISON WITH EXPERIMENT

7.1 INTRODUCTION

The earliest, and most persistent, phenomenon which was observed in the experiments was the extremely low level of scatter from the laser produced plasma. This led us to infer that the total absorption was very high. We now treat this particular aspect, and initially attempt to estimate the expected total absorption using a combination of classical model and associated anomalous effects. This will then lead into a discussion of the expected scattering level in order to ensure that this is consistent with the absorption estimates.

7.2 ABSORPTION PROCESSES

7.2.1 *CLASSICAL ABSORPTION*

Although we would not expect to entirely account for total absorption of $>85\%$ by means of the classical collisional theory, the fractional absorption that can be attributed to such a mechanism is an important and interesting parameter.

For fixed wavelength radiation incident on a plasma of known ion species and ionization level, the inverse bremsstrahlung absorption coefficient is a function of the background (or *cold*) electron temperature and the density profile and scale height. If we consider, however, that the cold electron temperature is set both by classical absorption and by heat conduction, it becomes obvious that the problem must be treated self consistently for a sensible estimate of the collisionally absorbed fraction. Such a self regulating model would then give us a consistent set of parameters to compare with experiment. Aspects of this particular work were performed in collaboration with MONTES (1981) and have previously been described by MONTES *et al.* (1980).

The fractional absorption f_a of incident radiation by inverse bremsstrahlung on the cold electron distribution, is given by:

$$f_a = 1 - \exp\,(-K_T) \tag{7.1}$$

where K_T is the integral along the light path (incident and reflected) of the absorption coefficient K. We take the expression for K given by Johnston and Dawson (JOHNSTON and DAWSON, 1973) as follows:

$$K = \frac{7.8 \times 10^{-9}\, Z\, n_e^2}{\nu^2 (k_B T_e)^{\frac{3}{2}}\, \eta} \cdot \ell n\, \Lambda(\nu)$$

where ν is the incident wave frequency, $\ell n\, \Lambda(\nu)$ is the Coulomb logarithm and all other parameters have their usual meaning. ($k_B T_e$ is in electron-volts). For integration over a linear density profile given by

$$n_e(x) = n_c(1 - x/L)\,,$$

K_T becomes:

$$K_T \approx 1.85 \times 10^{-5}\, \frac{Z\, k_0^2\, L}{(k_B T_e)^{\frac{3}{2}}} \cdot \ell n\, \Lambda(\nu) \tag{7.2}$$

(for an exponential profile, $n_e = n_c\, e^{-x/L}$, the constant in equation (7.2) becomes 2.31×10^{-5}). k_0 is in μm^{-1}, the density scale length L is in μm and $k_B T_e$ is now in keV. The Coulomb term Λ was taken to be given by

$$\Lambda = \frac{v_t}{\omega_0} \cdot \frac{m\, v_t}{\hbar}$$

(v_t = electron thermal velocity), or, in units of equation (7.2),

$$\Lambda = \frac{5.07 \times 10^3}{k_0} \cdot k_B T_e$$

This expression remains applicable as long as $k_B T_e > 10$ eV. It is noted that for electron energies $> 13.6\, Z^2$ eV, a quantum mechanical evaluation of the absorption coefficient should strictly be made. To do this, the $\ell n\, \Lambda$ term in equation (7.2) is replaced by

$$\ell n \left(\frac{2}{\alpha}\right) - 0.5777$$

where $\alpha = \dfrac{\hbar\omega}{2\, k_B T_e}$

However, this expression differs only slightly from the classical value used in this work. It is also important to state that for irradiances considered here, i.e. $\sim 10^{12}$ W/cm^2, the nonlinear absorption coefficient does not need to be invoked, although we are approaching the regime where the electron quiver velocity v_q is beginning to become significant compared to the electron thermal velocity v_t, (for $T_e = 300$ eV, $v_q/v_t = 1$ at $I \approx 10^{13}$ W/cm^2 for 10.59 μm radiation).

We require a self consistent solution of equation (7.1) and thus require independent equations for the density scale length L, and the cold electron temperature $k_B T_e$. To satisfy the first of these requirements we use the simple expression for L (see, for example, ALLEN and ANDREWS, 1970), as follows:

$$L = c_s \tau \,. \tag{7.3}$$

Equation (7.3) is more usually used for short pulse length interactions where τ is the incident pulse length and the density scale length follows from simple hydrodynamic expansion at the ion sound speed, c_s. In our case we equate τ with the time up to which one-dimensional expansion is valid and require that $\tau \ll t$, where t is the pulse length. We thus suppose that after this time a steady state has been reached with a constant density scale length L. Evidence for this assumption comes from holographic interferometry of the plasma (KLER, 1980) where high contrast fringes are observed even for long probe pulse durations. Figure 7.1 shows an interferogram taken with a 30 ns ruby probe pulse (cf. main pulse length of 50 ns).

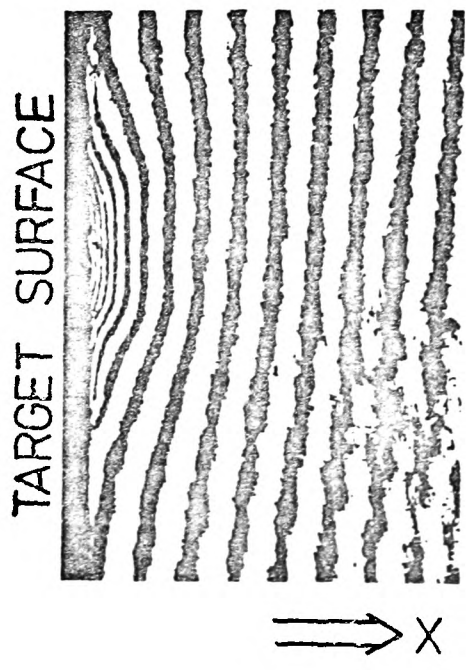


Fig. 7.1
Interferogram of plasma taken with 30 ns ruby laser probe pulse. The main CO_2 pulse is incident antiparallel to the X-axis. The target surface shadow can be clearly seen

We will take τ to be a free parameter in the model (within the restriction that $\tau \ll t$).

Substituting equation (7.3) into equation (7.2) and using

$$c_s = \left\{ \frac{Z\, k_B\, T_e}{A\, m_p} \right\}^{\frac{1}{2}}$$

($k_B T_e$ in joules)

we arrive at the following expression for K_T

$$K_T = 5.7 \times 10^{-3}\, \frac{Z(Z/A)^{\frac{1}{2}}}{k_B T_e}\, k_0^2\, \tau\, \ell n \left\{ \frac{5 \times 10^3}{k_0} \cdot k_B T_e \right\} \qquad (7.4)$$

where the units of equation (7.2) still hold, and τ is in ns. (For an exponential profile the factor 5.7×10^{-3} is replaced by 7.14×10^{-3}).

To obtain an expression for the cold electron temperature, we assume that the flux absorbed in the corona by the collisional absorption process, is carried away at the maximum rate given by the free streaming limit of classical heat conduction (BICKERTON, 1973). Furthermore, this free streaming limit is derived assuming that the electrons have a three dimensional Maxwellian distribution given by :

$$f(v) = \left\{ \frac{m_e}{2\pi\, k_B\, T_e} \right\}^{\frac{3}{2}} \exp \left\{ - \frac{m_e v^2}{2\, k_B\, T_e} \right\} \qquad (7.5)$$

where $v^2 = v_x^2 + v_y^2 + v_z^2$, and we consider transport across the whole surface of a hemisphere. We thus evaluate the integral

$$q = \int_0^{\infty} \int_0^{\pi/2} \int_0^{2\pi} \frac{m v^2}{2} \cdot \boldsymbol{v} \cdot \hat{\boldsymbol{n}}\, f(v) \cdot v^2\, dv \sin\theta \cdot d\theta \cdot d\phi \qquad (7.6)$$

where q is the electron energy flux. For a hemisphere centred on the origin of the coordinate system of velocity space, $\boldsymbol{v} \cdot \hat{\boldsymbol{n}} = v$ and we obtain

$$q_{\text{TOTAL}} = 2\pi\, \frac{m_e}{2}\, n_e \int_0^{\infty} v^5\, f(v)\, dv$$

$$= 1.596\, n_e\, v_t\, k_B T_e$$

for the velocity distribution given by equation (7.5). This result is

essentially the same as the more generally used expression

$$q_{\text{TOTAL}} = \tfrac{3}{2}\, n\, v_t\ k_{\text{B}}\, T_e \qquad (7.7)$$

which results from a product of the mean particle kinetic energy $(\frac{3}{2}\, k_{\text{B}}\, T_e)$ with the average particle flux $(n\, v_t)$. For convenience we use equation (7.7) in this work and note that we have, in effect, used an expression that maximizes the heat loss from a finite plasma. This is because equation (7.6) represents the maximum heat conduction into three dimensions, i.e. the free streaming limit. The expression is within the limit of the Fourier law of conduction,

$$q = -K\nabla T \quad \text{where} \quad \nabla T \sim T_e/\lambda_e$$

and λ_e is the electron mean free path, because the conduction is determined by the temperature gradient and the treatment is, therefore, self consistent.

Putting equation (7.7) into a form which is compatible with the parameters and units of equation (7.4), and setting the electron energy flux at the critical surface thus given by equation (7.7), equal to that fraction of the incident laser flux which is absorbed collisionally in the corona, we finally arrive at the expression

$$f_a\, I_0 \approx 8.97 \times 10^{12}\, k_0^2\, (k_{\text{B}}\, T_e)^{\frac{3}{2}} \ . \qquad (7.8)$$

We note that the electron density in equation (7.7) has been equated to the critical density to derive equation (7.8) because for the steady state, the flux of absorbed laser energy into the corona can be considered equal to the flux through the critical surface into the over-dense region. We also note that radiation losses from the thermal plasma have been neglected in the energy balance equation. Such losses occur at late times, after the initial absorption, and can thus be regarded as a cooling process not influencing the temperature T_e which we calculate.

Finally, we have assumed that thermalization of the hot electron distribution (measured experimentally (KLER, 1980) to be characterized by a

temperature of $1-2\,\mathrm{keV}$), has a negligible effect on the cold electron temperature. We thus consider the *hot* and *cold* components to be decoupled in the model. The magnitude of the mean free path of a hot electron in an underdense CO_2-laser generated plasma, justifies this assumption. In particular, the mean free path λ_e of a $1.5\,\mathrm{keV}$ electron ($1.5\,\mathrm{keV}$ being the mean kinetic energy of a $1\,\mathrm{keV}$ temperature distribution) can be found from the following expression (HAINES, 1979) :

$$\lambda_e = \frac{m_e^2}{Z \cdot 4\pi e^4 \ln\Lambda} \cdot \frac{v_t^4}{n_e} \qquad (7.9)$$

(cgs units)

For $n_e = n_c$, $\lambda_e = 100\,\mu\mathrm{m}$ for a carbon plasma, i.e. even at the critical surface, the mean free path is comparable to the typical density scale length. We would not, therefore, expect thermalization to occur in the coronal region of the plasma, but that the fast electrons cross the corona without imparting appreciable energy to the background cold electrons, by collisions.

Substituting equation (7.1) into equation (7.8) we arrive at an implicit expression for the cold electron temperature :

$$(k_B T_e)^{\frac{3}{2}} \approx \frac{I_0}{8.97 \times 10^{12}\ k_0^2} \left[1 - \exp\left(-K_T\right)\right] \qquad (7.10)$$

where T_e is now a function of the incident irradiance I_0, the radiation wavelength $2\pi/k_0$, the charge state Z and τ. For a self consistent solution for the cold electron temperature therefore, we solve equations (7.10) and (7.4) for fixed τ, Z, A and λ_0. The resultant value of T_e is then substituted into equations (7.3) and (7.8) to give L and f_a. From this closed solution we can investigate the variation of fractional collisional absorption, cold electron temperature and density scale length with incident intensity I_0 and charge state Z.

Figures 7.2(a), (b) and (c) show these variations for a carbon plasma ($A = 12$) with $Z = 4$, 5 and 6 and the free parameter τ set to 2 ns.

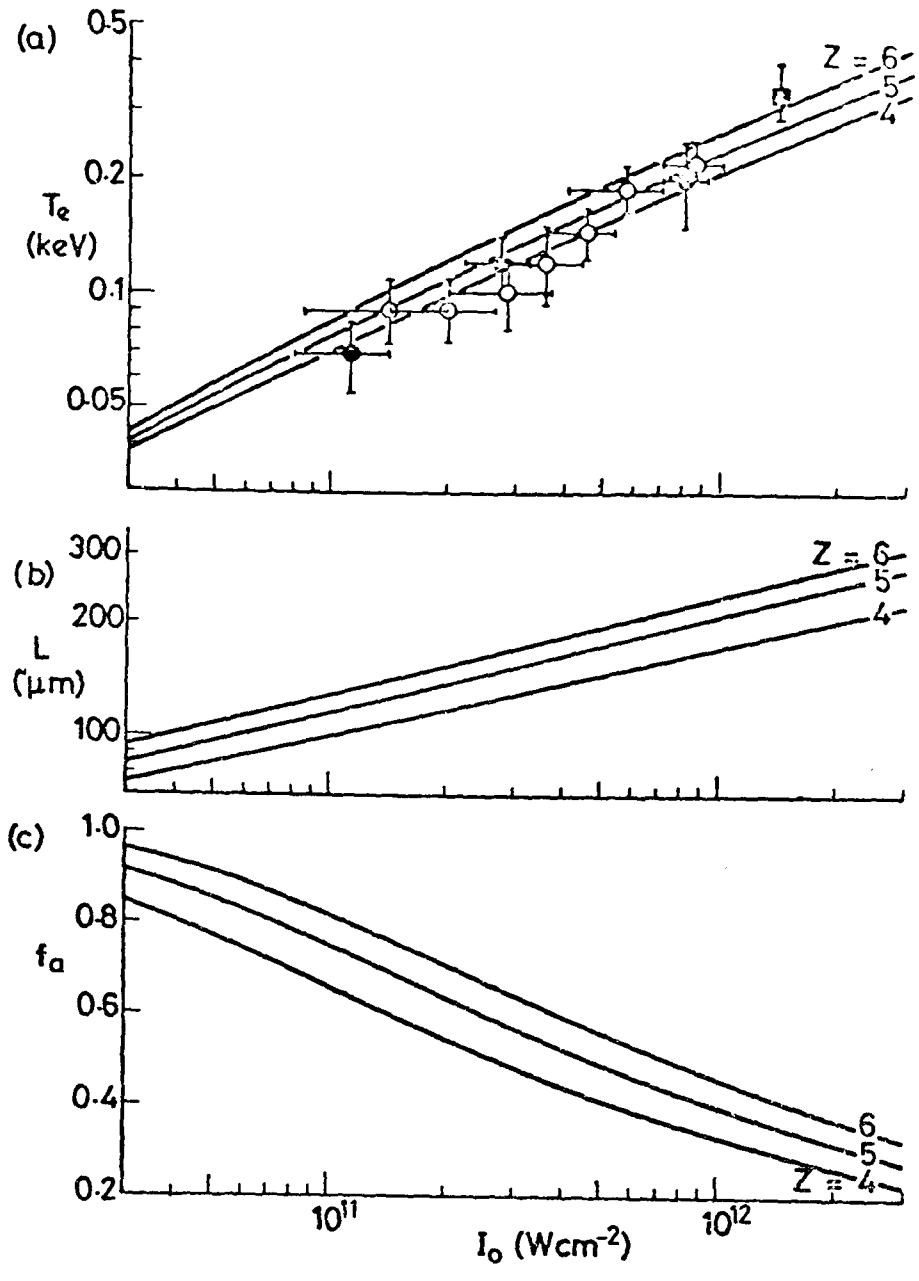


Fig. 7.2

Results of a simple model showing the variation of electron temperature (a), density scale length (b), and fractional absorption (c) with incident irradiance, for three values of the charge state Z. The solid square in (a) results from interpretation of the backscatter spectrum in terms of a Brillouin shift as described in Chapter 6. The open and closed circles result from X-ray transmission data (KLER, 1980)

This value of τ was found to give the best fit to the experimental values of the cold electron temperature, (which are also shown on Fig. 7.2(a)) and the density scale length.

The cold electron temperature as a function of irradiance was determined (KLER, 1980) from X-ray transmission data. This data was obtained at times throughout the pulse with a photomultiplier/scintillator combination having a temporal resolution of ~ 10 ns (open circles on Fig. 7.2 (a)) and also from time integrated data obtained by varying the target position relative to the focus (full circles on Fig. 7.2(a)). The full square on Fig. 7.2(a) is the cold electron temperature obtained from observation of the backscatter, as described in Chapter 6.

The simple model described above, therefore, predicts an electron temperature of around 300 eV, in good agreement with experiment. It is noted that this temperature was arrived at solely on the assumption of free streaming for the heat transport. No inhibition was introduced. It can

be shown that with the introduction of an inhibition factor α in equation (7.8); to account for transport reduction mechanisms such as self generated magnetic fields or ion acoustic turbulence (see KRUER, 1979(b)), for a discussion of these effects), the predicted temperature increases by a factor of $\alpha^{-0.45}$. Even for values of α much larger than theoretically predicted, therefore, (cf. $\alpha = 0.1$, from MANHEIMER and COLOMBANT, 1978), the model temperature would be larger than experimentally measured by an unacceptable amount. It would, of course, be possible to subsequently change the temperature back to its original value by a judicial change in the free parameter τ. Moreover, this procedure would have no effect on the final values for L and f_α, and so should be born in mind as a possible mechanism for introducing an inhibition factor into the model if required. However, because we have assumed τ to be a free parameter, no attempt was made to investigate conduction inhibition of the cold electron distribution in this way. It is also stressed that no such inhibition was necessary in order to account for the experimental results. We note that the possibility of flux limitation of the hot electron distribution is not precluded by these results, although theoretical work at LANSL (GITOMER and HENDERSON, 1979) has indicated that it does not need to be invoked to explain a wide range of currently available experimental data at 1.06 and 10.6 μm laser wavelengths.

Our simple model predicts a density scale length of ~ 200 μm for an incident irradiance of 10^{12} W/cm^2. This value agrees well with that measured using holographic interferometry (KLER, 1980). A typical profile is shown in Fig. 7.3, where x is the distance normal to the target surface.

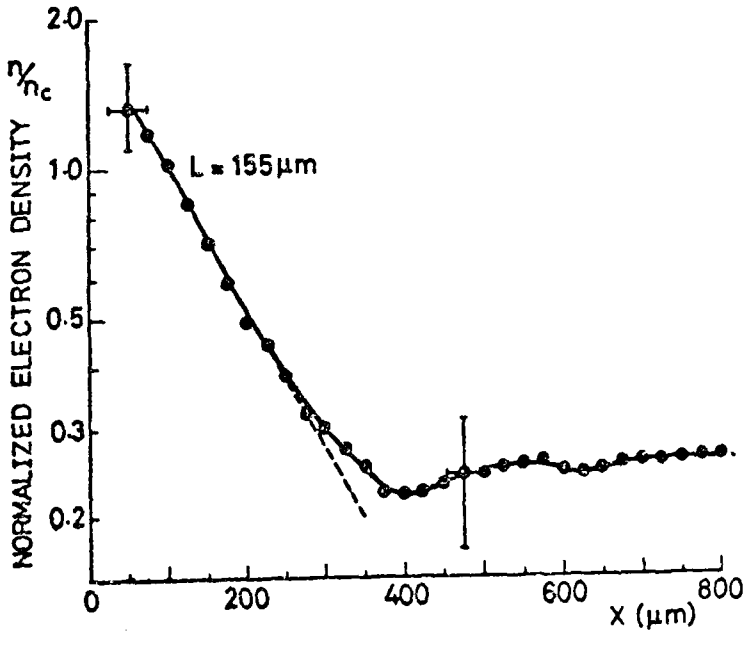


Fig. 7.3
Typical density profile as measured using holographic interferometry (KLER, 1980)

The calculated inverse bremsstrahlung absorption (~ 40%) although much lower than the absorption reported in chapters 3 (92%) and 4 (87%) is by no means a negligible contribution to that absorption. It is stressed that no other absorption processes have been considered so far. (It is also noted that the model has implicitly assumed planar plasma profiles and we would expect the inverse bremsstrahlung contribution to be higher for non-planar geometry where the ray paths in the corona would be longer.) Although these anomalous processes may preferentially heat the high energy tail of the distribution (with the exception of the ion acoustic turbulence discussed by Manheimer (MANHEIMER and COLOMBANT, 1978)) thus having a small effect on T_{COLD}, the effect on the overall absorption may be large and needs to be considered.

7.2.2 *RESONANCE ABSORPTION IN NON-PLANAR PLASMAS*

The ray tracing routine described in Chapter 5, was modified in order that the contribution to the total absorption due to the resonance absorption process could be estimated. In particular, the use of a ray tracing method enabled the absorption to be estimated in plasmas with density contours that were non-planar.

Non-planar geometries are indicated both experimentally and theoretically. In the present series of experiments, density cavities have been observed in holographic interferometric measurements (DONALDSON and SPALDING, 1976) whilst X-ray filamentation has been seen in time integrated and time resolved studies with a pinhole camera (DONALDSON *et al*, 1977). Other groups, too, have observed filamentation in X-ray pinhole photographs of CO_2-laser produced plasmas (GREK *et al*, 1978; HAAS *et al*, 1976). The correlation between modulation of the density contours and filamentation is discussed by Thomson (THOMSON *et al*. 1978), and modulations of the critical surface have been observed in computer simulations (ESTABROOK, 1976; VALEO and ESTABROOK, 1975, and FORSLUND *et al*. 1977).

The modified ray tracing routine is described in Appendix A 4 and selected results are presented by MONTES and HUBBARD (1979). Absorptions of 30% or greater were calculated for *normal* illumination of non-planar profiles. In particular, resonance absorption on a rippled surface was found to be high for large amplitude, low frequency modulations subtending an average angle of illumination of 10° or more. Significant absorption also resulted from elliptical geometry, the absorption increasing as the profile became more spherical, and as the density scale length increased. For example for a density scale length of 200 μm, the absorption of 10.59 μm radiation was calculated to be 17.5% for a plasma with elliptical density contours having an eccentricity of 0.94. For eccentricity equal to unity, 30% absorption was found. Experimental evidence for a large contribution to the overall absorption by resonance absorption in a CO_2-laser-plasma interaction was provided by recent experiments at Palaiseau (GARBAN-LABAUNE *et al.* 1980) where polyester targets were irradiated with 1 ns pulses at $\sim 5 \times 10^{12}$ W/cm^2, and the total absorption measured with a Ullbricht sphere and backscatter pyroelectric joulemeters, Total absorptions of around 30% were observed for normal illumination of the target and the authors concluded that resonance absorption alone was responsible; the inverse bremsstrahlung contribution being calculated as $\leqslant 5\%$ for the short density scale length of the interaction (10 – 20 μm, deduced from the angle of optimum absorption for *p*-polarized incident irradiation). Non-planar isodensity contours were invoked to account for the high absorption at normal incidence.

7.2.3 *BRIEF REVIEW OF OTHER ABSORPTION RESULTS*

Many authors have recorded a backscatter level of less than 10% in laser-plasma interaction experiments (e.g. MARTINEAU *et al.* 1974; BALDIS *et al.* 1975; MITCHELL *et al.* 1975; DYER *et al.* 1976; GREK *et al.* 1977; FABRÉ *et al.* 1977). Before the use of the 2π collection technique described in Chapters 3 and 4 of this thesis, however, the sidescatter fraction had always

been inferred by fitting an angular distribution to the results from discrete detectors and then integrating under this distribution. In this manner, for example, MARTINEAU *et al.* (1975) deduced that 60−90% of incident 10.59 μm radiation was scattered into 2π steradian from irradiation of a solid deuterium target at 10^{12} W/cm^2. Similarly, BALDIS *et al.* (1975), reported a 30% total reflectivity from CH_2 targets irradiated with 10.59 μm radiation (2 ns pulses) at 3×10^{12} W/cm^2, using a single detector at 45° in addition to a backscatter monitor.

Although the use of discrete angular detectors is an important diagnostic, and the angular distribution can yield much information on plasma processes (for example, the observed asymmetries in the distribution which were attributed to polarization dependent scattering processes, PHILLION (1977)), an accurate estimate of the total scattered fraction requires an integrated measurement at shot time. Apart from the work described in this thesis, experiments elsewhere have subsequently employed a variety of sidescatter collection techniques. Work performed at Garching, for example, (VAN KESSEL *et al.* 1976; SIGEL, 1977) showed a rapid variation of total reflectivity with target focal position with a maximum reflection of around 50% at best focus. The experiments were performed with 30 ps and 5 ns Nd-laser pulses, irradiating copper and glass targets at normal incidence at a maximum irradiance of 10^{12} W/cm^2. The sidescatter fraction was accounted for using either an ellipsoidal reflector or a Ulbricht sphere. It was also noted that for a target tilted at 11° to the beam axis, a much lower total reflectivity was measured (25%) at best focus, and away from this best focus position, no reflected signal was recorded for long pulse irradiation.

COTTLES *et al.* (1977) also used an ellipsoidal mirror to collect the sidescatter and note a total reflectivity of 45 ± 5%, independent of irradiance above 10^{12} W/cm^2, for 1.6 ns, 10.6 μm CO_2-laser pulses focused

to a spot of ~ 80 μm diameter onto CH_2 and Au foils.

Experiments employing a box calorimeter (GUNN, 1976) have perhaps provided the most accurate estimates of the total reflectivity due to the nearly 4π steridian subtended by the instrument around the target. HAAS *et al.* (1977) report experiments where parylene and tungsten-glass targets were irradiated with 1.06 μm laser pulses at irradiances of $10^{13} - 10^{15}$ W/cm^2. The results indicated absorbed fractions varying between ~ 50% (parylene, 200 ps pulses, 3×10^{13} W/cm^2) and 30% (parylene, 200 ps pulses, 6×10^{14} W/cm^2). A box calorimeter was employed by MANES *et al.* (1977) to investigate the polarization and angular dependence of 1.06 μm absorption on $C_8 H_8$ disc targets. A clear signature of resonance absorption was observed when the absorption peaked at ~ 45% for *p*-polarized radiation incident at 20°.

Much higher absorption was measured by RIPIN *et al.* (1979) at NRL where a box calorimeter was used to record the sidescatter fraction from 1.06 μm irradiation of thin polystyrene or aluminium targets. 85 ± 10% absorption was recorded at 10^{13} W/cm^2 dropping to 53 ± 10% as the irradiance increased to 7×10^{14} W/cm^2. Similar results were recorded at Sandia (ANTHES *et al.* 1979), where irradiation of metallic targets with 1.064 μm 8 ns pulses resulted in measured total absorptions of 90% at 10^{13} W/cm^2, and 80% at 10^{14} W/cm^2. The measurements were performed using an integrating sphere. It was claimed that these results could be qualitatively explained on the basis of absorption by classical inverse bremsstrahlung alone.

7.2.4 *CONCLUDING DISCUSSION*

In this chapter so far, it has been shown that the inverse bremsstrahlung contribution to the total absorption for the experimental conditions of this work, could be as high as 40% (see section 7.2.1). The contribution of resonance absorption has also been estimated (section 7.2.2) at 30% or greater, for non-planar plasma geometries. Thus we are approaching the point where we may claim agreement between observed and predicted total absorption

values, although there is still a small remaining discrepancy of the order of 10—20%. A small part of this discrepancy may result from the underestimate of losses around the entrance hole of the collecting mirror, as discussed in section 3.2.1. We also note that we have neglected other possible absorption processes which may well be expected to occur in the laser-produced-plasma. In particular, we mention the parametric absorption processes (e.g. the decay, or oscillating two stream, instability) and the possible absorption by ion acoustic turbulence (MANHEIMER and COLOMBANT, 1978). This latter mechanism is particularly interesting as it occurs in the underdense plasma and does not, therefore, compete with the resonance absorption process. However, this theory also predicts a possible flux inhibition factor of around 0.1. As was discussed earlier in this chapter, we do not believe that the results of this work are indicative of such an inhibition.

We conclude this section by stating that the high total absorption, as determined from independent estimates of the sidescatter, (2π-collecting mirror and calibrated burn paper) coupled with highly reproducible backscatter results, is in reasonable agreement both with simple models of possible plasma mechanisms and with the results of other workers (7.2.3).

7.3 BACKSCATTER

7.3.1 *INTRODUCTION*

In order to complement the absorption estimates of the previous section, an estimation of the level of backscatter should be made. In particular we have discussed in Chapter 6, the spectral observations which lead to the belief that stimulated Brillouin scattering had a dominant effect on the backscatter spectrum. We must, therefore, ensure that given the measured plasma conditions, the predicted level of backscatter is small enough to be consistent with the measured high absorption.

7.3.2 *BACKSCATTER LEVEL (SATURATION BY ION HEATING)*

We use a method first developed by Kruer (see for example, KRUER, 1979c) whereby the Brillouin generated ion acoustic waves grow to a saturation level determined by ion heating. These waves then damp into the ion distribution, heating the tail and thus raising the ion temperature. This temperature is determined by a simple energy balance equation, whereby the fraction of the incident energy given to the ion-acoustic waves (as determined from the Manley-Rowe relation) is carried away, as rapidly as possible by the ions, at some velocity v. We thus write:

$$2r I_0 \cdot \frac{k_0 \eta c_s}{\omega_0} = n_p T_i v \qquad (7.11)$$

where $n_p = n_e/Z$, r is the backscattered fraction, and all other quantities have their usual meaning. Kruer sets v equal to the ion thermal velocity in his work, whereas, EVANS (1980) equates v to the plasma ablation velocity and assumes that the ablation is approximately sonic, thus setting v equal to the ion sound speed c_s. In our case we use the measured expansion velocity as the velocity with which energy is carried away from the scattering region and thus put v equal to 0.67 c_s (see sections 6.5 and 6.6.1).

For ion wave saturation due to ion heating, it can be shown (TANG, 1966) that the reflectivity is given by:

$$r(1-r) = \beta \left\{ \exp \left[X(1-r) - r \right] \right\} \qquad (7.12)$$

where β is the normalized thermal fluctuation level, i.e., the initial noise source, and X is the spatial gain e-folding length given by

$$X = \frac{1}{4} \frac{n_p}{n_c} k_0 L \left(\frac{v_q}{v_t} \right)^2 \left[\frac{\Gamma_a}{\omega_{ia}} \left(1 + \frac{3T_i}{ZT_e} \right) \left(1 - \frac{n_p}{n_c} \right) \right]^{-1} \qquad (7.13)$$

where Γ_a, the Landau damping rate, is defined in Chapter 6 (equation (6.7)).

Solving equations (7.11) and (7.12) using a graphical method, the reflectivity was found as a function of electron density and β. Figure 7.4 shows the result for the parameters given in the figure caption. Thus

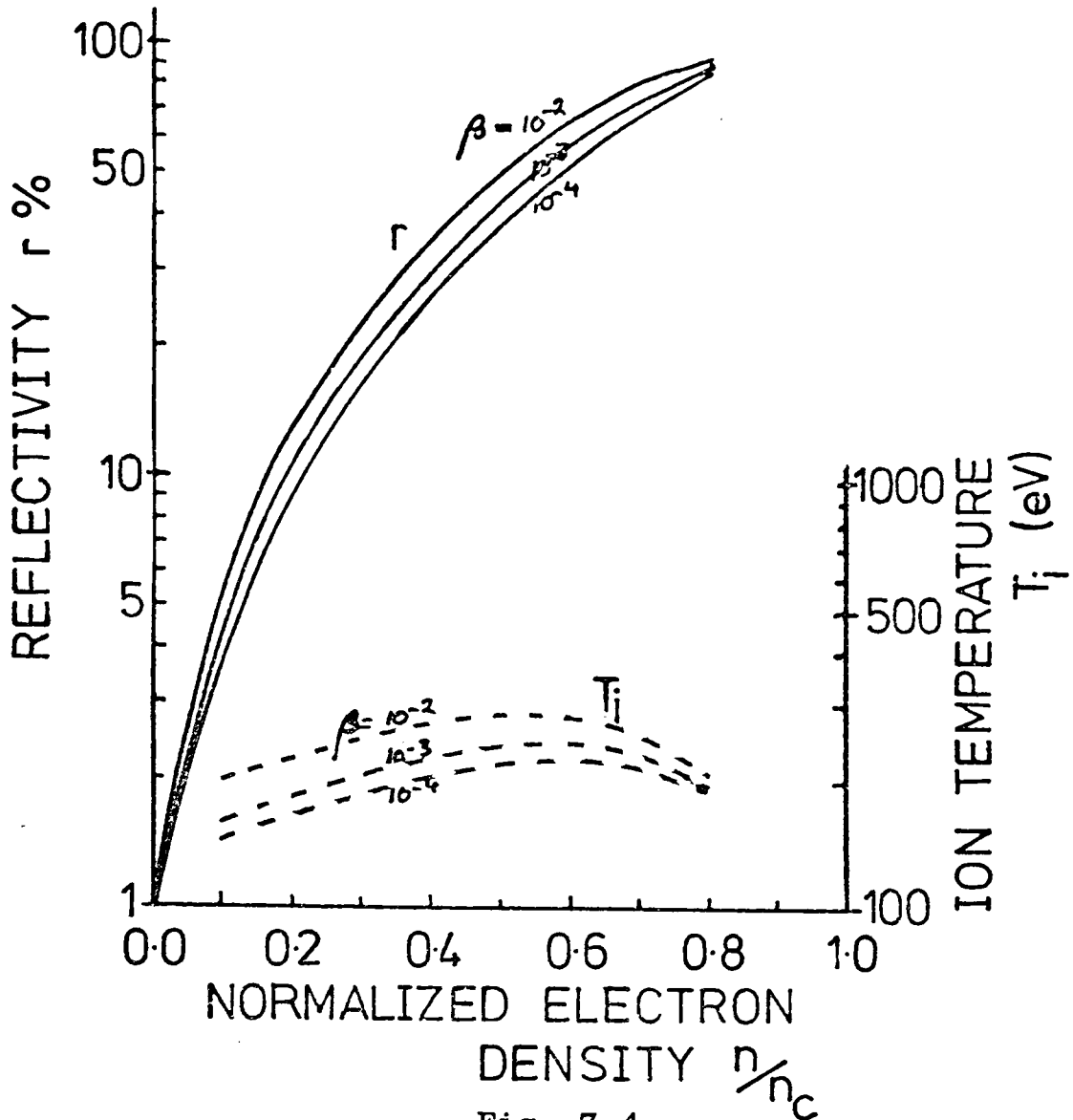


Fig. 7.4

Variation of stimulated Brillouin backscatter reflectivity as a function of electron density for three values of noise level β. The curves result from an ion heating model and the broken lines show the predicted variation of ion temperature with electron density for the same noise level values

at the densities of interest, i.e. $n/n_c = 0.3-0.5$ and over a range of noise levels β, the reflectivity is predicted to vary between 17% and 52%.

The reflectivity increases rapidly with density and weakly with noise level. For example the percentage change from $n/n_c = 0.3$ to $n/n_c = 0.5$ is ~ 120% (for β fixed at 10^{-2}) whereas for n/n_c fixed at 0.4, the reflectivity increases by only 30% as β increases by two orders of magnitude (from 10^{-4} to 10^{-2}). If we take a simple average over the density range of interest, therefore, and fix β at 10^{-4}, reflectivities less than 30% result. The effects of density gradient are, of course, important, and it is not clear whether one is justified in estimating the reflectivity by

taking an average over an extended spatial region. Earlier work indicates, however, that the spatial variation of ion acoustic wave growth rate is fairly broad (see Fig. 6.7) and thus such an average may not be unreasonable. This point is further discussed by KRUER and ESTABROOK (1980) who also point out that a spatially distributed noise source has to be assumed if we wish to consider an extended region. In the present calculations we have used β very much as a free parameter. It has also been assumed that specular reflection from the critical surface contributes to this noise level (see section 3.2). It was shown in section 3.2 that this specular contribution to β originated from mode beating between Doppler shifted incident and reflected light (the Doppler shift being introduced by the expanding plasma). For a plasma expansion velocity of 0.67 c_s (as deduced from spectral measurements — Chapter 6) we therefore calculate that the mode beating has a resonance at a density given by :

$$\sqrt{1-(n/n_c)_{\mathrm{RES}}} = M$$

where $M = 0.67$ in this case. Thus

$$(n/n_c)_{\mathrm{RES}} = 0.55.$$

Although this density is outside the predicted region of maximum growth, due to the finite width of the resonance we might still expect a contribution to the thermal noise level from the specular light. However, we would not expect a drastic increase in the backscattered reflectivity due to its predicted weak dependence on β, (however, note section 7.3.3). In calculating the resonance density for mode beating above, we have assumed that the critical surface has zero velocity. A fuller treatment should include the critical surface Mach number M_c thus giving

$$\sqrt{1-(n/n_c)_{\mathrm{RES}}} = M - M_c .$$

Thus, a suitable critical surface velocity would be capable of creating a resonance at the densities of optimum growth for the instability; such a motion was discussed in Chapter 6 (section 6.6.2).

Although Fig. 7.4 relates to a carbon plasma with an ionization state of $Z = 6$, the reflectivity is only very weakly dependent on Z (even though the final state ion temperature does vary). For example, for a carbon plasma with $Z = 4$ (and $\beta = 10^{-2}$) the model predicts a reflectivity of 24% and a final state ion temperature of 170 eV for $n/n_c = 0.3$ whereas for the same density but with $Z = 6$, the reflectivity remains almost the same at 23.5%, but the ion temperature has increased to 250 eV. Final state ion temperatures predicted by the model as a function of electron density are also shown in Fig. 7.4.

7.3.3 *BACKSCATTER LEVEL (SECONDARY DECAY INSTABILITIES)*

It is likely that the reflectivities predicted by the above simple model, represent an upper level due to the fact that we have neglected several other processes (in addition to the basic process of pump depletion) that can limit the total reflectivity. These additional processes act either by providing additional saturation mechanisms for the electrostatic wave or by re-absorption of the backscattered electromagnetic wave via further decay processes (KARTTUNEN and SALOMAA, 1979). In particular, the decay of the ion acoustic wave stimulated in the SBS process, into two new electrostatic modes, is shown by KARTTUNEN (1979) to be an efficient means of drastically reducing the reflectivity for sub-critical plasma densities. The effect is possible provided that $k^2 \lambda_D^2 \ll 1$ where k is the ion acoustic wave wave-number, and λ_D is the Debye length. This condition is necessary to ensure that we are in the linear regime of ion acoustic wave dispersion, so that phase matching can take place (FRANKLIN, 1977). For ion acoustic waves generated by SBS of 10.6 μm radiation, the condition can be written as

$$\frac{n}{n_c} \gg \left[1 + \frac{1.3 \times 10^5}{T_e(\mathrm{eV})}\right]^{-1} \qquad (7.14)$$

which holds for laser produced plasmas down to very low densities. The

upper limit of the reflectivity, r_∞, given by this process is obtained from the relation

$$\frac{n_c}{n} = 1 + \frac{1}{2}\left\{\frac{\ell n(2 + r_\infty/\beta)}{\ell n\left[\left(1 + r_\infty^{\frac{1}{2}}/(1 - r_\infty^{\frac{1}{2}})\right)\right]}\right\} \qquad (7.15)$$

which is plotted in Fig. 7.5 for various values of the noise level β.

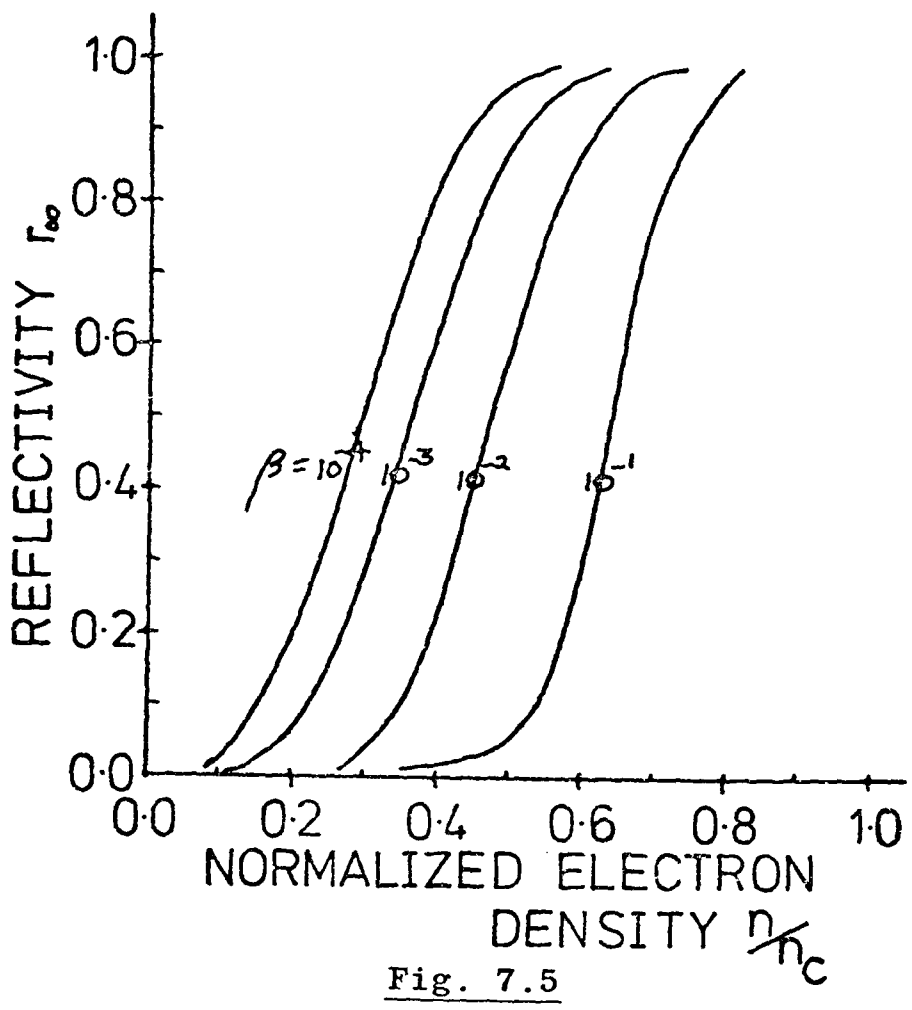


Fig. 7.5

Variation of reflectivity as a function of electron density for four values of noise level β. The curves result from a theory of secondary decay instabilities (after KARTTUNEN, 1979)

In contrast to the saturation mechanism of ion heating, it can be seen that the predicted reflectivity at a given electron density now *decreases* as the noise level increases. For example, for $\beta = 10^{-4}$, $r_\infty = 80\%$ at $n/n_c = 0.4$, whereas for $\beta = 10^{-1}$, $r_\infty = 2\%$! This drastic reduction in reflectivity for large noise levels is particularly interesting in view of our previous comments concerning the specular *pumping* of the SBS process. Large initial noise levels could now be tolerated because, although the reflectivity predicted by an ion heating theory would increase, the secondary decay process, having a much stronger β dependence, would act to keep the reflectivity to a low level. The competing nature of both processes

(and all the other saturation mechanisms) should ideally be treated in a self consistent way. However, the basic result that low reflectivities are permitted under conditions pertaining to the experiment is strongly indicated and is thus consistent with the absorption estimates of section 7.2, and with the experimental results.

CHAPTER 8

CONCLUDING DISCUSSION AND SUGGESTIONS FOR FUTURE WORK

8.1 INTRODUCTION

In Chapters 3, 4 and 6, the results of an experimental series performed to investigate the interaction of 10.6 μm laser radiation with the plasma produced by that radiation, have been presented. These experiments have centred around a study of the scattered radiation and its temporal, spatial and spectral characteristics. Although each particular observation has been discussed in the relevant section, a summary of the main conclusions is given here and ways in which the work could be continued are presented. All experiments were performed in the irradiance regime of 10^{12} W/cm^2 ; this value being determined after considerable effort to measure the far-field irradiance distribution (Chapter 2).

8.2 EXPERIMENTAL RESULTS

8.2.1 *SPATIAL DISTRIBUTION AND ABSOLUTE REFLECTIVITY OF THE SCATTERED RADIATION*

The first experiments which were performed were aimed at investigating the spatial structure of the backscattered radiation. A technique of aperturing annular portions of the back-reflected beam in order to build up an angular distribution was employed (Chapter 3) and the results revealed a non-isotropic distribution with a narrow spike at small backscatter angles and a side lobe at the periphery. The experiments were repeated many times and the possibility of the observed structure being an artifact of the experimental arrangement was checked, and dismissed. An explanation was presented which invoked non-uniform absorption across the focal region, non-uniform *pumping* of the stimulated Brillouin backscatter process, and the retro-reflecting nature of this parametric mechanism.

The absolute level of backscatter was found to be very low, but it was realized that, in order to correctly estimate the absorption, the side-

scattered fraction has to be taken into account. A collecting mirror technique was employed, therefore, and a total absorbed fraction of 92% was directly measured for the first time. The incident beam had a multi-mode structure and was focused by a 22cm focal length meniscus lens onto a massive carbon target. The experiments were later performed (Chapter 4) using the single transverse mode beam and a total fractional absorption of 87 ± 3% was found. This value was also confirmed using calibrated burn paper to record the sidescattered portion. A simple analytical model (Chapter 7) showed that classical inverse bremsstrahlung was an important contribution to the total absorption. Resonance absorption in a non-planar geometry was shown to account for the majority of the remainder, using a ray tracing method (Appendix A 4). The expected level of parametric back-scatter was found to be consistent with the experimental value given the uncertainty in the initial noise level from which the process originates. The difference between total absorption values for multimode and single mode (transverse) beams appeared to be manifest in the side-scattered fraction, the backscattered proportion being ~ 3% in both cases.

By performing experiments with tilted targets (with the multimode beam) the backscattered fraction was demonstrated to be dominated by perturbed constituents; a result which was later confirmed by spectroscopic analysis.

Careful measurements of the side-scattered distribution from tilted targets (single transverse mode irradiation) showed that even the expected specular component was not scattered into the specular direction; in all cases the angle of scatter being larger than the angle of incidence. In order to see whether this effect could be explained by coronal refraction in a non-planar geometry, a simple ray tracing routine was developed (Chapter 5) and convex, concave and rippled geometries studied for a large degree of parameter variation. It was found that coronal refraction would

not explain the observations but that the asymmetry might be introduced either by a curved critical surface contour of much larger dimension than the beam width, or by plasma expansion which was not parallel to the laser axis.

8.2.2 *TEMPORAL STRUCTURE OF THE BACKSCATTER*

The temporal behaviour of the backscattered pulses from multimode irradiation experiments showed an enhanced modulation of the inherent structure on the incident pulse. This effect was explained by considering that the reflection mechanism appeared as a nonlinear amplifier to the multimode pulse, thus increasing the contrast by suppression of the weakest modes.

The correlation between incident and reflected profiles was investigated using a single mode (transverse *and* longitudinal) pulse from an auxiliary laser which had smooth temporal behaviour. No structure was observed in the reflected envelope.

When the oscillator cavity of the APPLE laser was changed to permit single transverse mode lasing, parasitic oscillations were observed which were found to originate from the laser-produced plasma rather than from the target surface. It was concluded that the parasitics grew from parametrically scattered radiation and were enhanced as the target was tilted away from normal illumination.

8.2.3 *SPECTRAL ANALYSIS OF THE BACKSCATTER*

A grating monochromator system was set up which was capable of recording the backscattered spectrum on a single shot by using a pyroelectric detector array at the exit plane, or with higher resolution over a large number of shots using a single element detector. The backscattered spectrum showed considerable broadening from the incident shape in addition to a red sideband. This sideband was attributed to the stimulated Brillouin scattering process in the underdense plasma. The Doppler contribution to

the observed spectrum due to plasma expansion was determined by performing experiments with tilted targets. A Mach number of 0.67 was measured, and combining this with the spectral position of the Brillouin feature, an electron temperature of ~ 300 eV was estimated. In this estimate an electron density $n/n_e = 0.4$, was assumed; a value which had previously been obtained from numerical solution of the ion acoustic wave dispersion relation in order to find the density of maximum growth. The electron temperature value was in good agreement with that determined using an X-ray filter transmission method, and with the simple analytical model referred to earlier.

8.3 SUGGESTIONS FOR FUTURE WORK

In reviewing the work as a whole, the need to perform the experiments under more fully characterized conditions is indicated, for example, by the differences observed between results from multi-transverse mode and single transverse mode irradiation. It would, therefore, be particularly appropriate to re-perform the experiments with a laser giving a single transverse *and* longitudinal mode beam. Such a laser, OPALS , was under construction at Culham (STAMATAKIS, 1977) and the smooth temporal profile of the single mode output, coupled with enhanced focusability would provide an ideal device for a more fully specified series of experiments. (Also, the hybrid character of the device would enable diagnostic alignment to be performed with the CW CO_2 laser which lased within the same cavity as the main pulsed beam.)

Full use of a pyroelectric vidicon (mentioned briefly in Chapter 6) could also be made. In particular, near-field time-integrated back- and side-scatter distributions could be obtained on a single shot by imaging a diffuse scatterer (i.e. a matt gold screen) placed in the scattered beam lines. Similarly, the focal volume could be imaged directly, or a spectrograph employed to obtain spatially resolved spectral information by using the vidicon as a 2-D array at the exit plane.

The fact that no new type of measurement is suggested here is not meant to imply that a comprehensive series has already been carried out but rather that future emphasis should be placed on repeating the type of experiment reported in this thesis with a higher degree of characterization, such as would be provided by the use of a more highly quantified input beam, and more flexible diagnostics, such as by use of a pyroelectric vidicon.

APPENDIX A1

THE CO_2-LASER

A1.1 INTRODUCTION

The first demonstration of laser action in CO_2 gas by PATEL *et al.* (1964), led, as would be expected, to a dramatic increase in CO_2-laser research resulting in a corresponding increase in the output energy and the control of such parameters as pulse length and beam quality of the 10 micron beam. There exist many good reviews of the history of CO_2-laser development, in particular, the article by WOOD (1974) provides an excellent account of progress up until 1974. The many groups that still continue research into both theoretical and experimental aspects of CO_2-lasers indicate the importance that is attached to the production of a well characterized infared laser beam at 10 microns, in many fields besides that of laser fusion. Pulsed CO_2 lasers are used in chemistry research in spectroscopy and photochemistry, including isotopic enrichment. CW lasers have application to the cutting, drilling, and welding of metals, and to the fabrication and refurbishing of many other materials. In the field of medicine, CO_2 lasers are investigated for their application to surgery whilst high power pulsed and CW systems have direct military applications. CO_2 lasers are also used in atmospheric pollution monitoring and in optical communication systems.

A1.2 GENERAL THEORY

As with any laser system, the basis of CO_2-laser operation is the establishment of a population inversion; in this case between two energy levels in the CO_2 molecule. The two mechanisms for selective excitation of the upper laser levels are molecule – molecule vibrational-rotational excitation transfer, and the excitation by direct electron impact from the ground state. The former process relies on the fact that there is a

vibrational energy level coincidence in the N_2-CO_2 system between the first excited vibrational level of nitrogen $N_2^*(v=1)$, and the $00^01\ \Sigma_u^+$ vibrational-rotational level of carbon dioxide. The following process thus takes place.

$$N_2^*(v=1) + CO_2(00^00) \rightleftharpoons N_2(v=0) + CO_2(00^01) - \Delta E\,. \qquad \text{(A1.1)}$$

The excitation of the vibrational levels of nitrogen is considered to be due to the formation of a short-lived negatively charged compound as represented by the following processes,

$$\left.\begin{aligned} N_2 + e^- &\rightarrow N_2^- \\ N_2^- &\rightarrow N_2^* + e^- \end{aligned}\right\} \qquad \text{(A1.2)}$$

Since N_2 is a homonuclear diatomic molecule with no permanent dipole moment (thus forbidding radiative decay by selection rules) it is possible, considering also the large cross section of the excitation process, to see that a substantial population of $N_2^*(v=1)$ can be generated. The metastability of the N_2^* molecule to decay to the ground state also requires that the reaction represented by equation (A1.1) proceeds mainly in the forward direction.

The second excitation process, namely direct electron impact, can be represented as follows:

$$CO_2(00^00) + e^- \rightarrow CO_2(00^01) + e^-.$$

The probability of excitation of the 00^01 level is found to be greater than that of the 10^00 or 02^00 levels. However, it has also been shown that the 01^10 level can also be strongly excited. It is now generally accepted that formation of a CO_2^- negatively charged compound state (by a similar reaction to that represented by equation (A1.2)) is not required and that the excitation proceeds directly, at least for electrons with energy less than 3 eV.

Patel's first experiment to demonstrate laser action, used pure CO_2

gas as the lasing medium and thus the excitation process was by direct electron collision. However, he soon discovered that the addition of N_2 gas increased the output considerably (PATEL, 1964), and in this and subsequent work, resonant energy transfer between excited nitrogen molecules and ground state CO_2 molecules was the dominant process. Patel obtained laser action at seven wavelengths near 10.6 μm.

One final process that must be mentioned in any kinetic theory of CO_2 lasers is the relaxation of the lower laser level. Early in the development of CO_2 lasers, it was discovered (PATEL, 1965), that the addition of helium gas to the CO_2—N_2 mixture, significantly increased the output energy. It is now considered that collisions with helium molecules depopulate the metastable lower laser levels whilst essentially unaffecting the population in the $00^0 1$ state. Furthermore, the helium is considered to increase the excitation rate of the upper laser level as well as lowering the gas kinetic temperature of the mixture. Thus we have reached the situation where the lasing medium consists of a mixture of CO_2, N_2 and He. The optimum gas mixture has been investigated both experimentally and theoretically. In practice, the fine adjustments to the relative proportions of the gaseous constituents are usually made empirically.

The next section in this appendix, describes the mode of operation of the laser type used during this work, namely the Transversely Excited Atmospheric or TEA laser.

A1.3 THE TEA LASER

An important stage in the development of CO_2-lasers was the report by BEAULIEU (1970), that laser emission in CO_2 had been obtained at atmospheric pressure, and above, by means of a transverse excitation of the gaseous medium. In this configuration, the discharge was applied perpendicularly to the optic axis enabling the high voltages, usually required for gas breakdown at high pressures, to be substantially reduced, and gas volumes (and hence output energies) increased.

The tendency of the glow discharge to develop into an arc was inhibited by excitation pulses of length less than the arc formation time. Problems of discharge uniformity and the search for higher powers led to further research into an excitation geometry first reported by DUMANCHIN and ROCCA-SERRA (1969), namely, the 'double-discharge' configuration. In this method, the discharge gap is pre-ionized by an electron layer and ultraviolet radiation produced from the corona discharge, between trigger electrodes and the cathode. This pre-ionization of the gap initiates the main cathode-anode discharge in a very uniform manner, reducing not only the tendency of the system to form arcs, but also the effects of electrode surface irregularities. This method is the one employed in the APPLE laser of this work and is described in Chapter 1.

APPENDIX A2

DIAGNOSTIC ALIGNMENT

A2.1 INTRODUCTION

Alignment of the target chamber, targets, and all diagnostics was initially accomplished using beam-expanded He-Ne radiation co-axial with the main CO_2 beam. This was set up using a two mirror system, by directing it through a pinhole aperture onto a marker-point approximately 2 metres away. The aperture and marker point both defined the centre of the CO_2 beam as determined by the burn on exposed polaroid film. The alignment beam system is illustrated in Fig. A2.1.

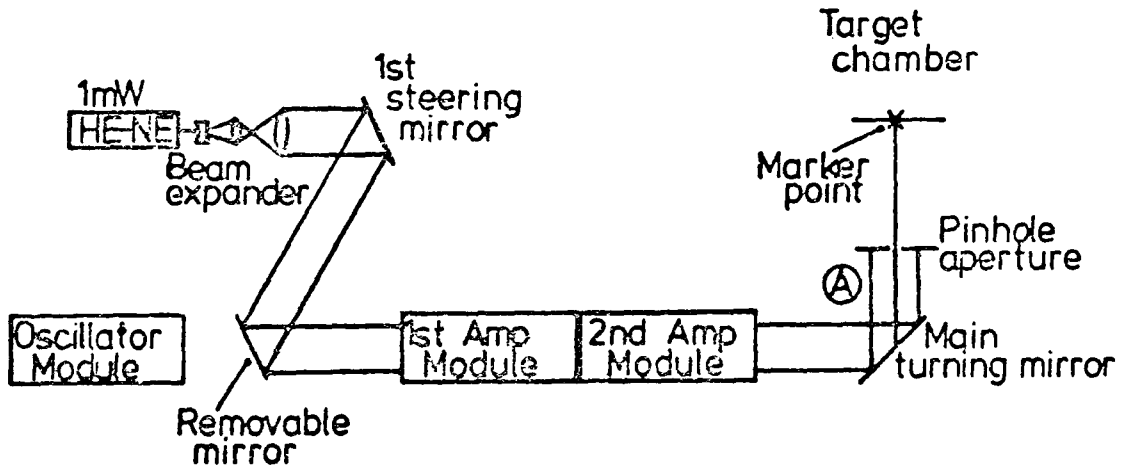


Fig. A2.1
Arrangement of the alignment He-Ne beam. Auxiliary He-Ne lasers were placed at position (A) as required, e.g. for alignment of the backscatter optics

The second steering mirror was made removable and accurately repositionable using a three point cone slot and plane mount. It could thus be easily inserted into the system whenever the alignment beam was required. In some applications, mainly the positioning of the backscatter optics, a more powerful alignment beam was required and this was achieved by placing a 3 mW or 5 mW He-Ne laser at position (A) in Fig. A2.1, and pointing it through two pinhole apertures that had previously been positioned using the first CW beam.

The diagnostics for the reflected beam were set up using a retro-reflected beam from a mirror positioned in front of the target chamber. This

mirror was adjusted until the reflected He-Ne beam returned through the pin-holes defining the centre of the CO_2 beam. This procedure was facilitated by the insertion of a diffracting mesh in the reflected beam so that the diffraction pattern provided an alignment aid.

A2.2 DETECTOR CALIBRATION

Two basic functions were required from the monitors used in this work. First, an absolute measure of the incident energy and pulse shape was required in order that the target irradiance could be calculated. Due to the fact that the irradiance is more strongly dependent on focal energy distributions than on absolute energy focused, the 10% accuracy (manufacture data) of the Gen-Tec® monitors did not present a serious problem. Of far more importance was the second requirement, namely that the *relative* sensitivity of the detectors was well known in order that accurate measurements of reflectivity could be made. Coupled with this requirement was the need to account for the effect of the various combinations of beam splitters, lenses and attenuators in each beam line. Thus, the two main calibration procedures were as follows:

(1) a comparison of the sensitivities of photon drag and Gen-Tec joulemeters, and

(2) a calibration of the beam lines.

The first procedure was carried out using the arrangement shown schematically in Fig. A2.2.

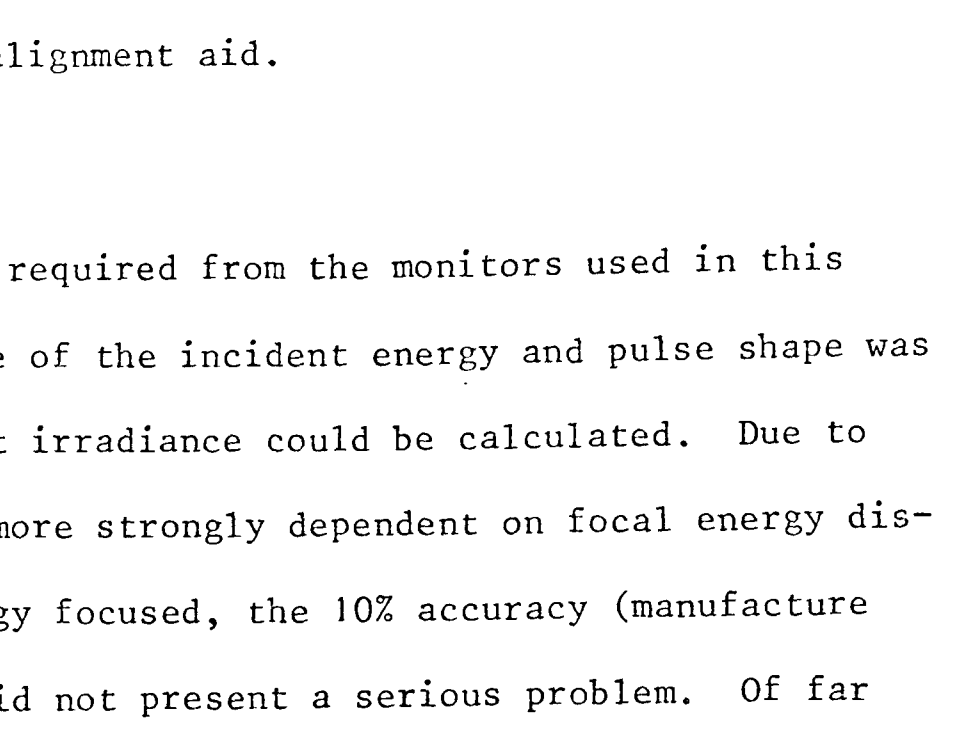


Fig. A2.2
Schematic of the arrangement for detector calibration

Both beam splitters were identical and were set up at the same angle relative to the incident beam. The effective attenuation of each arm was made the same by using identical combinations of focusing lenses and polyethylene attenuators. An attenuated incident beam from the oscillator alone was used in order that plasma formation on the mirror did not occur. This mirror was diamond turned in oxygen free copper and gold plated to give reflectivity approaching 100% for the 10 μm incident beam. The reduced energy in the incident beam also prevented damage to the laser chain via feedback through the first beam splitter. The amount of attenuation in beam line (A) was determined by that required to limit the signal to levels of similar order to that observed during the experiments, thus correcting for nonlinearity. Thus, each detector in beam lines (A) and (B) received identical fluxes. In this way the relative sensitivities of any two detectors were directly compared. By using a Gen-Tec® joulemeter for one detector, the absolute sensitivity of each photon drag detector was measured to within the accuracy of the Gen Tec® instrument, by integrating under the output pulse from the photon drag. It was found that all Gen Tec's® had the same sensitivity to within 3%. It was also found that the photon drag detector sensitivities agreed well with the manufactures data to within the accuracy of the Gen Tec® used in the calibration measurement.

Having measured the relative sensitivities of the monitors to be used during the experiments, the second requirement could be satisfied, namely the calibration of the various beam line geometries. This was accomplished by placing various combinations of beam splitters and attenuators in the beam lines (A) and (B), and recording the relative signals on Gen-Tec detectors.

APPENDIX A3

THE USE OF A 2-D DIFFRACTION ARRAY TO OBTAIN THE FAR FIELD INTENSITY DISTRIBUTION – THEORY

There are three main principles behind the techniques:

(1) The envelope distribution of the principal maxima of the pattern has a functional dependence directly related to the geometry of a diffracting element in the array.

(2) The intensity distribution of each principal maximum is a good approximation to the flux density distribution obtained in the absence of the grating.

(3) The geometry of the diffraction pattern is determined by the geometry of diffracting elements in the diffraction array.

These three principles are illustrated schematically in Fig. A3.1.

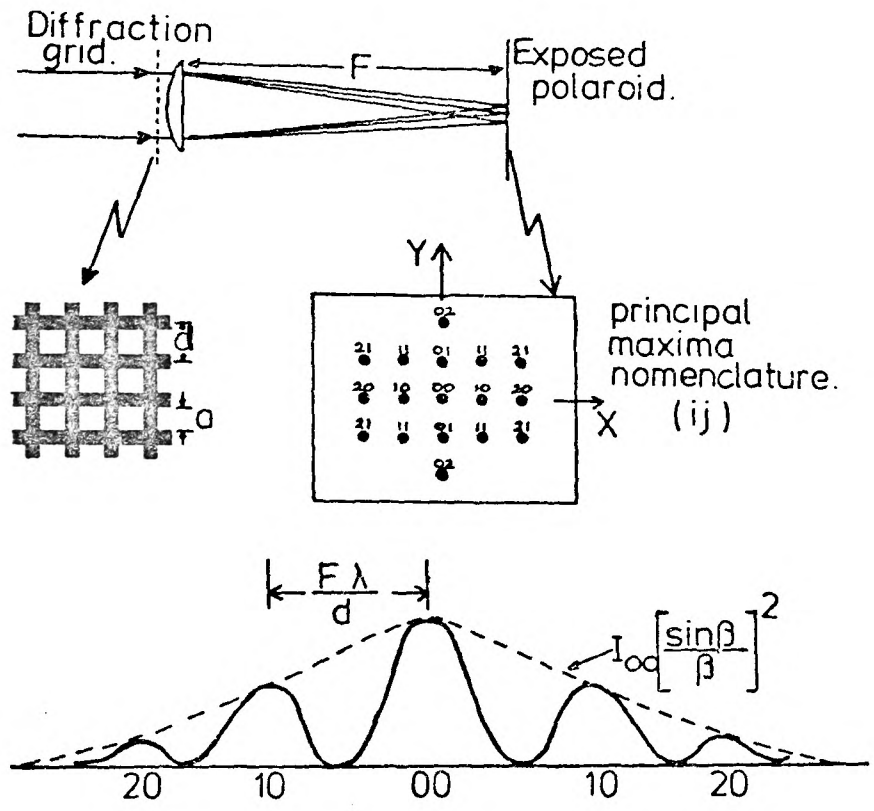


Fig. A3.1
Schematic, illustrating the principles of the diffraction grid technique for far-field intensity distribution determination, the definition of grid aperture, a, and pitch, d, are shown on the figure as are the grid geometry and diffraction pattern nomenclature

For an array of square diffracting elements arranged on a square lattice, the envelope distributions along the x and y axis of the diffraction pattern are as follows:

$$I_x = I_{00}\left(\frac{\sin\beta}{\beta}\right)^2 \quad \text{where} \quad \beta = \frac{\pi}{\lambda}\cdot\frac{x}{F}\cdot a$$

$$I_y = I_{00}\left(\frac{\sin\beta'}{\beta'}\right)^2 \quad \text{where} \quad \beta' = \frac{\pi}{\lambda}\cdot\frac{y}{F}\cdot a$$

where I_{00} is the peak intensity of the zeroth order. The principal maxima are located at the following positions along the x and y axis respectively,

$$x = i\,\frac{F\lambda}{d} \quad , \quad y = j\,\frac{F\lambda}{d}$$

(where (i, j) is the order of the particular maximum.) Thus, their intensities can be written:

$$\left.\begin{aligned} I_{i0} &= I_{00}\left\{\frac{\sin\gamma}{\gamma}\right\}^2 \quad \text{where} \quad \gamma = i\,\pi\frac{a}{d} \\ \text{and} \qquad & \\ I_{j0} &= I_{00}\left\{\frac{\sin\gamma'}{\gamma'}\right\}^2 \quad \text{where} \quad \gamma' = j\,\pi\frac{a}{d} \end{aligned}\right\}. \qquad \text{(A3.1)}$$

If we set I_{00} equal to unity, the following relations apply_

$$\left.\begin{aligned} I_{ij} &= I_{ji} \\ I_{ij} &= I_{0i} \times I_{0j} \\ I_{ii} &= I_{i0}^2 \\ I_{jj} &= I_{j0}^2 \end{aligned}\right\}. \qquad \text{(A3.2)}$$

Let the intensity distribution of the central spot in the diffraction pattern be written as follows

$$I(r) = I_{00}\,f(r)\,. \qquad \text{(A3.3)}$$

Let the damage threshold for the recording medium be I_t, then the radius of the central spot $= r_{00}^t$ where the situation is as shown in Fig. A3.2.

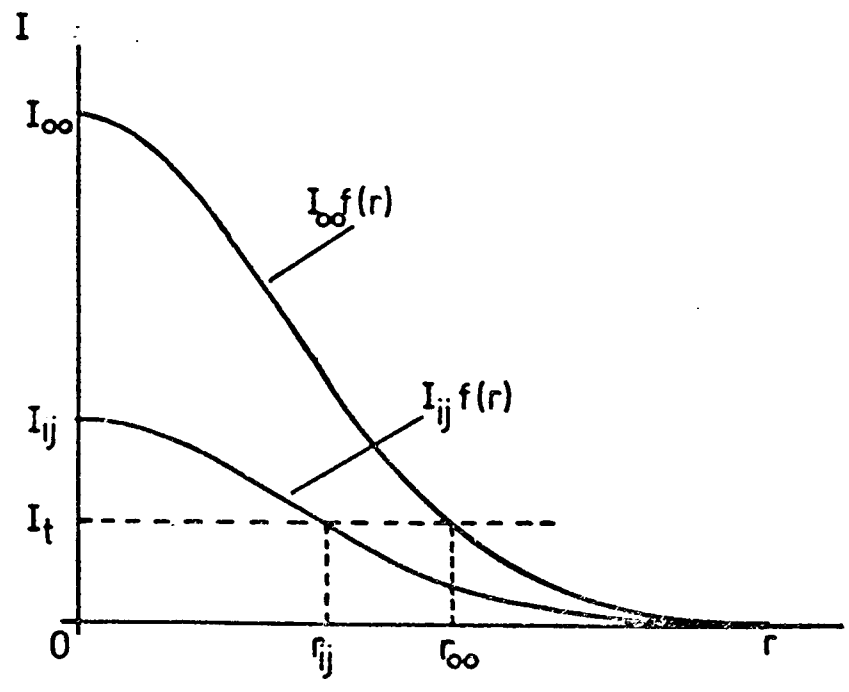


Fig. A3.2
Illustration of the relationship between the functional form of the intensity distribution of each diffraction order, and the burn spot radius on the recording medium

We can, therefore, write:

$$I(r_{00}^t) = I_{00}\,f(r_{00}^t) = I_t\,. \qquad \text{(A3.4)}$$

Similarly, the radius of the $(i,j)^{\text{th}}$ maximum will have a radius r^t_{ij} where

$$I(r^t_{ij}) = I_{ij}\ f(r^t_{ij}) = I_t\ . \qquad \text{(A3.5)}$$

Therefore, from (A3.4) and (A3.5),

$$f(r^t_{ij}) = \frac{I_{00}}{I_{ij}}\ \cdot f(r^t_{00}).$$

Thus, the height of the profile at a radius r^t_{ij} is a factor $\frac{1}{I_{ij}}$ greater that its height at r^t_{00}. Hence, by ascribing a value of unity to $f(r^t_{00})$, a *normalized* distribution can be drawn by plotting a point of height I_{00}/I_{ij} at radius r_{ij}. Values of I_{00}/I_{ij} are found from the diffraction grid parameter a/d, and by use of equations (A3.2) and (A3.3). Values of r_{ij} are found by microscopic analysis of the diffraction pattern burn.

APPENDIX A4

RESONANCE ABSORPTION IN NON-PLANAR PLASMAS

In the linear resonance absorption theory for plane-parallel plasmas, the absorption coefficient is an exclusive function of the distance from the turning point to the critical surface, d_t. This no longer holds for non-planar plasmas because we no longer know, *a priori*, how the tunnelling mechanism is affected by the geometry of the plasma in this region. However, because we use the WKB approximation we can assume, without introducing large errors, that the region between the turning point and the critical surface is well represented by a plane-parallel geometry. Thus the problem reduces again to a determination of d_t. We need, therefore, a method of finding d_t in non-planar plasmas and in our case this is accomplished by means of the ray tracing routine CUPID described in Chapter 5.

We use the ray tracing routine to determine the minimum value of the refractive index n_t obtained on the ray path. This effectively determines the distance from the turning point to the critical surface d_t. n_t is then used in the determination of the parameter τ, where τ is defined in the usual manner (GINZBURG, 1970) as follows :

$$\tau = (k_0 L)^{\frac{1}{3}} \sin\theta_{\mathbf{eff}} , \qquad \text{(A4.1)}$$

$\theta_{\mathbf{eff}}$ is given by

$$\sin\theta_{\mathbf{eff}} = n_t , \qquad \text{(A4.2)}$$

and equation (A4.2) is validated by our assumption that the region between the turning point and the critical surface can be described by a plane-parallel geometry. Once we know the value of τ, the absorption coefficient for this ray is calculated from an approximate expression for the linear absorption coefficient (see, e.g. AHLSTROM, 1977)

$$A(\tau) \simeq \frac{\Phi^2(\tau)}{\pi} \qquad \text{(A4.4)}$$

$\Phi(\tau)$ is the well known Ginzburg function (GINZBURG, 1970), for which we use the following expression:

$$\Phi(\tau) \simeq 2.24\ \tau \exp\left\{-\frac{2}{3}\tau^3\right\} . \qquad \text{(A4.5)}$$

Thus as a ray is traced through the plasma we can ascribe to it a particular absorption coefficient A_r calculated as described above. We approximate the laser beam by a large number of rays, tracing each ray through the plasma, and attributing to each an absorption coefficient A_{ri}, where i is the index of the ray. If we assume that all rays have the same intensity, the overall absorption coefficient for the beam is given by

$$A = 100\left\{\frac{1}{N}\sum_{i=1}^{N} A_{ri}\right\} \text{ percent} \qquad \text{(A4.6)}$$

where N is the number of rays in the beam.

By choosing a particular geometry, i.e. planar, elliptical or rippled, the resonance absorption can be estimated by a summation over all the rays in the incident beam. It is noted that this absorption fraction will be affected by the spatial profile in the incident beam, i.e. the number density variation across it (HOWARD, 1979). However, the routine was developed to enable a general estimate of the importance of the resonance absorption, and a comparison between geometries, to be obtained. It was, therefore, felt that the use of a uniform collimated incident beam would serve these requirements best, rather than to introduce a further parameter such as beam spatial profile — especially as this parameter is far from well-known in the focal region of a high power laser beam, formed by a nonideal system, in a highly nonlinear medium. It is also noted that the results obtained from the routine, were only as good as the modelling of the iso-density contours used, and that it is only through this modelling that self-consistency can be introduced into the problem.

REFERENCES

ABRAMS, R.L., 1974, Appl. Phys. Lett., 25, 609
AHLSTROM, H.G., 1977, LLNL Report, UCRL-79819
ALLEN, J.E. and ANDREWS, J.G., 1970, J. Plasma Phys., 4, 187
ANTHES, J.P. *et al.*, 1979, Appl. Phys. Lett., 34, 841
AZECHI, H. *et al.*, 1978, Paper IAEA-CN-37-M-4 presented at the 7th Int. Conf. on Plasma Physics and Controlled Nuclear Fusion Research, Innsbruck, 23-30 August, 1978

BALDIS, H.A. *et al.* 1975, Opt. Commun. 15, 311
BASOV, N.G. and KROKHIN, O.N., 1964, Sov. Phys. JETP, 19, 123
BASOV, N.G. *et al.*, 1975, Sov. Phys. JETP, 40, 61
BASOV, N.G. *et al.*, 1979, Sov. J. Plasma Phys., 5, 407
BEAULIEU, A.J., 1970, Appl. Phys. Lett., 16, 504
BEGG, I.M. and CAIRNS, R.A., 1976. J. Phys. D., 9, 2341
BICKERTON, R.J., 1973, Nucl. Fusion, 13, 457
BORN, M. and WOLF, E., 1970, *Principles of Optics*, Chapter 9, Pergamon Press, Oxford.
BUCHL, K. *et al.*, 1972, Appl. Phys. Lett., 20, 3

COLE, A.J. *et al.*, 1981, Opt. Commun., 36, 51
COLOMBANT, D.G. and MANHEIMER, W.M., 1979, NRL Memo Report 4083
CONRADY, A.E., 1957, *Applied Optics and Optical Design*, Dover Publications Inc., New York.
COTTLES, V. *et al.*, 1977, LANSL Progress Report LA-7328-PR, pp.99-103

DENISOV, N.G., 1957, Sov. Phys. JETP, 4, 544.
DONALDSON, T.P. and SPALDING, I.J., 1976, Phys. Rev. Lett., 36, 467
DONALDSON, T.P., HUBBARD, M. and SPALDING, I.J., 1976, Phys. Rev. Lett., 37, 1348
DONALDSON, T.P., SPALDING, I.J. and WOOLEY, R.A., 1977, Opt. Commun. 22, 207
DRAKE, J.F. *et al.* 1974, Phys. Fluids, 17, 778
DUMANCHIN, R. and ROCCA SERRA, J., 1969, C.R. Acad. Sci., 269, 916.
DYER, P.E. *et al.* 1976, J. Phys. D., 9, 373

ESTABROOK, K., 1976, Phys. Fluids, 19, 1733
ESTABROOK, K. and KRUER, W.L., 1977, LLNL Annual Report, UCRL-50021-76, section 4
EVANS, R., 1980, SRC Rutherford Laboratory Annual Report RL-80-026

FABRÉ, E. *et al.*, 1974, Paper IAEA-CN-33-F3-6 presented at the 3rd Int. Conf. on Plasma Physics and Controlled Nuclear Fusion Research, Tokyo
FABRÉ, E. *et al.*, 1977, Paper I.4 presented at the 11th European Conference on Laser Interaction with Matter, Oxford.
FOSTER, J.M. *et al.*, 1979, AWRE unpublished report SPE N 26/79
FORSLUND, D.W. *et al.*, 1977, *Recent Advances in Plasma Physics, Workshop*, pp.107-122, (B. Buti, ed.), Indian Acad, Sci.
FRANKE, G. 1966, *Physical Optics in Photography*, p. 84, Focal Press Ltd – London and New York.
FRANKLIN, R.N. 1977, Rep. Prog. Phys., 40, 1369

GARBAN, C. *et al.* 1978, J. de Physique – Lett, 39, L 165.
GARBAN-LABAUNE, C. *et al.*, 1980. J. de Physique – Lett., 41, L 463.
GATENBY, P. and WALKER, A.C., 1979, Culham Laboratory Report CLM-R 192
GINSBURG, V.L., 1970, *Propagation of Electromagnetic Waves in a Plasma* Pergamon Press, Oxford.

GITOMER, S.J. and HENDERSON, D.B., 1979, Phys. Fluids, 22, 364
GODWIN, R.P. *et al.*, 1977, Z. Nat. 32a, 1100
GOLDMAN, L.M. *et al.*, 1973, Phys. Rev. Lett., 31. 1184
GORBUNOV, L.M. *et al.*, 1978, JETP Lett., 27, 226
GORBUNOV, L.M. and POLYANICHEV, A.N., 1978, Sov. Phys. JETP, 47, 290
GORBUNOV, L.M. and POLYANICHEV, A.N., 1979, Sov. J. Plasma Phys., 5, 316
GRAY, D.J. *et al.*, 1980, Plasma Phys., 22, 967
GREK, B. *et al.*, 1977, Phys. Rev. Lett., 38, 898
GREK, B. *et al.*, 1978, Phys. Rev. Lett., 41, 1811
GUNN, S.R., 1976, LLNL Report UCID 17308

HAAS, R.A. *et al.*, 1976, J. Appl. Phys., 47, 1318
HAAS, R.A. *et al.*, 1977, Phys. Rev. Lett., 39, 1533
HAINES, M. 1979. Scottish Universities Summer School in Physics — Laser-Plasma Interaction, St. Andrews
HOWARD, J.E., 1977, University of Wisconsin Report UWFDM-188
HOWARD, J.E., 1979, (Private communication)
HUBBARD, M. and MONTES, A., 1978, Culham Laboratory Report CLM R 189
HULL, D. *et al.*, 1979, AWRE unpublished report SFON 8/79
JANNITTI, E and TONDELLO, G., 1974, Opt. Commun. 10, 186
JANNITTI, E. *et al.*, 1975, J. Appl. Phys., 46, 3096
JOHNSTON, T.W. and DAWSON, J.M., 1973, Phys. Fluids, 16, 722

KARTTUNEN, S.J. and SALOMAA, R.R.E., 1979, Plasma Phys., 21, 247
KARTTUNEN, S.J., 1979, D. Tech. Thesis, Helsinki University
KESSEL, van C.G.M., *et al.*, 1976, Paper presented at the 10th European Conf. on Laser Interaction with Matter, Palaiseau, October, 1976.
KLER, C., 1980, (Private communication)
KRUER, W.L. *et al.*, 1975, Phys. Rev. Lett., 35, 1076.
KRUER, W.L., 1979(a), (Private communication)
KRUER, W.L., 1979(b), LLNL report UCRL-82585
KRUER, W.L., 1979(c), LLNL report UCRL-82701
KRUER, W.L. and ESTABROOK, K.G., 1980, LLNL Annual Report UCRL-50021-79, section 3

LANDAU, L.D. and LIFSHITZ, E.M, 1960, *Electrodynamics of Continuous Media*, vol. 8 of course on Theoretical Physics—Ch. X, Pergamon Press, Oxford
LEHMBERG, R.H., 1978. Phys. Rev. Lett., 41, 863.
LITTLE, V.I., SELDEN, A.C. and STAMATAKIS, T., 1974, J. Phys. E., 7, 962
LIU, C.S., 1976, Advances in Plasma Physics, 6, 121

MANES, K.R. *et al.*, 1977, Phys. Rev. Lett., 39, 281
MANHEIMER, W.M. and COLOMBANT, D.G. 1978, Phys. Fluids, 21, 1818
MARTIN, T.J., 1971, Culham Laboratory Note CLM-PDN-3/71 - Unpublished
MARTINEAU, J. *et al.*, 1974, Opt. Commun., 12, 307
MARTINEAU, J. *et al.*, 1975, Opt. Commun., 15, 404
MAYER, F.J. *et al.*, Phys. Rev. Lett., 44, 1498
MITCHELL, K.B., *et al.*, 1975, Appl. Phys. Lett., 27, 11
MONTES, C. and PEYRAUD, J., 1980, J. de Physique, 41, C3-387
MONTES, A. and HUBBARD, M., 1979, Plasma Phys., 21, 885
MONTES, A., HUBBARD, M., KLER, C. and SPALDING, I.J., 1980, Appl. Phys. Lett., 36, 652
MONTES, A., 1981, D. Phil. Thesis, Oxford University
MORGAN, F. *et al.*, 1978. AWRE Unpublished Report SFO N 4/78
MUELLER, M.M., 1973, Phys. Rev. Lett., 30, 582
MUELLER, M.M., 1977, LANSL Report LA-7328-PR
NG, A. *et al.*, 1978, Opt. Commun., 25, 116
NG, A. *et al.*, 1979(a), Phys. Rev. Lett., 42, 307
NG, A. *et al.*, 1979(b), Phys. Rev. Lett., 43, 1502
NG, A. *et al.*, 1981, Opt. Commun., 36, 200

NUCKOLLS, J. *et al.*, 1972, Nature, 239, 139

OFFENBERGER, A.A. *et al.*, 1978, Can. J. Phys., 56, 381

PANT, H.C. *et al.*, 1980, Appl. Phys., 23, 183
PHILLION, D., 1977, LLNL Annual report UCRL-50021-76, section 5
PATEL, C.K.N., 1964, Phys. Rev. Lett., 13, 617
PATEL, C.K.N. *et al.*, 1964, Bull. Amer. Phys. Soc., 9, 500
PATEL, C.K.N. *et al.*, 1965, Appl. Phys. Lett., 7, 290

RANDALL, C. *et al.*, 1979, Phys. Rev. Lett., 43, 924
RANDALL, C. and DeGROOT, J.S., 1979, Phys. Rev. Lett., 42, 179.
RAVEN, A.L. *et al.*, 1978, Phys. Rev. Lett., 41, 554
RIPIN, B.H., 1977, NRL Memo report 3684
RIPIN, B.H. and McLEAN, E., 1979, NRL Memo report 3964
RIPIN, B.H. *et al.*, 1979, NRL Memo report 3965
ROSEN, M.D. *et al.*, 1978, LLNL Preprint UCRL-82146

SCHAPPERT, G.T. and HERBST, M.J. 1975, Appl. Phys. Lett., 26, 314
SEELEY, J. 1978, *Narrow bandpass Filters at* 10.6 μm *for Laser Applications*, (Private communication)
SHEARER, J.W. and BARNES, W.S., 1971, *Laser Interaction and Related Plasma Phenomena*, (H.J. Schwartz and H. Hora, eds), vol. 1, 307, New York - Plenum
SIEGMAN, A.E., 1971, Laser Focus, May 1971, 42
SIGEL, R., 1977, Invited paper presented at the 3rd International Congress on Waves and Instabilities in Plasmas, Palaiseau
STAMATAKIS, T. and SELDEN, A.C., 1976, Phys. Lett., 58A, 221.
STAMATAKIS, T., 1977, Ph. D. Thesis, Royal Holloway College, University of London
STAMPER, J. and RIPIN, B.H., 1978, Phys. Rev. Lett., 40, 1177

TANG, C.L., 1966, J. Appl. Phys., 37, 2945
TEWARI, D.P. and SHARMA, R.R., 1979, J. Phys. D., 12. 1019
THOMSON, J.J. *et al.*, 1978, Phys. Fluids, 21, 707
TONON, G. and RABEAU, M., 1973, Plasma Phys., 15, 871
TURNER, R.E. and GOLDMAN, L.M., 1980, Phys. Rev. Lett., 44, 400
TUTTLEBEE, W.H.W., 1979, Report to the University of Southampton Faculty of Engineering and Applied Sciences.

VALEO, E.J. and ESTABROOK, K.G., 1975, Phys. Rev. Lett., 34, 1008

WALKER, A.C. *et al.*, 1978, J. Phys. D., 11, 2285
WHITE, R.B. and CHEN, F.F., 1974, Plasma Phys., 16. 565
WOOD, O.R., 1974, Proc. IEEE, 62, 355
WRIGHT, R. 1978, (Private communication), AWRE unpublished note